UNIVERSIDADE DE SANTIAGO DE COMPOSTELA

Departamento de Física de Partículas
Instituto Galego de Física de Altas Enerxías

TESE DE DOUTORAMENTO

Development and operation of tracking detectors in silicon technology for the LHCb upgrade

Presentada por:
Pablo Rodríguez Pérez

Dirixida por:
Abraham Antonio Gallas Torreira
Bernardo Adeva Andany

Data:
23 de Decembro de 2013

USC
UNIVERSIDADE
DE SANTIAGO
DE COMPOSTELA

D. ABRAHAM GALLAS TORREIRA, profesor contratado doutor de Física Atómica, Molecular e Nuclear da Universidade de Santiago de Compostela e D. BERNARDO ADEVA ANDANY, Catedrático de Física Atómica, Molecular e Nuclear da Universidade de Santiago de Compostela,

FAN CONSTAR:

Que a memoria titulada "*Development and operation of tracking detectors in silicon technology for the LHCb upgrade*" foi realizada por **Pablo Rodríguez Pérez** baixo a súa dirección e que constitúe a Tese que presenta para optar ao Grao de Doutor en Física.

Santiago de Compostela, a December 30, 2013.

Asdo. **Abraham Gallas Torreira**
Codirector da tese

Asdo. **Bernardo Adeva Andany**
Codirector da tese

Asdo. **Pablo Rodríguez Pérez**
Autor da tese

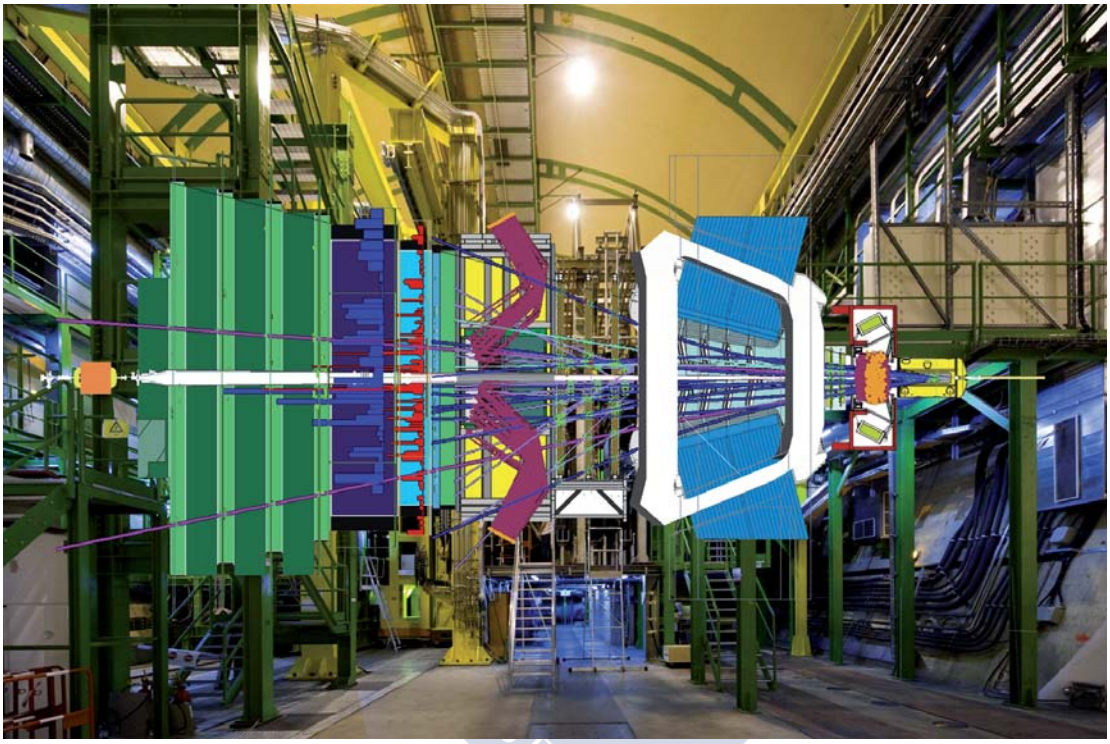

Figure 1: The LHCb experiment

Figure 2: The LHCb collaboration

Acknowledgments

I'm quite sure that every single person interested in Physics knows about CERN. *The European Organization for Nuclear Research* is like an utopia come true, a place where people can focus in their cutting edge investigations, and the technology is pushed to their limits with the aim of the understanding of the Universe. WOW!. As physicist, it was an honour for me to work at CERN, the world's most stimulating place, and I want to use this opportunity to thank all the people who help me to get here (some of them are listed below).

I would like to begin expressing my appreciation to my supervisors, Abraham Gallas and Bernardo Adeva, for give me the opportunity to join the High Energy Physics group, for their support and time dedicated to my learning.

Many people help me at CERN during these years, and I learned a lot from them. An incomplete list of them will contain to Helge Voss, Fred Blanc, Mark Tobin, Sandra Saornil and Frédéric Dupertuis. Also to Paula Collins, Lars Eklund, Chris Parkes, Daniel Hynds, Heinrich Schindler, Panagiotis Tsopelas and Jan Buytaert.

Tamén lles debo moitísimo os meus compañeiros da Universidade de Santiago, tanto no apartado profesional coma no persoal. Quero aproveitar esta ocasión para darlle as gracias a Eliseo, Pablo V., Daniel Esperante, Antonio Pazos e Antonio Romero, a Víctor, Marcos, Álvaro, Paula, Saborido e Cibrán, Xabier, Diego, Juan Llerena, Mari Carmen e a *Rolando*.

Remato cos máis importantes: os meus pais e irmáns que me apoiaron incondicionalmente durante toda a miña carreira. E sobre todo, gracias a Sonia, por animarme a comezar este proxecto e por confiar en min e estar sempre o meu carón.

A adicatoria desta tese ten dúas partes. Por un lado, botando unha ollada ó camiño que percorrín ata aquí, quero adicarlle a tese á memoria do meu irmán **Víctor Rodríguez Pérez**. Mirando cara ó futuro, adícolle esta tese os meus fillos **Mar** e **Tomás**, que son certamente os pequechos máis grandes do mundo.

USC
UNIVERSIDADE
DE SANTIAGO
DE COMPOSTELA

Poets say science takes away from the beauty of the stars - mere globs of gas atoms. I, too, can see the stars on a desert night, and feel them. But do I see less or more? (*Comic strip from "Calvin & Hobbes", created by Bill Patterson*)

Richard P. Feynman

This picture was taken by *Voyager 1* on 1990, at 6.000.000.000 Km from Earth.

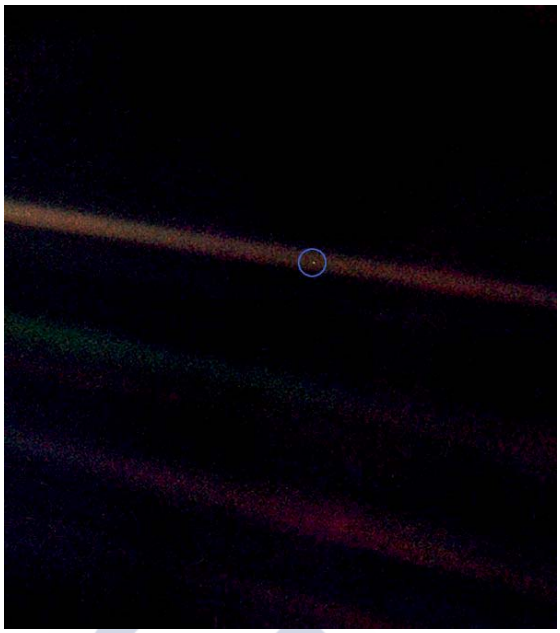

From this distant vantage point, the Earth might not seem of any particular interest. But for us, it's different. Consider again that dot. That's here. That's home. That's us. On it everyone you love, everyone you know, everyone you ever heard of, every human being who ever was, lived out their lives. The aggregate of our joy and suffering, thousands of confident religions, ideologies, and economic doctrines, every hunter and forager, every hero and coward, every creator and destroyer of civilization, every king and peasant, every young couple in love, every mother and father, hopeful child, inventor and explorer, every teacher of morals, every corrupt politician, every "superstar," every "supreme leader," every saint and sinner in the history of our species lived there – on a mote of dust suspended in a sunbeam.

Desde este alejado punto de vista, tal vez la Tierra no tenga un interés particular, pero para nosotros es diferente. Consideremos nuevamente este punto. Eso de ahí, es nuestro hogar. Somos nosotros. En él estan todos los que amamos, todo los que conoces, todos de quiénes haz oído hablar, y todos los seres humanos que existieron, que han vivido. La suma de nuestra alegría y sufrimiento, miles de religiones verdaderas, ideologías y doctrinas económicas, cada cazador y recolector, cada héroe y cobarde, cada creador y destructor de civilizaciones, cada rey y cada campesino, cada joven pareja de enamorados, cada madre y padre, cada niño ilusionado, inventor y explorador, cada maestro de moral, cada político corrupto, cada "superestrella", cada "líder supremo", cada santo y pecador en la historia de nuestra especie vivió ahí: en una mota de polvo suspendida en un rayo de Sol.

Carl Sagan

Contents

Glossary

ADC Analog to Digital Converter. 39, 114, 129

ASIC Application-Specific Integrated Circuit. 76, 77, 161, 162, 166, 171, 199

CB Control Board. 38, 55, 60

CERN European Organization for Nuclear Research. 9, 13, 15, 163

CNM Centro Nacional de Microelectrónica (http://www.cnm.es/). 78

CU Control Unit. 66

DAQ Data Acquisition. 27, 54

DB Digitizer Board. 34, 37, 38, 41, 55, 60

DCS Detector Control System. 45, 52, 54, 177, 185

DPE Data Point Element. 49

DPT Data Point Type. 48

DSS Detector Safety System. 43, 45, 53, 66, 186

DU Device Unit. 53, 66

DUT Device Under Test. 78, 79, 117, 131, 168

DXF Drawing eXchange Format. 124

ECS Experiment Control System. 27, 41, 43–46, 51–55, 57, 61, 64, 66

EDV Effective Depletion Voltage. 80, 98

FDV Full Depletion Voltage. 157

FE Front End electronics. 27, 34, 35, 55

FIR Finite Impulse Response. 132

FSM Finite State Machine. 48, 51–53, 55, 62, 64, 67, 68

GAES Grupo de Altas Energías de la Universidad de Santiago de Compostela. 107, 136, 189

HLT High Level Trigger. 25, 26, 41, 53, 54, 72, 75, 188

HPK Hamamatsu Photonics. 103, 120

HV High Voltage. 27, 54, 76

IP Impact Parameter. 27

IT Inner Tracker. 19, 22, 31, 33, 35–39, 41, 42, 45, 48, 55, 58, 64, 66, 68, 105, 184, 189

JCOP Joint COntrols Project (http://en-dep.web.cern.ch/en-dep/internal/JCOP/index.htm). 44, 45

L0 Level 0 trigger. 25, 26, 34

LED Light-Emitting Diode. 151

LEP Large Electron Positron collider. 16, 18

LHC Large Hadron Collider. 9, 10, 15–18, 20, 21, 25, 27, 41, 72, 101, 184

LHCb Large Hadron Collider beauty experiment. 9, 10, 17–22, 24–27, 31, 33, 38, 41, 43–46, 52–55, 57, 58, 64, 68, 184–186

LU Logical Unit. 66

LV Low Voltage. 27, 76

MIP Minimum Ionizing Particle. 94, 95, 118, 158

MPV Most Probable Value. 118, 156, 158, 175

MWPC Multi-Wire Proportional Chamber. 24

NIEL Non-ionizing Energy Loss. 98

PA Pitch Adapter. 122–125

PV Primary Vertex. 18, 20, 27, 72

S/N Signal Noise ratio. 158

SB Service Box. 33, 34, 37, 38, 41

SCADA Supervisory Control And Data Acquisition. 45

SM Standard Model. 14, 15, 183

SPECS Serial Protocol for the Experiment Control System. 185

SPS Super Proton Synchrotron. 11, 13, 16

ST Silicon Tracker. 27, 31, 41, 46, 53, 55, 58, 61, 177, 183–185

SV Secondary Vertex. 18, 72

TDC Time Digital Converter. 115

TFC Time and Fast Control. 27, 37, 38, 41, 45, 53, 54, 186

ToA Time of Arrival. 107, 126, 163

ToT Time over Threshold. 107, 126, 164, 175

TPG Thermal Pyrolitic Graphite. 73

TT Tracker Turicensis. 19, 21, 22, 31, 33, 35–39, 41, 42, 122, 136, 184, 189, 194

USC Universidad de Santiago de Compostela. 107, 137, 145, 189

VELO VErtex LOcator. 10, 11, 19–22, 25, 27, 71–73, 75–78, 80, 129, 177, 186–188

VLSI Very Large Scale Integration. 101

USC
UNIVERSIDADE
DE SANTIAGO
DE COMPOSTELA

1 Introduction

Nowadays the European Organization for Nuclear Research (CERN) is focused in its last accelerator, the *Large Hadron Collider* (LHC), and the associated experiments which are running since November 2009. The LHC is the most powerful accelerator ever build, able to achieve energies at which some of the fundamental particles, which were never seen before, are measurable. The experiments around the four interaction points of the LHC were designed to provide independent and comparable results from the collision. The goal is to get information from energy densities never achieved before in laboratory conditions, and face them with the Standard Model predictions.

One of the experiments at the LHC is dedicated to the study of heavy flavour physics: the LHCb experiment [1]. Its primary goal is to look for indirect evidence of new physics in CP violation and rare decays of beauty and charm hadrons. This knowledge will help us to understand the reason why there is a lack of antimatter in our Universe, as our theories predict that just after the Big-Bang the balance between matter and antimatter was equilibrated.

This thesis is devoted to the design, building and commissioning efforts of silicon tracker detectors for the LHCb experiment and its upgrade, planned for 2018.

1.1 Context

The antimatter and antiparticles were predicted in 1928 by Paul Dirac. Dirac realised that his relativistic version of the Schrödinger wave equation for electrons predicted the possibility of antielectrons. These were discovered by Carl D.

Anderson in 1932 and named positrons, winning the Noble Prize in 1936 for such discovery. Since then, many other types of antiparticles were found to be produced naturally in radioactive decays or in cosmic rays. They were also produced artificially in accelerators and studied under well controlled conditions [2].

So far, our models predict that in the Big-Bang, 13700 million years ago, when the Universe cooled enough the energy was converted into same amount of particles of matter and antimatter. For a short time there was a perfect balance, or symmetry, between matter and antimatter. However, shortly after the birth of the Universe the particles acquired their characteristic masses and a phenomenon occurred that differentiated matter and antimatter, causing asymmetry between the two.

When the Universe was 10^{-11} seconds old, the quantity of matter in the Universe already outweighed antimatter, although only by one particle in a billion. Nowadays almost all the objects observable from the Earth seem to be made of matter rather than antimatter. If antimatter-dominated regions of space existed, the characteristic gamma rays produced in annihilation reactions along the boundary between matter and antimatter regions would be detectable.

In 1966 Russian physicist Andrei Sakharov outlined three conditions necessary for the matter to predominate in the Universe. One of which, called *CP violation*, says that there should be a measurable difference between matter and antimatter. The Standard Model of particle physics tell us that an experiment made of particles witch charge C and parity P will get almost the same results than the experiment made with antiparticles which charge -C and parity -P. It would not be completely identical because the Standard Model allows some degree of asymmetry between matter and antimatter, although this asymmetry is three orders of magnitude less than the needed to explain the amount of matter that survived after the Big-Bang. Therefore a new model which could explain a higher asymmetry degree between both is needed, and ultimately to explain our universe.

The experiment LHCb uses the energy density provided by the LHC to try to discover asymmetry between particles and antiparticles (CP violation) that can not be explained by the Standard Model, and thus have evidence that allow us to build a new model for Physics.

1.2 Thesis arrangement

This thesis is devoted to silicon tracking detectors for the current and future LHCb experiment. The LHCb experiment is introduced in Chapter 2, together with its goals and a brief description of its detectors. Afterwards it begins the first part of the thesis, devoted to the Silicon Tracker detector. Chapter 3 covers a detailed description of the Silicon Tracker infrastructure. A description of the Detector Control System, which I developed together with Daniel Esperante [3], Alba Sambade [4], Angela Buechler and Sandra Saornil, is given in Chapter 4.

The second part of the thesis is devoted to the LHCb upgrade, in particular to the VErtex LOcator upgrade. The VErtex LOcator (VELO) upgrade goals

and constraints are described on Chapter 5. The thesis covers my work with two different silicon technologies, pixels and micro-strips, for that reason a brief introduction of the silicon detectors is given in Chapter 6.

Several silicon micro-strip prototypes were characterized in test-beam campaigns and in laboratory as part of the VELO Upgrade project. The results of these test are showed in Chapter 7. Three pixel detectors, two of them irradiated up 2.5×10^{15} $1\text{MeVn}_{\text{eq}}/\text{cm}^2$, were also characterized in the Super Proton Synchrotron (SPS) test-beam area. The results are detailed in Chapter 8.

The thesis ends with the conclusions in Chapter 9 and two summaries, first in English (Chapter 10) and then in Galician (Chapter 11) which are mandatory to present a thesis at the USC. Two appendix with more detailed information about the runs taken in the test-beam campaigns and metrology data for a micro-strip prototype are added at the end.

USC
UNIVERSIDADE
DE SANTIAGO
DE COMPOSTELA

2

The LHCb experiment

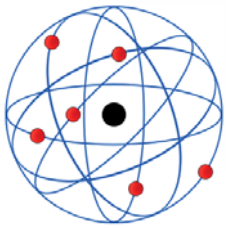

Our understanding of the matter we are made of has dramatically changed in the last century, and still is evolving. Up to the beginning of the XX century atoms were the utter explanation of the matter, and the difference between two elements like iron and oxygen was explained in terms of the difference between their atoms. Then, in 1897, Thomson discovered the electron and proposed a new atomic model in 1904 according to which all the atoms were essentially the same, with the only difference of the number of electrons inside of it. Based on the *gold foil experiment*, Rutherford introduced in 1911 the atomic nucleus containing the positive charge of the atom, balancing the electron's negative charge. He also proposed the existence of neutral charged particles (neutrons) in 1920 to explain the discrepancy between the atomic mass and the atomic number.

In 1930, to explain the energy spectrum of the electron observed in β decays, Pauli postulated the existence of the electronic neutrino [5] (ν_e), which was observed much later in 1956 [6] because of his small probability of interaction. In the 1960s, experiments showed that the proton and the neutron are also made of smaller particles, the u and d quarks. Those four particles constitute the first family of elementary particles: the leptons e^- and ν_e and the quarks u and d and their respective antiparticles. The whole picture of the particles (Figure 2.1) was completed in 1983 by Carlo Rubia and Simon van der Meer when they found the W [7] and Z [8] bosons at CERN, using the most powerful accelerator of the moment: the SPS.

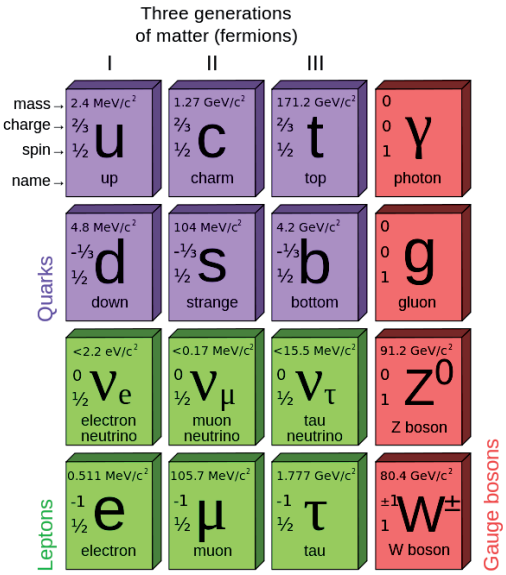

Figure 2.1: The particles in the standard model can be sorted into two groups: fermions and bosons. Fermions are the building blocks of matter. They all obey the Pauli exclusion principle. Bosons are force-carriers. They carry the electromagnetic, strong, and weak forces between fermions.

2.1 The Standard Model

The Standard Model (SM) emerged as the theory that describes matter components and their interactions. It was built over 50 years and evolved to include successive observations. The SM asserts that the material in the universe is made up of elementary fermions interacting through fields, of which they are the sources. The particles associated with the interaction fields are bosons. Although the SM is probably one of the most predictive and tested physics theory, it suffers from a few issues that hint for a more complete underlying theory.

2.1.1 The Higgs boson

The SM has been supported by a great deal of experimental evidence and it has proven particularly successful in anticipating the existence of previously undiscovered particle like the W^+, W^-, and Z^0 bosons; the force mediators of the weak interaction. The theory identifies the force mediators of the strong interaction as gluons, massless electrically neutral bosons that carry color charge and bind the quarks together in nucleons. However, the SM does not explain the origin of the mass of the particles, nor why some particles are very heavy while others are massless. The answer is the so-called Higgs mechanism. In this theory, the whole space is filled with a *Higgs field*, and by interacting with this field, particles acquire their mass. This Higgs field has at least one new particle

associated with it, the Higgs boson, which was detected[1] at LHC [9, 10].

Although the Higgs boson is covered, the SM does not offer a unified description of all the fundamental forces, as it remains difficult to construct a theory of gravity similar to those for the other forces.

2.1.2 Dark matter and dark energy

Cosmological and astrophysical observations have shown that only a tiny 4% of the entire Universe is made of bosons and fermions as described by the SM. Most of the Universe is made up of invisible substances known as 'dark matter' (23%) and 'dark energy' (73%). These do not emit electromagnetic radiation, and we detect them only through their gravitational effects. A possible hypothesis is that dark matter is made of neutral (but still undiscovered) supersymmetric particles. Although these particles will not be seen by the detectors, their existence can be proven if there is a systematic lack of energy detected in some disintegration channels.

Dark energy appears to be associated with the vacuum in space. It is homogeneously distributed throughout the Universe and its effect is not diluted as the Universe expands. The even distribution means that dark energy does not have any local gravitational effects, but rather a global effect on the Universe as a whole. This leads to a repulsive force, which tends to accelerate the expansion of the Universe. The rate of expansion and its acceleration can be measured by observations based on the Hubble law. These measurements, together with other scientific data, have confirmed the existence of dark energy and provide an estimate of just how much of this mysterious substance exists.

2.1.3 The antimatter mystery

For the past 50 years and more, laboratories like CERN have routinely produced antiparticles, and in 1995 CERN became the first laboratory to create anti-atoms artificially [11]. The LHC accelerator can achieve energy densities never reached before since the birth of the Universe, when equal amounts of matter and antimatter must have been produced after the Big-Bang. So if matter and antimatter annihilate, and we and everything else are made of matter, why do we find ourselves living in a Universe made exclusively of matter? The way to solve the disappearance of antimatter is by studying both particles and antiparticles. For a short time there was a perfect balance or symmetry between matter and antimatter. However as the Universe expanded and cooled it went through a series of changes in its composition. Particles acquired their characteristic masses and a phenomenon occurred that differentiated matter and antimatter, causing asymmetry between the two. I.e. antimatter is not a perfect *reflection* of matter. In other words, after the Big-Bang, physical laws must have acted differently for matter and antimatter.

[1] To be more precise, a particle compatible with the Higgs boson

2.2 The LHC

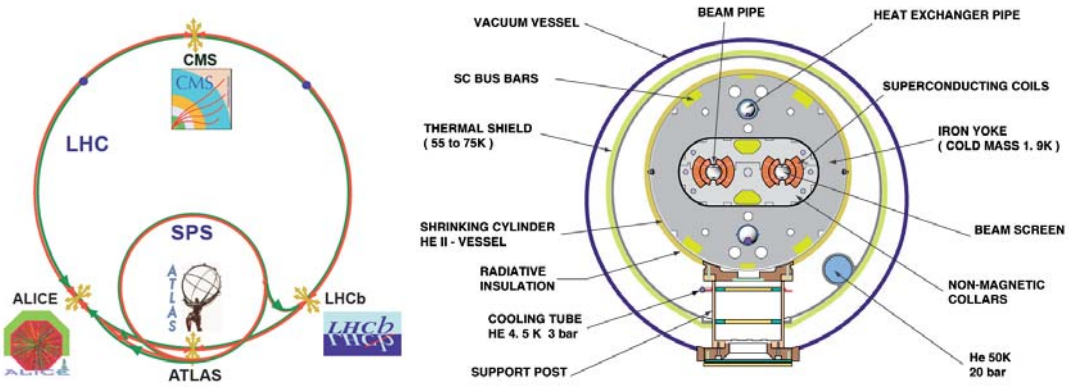

(a) LHC ring (b) LHC dipole magnet

Figure 2.2: Left figure shows the location of the LHC ring and its four experiments. Right figure is a sketch of a LHC superconducting dipole magnet

The Large Hadron Collider (LHC) [12] is currently the world's most powerful particle accelerator located in the world. Being situated in a 27 km ring buried 100 m deep below the countryside on the outskirts of Geneva (Switzerland), the LHC is installed in the tunnel that previously housed the Large Electron Positron collider (LEP).

The aim of the LHC project is to test the Standard Model, and, even more, to look for signals of physics beyond it. In the LHC, protons collide at a centre-of-mass energy of $\sqrt{s} = 8$ TeV, the highest ever achieved in pp collisions. At these energies new discoveries, as, e.g., the existence of supersymmetry (SUSY), are likely to be made. Also, the until now unobserved particle in the Standard Model, the Higgs-boson, was detected. Other research topics concern high-precision B physics, and the study of a new phase of matter produced in heavy-ion collisions. For the latter, the LHC is filled in dedicated runs with heavy ions (e.g., Pb) instead of protons.

The proton beams in the circular ring are accelerated in opposite directions to an energy of up to 4 TeV. Before reaching that energy, they have passed through a chain of preaccelerators. At the last stage of the preacceleration, the SPS delivers 450 GeV protons to the LHC, where they are boosted to the final energy.

At such an energy, protons require a huge magnetic field to maintain their orbit. This field is provided by superconducting magnets. As the two proton beams travel in opposite directions through the ring, separate beam pipes with opposite magnetic field directions are needed. A two-in-one solution is chosen, where the magnet coils surrounding the two beam channels are firmly embodied inside the same iron yoke. The whole superconducting magnet is placed inside a cryostat, containing superfluid helium with a temperature of 1.9 K (see Figure 2.2b).

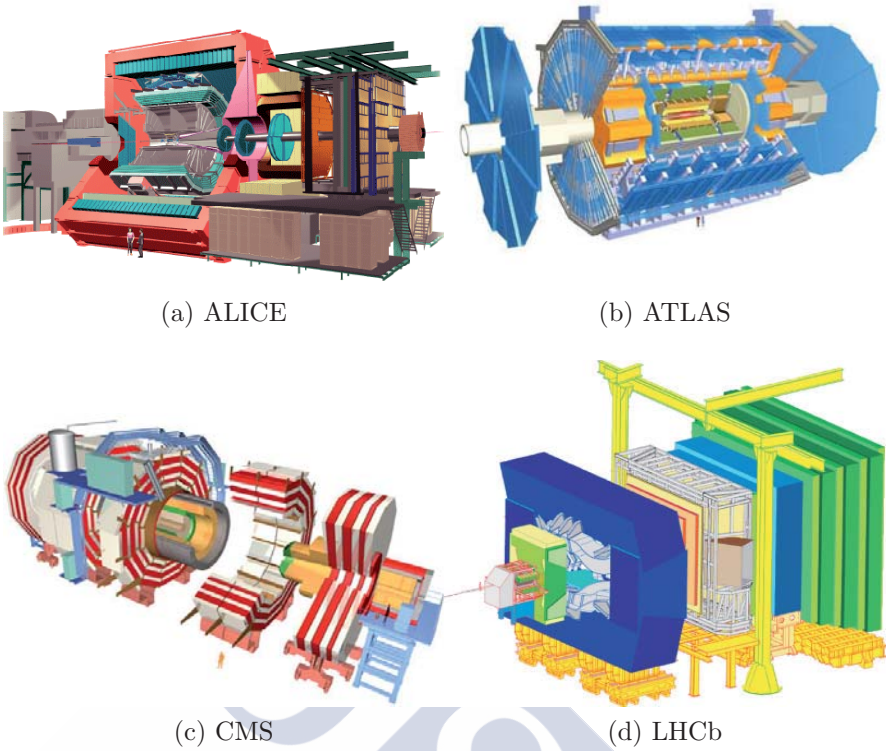

(a) ALICE (b) ATLAS

(c) CMS (d) LHCb

Figure 2.3: LHC experiments

The four experiments at the LHC are located at each of the four interaction points. Here, the beams cross over to the other beam pipe and collide under a small angle. After filling, both beams consist of 2808 bunches with 10^{11} protons each. The time between two consecutive bunch crossings is 25 ns, which sets the basic clock frequency for the detector electronics to 40 MHz. As a consequence of the filling procedure, however, some bunches are empty. Therefore, the average bunch crossing frequency of filled bunches is somewhat lower, namely 30 MHz.

Figure 2.2 shows the location of the four experiments along the LHC ring. ATLAS [13] (figure 2.3b) and CMS [14] (figure 2.3c) are two general-purpose experiments. Both are central detectors constructed by large, international collaborations. Their main physics goals are the search for the Higgs boson and SUSY particles. In addition, these experiments plan to study B physics, heavy-ion collisions, and many other interesting phenomena. The ALICE [15] (figure 2.3a) experiment focuses on studying strongly interacting matter at the extreme energy densities in heavy-ion collisions, and performing measurements of the phase transition between hadronic matter and the quark-gluon plasma. The ALICE detector is designed to cope with the higher particle multiplicities that are characteristic for heavy-ion collisions. Finally, LHCb [1] (figure 2.3d) thought for B physics, will be treated in next section.

2.3 The LHCb experiment at the LHC

The LHCb collaboration is currently composed by 565 scientists from 47 universities and laboratories from 15 countries. As ALICE, and in opposition to ATLAS and CMS, LHCb is an experiment with a specific scientific purpose: the study of new physics in the decays of beauty and charm hadrons produced in proton collisions at LHC.

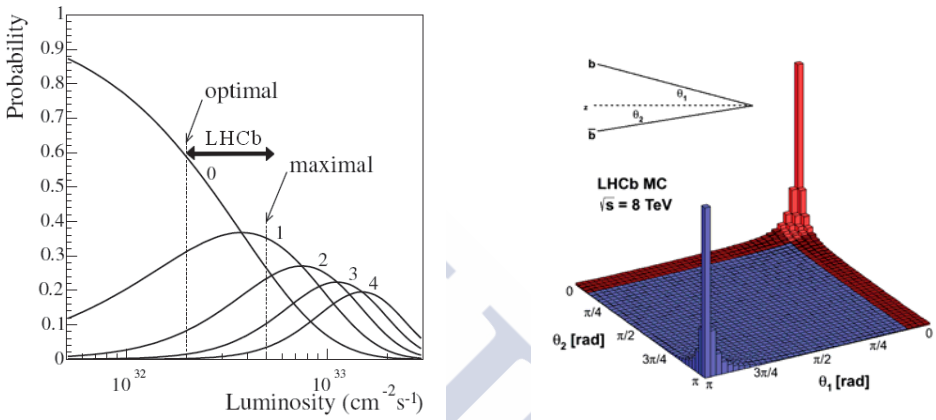

(a) Probability for 0, 1, 2, 3, or 4 inelastic collisions per bunch crossing as function of the luminosity

(b) Angular distribution of b and $\bar{b}$ quarks

Figure 2.4: Some characteristics of pp interaction at LHCb

LHCb experiment is quite different from the others LHC detectors because it is focused in to achieve an excellent momentum and particle identification. Determining correctly the Primary Vertex (PV) and Secondary Vertex (SV) is essential for the physics in the experiment. This is achieved defocusing proton beams near LHCb's interaction point, so the LHCb was designed to work with an instant luminosity of $2 - 5 \cdot 10^{32}\ cm^{-2}s^{-1}$, smaller than LHC's nominal $10^{34}\ cm^{-2}s^{-1}$. In Figure 2.4a we can see that the higher the luminosity the bigger the probability to have more than one PV.

2.3.1 Detectors

Intersection Point 8 of the LHC, previously used by the DELPHI experiment during the LEP time, has been allocated to the LHCb experiment. A modification to the LHC optics, displacing the interaction point by 11.25 m from the centre, has permitted maximum use to be made of the existing cavern for the LHCb components.

LHCb is a single-arm spectrometer with a forward angular coverage from approximately 10 mrad to 300 (250) mrad in the bending (non-bending) plane. The choice of the detector geometry is justified by the fact that at high energies

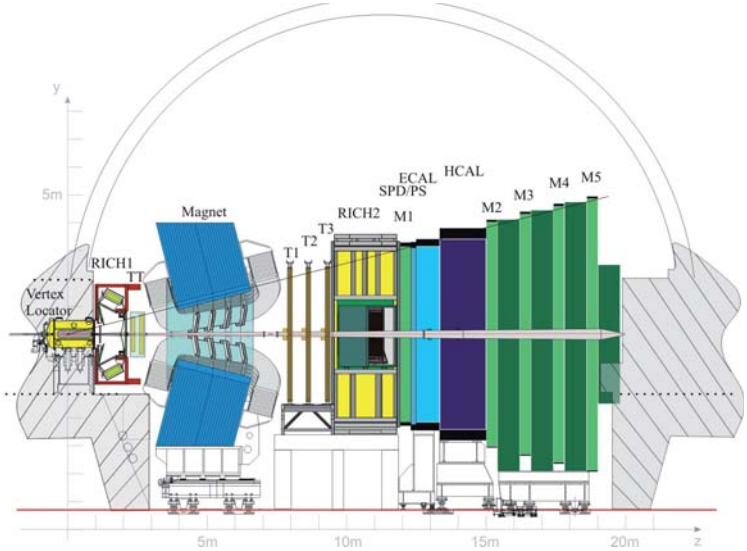

Figure 2.5: Side view of LHCb

both the b and $\bar{b}$ hadrons are predominantly produced in the same forward or backward cone as is shown in Figure 2.4b.

The layout of the LHCb spectrometer is shown in Figure 2.5. The right-handed coordinate system adopted with the z axis along the beam, and the y axis along the vertical. Main elements of LHCb are:

- a spectrometer magnet (warm dipole) providing an integrated field of 4 Tm
- a VErtex LOcator (VELO) system (including a pile-up veto counter)
- a tracking system, made of the Tracker Turiciensis (a silicon micro-strip detector, TT) in front of the spectrometer magnet, and three tracking stations behind the magnet, made of silicon micro-strips in the inner parts (Inner Tracker or IT) and of Kapton/Al straws for the outer parts (Outer Tracker or OT)
- two Ring Imaging Cherenkov counters (RICH1 and RICH2) using Aerogel, C_4F_10 and CF_4 as radiators, to achieve excellent p-K separation in the momentum range from 2 to 100 GeV/c
- a calorimeter system composed of a Scintillator Pad Detector and Preshower (SPD/PS), an electromagnetic (shashlik type) calorimeter (ECAL) and a hadronic (Fe and scintillator tiles) calorimeter (HCAL)
- a muon detection system composed of Multi-Ware Proportional Chambers (MWPC) (except in the highest rate region, where triple-GEM's are used).

2.3.2 The tracking system

The VErtex LOcator

The VErtex LOcator (VELO) [16] contains 88 silicon sensors, positioned along and perpendicular to the beam axis. Figure 2.6 shows a partial view of the VELO as seen from above. Two types of silicon sensors are used: one measures the R coordinate with circular strips centered around the beam axis, the other measures the ϕ coordinate with straight, radial strips. The half-disc modules, shown in 2.6, are arranged in pairs of R and ϕ sensors and mounted back-to-back.

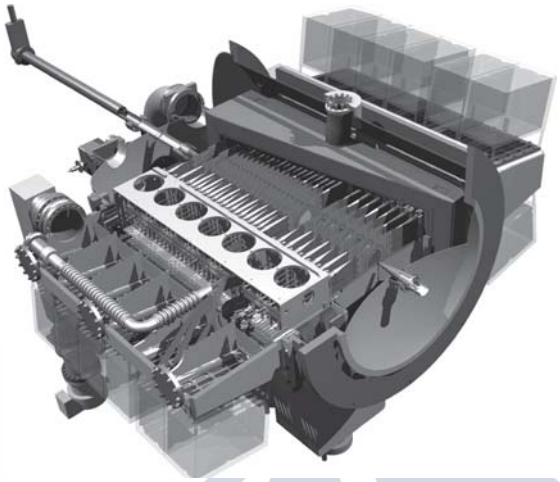

Figure 2.6: Overview of Vertex Locator

The $R-\phi$ geometry has the advantage that it directly gives a projection in the rz plane by using only r measurements. In this projection, forward-going tracks with a high Impact Parameter[2] with respect to the production vertex are easily identified. As it will be seen in section 2.3.4, the trigger exploits this idea by first reconstructing all tracks in the $r-z$ projection, before reconstructing only the ones with a large impact parameter in three dimensions.

Two dedicated silicon stations located upstream of the VELO are used for pile-up veto in the trigger. These two stations, containing r sensors only, have a fast readout that allows them to be used to veto bunch crossings with multiple collisions, as these collisions can not be properly analysed by the LHCb.

As the determination of the PV depends of the distance to the interaction point, the VELO detector was designed to be placed inside the beam pipe. The shorter the extrapolation of a track from its first measurement to the interaction region, the smaller is the error on the reconstructed position of the vertex. The sensitive area of the sensors starts at 8 mm from the beam axis, such that the first measurement of the track is as close to the PV as possible. In order to avoid severe radiation damage, a minimal distance of 3 cm is required when LHC is

[2]The Impact Parameter (IP) is defined as the perpendicular distance between a track and the collision point, also know as *Primary Vertex* or PV.

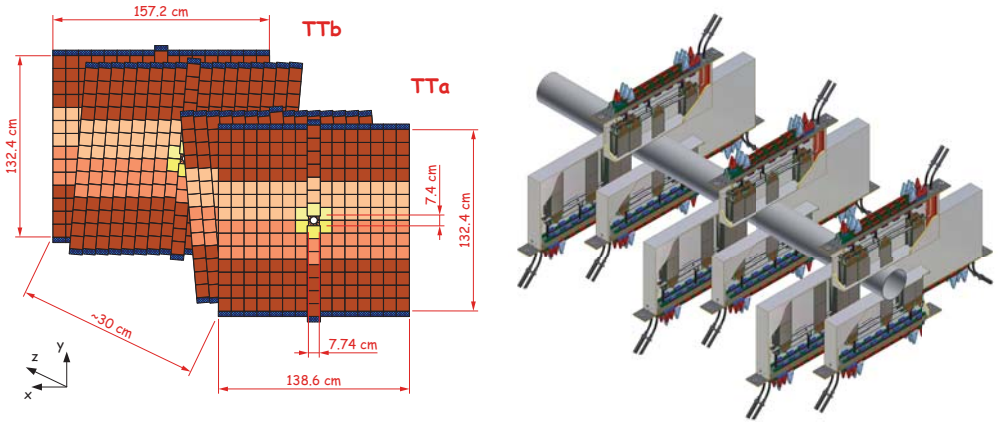

(a) TT's XUVX layers

(b) The 12 boxes (3 stations) of the IT

Figure 2.7: ST Sketches

being filled. Consequently, the VELO is designed so that the two detector halves can be moved away from the beam in the horizontal direction.

A more detailed description of the VELO detector will be given in Chapter 5.

The Tracker Turicensis

The Tracker Turicensis (TT) [17] is located upstream of the LHCb 4 Tm dipole magnet. A sketch of the TT station is show in Figure 2.7a. This 150 cm wide and 130 cm high planar tracking station covers the full detector acceptance. It has been constructed using p-on-n type sensors with a pitch of 183 μm and a thickness of 500 μm with the same design as in the CMS barrel tracker. It is composed of four layers arranged into two half stations separated 30 cm along the beam axis, and in orientation 0^o, 5^o, -5^o, 0^o. Depending on the position in the layer up to four sensors are bonded together giving strip lengths up to 37 cm.

The Inner Tracker

The Inner Tracker (IT) [18] covers the region of highest particle density closest to the LHC beam pipe in the three tracking stations (T1-T3) located downstream of the magnet. An IT station consists of four independent boxes arranged around the beam pipe in a 125 cm wide and 40 cm high cross shape (Figure 2.7). Each box contains four layers of silicon micro-strips in orientation 0^o, 5^o, -5^o, 0^o. The ladders placed left and right of the beam pipe are 22 cm long with a thickness of 410 μm, the ladders above and below the beam pipe are 11 cm in length and with a thickness of 320 μm, in both cases the read-out pitch is 198 μm.

The IT and TT sub-detectors will be described in detail in Chapter 3.

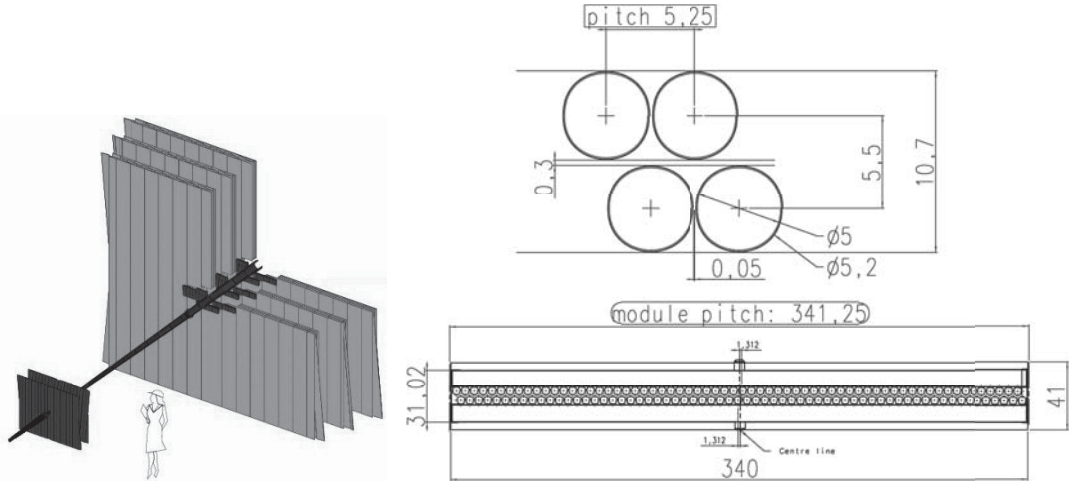

(a) OT Station arrangement in green

(b) Cross section of a straw tube module

Figure 2.8

The Outer Tracker

The Outer Tracker (OT) [19] is a straw-tube detector surrounding the IT in the T1-T3 tracking stations (Figure 2.8). This detector determines the positions of the charged particles by measuring the drift times in straw tubes. The maximum drift time is kept below 50 ns and the drift coordinate resolution is about 200 μm. The OT modules are arranged in three stations like the IT. Each station consists of four layers in the same orientations as the IT and TT. The modules that make up an OT layer consist of two staggered "monolayers" with 5 mm diameter straw-tubes, as it is shown in Figure 2.8b.

2.3.3 The Particle identification system

The Cherenkov detectors

Reliable particle identification is one of the main requirements of the physics program of the LHCb experiment. In particular, we need to separate pions from kaons in B meson decays to reduce the background from $B_d \rightarrow K^{\pm}\pi^{\pm}$, $B_s \rightarrow K^{\pm}\pi^{\pm}$ and $B_s \rightarrow K^{\pm}K^{\mp}$. Cherenkov radiation is emitted by relativistic charged particles when it passes through a material. The Cherenkov photons are emitted in cones around the particle track, and the angle of the photons depends of the particle's velocity. Two Ring Imaging Cherenkov (RICH) [20] detectors are used in the LHCb. The RICH system has the task of identifying charged particles over the momentum range 1-150 GeV/c. This is achieved by using three different radiators: aerogel and C_4F_{10} in RICH1 (1-60 GeV/c) and CF_4 in RICH2 (15-100 GeV/c). RICH1 is placed upstream the dipole magnet, between the TT and the VELO, while RICH2 is situated between tracking station T3 and the first muon

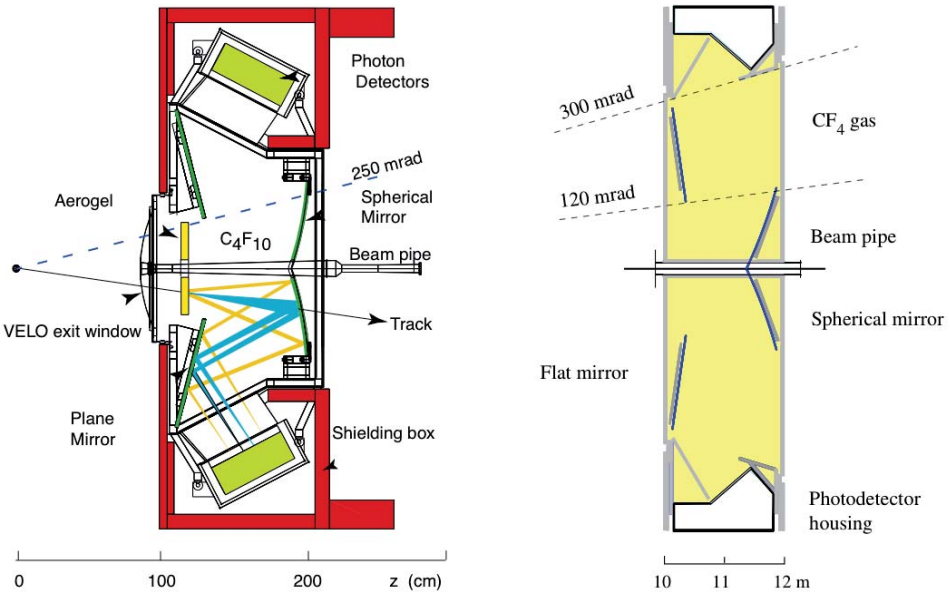

Figure 2.9: RICH1 detector in the leftmost picture, and RICH2 in the rightmost.

station. The design of the two detectors is depicted in Figure 2.9. Both RICH detectors use hybrid photon detectors (HPDs) to measure the positions of the emitted Cherenkov photons. The HPD is a vacuum photon detector in which a photoelectron, released when an incident photon converts within a photocathode, is accelerated by a high voltage onto a reverse-biased silicon detector. The tube focuses the photoelectron electrostatically onto a small silicon detector array, with a binary resolution per pixel.

The Calorimeters

The calorimeter system [21] is placed between the muon stations M1 and M2. It has three main purposes: it will trigger on electrons, photons and hadrons, it will measure energies and positions of traversing particles and it will identify photons and neutral pions to study specific B meson decays. The whole system consists of several layers: the Scintillating Pad Detector (SPD), the Pre-Shower (PS), the Electromagnetic Calorimeter (ECAL) and the Hadron Calorimeter (HCAL). The SPD determines whether particles hitting the calorimeter system are charged or neutral, while the PS indicates the electromagnetic character of the particle. They are used at the trigger level in association with the ECAL to indicate the presence of electrons, photons, and neutral pions. The ECAL has been designed to fully contain the shower of electrons and photons, while the HCAL fully absorbs the energy of the hadrons.

The calorimeter modules consists of scintillating pads interspaced lead/iron absorbers as seen in Figure 2.10. Incident particles interact strongly with the

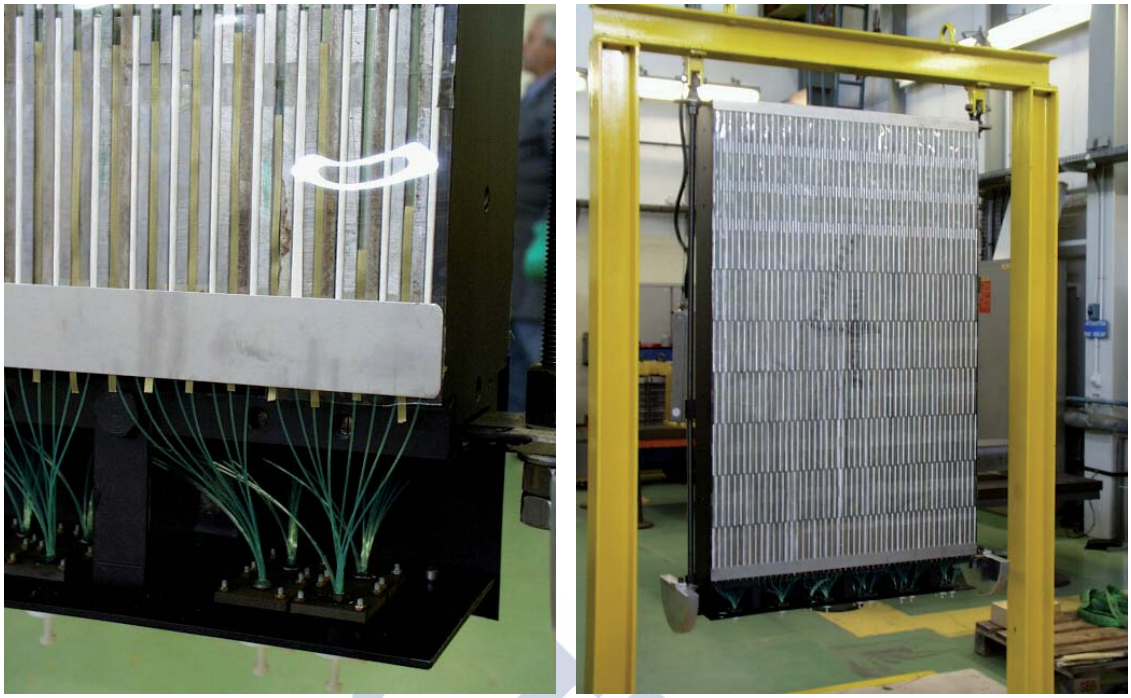

(a) Detail of the sandwich scintillator-absorber (b) HCAL module

Figure 2.10: Modules of the Hadronic Calorimeter (HCAL)

absorber creating showers of secondary particles that will produce light as they pass through the scintillators pads. Light is collected using wavelength-shifting fibers and both ends of the WLS fiber are used to transmit the light to multi-anode photomultipliers (MAPMTs) located at the periphery of the detector. The amount of collected light can be related to the energy of the original incident particle. The hit density depends on the distance to the beam axis and varies over the calorimeter acceptance by two orders of magnitude.

The Muon chambers

Since muons are present in the final states of many CP-sensitive B decays, therefore muon triggering and muon offline identification are fundamental requirements of the LHCb experiment. The muon system [22, 23, 24] consists of five stations (M1-M5), placed around the beam pipe, situated downstream of the RICH2 detector (see Figure 2.11). Each station contains chambers filled with a combination of three gases (CO_2, Ar, and CF_4) which are ionized by the muons. The detector technology used in the muon system is the radiation hard Multi-Wire Proportional Chamber (MWPC) with 2 mm wire spacing and a small gas gap (5 mm). In the inner region of M1 Triple-GEM detectors are installed because the occupancy is too high for the MWPC. Iron absorbers (80 cm thickness) are interleaved between stations M2-M5 and behind M5. Together with the calorimeter system, they remove the hadronic background and shield the

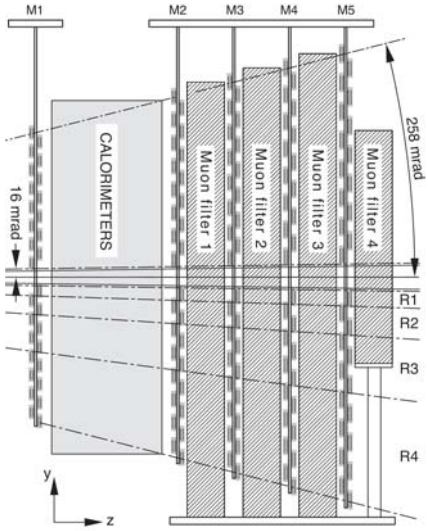

Figure 2.11: Muon chambers

muon detector from particles that have been strayed from the LHC beam. The minimum momentum a muon must have to reach M5 is approximately 6 GeV/c. The muon system is used in the trigger system to select events with muons of high transverse momentum (p_T) and in the High Level Trigger (HLT) and in the offline analysis for muon identification.

2.3.4 The trigger system

The purpose of the trigger system [25] of the LHCb experiment is to reduce the 40 MHz bunch crossing rate to about 2 kHz which is the rate at which the events can be stored for offline analysis. As the B decays interesting for new physics are very rare, so the offline limitations does not implies limitations in the physics output of the experiment. Nevertheless, is clear the utmost importance of a reliable and very efficient trigger system for the performance of the LHCb experiment. The LHCb trigger system is implemented in two levels: Level Zero (L0) and the High Level Trigger (HLT). The trigger scheme is illustrated in Figure 2.12.

The Level 0 trigger

The L0 trigger operates at 40 MHz synchronous with the LHC clock. It uses custom made electronics to make a trigger decision using information from the calorimeters, the muon system and the pile-up veto sensors in the VELO. Due to the large mass of the B-mesons, the decay products often have large p_T and E_T. The L0 decision is based on the observed values of the two highest p_T muons and the highest E_T hadron, electron and/or photon clusters. In addition the pile-up detector information is used to reject multiple interaction crossings. All this information is collected by the L0 Decision Unit that evaluates the data and

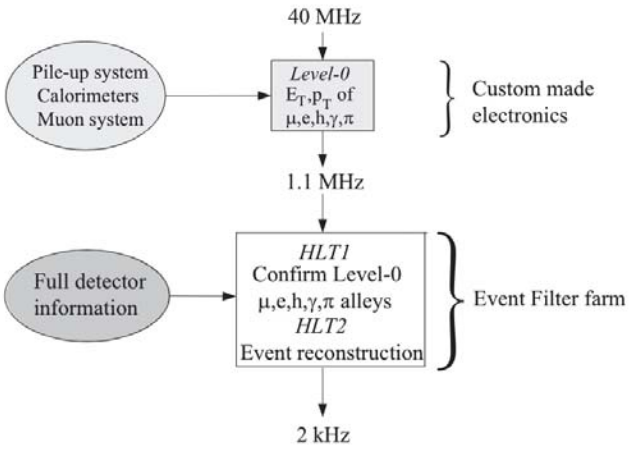

L0 criteria		
μ_1	p_T	> 1.3 GeV/c
$\mu_1+\mu_2$	p_T^{total}	> 1.5 GeV/c
h	E_T	> 3.5 GeV
e	E_T	> 2.6 GeV
γ	E_T	> 2.3 GeV
π^0	E_T	> 4.3 GeV

Figure 2.12: Left: Flow chart of the Trigger system reducing the 40 MHz bunch crossing rate to the 2 kHz of the storage rate. Right: L0 trigger criteria for nominal luminosity.

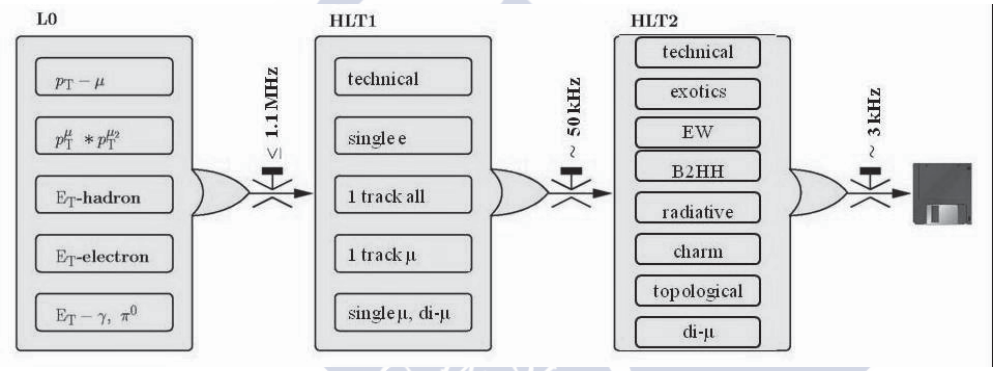

Figure 2.13: Schematic of the overall LHCb trigger scheme

checks whether one or more of the required criteria in the table in Figure 2.12 is matched. If that is the case, a signal is sent to the front-end electronics of all the sub-detector system, triggering them to be read out. The L0 latency, the total time between bunch crossings and the arrival of the L0 trigger signal to all the sub-detector front-end electronics, is fixed to 4 μs. The maximum allowed output rate of the L0 is 1.1 MHz.

The High Level Trigger

The High Level Trigger (HLT) is the second (and last) level of trigger of LHCb, running over the events that passed the L0 trigger. It is a `C++` computer program that runs on a farm of $\sim$ 1000 multi-core computer nodes. It has access to the full event information from all the sub-detectors. Its goal is to reduce the 1.1 MHz input rate from L0 to a 2 kHz output rate at which events are stored to disk

for further offline analysis. The HLT has two stages in order to meet the time limitations imposed by the previous requirement.

The HLT1 reconstructs particles in the VELO and determines the position of the primary vertices (PV) in the event. To limit the CPU consumption, a selection of VELO tracks is made based on their smallest impact parameter (IP) to any PV, and their quality. For these selected VELO tracks their track-segment in the T-stations are sought to determine their momentum (p), so-called forward tracking. HLT1 selects events with at least one track which satisfies minimum requirements in IP, p, p_T and track quality. It reduces the rate to a sufficiently low level to allow forward tracking of all VELO tracks. The majority of the uninteresting events is rejected at this stage, reducing the rate to approximately 30 kHz.

The HLT2 then reduces the event rate to the $\sim$3 kHz by performing a full event reconstruction with information from all the sub-detectors and makes the final trigger selection. HLT2 searches for secondary vertices, and applies decay length and mass cuts to reduce the rate. It first performs a complete pattern recognition to find all particle tracks in the event, using VELO tracks as seeds. Then, a set of different selections are applied attending to physics requirements aiming to cover all B decays with a displaced vertex, and with at least two charged particles in the final state.

2.3.5 The online system

The main purpose of the LHCb online system is to monitor and control de data transmission from the front-end electronics to the final storage. The online system can be divided into three subsystems that runs in parallel.

- The Data Acquisition (DAQ) system guarantees a proper configuration of the FE electronics and a safe data transfer from the sub-detector electronics to the final storage.
- The Time and Fast Control (TFC) system synchronizes trigger decisions and beam- synchronous commands to the LHC clock and orbit signal provided by the LHC.
- The Experiment Control System (ECS) monitors the systems described above and all the sub- detectors of the LHCb experiment. The ECS controls and monitors the DAQ system, the TFC system, the trigger system and as well the operational and environmental parameters of all the subdetectors like HV and LV, pressures, gas flows, temperatures, radiation doses, etcetera.

The DAQ and ECS parts are subdetector specific, so each one has to do a specific implementation. The way this has been done for the ST will be explained in Chapter 4.

USC
UNIVERSIDADE
DE SANTIAGO
DE COMPOSTELA

Part I

The LHCb Silicon Tracker Description and Control System

USC
UNIVERSIDADE
DE SANTIAGO
DE COMPOSTELA

3

The Silicon Tracker detector

The LHCb Silicon Tracker (ST) detector is a silicon micro-strip detector which provides precise momentum measurements. The sensitive area is approximately 12 m^2 with a total of 272.600 readout channels. The ST consists of two sub-detectors, the Tracker Turicensis (TT) before the magnet and the Inner Tracker (IT) after the magnet (Figure 3.1).

For the TT station a 500 μm thick sensors with 512 strips and 183 μm pitch is used, while the three IT stations feature 320 and 410 μm thick sensors of 384 strips each and 198 μm pitch. In both cases the the silicon is p-on-n type. In total there are 143.600 readout channels in the TT station and 129.000 in the three IT stations.

Although the mechanics of the the IT and TT sub-detectors are completely different their electrical layout is largely the same. This allows to develop similar detector control systems, sharing resources, know-how and easer the supervision and control by non-expert operators.

This chapter covers a detailed description of the Silicon Tracker detector. During 6 years I was involved in the installation, commissioning and operation of the detector.

3.1 Detector description

The IT detector consists of three identical stations (IT1-IT3) with four boxes in each station named *Top, Bottom, Access* and *Cryo*. A front view of one entire station is shown in Figure 3.2a. Each station consists of two retractable support frames (A-side and C-side), carrying two detector boxes per frame. Every one of the detector boxes contains 28 detector units arranged in four layers named

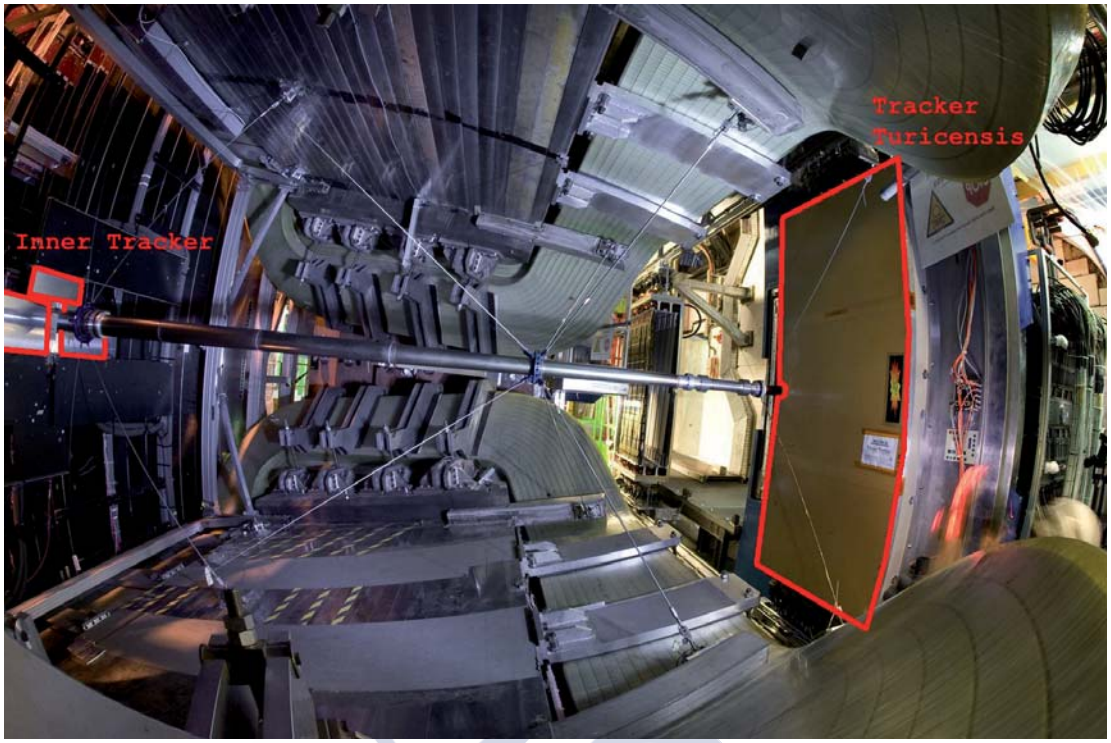

Figure 3.1: Picture taken from inside the magnet. In the left side the 3 out of 4 boxes of the first IT station can be appreciated. The 4th box is below the beam pipe, and it is covered by the carbon fibre support. In the right side, the access side of the TT can be seen in closed configuration, near the beam pipe.

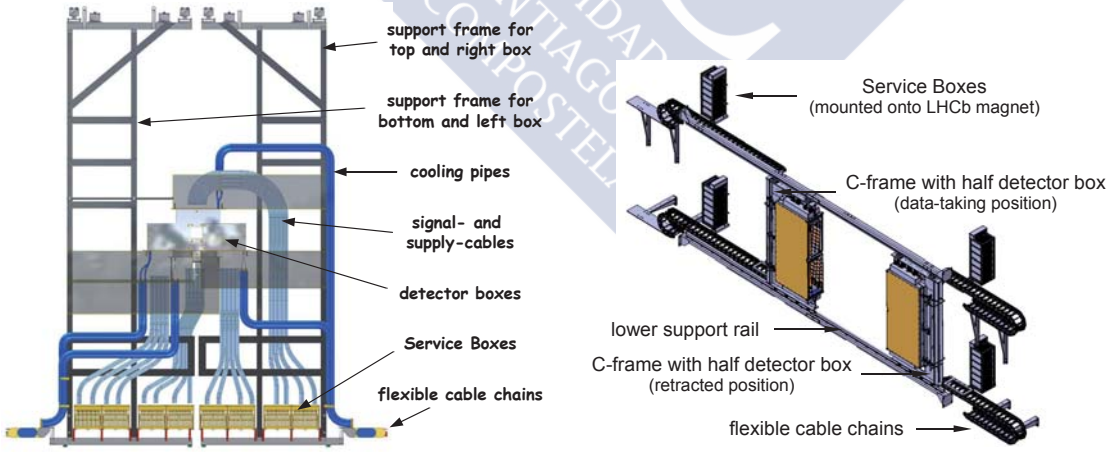

(a) Sketch of one IT Station

(b) View of the TT Station with de C-side retracted from the beam pipe

Figure 3.2: Sketch of the IT and TT stations

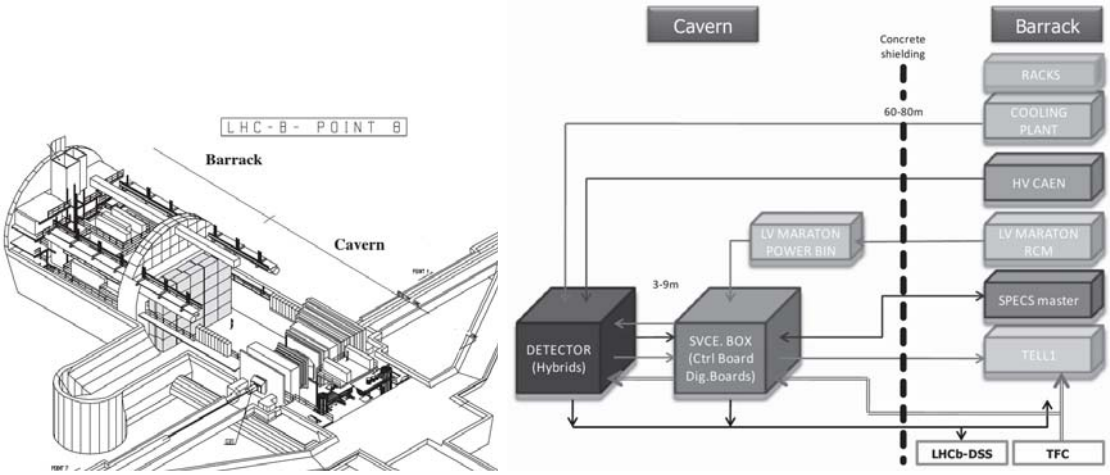

(a) The LHCb cavern. Note the concrete wall separating the barrack from the cavern

(b) Equipment distribution

Figure 3.3: Silicon Tracker equipment distribution

as *x-u-v-x*. The sensors of two x layers are vertically orientated whereas the u and v are tilted under a stereo angle of $\pm 5^{o}$. Four Service Box (SB), two for each detector box, are fixed to the lower end of each support frame. A flexible cable chain guides cables and fibers from the SBs to the LHCb bunker. The IT reconstructs 20% of all tracks passing through LHCb despite covering only 1.2% of the total acceptance.

The TT detector is shown in Figure 3.2b. It consists of 280 detector units that are contained in one large detector volume and arranged in four layers (*x-u-v-x*) tilted in the same way than in the IT detector. This detector volume is made out of two half-boxes (*A-side* and *C-side*) that can be retracted individually from the beam pipe. Detectors are read out from the top and from the bottom of each half-box, keeping the readout hybrids out of the experiment acceptance and less exposes to radiation. This defines four quadrants (*A-top, A-bottom, C-top* and *C-bottom*) over which the detectors are equally distributed. Each quadrant is connected via flexible cable chains to a column with six SBs, which are fixed.

3.1.1 Equipment Location

The detector equipment is placed both in the experimental area (cavern) and in the barracks (behind the concrete shielding wall) as sketched in Figure 3.3. The electronic elements located in the cavern are the service boxes and the detector boxes, in addition to the MARATON low voltage AD/DC converters which are under the experiment in an area called *the bunker*. All the devices in the cavern need to withstand both the radiation and magnetic fields levels present there. Part of the electronic devices were custom-made for that purpose while others

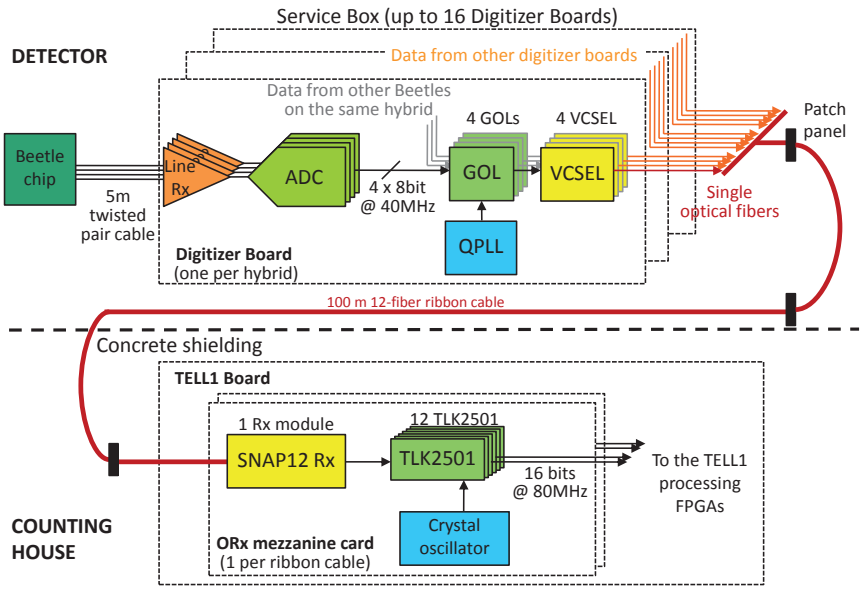

Figure 3.4: Overview of the Read-Out chain

are commercial chips which have been rated for radiation tolerance in several irradiation campaigns [26, 27, 28, 29]. In the barrack are placed all the detector elements that are not rated for radiation tolerance as well as the ones that may need human accessibility when the experiment is running.

3.2 The DAQ chain

The silicon micro-strip sensors and the Front-End (FE) readout hybrids are accommodated in the detector boxes. The FE electronics capture, amplify and store signals generated by ionizing particles when they pass through the silicon sensors. Captured data are stored in the Beetle pipeline buffer, until the Level 0 (L0) trigger decision accepts or rejects data from a given bunch crossing. Accepted data is extracted from the pipeline buffer and temporarily stored in the L0 derandomizer buffer (also implemented within the Beetle chip). The analogue data from the Beetle chips are sent via differential lines on up to 9 m long twisted pair cables to the SBs located outside the detector acceptance. Then the data is digitized by the Digitizer Board (DB) with 8-bit resolution, multiplexed and converted to optical. The digital-optical signal is further transmitted via fibres of up to 120 m length to the barracks to an optical receiver card, which is placed in the TELL1 board.

A detailed description of the components of the DAQ chain is given below.

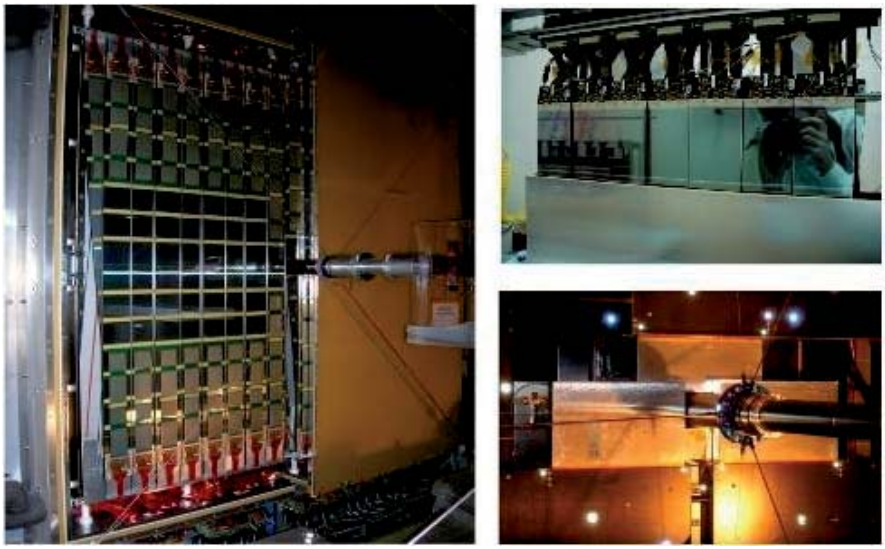

Figure 3.5: View of the TT installed in LHCb (left) with one boxes open and the sensors inside. View of the first IT station (bottom right), and detail of one of the detector boxes in semi-open position (top right).

3.2.1 The detector box

The detector boxes for the IT and TT provide electrical and thermal insulation. The detector units (also called *ladders*) are housed inside the detector box (Figure 3.5), with the cooling roots and nitrogen inlet pipes. Low voltage and bias voltage as well as detector signals, control signals and monitoring signals are fed through the top wall of the detector box. The volume is over-pressurized with nitrogen to keep the humidity under control at the operation temperature (between -15°C and $+5$°C).

Several temperature (PT1000) and humidity (HMX2000) sensors are distributed in the inner side of the box. The IT detector boxes has 4 PT1000 and 1 HMX2000 per box, glued to the side walls, giving a total of 48 temperature and 12 humidity sensors. The TT sensors are distributed through the cooling plates, side walls, near the beam pipe and in the cooling supply lines because the box volume is much higher. In total, TT counts with 30 temperature and 8 humidity sensors.

The main heat source inside the detector boxes are the Beetle chips placed on the hybrids. Each FE chip dissipates ~ 0.625 W and that this heat is removed by cooling roots attached to the hybrids. The chosen refrigerant is C_6F_{14} because in case of leaking such liquid is an electrical insulator.

Custom-made shielded copper cables transport power and signals from the detector boxes to the Service Boxes that are located at a distance of a few meters from the detectors. The cable's path can be seen in Figure 3.2.

Figure 3.6: Skilled technician performing the wire bonding on an IT module

Modules

A detector unit (*ladder*) consists of a hybrid and the corresponding silicon sensors. For the TT station a 500 μm thick sensors with 512 strips are used, while the IT sensors has 384 strips. There are two different IT sensors, the so-called *short ladders* are a single silicon sensor, 320 μm thick, 129.35 mm long and 80 mm wide, and are installed in Top and Bottom boxes. *Long ladders* are build by wire bonding two sensors, 410 μm thick, 110 mm long and 80 mm wide. These ladders are installed in lateral boxes, where the occupancy is lower because it belongs to the bonding plane. TT ladders are build by 1, 2, 3 or 4 sensors, as can be seen in Figure 3.2b. In all the cases the pitch is 183 μm and the silicon is p-on-n type.

The sensors are mounted in carbon fibre supports guaranteeing mechanical stability, while intercalated Kapton foil are used to isolate the sensor from the carbon fibre layer.

Hybrids

The hybrid packages for the IT and TT detectors consists of the Beetle chips mounted together with passive electronic components. Ceramic pitch adapters are used to match the silicon sensor pitch to the pitch of the Beetle input pads. Such pitch adapter accommodate the Beetle's pad pitch (20 μm) to sensor's pad pitch (183 μm in TT and 198 μm in IT). IT sensors were wire bonded to the ceramic pitch adapter by Eliseo Pérez, picture 3.6 was taken during the process, while TT sensors were wire bonded by an external company. This assembly is then glued with silver epoxy to an aluminium balcony providing cooling for electronics and grounding.

The TT silicon detector modules are 160 cm long and are longitudinally segmented in four or six independent readout units. The TT hybrid packages

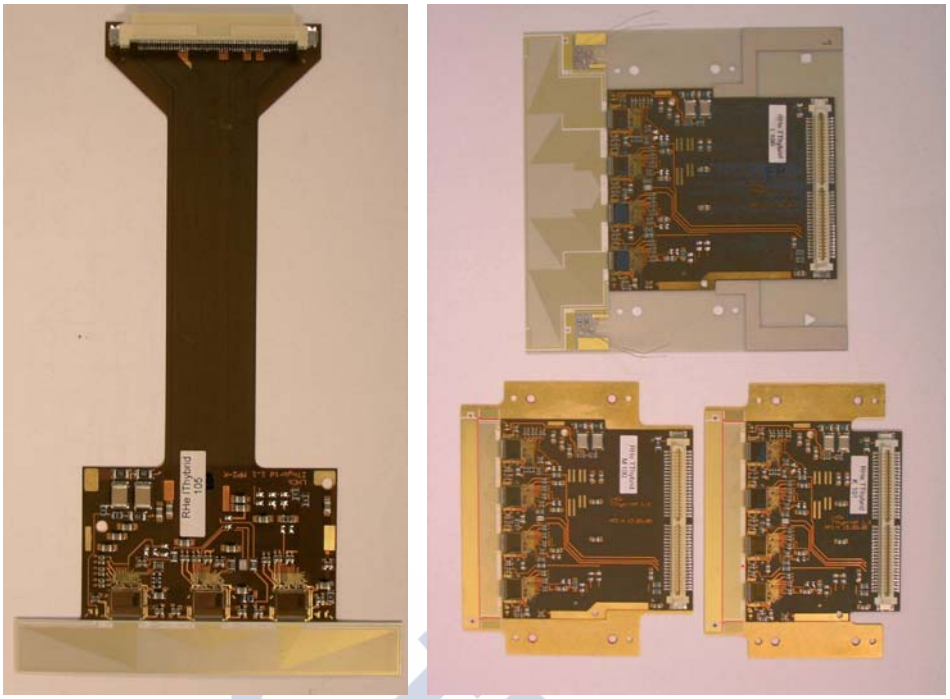

(a) (b)

Figure 3.7: Photographs of the IT (a) and TT (b) hybrids

are located at both ends of a detector module (Figure 3.7b). Therefore, a stack of up to three hybrids at each end is necessary for the readout. The stacked hybrid design of the TT detector requires the use of three different hybrid subtypes each having four Beetle chips. The hybrids for the TT detector differ in the overall length and in size and material of the heat spreaders, as can be seen in Figure 3.7b, while all the IT hybrids are equal (Figure 3.7a).

3.2.2 The service box

While the silicon sensors and the hybrids are located in the detector boxes, the digitizing and control electronics are located in the Service Boxes, out of the detector acceptance (see location in Figure 3.2). This reduces the amount of material in the acceptance of the experiment, the radiation doses and access for cooling and maintenance is easer.

The SBs are custom-made crates that contain up to sixteen (IT) or twelve (TT) Digitizer Boards, a Control Board [30] and a custom-made backplane for the low voltage power regulation and distribution of TFC signals[1] and other control signals. Each DB is linked to one front-end readout hybrid and carry out the digitization and optical transmission of the data [31] coming from that hybrid.

[1]The **T**ime and **F**ast **C**ontrol signals (**TFC**) are the LHC clock (locked at 40.079 MHz), the L0reset, the L0accept and the data IP destination address.

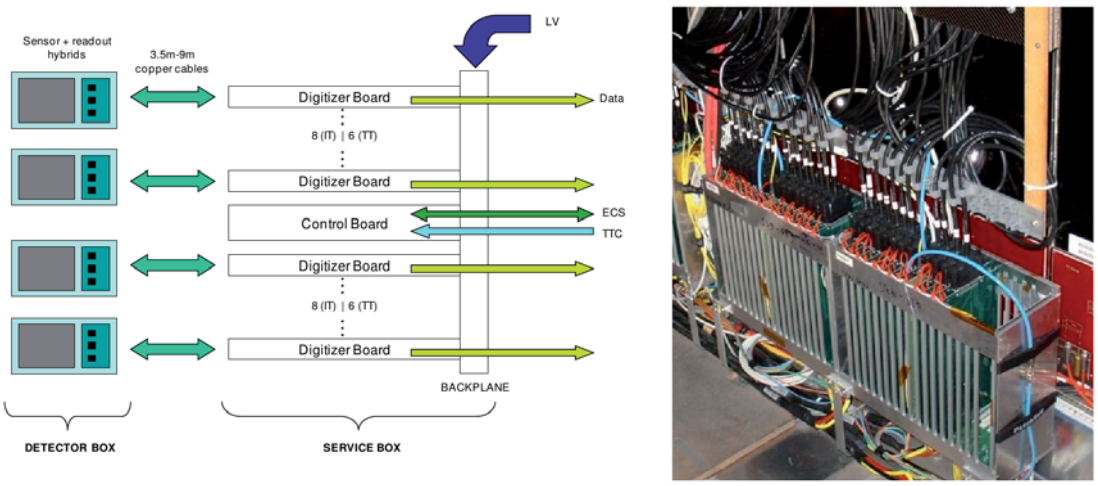

Figure 3.8: Service Box scheme (left) and two installed IT service boxes (right).

The power for the Beetle chips (2.5 V) is filtered and regulated on the SB backplane and provided to the front-end hybrid via the corresponding DB. In addition, low-voltage levels of 2.5 V, 3.3 V and 5 V are provided to power the various electronics components on the Control Board (CB) and the DB themselves.

From the SBs, commercial copper cables and optical fibres lead to the bunker and the LHCb counting room (in the barrack) where the power supplies,TELL1 readout electronics, and master control electronics are located. There are some patch-panels for all these cables some meters away from the SB. An overview scheme and two finally installed SBs are shown in the Figure 3.8.

The Control Board

The Silicon Tracker Control Board [3] has been designed and developed to control the ST hardware in the cavern. It connects to the ECS [32] using the SPECS field-bus system [33] and provides interface to TFC [34] signals. As the structure of the IT and TT are very similar (although the partitioning scheme is slightly different) a common controller card has been designed for both detectors. This card provides the necessary functionalities to carry out several control and monitoring tasks, namely:

- the slow and fast control of the Silicon Tracker readout and digitizing electronics
- the control and monitoring of the LV power regulators
- the monitoring of the detector box temperatures and humidity

A requirement that the Control Board has to meet is that the devices and components on it need to tolerate the radiation levels present in the cavern where the SBs are located. For this reason some specific radiation hard devices developed at CERN are used.

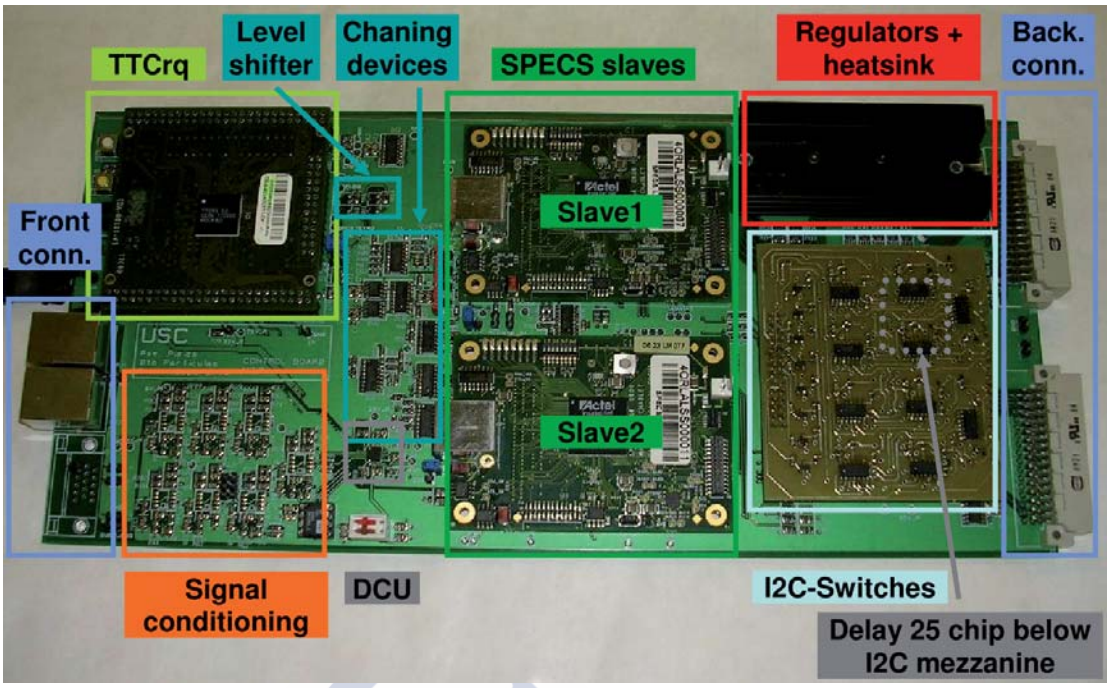

Figure 3.9: The Silicon Tracker Control Board. Figure from Ref. [3]

The Digitizer Board

Any Beetle readout hybrid is connected with a 68-wire twisted-pair round cable of up to 9 m of length to a Digitizer Board. The Figure 3.4 already showed a simplified scheme of it. The line receiver suppresses the common mode introduced in the cable and matches the signal amplitude to the input of the 8-bit Analog to Digital Converter (ADC). Data of four ADCs, corresponding to the four analogue output ports of one Beetle are encoded by the CERN GOL ASIC [35] into the Gigabit Ethernet protocol and modulated onto a 850 nm VCSEL diode. Therefore, each optical link corresponds to the digitized data from one single Beetle.

A QPLL [36] provides clock jitter filtering, which is mandatory to ensure the proper functioning of the GOL transmitter. In addition, there is also and a slow control 6-channel ADC. This ADC is the CERN DCUF25 chip [37] which is used for reading the hybrid temperature, the QPLL status signal and LV regulators flags. This device is also controlled via I2C.

Two versions of Digitizer Boards have been designed: a TT version (Figure 3.10) with 16 ADCs corresponding to a 4-Beetle TT hybrid and an IT version with 12 ADCs only to match a 3-Beetle IT hybrid.

3.2.3 The TELL1 board

The purpose of the TELL1 board is to handle L0 accepted data before transmission to the DAQ network. The data are transferred by optical lines

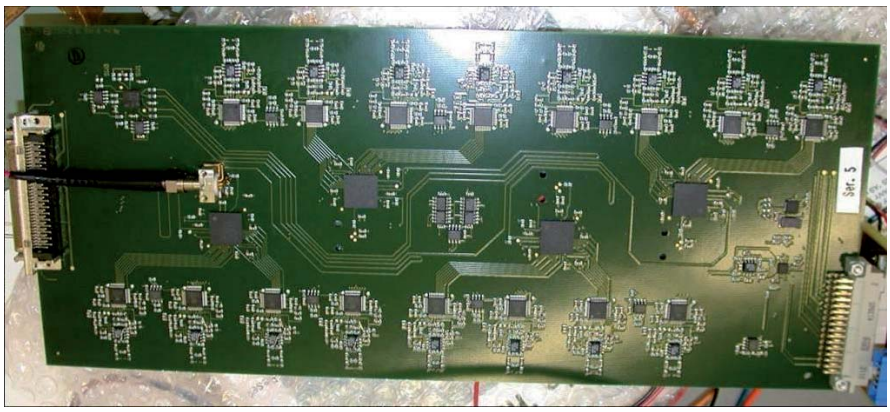

Figure 3.10: A TT Digitizer Board

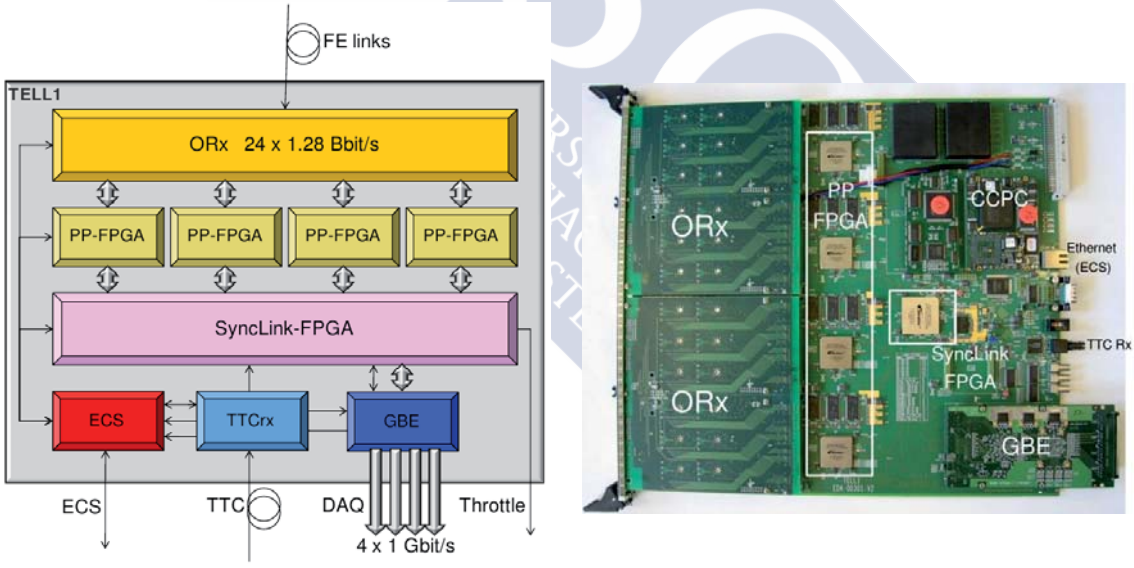

(a) (b)

Figure 3.11: A Silicon Tracker TELL1 board.

from the service boxes to the counting house where the TELL1 board is located. They are placed behind a shielding wall, 60 m away from the interaction point to minimize the amount of electronics exposed to radiation. In the TELL1 boards the data is deserializated, processed, compressed and transmitted to the HLT CPU farm.

To preserve synchronization over large distances LHCb has a global clock and fast signal transmission network, the so-called TFC system. The TFC is driven by the Readout Supervisor [38], responsible for distributing the LHC clock and scheduling the trigger decisions. The TELL1 are custom developed boards for being used by different detectors in LHCb, each with its own data processing algorithms. The ST is one of the LHCb most demanding detectors in terms of data processing. The main processing units of the TELL1 are five large FPGAs which can handle ~ 60 Goperations/s.

Figure 3.11 shows a simplified block diagram of the ST TELL1. Two optical receiver (ORx) mezzanine cards provides an input for 24 optical links from the SBs. As it was already mentioned, each optical link corresponds to the digitized data from one Beetle. Each of the PP-FPGAs processes the data from 6 Beetles at a maximal event rate of 1.1 MHz. After this stage the SynchLink-FPGA receives the fast signalling from the TFC system via TTCrx chip and distributes the synchronization signals (clock, L0accept and event identification) to the PP-FPGAs. It is also in charge of collecting and merging the data fragments from the PP-FPGAs, to assemble multiple events into the so-called multi-event packets, and to perform Ethernet and IP framing before transmission to the readout network. The readout network is interfaced by a four-port Gigabit Ethernet cards delivering 4 Gbit/s data bandwidth. The fast control signals received via TTCrx are the LHC clock (locked at 40.079 MHz), the L0reset, the L0accept and the data IP destination address. A Credit-Card sized PC mezzanine board is used to provide an interface for local board control via Ethernet and hence connect with the ECS [39].

3.3 Silicon Tracker performance

Data collected during 2011 and 2012 with multiple pile-up events at far higher instantaneous luminosities than the design, showed that the Silicon Tracker works extremely well despite operating under very different conditions compared to its design [40].

The S/N for the TT was found to be in the range 12 to 15 and is shown in Figure 3.12 for the different strip capacitances. The long and short ladders in IT have a S/N of 16.5 and 17.5 respectively. The fraction of working channels in September 2012 was 99.72% and 98.81% for the TT and IT respectively. The main source of inefficiency is caused by the failure of VCSEL diodes used in the optical transmission from the DB to the TELL1 boards. The broken VCSELs can easily be replaced during short shutdowns in the TT, as the TT service boxes are easily accessible during short technical stops. Repairs to the IT electronics

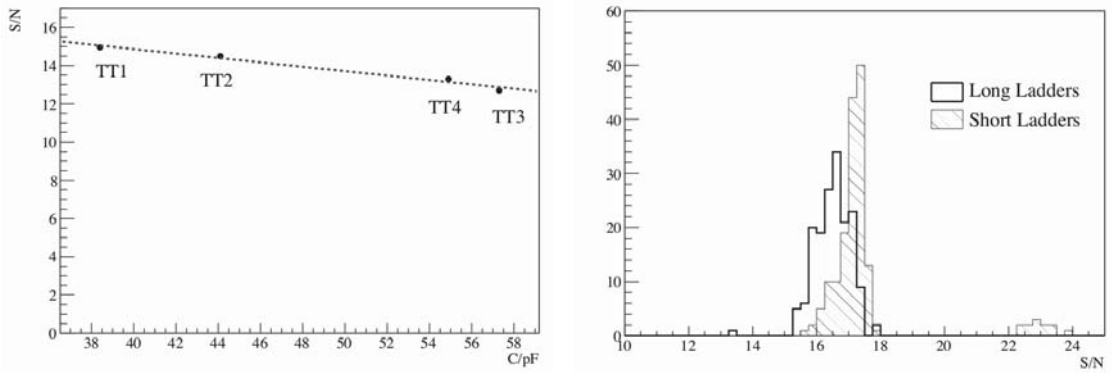

(a) (b)

Figure 3.12: Measured signal to noise ratio as a function of strip capacitance in TT (a) and for different strip lengths in IT (b). Plots form Ref. [40]

are much harder due to its location under the IT which requires the detector to be open for access. The IT also has two modules which cannot be configured. Repairs will be made during the long shutdown in 2013. The hit resolution was measured to be 59 μm and 50 μm for the TT and the IT respectively.

4

The Silicon Tracker Control System

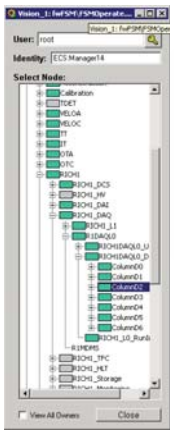

The LHCb's Control System is a hierarchical and distributed system which controls the whole LHCb machine. The Silicon Tracker collaboration was in charge of the design, development and maintenance of the control system directly linked with the hardware. As it must be included into a superior hierarchy, therefore restricted rules must be followed. These rules includes some guidelines about the hierarchy of the Silicon Tracker control tree. In order to gain more flexibility, a parallel tree or *Safety Tree* was conceived and implemented to link several parts of the control tree which were not connected otherwise. Specifically in case of a DSS alarm the affected sub-system will be switched off without hesitation. A sudden switch off of the whole detector could have catastrophic consequences in such a delicate hardware, so it must be avoided as much as possible. The idea behind the Safety Tree is to use the monitoring signals in order to prevent a DSS action and perform, if necessary, a controlled switched off in the shortest partition possible.

In this chapter a detailed description of the developed control system for the Silicon Tracker is described, together with the parallel Safety Tree. A more detailed description can be found in [3].

4.1 LHCb ECS

The ECS [41] , also know as *slow controls*, were traditionally developed independently by each experiment at CERN, and in some cases by each subdetector. For the LHC, the experiment's management jointly decided to develop a

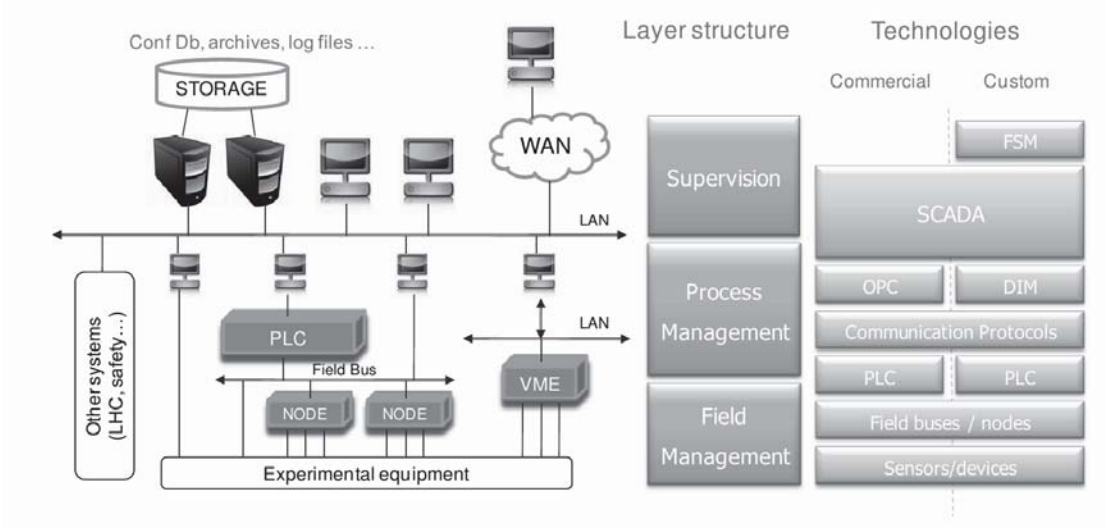

Figure 4.1: LHCb ECS technologies and layer structure.

common ECS due to the huge number of development teams, the size, complexity and long lifetime ($\sim$ 20 years) of the LHC experiments.

The ECS allows to control the whole LHCb detector from a single computer. LHCb's ECS (Figure 4.1) is in charge of the configuration, control and monitoring of all the components of the online system. This includes all the devices in the areas of: data acquisition, detector control, detector monitoring, trigger, timing and the interaction with the operators.

The way to build a common, consistent and integrated control system for the whole experiment has been based on the use of the same technologies and devices by all the development teams [42, 43]:

- the software tools and protocols used by the development teams are the same for everybody: LHCb makes extensive use of the JCOP tools [44], some of them are specific for the LHCb and others are generic for the LHC. The physical and software protocols for communication with devices and between software components is also common to all the detectors as much as possible. One of the major agreement points is the use of the PVSS SCADA (now SIMATIC WinCC Open Architecture) [45] by all LHC experiments.

- all the teams follows a set of guidelines for building the hierarchical distributed control system of each detector, which were defined since the starting stages. A common *look and feel* for the user graphical user interfaces has been adopted, which enormously helps the operator. Also the way of operating the system presents common features to everybody, such as the partitioning modes and naming conventions.

- common hardware developments such as the SPECS and systems such as the Power Supplies have commonly been adopted by all sub-detectors. In

addition, the network infrastructure is common to every sub-detector and sub-system and isolated from the outside world.

From the detectors point of view, the main task of the Detector Control System (DCS) is to enable the proper and safe operation of the detector and provide a link to the general LHCb ECS. The tasks that the Detector Control System (DCS) has to fulfil can be summarized as follows:

- it has to control, configure and monitor the status of the detector electronics, temperatures, humidity...
- it has to implement functionalities to perform calibration runs on the detector
- it has to perform exhaustive tests of individual modules
- it has to interface to external systems such as databases, the DSS system, the LHCb higher level control units, the TFC system...

Although the ECS will operate the experiment as a whole during physics data taking, it provides the functionality to operate each detector as an individual unit. This is the case during testing, calibration or commissioning periods. The automation level allows, in normal circumstances, run the whole LHCb experiment with just a couple of persons on site.

4.1.1 JCOP Framework

The Joint Controls Project (JCOP) was set up as a collaboration between the controls teams on the LHC experiments, the support groups of CERN's IT and physics departments.

The JCOP team undertook evaluations to assess the suitability of a number of technologies, primarily commercial ones, commercial programmable logic controllers (PLCs), as well as supervisory control and data acquisition (SCADA) products. The evaluation of SCADA products eventually led to the selection of the Prozessvisualisierungs und Steuerungs System (PVSS) tool as a major building block for the DCS. Where suitable commercial solutions were not available, products developed at CERN were also evaluated. This led to JCOP's adoption and support of CERN's distributed information manager (DIM) middleware system and the `SMI++` finite-state machine (FSM) toolkit.

The development of the so-called JCOP framework, based on specifications agreed with the experiments, offers many ready-to-use components for the control and monitoring of standard devices in the experiments (e.g. Wiener and CAEN power supplies). This provides a customized layer on top of the technologies chosen, such as `PVSS, SMI++` and `DIM`, but also extends the functionality of the underlying tools, such as the configuration database tool and installation tool.

Although JCOP provides the basic building blocks and plenty of support, there is still considerable work left for the subdetector teams around the world who build the final applications (Figure 4.2).

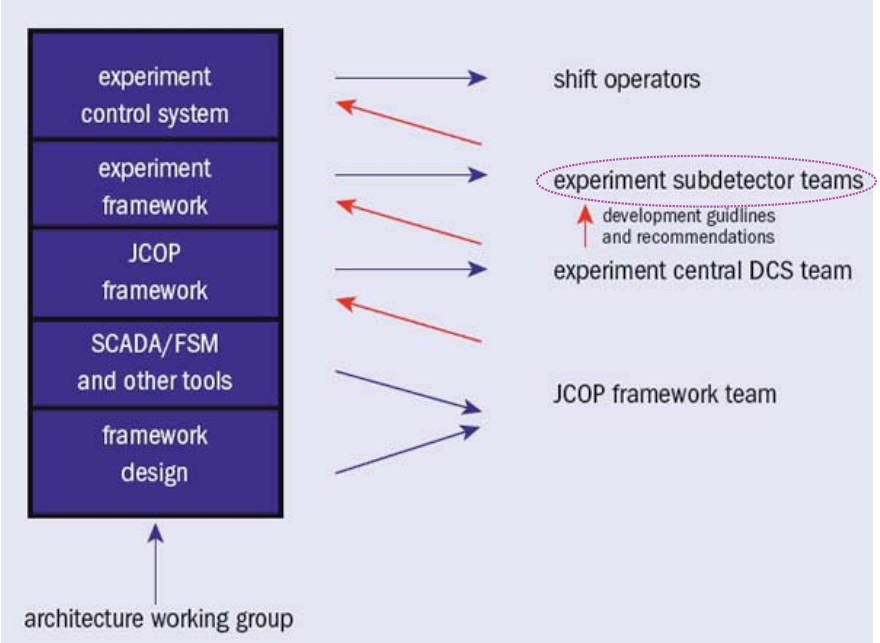

Figure 4.2: Software development teams involved in the LHC ECS.

As member of the ST team, I was involved in the development of a customized application which controls all the detector's hardware and which is integrated into the LHCb ECS. Such application was built using the tools provided by the JCOP framework, and following the LHCb ECS Integration Guidelines [46].

4.1.2 PVSS SCADA Software

The SCADA package chosen for the LHC experiment control system was PVSS, which belongs to ETM [45]. Since March 2007, ETM is part of Siemems and PVSS long time support was assured. Although the name was changed to **SIMATIC WinCC Open Architecture** in 2011, the old name is used all along this document.

PVSS is an open, flexible and distributed architecture that eases the development of custom designs for specific application areas. The PVSS internal architecture is implemented as a set of different functional modules that perform different specific tasks. These modules are called managers and run as separate software processes.

The most remarkable managers are:

- **Drivers (D)**: are the PVSS manager which works at the lowest level. They provide the interface to the devices to be controlled and can use commercial drivers like OPC or user-made drivers.
- **The Database Manager (DB)**: provides the interface to the (run-time) database.

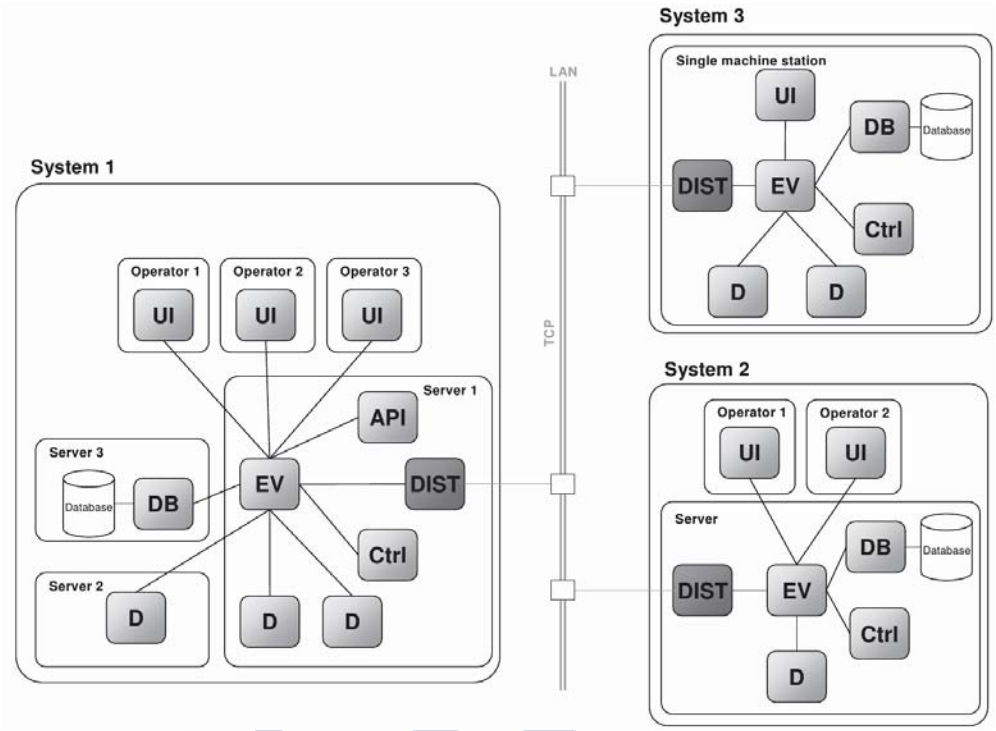

Figure 4.3: PVSS Distributed System

- **User Interface Managers (UI)**: they correspond to the highest level of abstraction providing the interface with the user. These include a graphical editor (GEDI), a database editor (PARA module) and general application user interface. In the UI, values and trends are displayed, commands are launched and reports are showed.

- **Ctrl Managers (CTRL)**: running as background processes provides the data processing. They are implemented in a scripting language, similar to C, which is interpreted during run-time (i.e. not compiled). It permits multi-thread programming as well as provides a large library plenty of useful functions for data and process handling.

- **API Managers (API)**: allow users to write their own programs in `C++` using a PVSS API (Application Programming Interface) to access the data in the database. This is the most powerful and flexible way to add extra functionalities to PVSS such as adding self-contained managers.

- **Distribution Manager (DIST)**: used to build PVSS distributed systems (either Windows or Linux based systems).

- **The Event Manager (EV)**: is responsible for all internal communications. It receives data from drivers (D) and sends it to the Database Manager (DB) in the database. The EV maintains the process image of all current

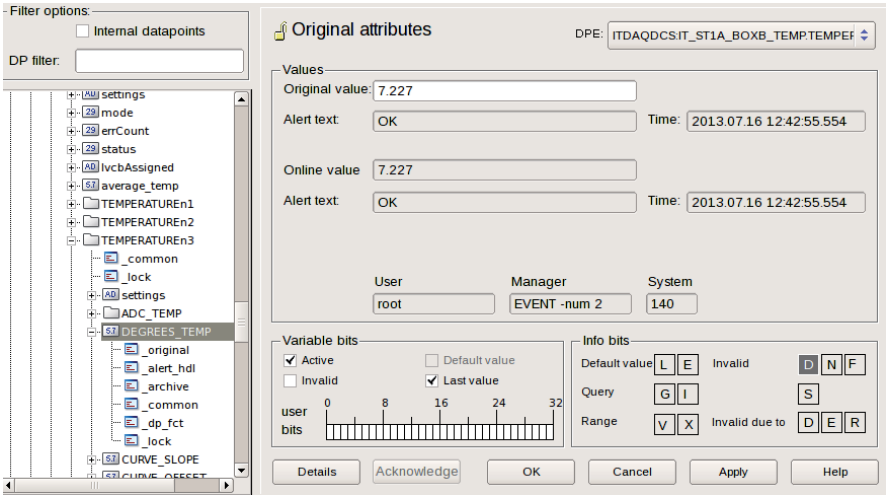

Figure 4.4: Configs of a temperature datapoint

data values in memory and ensures that the data is distributed to all the managers subscribed to it. It is also the responsible for the alarm generation and handling.

PVSS is based in the client-server architecture that allows practically unlimited scaling of the system. PVSS is used from small single-site systems to distributed, redundant multi-site systems in a wide range of configurations. Therefore, system resources can be distributed across multiple computers. In a PVSS Distributed System (Figure 4.3) a distribution manager must be added to each of the systems and then they must be configured to connect to each other.

The Datapoint Concept

The device data in the PVSS database is structured as, so called, DataPoints (DP) of a pre-defined DataPoint Type(DPT). It allows all data associated with a particular device to be grouped together rather than being held in separate variables.

A DPT describes the data structure of the device and a DP contains the information related to a particular instance of such a device. The DPT structure is user definable and can be as complex as one requires and may also be hierarchical as shown in the example. In the Figure 4.4 we see a DPT representing a temperature sensor implemented in the IT Finite State Machine (FSM) tree. This has a set of read (readings) and write (settings) parameters, called Data Point Elements (DPEs) associated with it as well as associated display information.

After defining the datapoint type, the user can then create datapoints of that type which will hold the data of each particular device.

In Figure 4.4 we can see several instances of the temperature DPT called *TEMPERATUREn1, TEMPERATUREn2, TEMPERATUREn3*. For *TEMPERATUREn3* we can see that for the *DEGREES_TEMP* parameter a

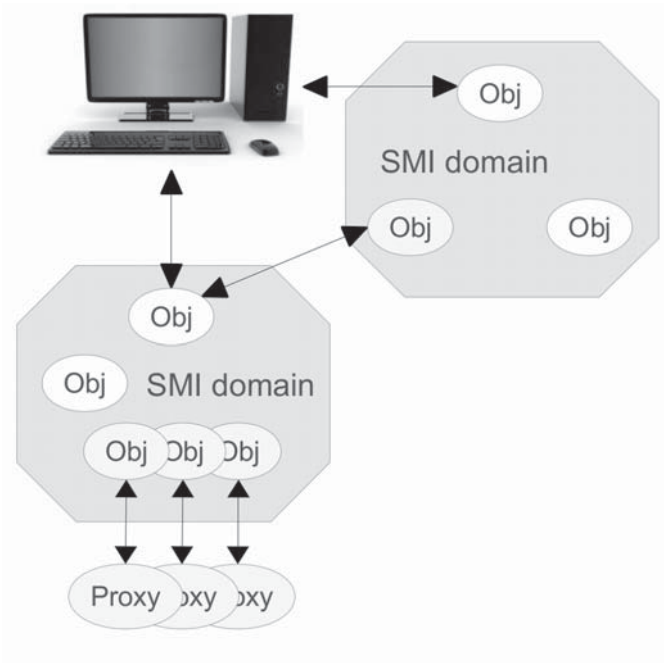

Figure 4.5: SMI++ Run-time Enviroment

number of sub-element are present (alert_hdl, archive, original, dp_fct, common and lock). These are known as *configs* and enable specific behaviour to be configured for a DPE e.g. alarm handling or archiving as well as to hold attributes of that DPE e.g. its temperature value or its hardware address.

In this example the datapoint elements mapping to the device data are only of types float, boolean and string but several more data types are available. In particular dynamic arrays of the simple data types, like dyn_int, dyn_float, dyn_string, etc. Dynamic arrays can hold a variable number of elements of the same type. Datapoint elements can also contain references to other datapoints or dynamic arrays of such references.

4.1.3 The SMI++ toolkit

`SMI++` is a toolkit for designing and implementing distributed control systems. It was developed at CERN for Delphi experiment, and latter improved for the LHC.

`SMI++`'s methodology combines three concepts: object orientation, Finite State Machines (FSM) and rule-based reasoning. Classes and objects allow the decomposition of a complex system into smaller manageable entities. Each entity is described as a finite state machine, allowing the modelling of its behaviour in terms of simple states and actions. For each state, a well defined and sorted list of rules can be declared. These rules will determine when the state will be changed or an action will be triggered.

`SMI++` objects can be *concrete* or *abstract*. Concrete objects interface to real-

```
state: ERROR
   when ( $ALL$FwCHILDREN in_state EMERGENCY_OFF )  move_to EMERGENCY_OFF
   when ( $ALL$FwCHILDREN not_in_state {ERROR, EMERGENCY_OFF} )  move_to NOT_READY
      action: Recover
         do Recover $ALL$FwCHILDREN
         if ( $ANY$FwCHILDREN in_state ERROR ) then
            move_to ERROR
         endif
         move_to NOT_READY
      action: Do_Emergency_OFF
         do Do_Emergency_OFF $ALL$FwCHILDREN
         if ( $ANY$FwCHILDREN not_in_state EMERGENCY_OFF )  then
           move_to ERROR
         endif
         move_to EMERGENCY_OFF
state: EMERGENCY_OFF
      action: Clear_Emergency
         do Clear_Emergency $ALL$FwCHILDREN
         move_to NOT_READY
```

Figure 4.6: SML Code Examples for Control Units of type DCS_LV_REG

world devices, like a power supply or a temperature sensor, through an associated process: a proxy. Abstract objects represent logical entities, like a Run or the Detector Control System, and are implemented within SMI Logically related objects, abstract and concrete, can be grouped inside `SMI++` *domains* representing a given sub-system. The already introduced Device Units are defined as concrete `SMI++` objects, while Control Units and Logical Units are abstract. Figure 4.5 shows the interconnections between the components of the SMI toolkit. In this figure two `SMI++` domains are depicted, one of them containing several connections to hardware devices, through proxies. A user interface can attach to the different domains in order to view the states of their objects or to send commands to them.

Concrete objects are simply declared in SML, i.e. only their list of states and possible actions for each state are defined. The actual implementation is provided externally by a process written in `C`, `C++` or by a `PVSS` script, if the device is implemented within PVSS. Abstract objects are completely implemented in SML.

Abstract object description will contain not only the possible states and actions, but also the code that implements each action and the rules for asynchronous transitions. The SML instruction set is reduced to a small number of simple and intuitive instructions. The most important instructions are:

- *do* instruction: send a command to an object or to a set of objects.
- *if* instruction: test the state of an object or a group of objects.
- *move_to* instruction: end the action by moving to a new state.
- *when* instruction: while the object is in a given state whenever the condition gets achieved, execute an action (*do* action) or change state (*move_to* state).

A real example of SML instructions are showed in Figure 4.6.

4.1.4 The FSM

The JCOP Finite State Machine (FSM) [47] is the component that provides a high-level interface to model the different parts of the experiment. It is written using the `SMI++` toolkit developed at CERN. The FSM follows a hierarchical structure, with different levels of abstraction, across different systems using the PVSS distributed architecture.

The concept of Finite State Machines (FSM) is used to model the behaviour of a system by means of a limited number of states, transitions between these states, actions and events. A current state is determined by past states of the system, i.e. it reflects the input changes from the system start to the present moment. A transition indicates a state change and is described by a condition that would need to be fulfilled to enable the change. An action is a description of an activity that is to be performed at a given moment (like to send a command). Finally, events, which are either externally or internally generated, trigger actions and can lead to state transitions.

The ECS is organized in a tree like structure, segmented into sub-detectors, systems, sub-systems, etc. The hierarchical control and operation of the different sub-detectors is performed by means of FSMs, which handle the states and transitions of the different parts of the detector.

The FSM hierarchy is composed of two types of nodes: "logical" and "real" entities. Whilst real entities normally model and control directly hardware devices (e.g. a sensor), the logical entities group these devices and control them from a more abstract hierarchical level (e.g. a sub-detector). The real entities are called Device Units (DU), whereas the logical ones can either be Control Units (CU) or Logical Units (LU). Device Units are implemented with `SMI++` concrete objects, while CUs and LUs with abstract objects.

The Control Units can contain children of any type (i.e. CUs, LUs or DUs) and implement the logic behavior in terms of FSM. Therefore they can take decisions and send commands to their children based on their States. State transitions cause the evaluation of logical conditions and possibly Commands to be sent to the children.

Logical Units also represents an abstract object, but they are embedded in an overlying CU. It can contain children, but not of type CU. LUs have restricted functionality compared with CUs, but by using LUs the number of processes is reduced, and thus the performance improved by the use of computing resources. Hence, by using LUs hierarchies with larger number of nodes can be created.

The Device Units implement the interface with the lower level components (Hardware or Software) and, in that case, they cannot contain children of any type (they are always a tree *leaf*). They can receive commands and act on the device, as well as they can gather device data and translate it into a state. A time-out mechanism is implemented in the DUs, changing the state to ERROR if the

time-out condition is reached. With this mechanism the actions are propagated down the tree, while the *States* are propagated upwards.

Therefore, the operator can launch an event from a CUs to send a command to its children (CUs, LUs or DUs). These commands will be propagated downwards until they reach the DUs, where an action will be taken over the appropriate hardware, and the DU will change its state accordantly. Then, the new state will be propagated upwards because the states of the CU's children will change, and new conditions will be accomplished.

In addition to such simple example, the nodes have a property called **ownership**. The operator must be the *owner* of the CU to be able to send any command. The ownership values can be several:

- Taken: one, and only one operator is the owner of the CU.
- Ignored: commands are send from parent to children, but states are not propagated upwards.
- Excluded: neither commands nor states are propagated between parents and children.
- Not taken: the CU has no owner, and the CU and its children are not part of the FSM tree to practice effects. This situation will be reversed when an operator takes the control in a upper level. This state is a transition state which appears when an operator release the ownership of a CU to be taken by another operator.

Taken advantage of the ownership properties already described, a sub-detector like the Inner Tracker can run as part of the whole LHCb ECS tree, or in a stand-alone mode. This is a very useful, and very used feature, as allows an expert to take the control of a sub-detector to test improvements or perform calibration task without disturb the rest of sub-detectors.

4.1.5 The LHCb domains

At the top level of the LHCb ECS, the FSM tree is divided into different domains depending on their activity:

- DAQ (Data Acquisition): consisting of the devices or elements taking part in the data acquisition process such as the FE electronics, the L1 electronics and the readout network.
- Detector operations (DCS) and High Voltage (HV) domains: elements such as the Low Voltage (LV) power supply system, the cooling system, the temperature monitoring devices, the gas system (for gas technology detectors), the high voltages...
- The DAI: it consists of the data acquisition infrastructure, such as crates, computers...

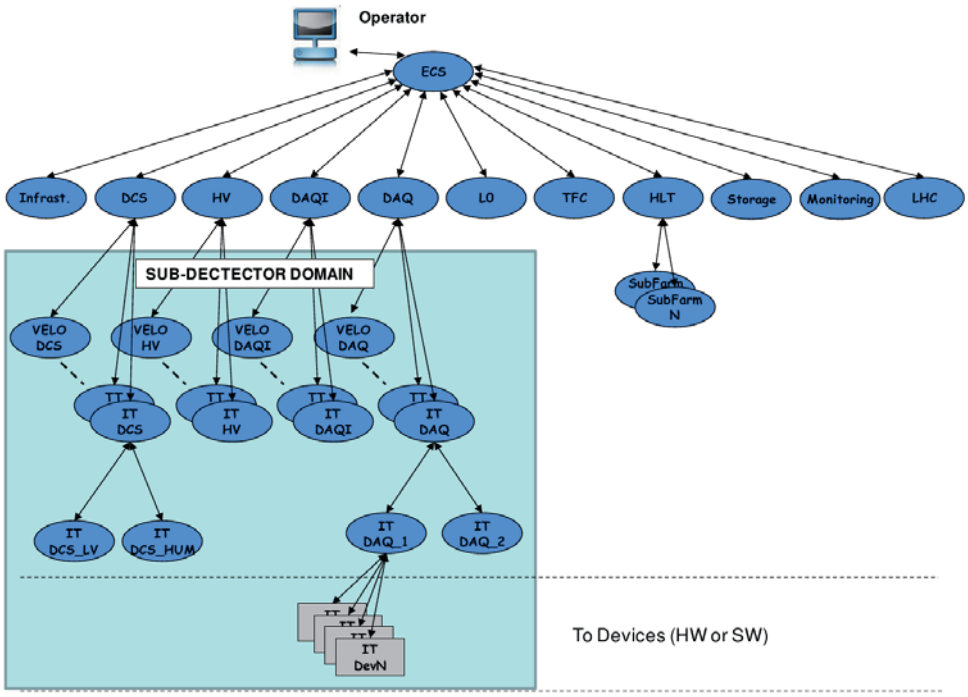

Figure 4.7: LHCb ECS tree

- The Time and Fast Control (TFC) system.
- The High Level Trigger (HLT).
- The L0 trigger system.
- The monitoring farm.
- External independent systems such as the LHC accelerator, the CERN safety system, the Detector Safety System (DSS), etc.

These domains are linked to the sub-detectors in the way that is showed in Figure 4.7. Such distribution is covered by the LHCb ECS Guidelines [46], and in order to simplify the design of the ECS system and to exhibit a common look and feel to the operators a common FSM scheme with common standardized states and transitions has been defined to implement in all the CU nodes within a given domain. The same states and actions are also recommended for the DUs in the same domain whenever possible. In the following sections we will describe the implementation of these ECS domains in the ST.

4.1.6 ST integration with LHCb

During stand-alone operation the sub-detectors need some resources that are not part of the ST infrastructure itself but LHCb wide: TFC, HLT, Storage

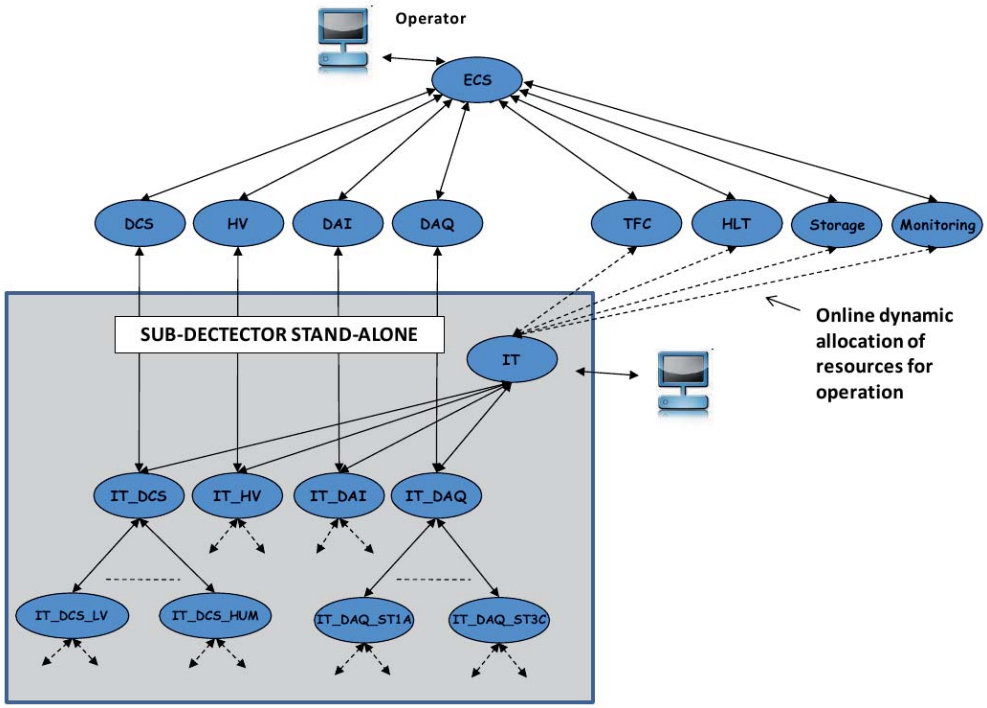

Figure 4.8: ST interconnection with LHCb

and Monitoring. To perform/emulate a run with all the detector capabilities enabled an online partition is needed. Such partition includes a TFC branch for driving the fast control signaling as well as resources from the HLT, the Storage and the Monitoring for handling the acquired data. This partition with all the resources is dynamically created and assigned to the detector. This is achieved by implementing a parallel hierarchy that can switch the four top domains (DAI, DCS, HV, DAQ) between the LHCb ECS tree and the stand-alone sub-detector top CU, as shown in the Figure 4.8. In the later case, online resources are requested from the pool of not assigned ones, allocating the needed quantity.

4.2 ST ECS

The Silicon Tracker Experiment Control System is capable of controlling and configuring the detector electronics infrastructure in different running modes, monitors all the relevant environmental parameters and is able to perform automatic corrective actions ensuring the safe running of the detector. The ECS has the responsibility for providing for the automation of standard procedures and for the automatic recovery from error conditions in a hierarchical way.

Several thousands of elements between devices and sensors, placed in the cavern and the barracks are controlled and monitored. A Control Board [30] was developed in order to provide among other functionalities, slow control (I2C

interfaces, PT1000 temperature readings...) and fast control signaling for the ST front-end electronics using the LHCb SPECS electronics interface system.

The ST consists of two sub-detectors, the IT and the TT, each of which is controlled by an independent FSM tree structured in a functional and a spatial division basis. Thanks to a care design of the hardware partitioning, common electronics cards, power supplies and cooling system, and to the development of a common CB, a similar ECS could be developed for both detectors.

As it was explained, the ECS has to take care of the DCS electronics (monitoring of temperatures, humidity, voltages, current...) and the DAQ equipment, i.e., configuring and monitoring the Beatles and TELL1 electronics. The ST ECS not only controls the detector hardware but also interfaces to the LHCb central ECS, which during normal running will take control of the detector.

4.2.1 ST Partitioning

The top level division into functional domains has already been mentioned: DAQ, DCS, DAI and HV. The DCS is further subdivided into LV, TEMP, HUM and COOLING. From these top layers downwards the control system follows a subdivision based on the detector physical structure.

In the IT detector the previously mentioned domains are first subdivided into six half-stations. These half-stations corresponds to the *ACCESS* and *CRYO* sides of the 3 tracking stations. Each half-station node has two detector boxes below, except for the*DCS/COOLING* domain and the *DCS/HUM* which have all the box-nodes hanging directly from the half-station node (see Figure 4.9), and the DAQ domain which has also a node with all the TELL1 boards linked to that half-station. In the others domains, the box-nodes are subdivided into two service boxes and seven partitions which are the final element of the hierarchy, that means that they are *Device Units*. One of the service boxes is fully used and houses one CB and four partitions of FE boards and the other one is just utilized partially with one CB and three partitions, except in the DAQ domain where the partitions have below the DB and FE hybrids, and also at the half-station level there is a separate subdivision for the TELL1s.

The TT subdivision follows the same phylosophy but as is made of a single tracking detector. In the TT the subdivision follows a similar philosophy but starting the division into regions. The cooling system and the humidity control underlie directly below their respective domains without subdivisions. Just underneath the regions there is a subdivision into top/bottom location of the service boxes and then the service boxes with four partitions each. The TELL1s fit just under the regions sub-division. The Figure 4.10 corresponds to the hierarchical structure of the DAQ domains for IT and TT. The difference among them is the physical division of the detector and the placement of the TELL1s in different levels of the hierarchy.

The HV partitioning is the same than the Temperature tree, so to avoid redundancy is not depicted. The only difference is that below each box there

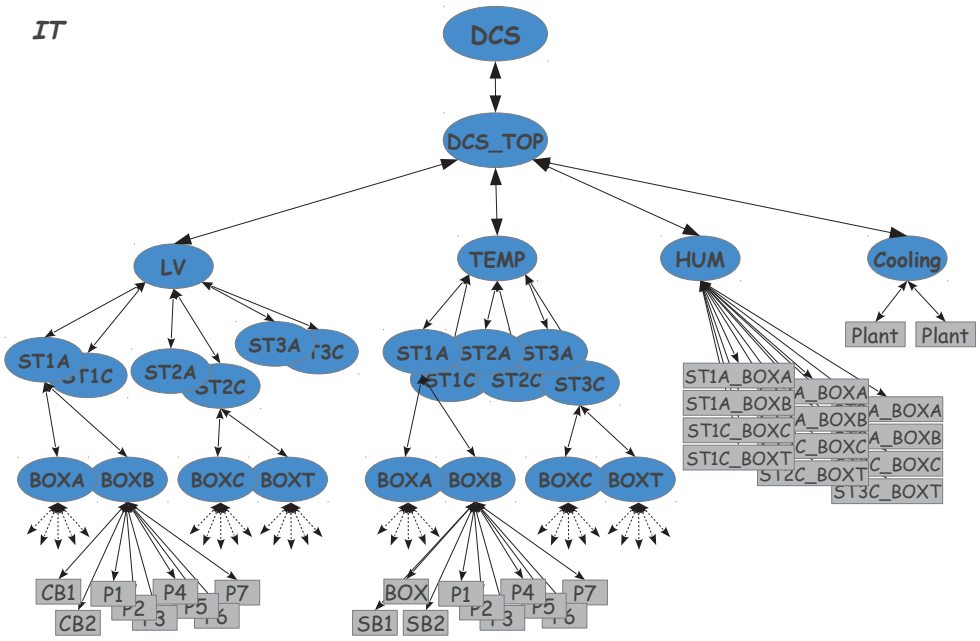

(a) IT DCS partitioning

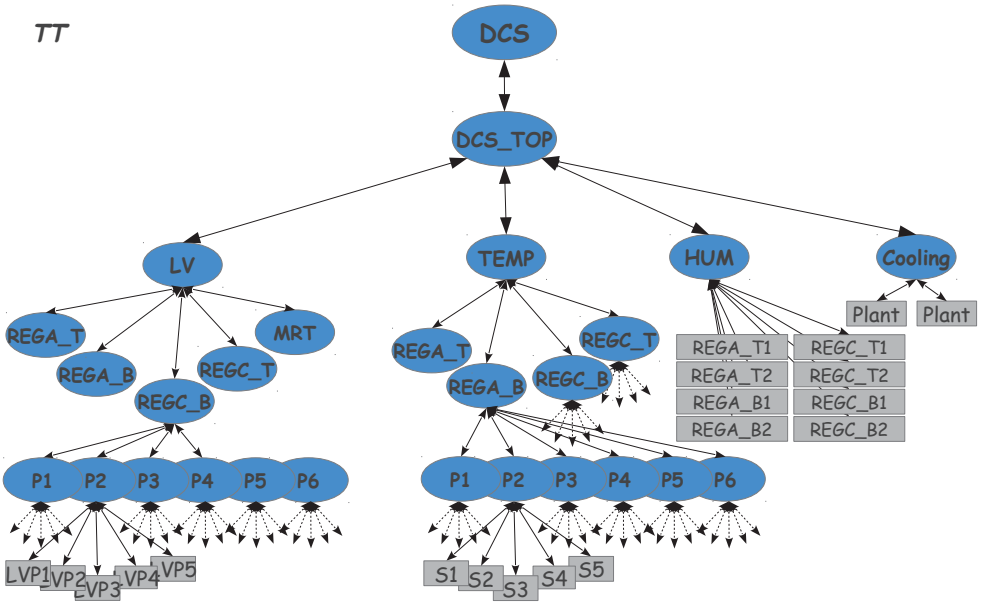

(b) TT DCS partitioning

Figure 4.9: ST DCS partitioning

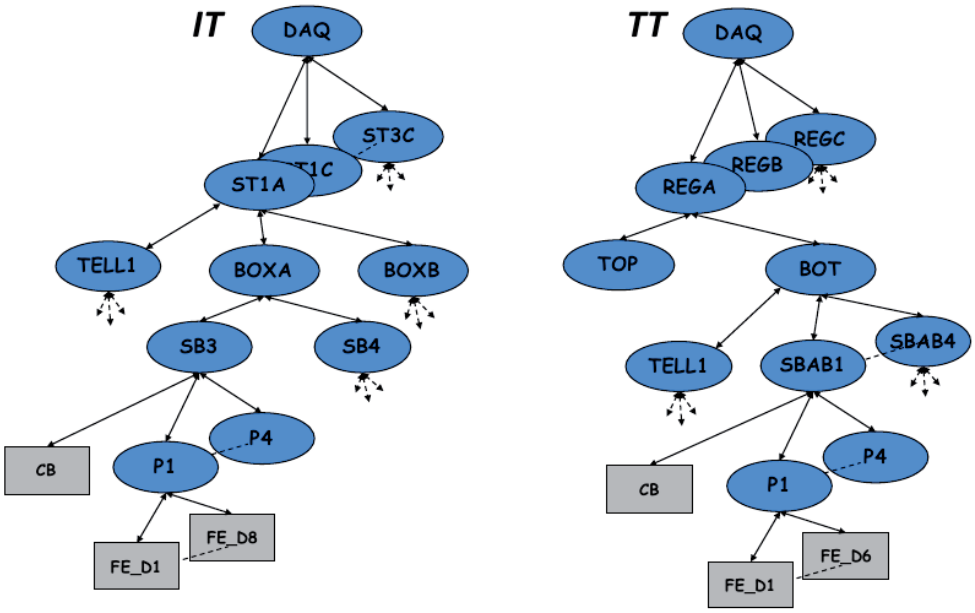

Figure 4.10: IT (left) and TT (right) DAQ partitioning

is only 7 partitions, corresponding to 7 groups of 4 ladders each which are linked to the same HV channel.

The DAI Domain does not have any partitioning below, just a link to the infrastructure tree with the corresponding electronic racks.

4.2.2 DCS Domain

The Detector infrastructure (DCS) domain includes all the components related to the correct detector operation, including monitoring sensors related to temperature, humidity, and also the control of the low voltage supply to the electronics. It also contains the supervision of systems like: cooling systems, electrical supply systems, etc. These components are normally stable throughout a full running period. The DCS tree is subdivided into LV (low voltage), TEMP (temperature), HUM (humidity) and COOLING sub-domains.

The DCS Domain States and Commands are showed in Figure 4.11. State and command names, and state colors are common to the whole LHCb ECS, and defined in the Guidelines [46]. The *Switch_ON* command will carry a parameter *RUN_TYPE*[1], specifying the desired running mode. The *ERROR* state is typically triggered by Alarms or configuration problems. The *EMERGENCY_OFF* state is triggered by the *Do_Emergency_OFF* command, which is send by a CU due to external causes.

[1]The RUN_TYPE is a tag that allows to use different configuration values in the new state. For instance, during normal operation the Beetles are configured with the RUN_TYPE *PHYSICS*, while during test runs the tag *TEST* is used. Both tags corresponds to slightly different Beetle parameters, however both sends the DAQ tree to *READY* state.

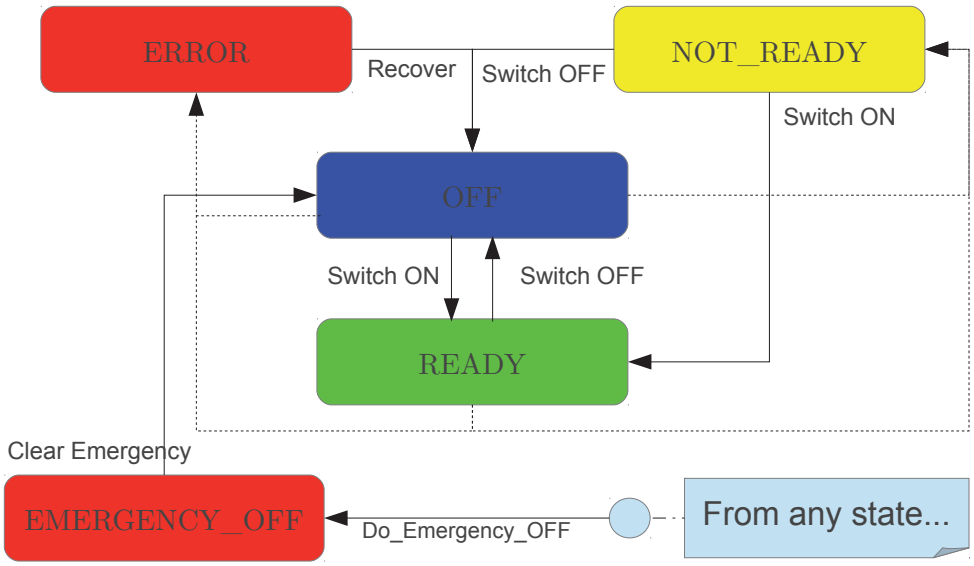

Figure 4.11: DCS Domain States and Commands

The DCS states and commands are detailed in Figure 4.11.

DCS_TOP

In the ST there is an additional layer between the DCS level and the partitioning in half-stations (IT) or regions (TT). This layer, named DCS_TOP (see Figure 4.9), allows to make compatible an special ST state called *Hybrids_OFF* with the DCS states. The reason is that according to the LHCb Guidelines the ST sub-detectors must be either in *READY* or in *OFF* state, and the others states involves an action from the operator. The problem is that when the ST is in state *OFF* all the electronics is switched off, and we lose the ability to keep monitoring the detector. To avoid such undesired situation, an special state called *Hybrids_OFF* was developed to be compatible with the DCS *OFF* state, while keeping the electronics needed to readout the humidity and temperatures sensors *ON*.

4.2.3 HV Domain

The HV domain (HV) contains all the components related with the high voltage power supply channels which polarize the sensors.

The switch on of HV channels is a time consuming operation that is necessary to minimize. Typically it takes several minutes to rise from 0 to the operational voltage. To minimize this lag the switch on procedure was divided in several steps, with intermediate standby values. The intermediary states for the various RAMPING stages are named *STANDBY1* and *STANDBY2*. As it happens with the DCS domain, the commands sent to change the state carries a parameter

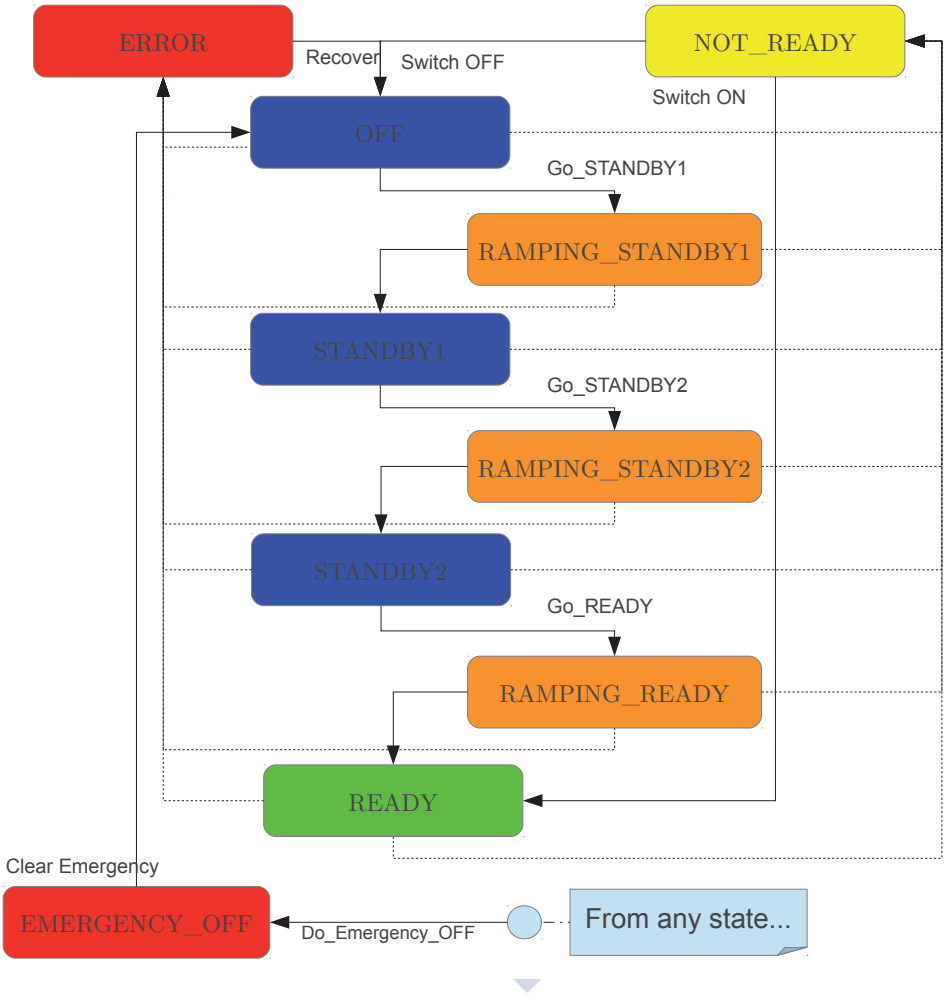

Figure 4.12: HV Domain States and Commands

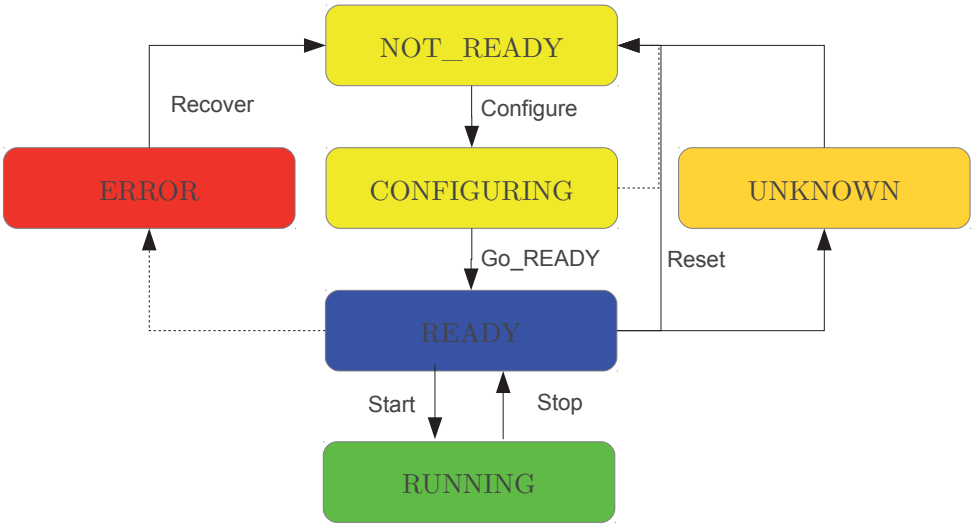

Figure 4.13: DAQ Domain States and Commands

named *RUN_TYPE* so that different voltage settings can be applied for different running modes.

A detailed scheme of the HV states and commands is shown in Figure 4.12.

4.2.4 DAQ Domain

The data acquisition domain (DAQ) includes all the components which participated in the acquire and the first processing stage of the data. The components included in this domain are the front-end boards (DBs and hybrids), readout boards (TELL1s) and trigger components included in the CB.

Every time than a hybrid is powered off, the DAQ tree must be configured with the proper settings, as the Beetles can not keep the settings without power. As in the others domains, the configuration settings depend on the desired running mode which is specified in the *RUN_TYPE* parameter. The devices must be reconfigured also when the running mode changes, for example from *PHYSICS* to *CALIBRATION*.

The DAQ states and commands are depicted in Figure 4.14.

4.2.5 DAI Domain

The DAQ infrastructure (DAI) includes all the components that provides power, network and computing resources to the data acquisition system. They are basically the CAEN, MARATON RCMs and TELL1 crates power. These components are normally stable throughout a full running period. The DAI components publish a state that simply shows if they are *READY* to be used or not.

The DAI states and commands are shown in Figure 4.14.

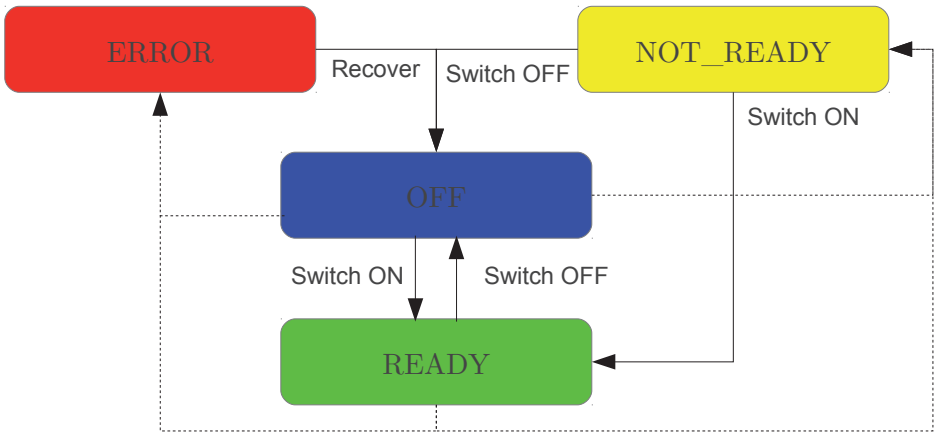

Figure 4.14: DAI Domain States and Commands

4.3 ST Safety System

Previous sections were dedicated to the ST control and monitoring tasks. In this section the different safety systems of the Silicon Tracker are detailed.

4.3.1 Alarm system

PVSS has an integrated alarm concept for safe and reliable monitoring of sensitive equipment. The alarms are triggered automatically by the DUs, when the measurements of the linked equipment (typically sensors) goes beyond the specified limits. Alarms can be send via speech output, pager, SMS or e-mail to operators and experts of the concerning equipment, however the aim of the alarm handling system is that all problems related to the detector equipment should be reported to the operator using one single tool: The Standard *Alarm Screen*. The Alarm Screen shows alarms for as many systems as it can be reached, but usually it is configured to show only the alarms of a single detector.

Alarms can have three severities: WARNING, ERROR and FATAL, however the last value is not used in the ST ECS as far as the ERROR state will already trigger an action. The meaning of the different severities varies depending of the domain. In the DCS and HV domains the severity of the alarm depends of the value of the sensor or channel with respect to some predefined limits, going from no-alarm to ERROR as the readout value grows (for instance due to a current trip). The action to be taken depends of the severity:

- WARNING: action may need to be taken, the problem needs to be followed up (a temperature or humidity level is starting to raise, for example)
- ERROR: action should be taken, but there is no immediate danger. The DU's state will be automatically changed to ERROR.

- FATAL: action should be taken immediately otherwise there could be damage to the detector (HV, Gas, Cooling problems for example).

In the DAQ domain the meaning of the severities is less straightforward:

- WARNING: problems that do not prevent from running and do not affect permanently the quality of the data but should be followed up.

- ERROR: a component failed to configure or problem was detected during the data-taking which could affect permanently the quality of the data. It should also trigger the FSM to go to ERROR state.

In general the idea is that WARNING alarms will inform the operators about a potential problem in order to take corrective actions. The operator should find in the Alarm Screen relevant information from the source of the problem, and contact the experts if needed. Whenever an alarm reach the ERROR level the DU concerned will change its state to another pre-established (like ERROR state), and such new state will be propagated upwards the FSM tree. In parallel, some automatic actions can be taken by CUs in upper levels (like switch-off the power supplies when a temperature alarm is triggered). The alarm should disappear from the Alarm Screen as soon as the problem is gone, although all the relevant information is written in the logs of the system.

Trends

Alarms are triggered due to unexpected problems like a failure in the cooling pumps, but in some cases they can be foreseen. The second kind of problems can be anticipated and as their reasons are well understood they should be avoided. This is the usual case when we look at the HV currents (Figure 4.15), as the leakage currents are growing constantly following the delivered luminosity. Using trends we can track this kind of values, and the alarm limits can be increased accordantly.

Although the trends are natively supported by `PVSS`, the JCOP team developed a tool to eases the implementation of the trends and to keep a consistent look-and-feel through all the detectors of the experiment.

4.3.2 Detector Safety System

The Detector Safety System (DSS) [48], developed at CERN in common for the four LHC experiments under the auspices of the Joint Controls Project (JCOP), is responsible for assuring the equipment protection for these experiments.

According to CERN rules there are three alarm levels. The responsibility for the highest level of safety, which is defined as "accident or serious abnormal situation, especially where people's lives are, or may be, in danger", is delegated to the CERN Safety System (CSS). Normal operation of the detectors is performed by the corresponding detector control systems (DCS). This left an area of

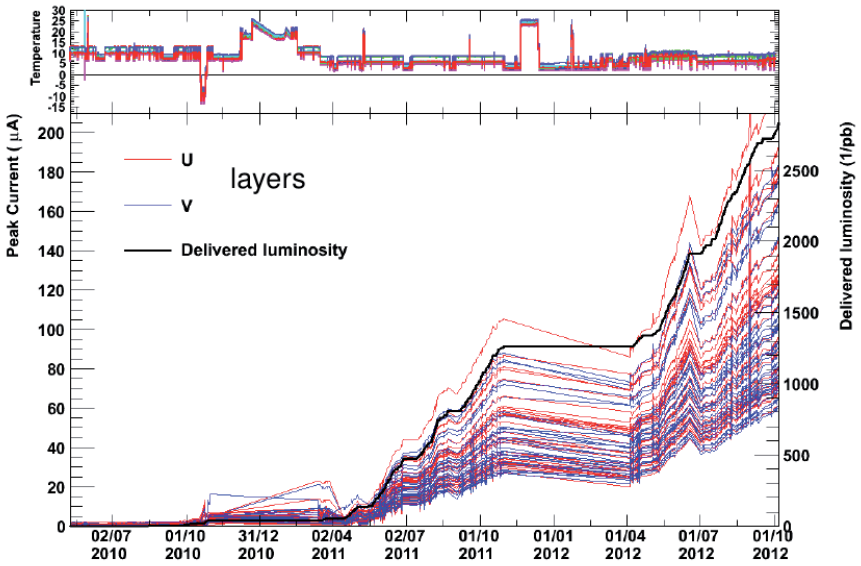

Figure 4.15: Trend of the HV current in the IT sub-detector. This current is mainly leakage current and is function of the radiation damage, as it can be seen when we compare it with the delivered luminosity. This trend can be used to periodically increase the alarm limits to avoid trigger alarms for a well understood reason.

uncertainty, especially as the availability and reliability of a PC-based DCS does not seem to be sufficient to ensure proper equipment protection.

The main goal of the DSS is to detect abnormal and potentially harmful situations, and to minimize the consequent damage to the experiment's equipment by taking *protective actions*.

As a consequence of the above mentioned goals, the following main requirements were defined for the DSS. It has to be:

- highly reliable and available, as well as simple and robust
- a cost-effective solution for experiment safety
- operated permanently and independently of the state of DCS and CSS
- able to take immediate action to protect the equipment
- scalable, so that it may evolve with the experiments during their assembly, commissioning, operation and dismantling (a time-span of approximately 20 years)
- maintainable over the lifetime of the experiments
- configurable, so that changes in the setup can be accounted for

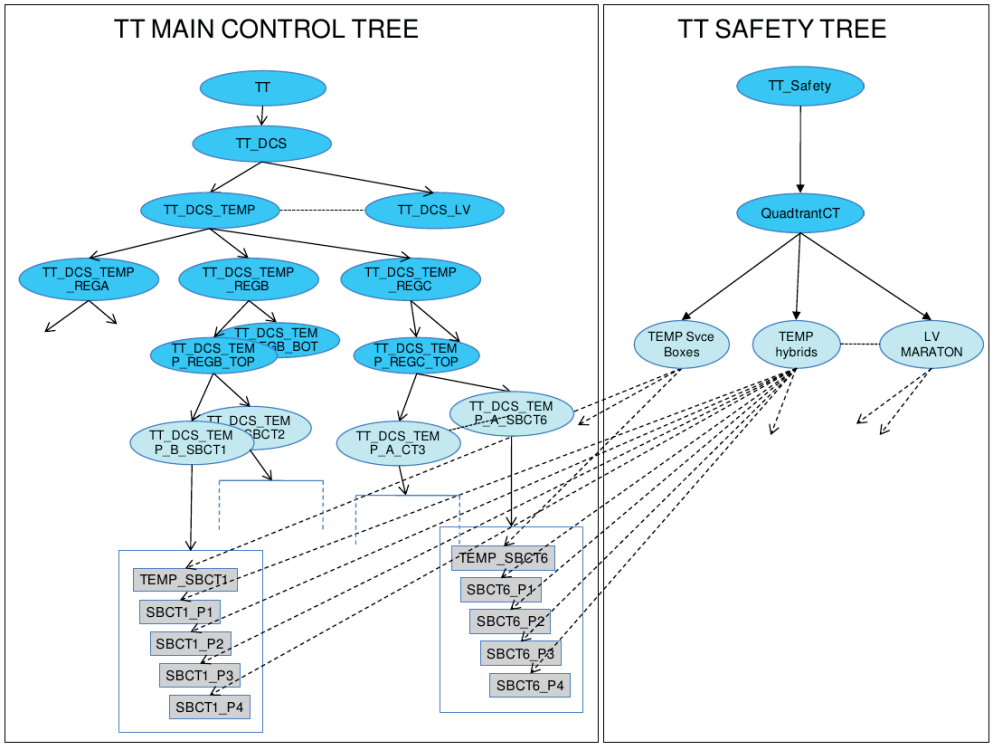

Figure 4.16: ST Safety tree

- connectable to other sub-(detector-)systems
- integrated into the DCS, so that existing tools can be reused, and that the look & feel, monitoring, and logging are standardized.

4.3.3 Safety tree

The Safety Tree is a unique tool developed for the Silicon Tracker, which links several FSM domains which are not connected in the FSM tree. As it was already explained, the LHCb ECS Guidelines establish a set of domains which are placed at the top of the IT and TT FSM tree. These domains are DAQ, DAI, HV and DCS, and below them the structure of the tree tends to follow the sub-detector distribution. However there is a potential risk in this model which is that in case of problem in small region of one domain, the rest of the domains must be powered off. As the involved hardware is very sensible, the emergency switch off must be avoided to enhance the lifetime of the equipment. The Safety tree solves this problems, as links all the domains but sorted by the minimum possible partition (half-station in the IT and quadrant in the TT). Thus, when a problem appears and an emergency switched off command must be send, only the affected partition will receive the command, and the rest of the sub-detector will remain in its previous state.

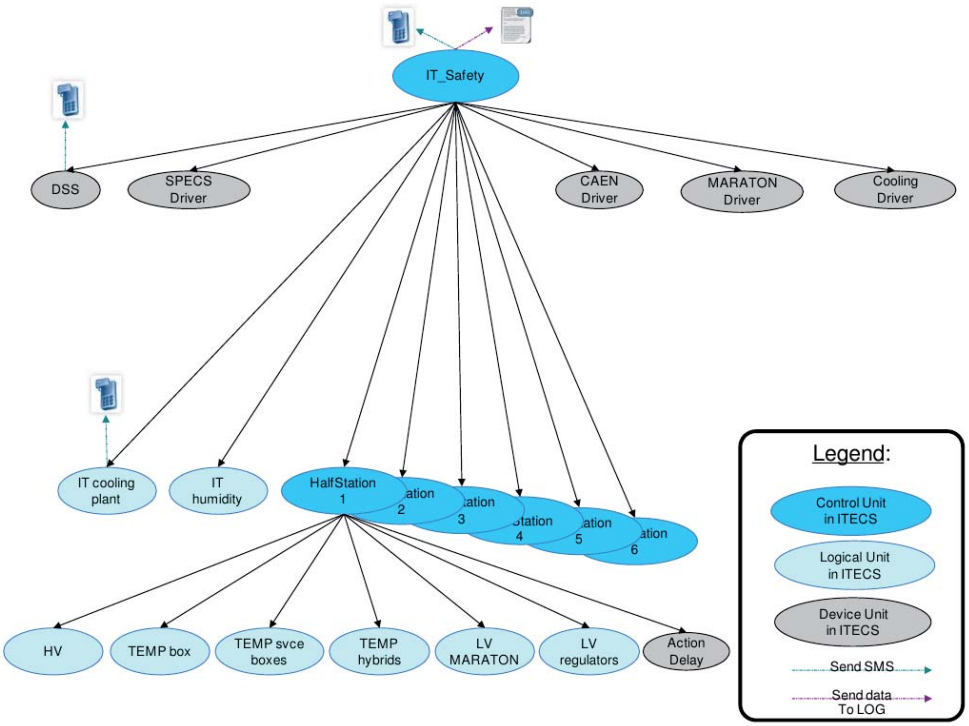

Figure 4.17: IT Safety tree

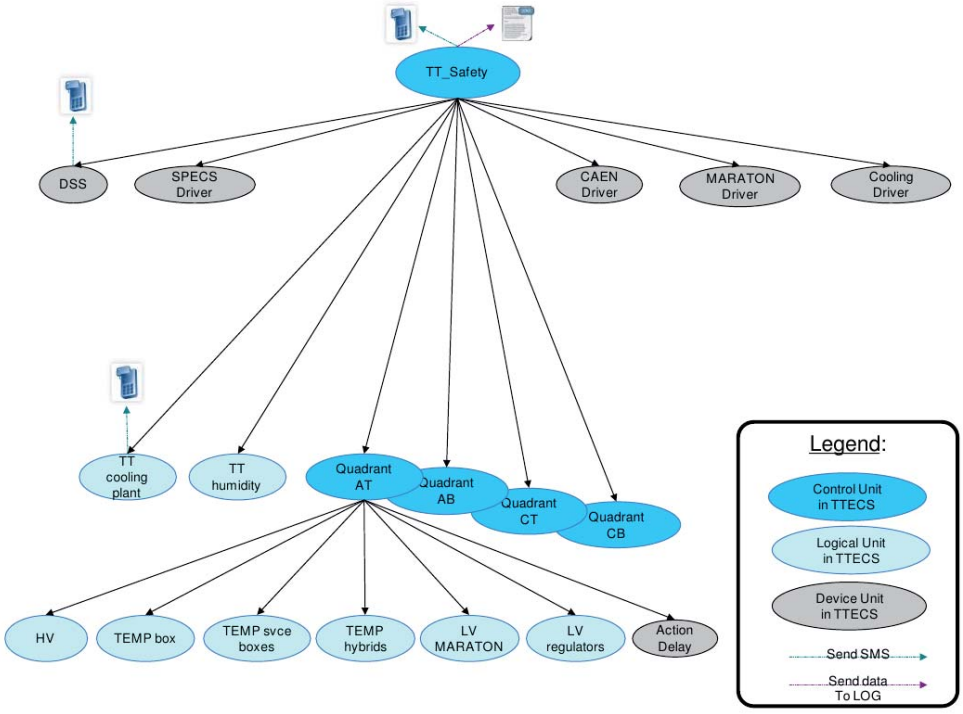

Figure 4.18: TT Safety tree

The Figure 4.17 and Figure 4.18 show the parallel control trees which implement the detector intrinsic safety procedures for IT and TT respectively. The dark blue color corresponds to CUs, the light blue to LUs and the grey box represents the DU that provides the DSS information. There is a top CU that summarizes the overall status and takes high level actions and then a spatial subdivision of the detector into half-stations or quadrants, also implemented as CUs. The DSS DU hangs directly from the top node, as well as the humidity, cooling plant control and other DUs intended to monitor the status of several relevant software entities. A subset of LUs hung from the half-station (quadrant) CUs.

This domain oriented subdivision links to the respective nodes of the main control tree, i.e. each of the LUs of the safety tree connects to the corresponding CUs, LU or DUs of the ECS tree (see Figure 4.16):

- HV: connects the HV CU that controls the channels corresponding to that half-station (quadrant).
- TEMP box: links to the DUs which read the interior box temperatures of the half-station (quadrant).
- TEMP Svce boxes: connects to the DUs used for the temperatures monitoring of backplanes and CB in the same half-station (quadrant).
- TEMP hybrids: links to the PT1000 sensors on the hybrids.
- LV MARATON: connects to the LUs that control the MARATON channels that power the service box in the same half station (quadrant).
- LV Regulators: connects to the DUs which control the LV regulators which power the hybrids and digitizer boards in the same half station (quadrant).
- Humidity: links to the CU that holds the humidity sensors installed in the detector.
- Cooling plant: the C6F14 cooling plant.

The state of the Safety tree is showed in the Safety Panel (see Figure 4.19). Together with with LUs described, several device units are showed also in the Safety Panel. These DUs are linked to the OPC CAEN and Wiener drivers (responsible of the communication with the HV and LV power supplies), the Cooling driver (responsible of the communication with the Cooling system) and the DSS system.

The DSS Device Unit

The underlying idea behind the DSS DU is to power OFF the equipment in a gentle way before the DSS system triggers a sudden power off of the racks. The DSS info is available in the ECS via the DIP protocol, so this DU implements the

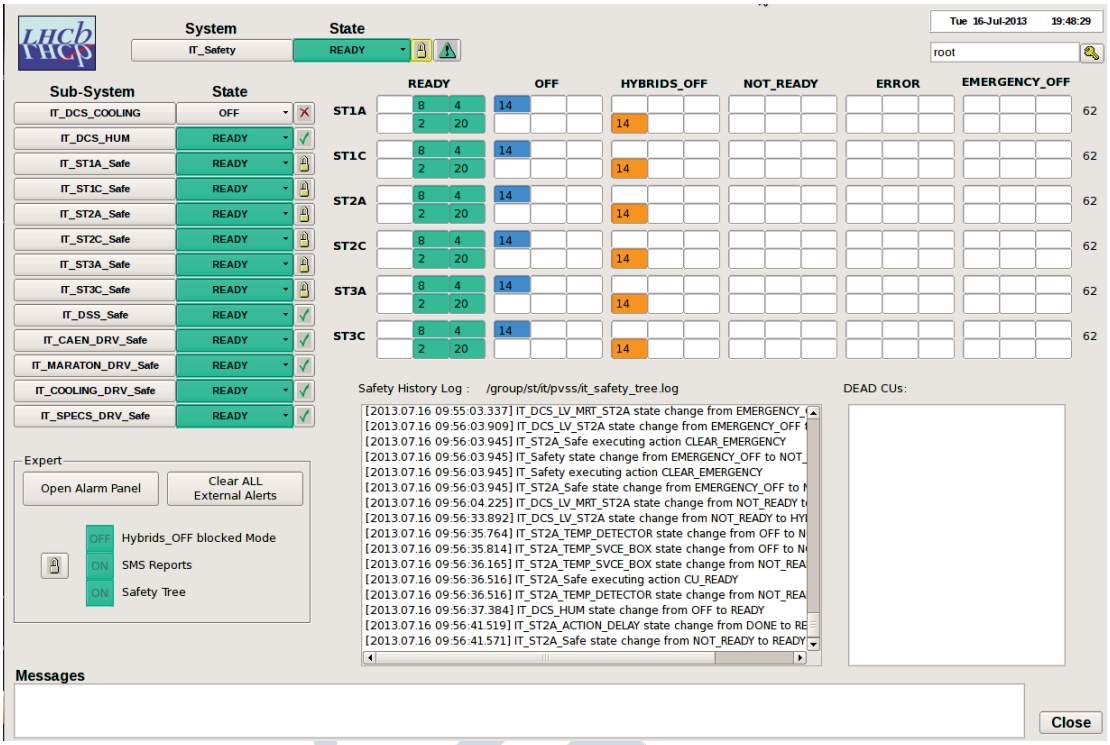

Figure 4.19: IT Safety Panel

subscription of the different signals. In the DSS most of the actions power off the equipment within a reasonable delay, time enough for the safety FSM to power off beforehand. The DSS DU implements the next FSM states:

- READY: The DU is actively monitoring the status of the DSS signals and they are all fine.
- ERROR: Any DSS signal has been triggered and a DSS action will take place within the programmed 10 or 30 s delay.
- NOT_READY: The DIP communication with the DSS is not established properly.

The SPECS, OPC and Cooling drivers status

In addition is crucial to introduce some additional safety measures to check that some relevant software entities are running, namely:

- The SPECS DIM-server and DIM-client. If any is not running this DU will be sent to *NOT_READY*.
- The status of the CAEN and Wiener MARATON OPC servers. This DU will be sent to *NOT_READY* if the servers are not running or stuck.

- The status of the PVSS manager that provides control and supervision for the cooling plant parameters.

These dedicated DUs hang from the top IT and TT safety node. An alert message will be sent to the main LHCb alert screen in case any of these elements stops running properly. The FSM corresponding to these DUs only need two states:

- READY:The software entity (SPECS Server/Client, the OPC server or the Cooling manager) is properly running.
- NOT_READY:The software unit is not running.

Part II

Sensor technology for the VELO upgrade

USC
UNIVERSIDADE
DE SANTIAGO
DE COMPOSTELA

5

The VErtex LOcator Upgrade

The VErtex LOcator (VELO) is the silicon detector surrounding the LHCb interaction point. The VELO sensors are placed inside the beam pipe, at only 7 mm from the beams, enclosed in a secondary vacuum box called RF-foil. The role of the VELO is critical in the overall performance of LHCb, providing excellent vertex and impact parameter resolution, high efficiency, and fast pattern recognition for triggering purposes.

5.1 The VELO detector at the LHCb experiment

The VELO [16] consists of an array of 42 modules spaced by 3 cm which extend from 25 cm upstream to 75 cm downstream of the interaction region. Every module has two single sided micro-strip silicon sensors, providing orthogonal information in the radial (R sensor) and angular (ϕ sensor) coordinates. The detector is operated in vacuum and a bi-phase CO_2 cooling system is used.

The innermost sensitive strip is located at only 8 mm from the beams, which means that the risk of damage in case of a problem with the beam is not negligible. That is the reason why the modules are mounted in two retractable halves, and only when the stable beam flag is raised both halves are closed, allowing a small overlap in the inner region. In any other case, the two halves are retract, occupying a "garage" position in the shadow of machine elements at a distance of about 30 mm from the beam line. The safety of the VELO closure around the colliding beams is assured by the fact that the VELO can reconstruct tracks and primary vertex positions even when open, and the information from this reconstruction is used to guide the detector to perfectly centre around the beams in an efficient

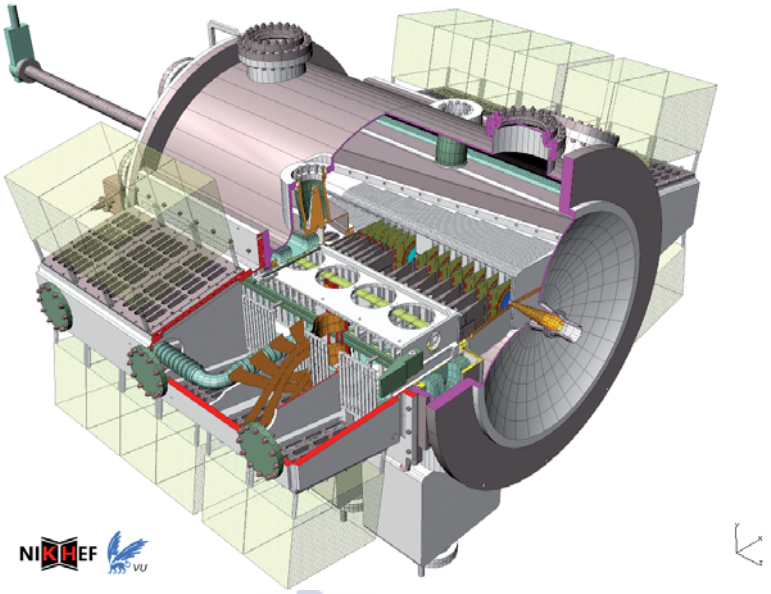

Figure 5.1: CAD image of the VELO detector. The beam pass through the center of the detector where the collisions occur.

and safe way, even allowing for beam movements of several mm between fills.

The main purposes of the VELO can be summarized as follow:

- Distinguish between the collision and the disintegration points at each bunch crossing. By registering the passage of charged particles within its silicon sensors, and after reconstruction of forward and backward-going tracks, the VELO allows the measurement of the coordinates of the vertices. The distance between the point where a B meson is produced, the primary vertex (PV), and the point where it decays, the secondary vertex (SV), is a key observable for B physics.

- Hits in the silicon are used to reconstruct straight track segments within the subdetector. Those tracks segments are used as seeds for the LHCb track reconstruction software. As the magnetic field is low enough in the VELO, the bending in the trajectory of charged particles is insignificant.

- The VELO is also used in the first-level L0 trigger, as Pile-Up detector. The pile-up system consists in two planes of silicon strip detectors which are used to determine the number of primary interactions and the track multiplicity within one bunch crossing. The goal is to identify events that contain more than one interaction. Single interaction events are indeed easier to treat, both in the higher levels of trigger and the offline analysis. The VELO is also used in the software High Level Trigger (HLT), together with the other LHCb subdetectors.

The unique acceptance and positioning of the VELO has also allowed imaging of the LHC beams, which allows a non-disruptive luminosity measurements and

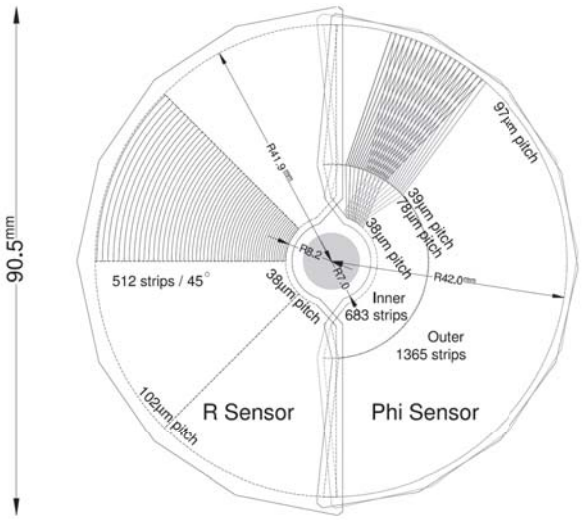

(a) Sketch of a R and ϕ sensors with the most meaningful dimensions

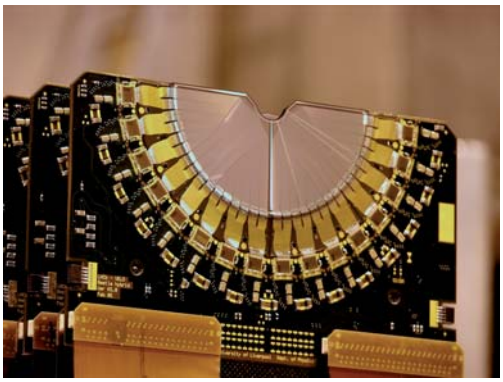

(b) Picture of a VELO module with a R sensor in foreground

Figure 5.2: VELO modules

has proved useful for many beam profiling analyses [49] and the good track precision allows an accurate "self-radiography" via the reconstruction of hadronic interaction vertices, which has proved essential in understanding the detector material composition and performance.

5.1.1 VELO modules

Every module is composed of two n^+-on-n 300 μm thick half disc sensors with R and ϕ-measuring micro-strip geometry. The two sensors are glued onto individual hybrid circuits which are laminated to either side of a carbon fibre coated 400 μm thick thermal pyrolitic graphite (TPG) core which acts as the thermal highway for the module. The sensors are all n-implant on n-bulk type, with the exception of one module mounted in the the most upstream position which is "n-on-p" type. The pitches range from 38 μm in the innermost region to 102 μm in the periphery. Each sensor has 2048 strips, readout with 16 analogue front-end chips (Beetle [50]). The module produces about 20 W and is cooled with an evaporative CO_2 system which delivers the coolant via stainless steel tubes to 5 aluminium cooling blocks clamped to the base of the hybrid circuits. The silicon sensors are maintained at -7^o during normal operation and $\sim -30^o$ when the VELO is powered off between periods of stable beam collisions.

5.1.2 VELO performance

The 1 MHz L0 trigger rate is reduced to a few kHz by full event reconstruction in the computer farm. The VELO plays a crucial role providing vertexing information for this decision. On the tracking and vertexing side, the VELO

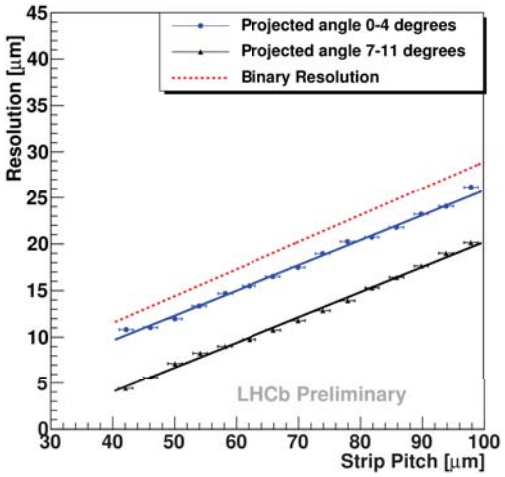

(a) Point Resolution

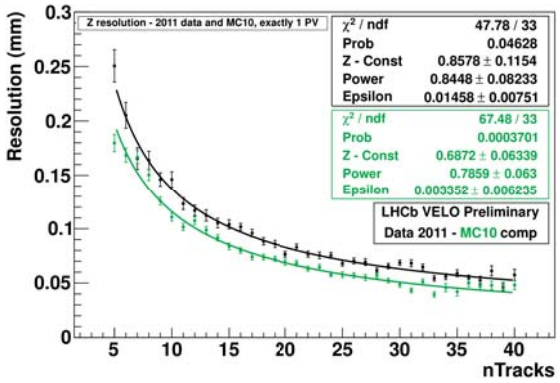

(b) Primary Vertex

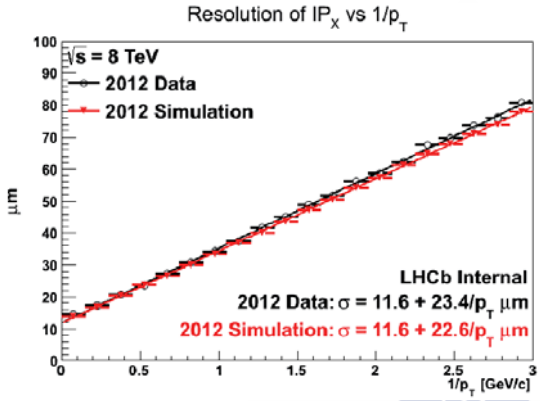

(c) Impact Parameter

Figure 5.3: Figure (a) shows the single hit resolution of R-sensors as function of strip pitch for two different projected angles. The binary resolution is shown as reference (Credits Silvia Borghi). Figure (b) shows the vertex resolution along the beam axes (Z) as function of the number of tracks (Credits Silvia Borghi). Figure (c) shows the impact parameter at optimal angle (Credits Michael Alexander).

provides accurate reconstruction of primary and decay vertices, reaching a point resolution of 4 μm in the 40 μm pitch region at optimal angle ($\sim 10^{o}$, Figure 5.3a). The primary vertex resolution (PV) is 13 μm in the longitudinal direction for about 25 tracks (Figure 5.3b). The final momentum dependent impact parameter resolution (IP) is $11.5 + 24.5/p_T$, where p_T is the transverse momentum in GeV/c (Figure 5.3c). Accurate determination of the IP is very important for LHCb. The relationship between the IP and the PV for a particle is used in the trigger as cut in many physics analysis.

As result, a lifetime resolution of $\sim$ 50 fs was achieved for the flagship channel $B_s \rightarrow J/\psi\phi$ [51], typical of those channels where the resolution is necessary to resolve fast B_s oscillations. Excellent resolution is also very important for background suppression in rare decay channels.

5.1.3 Radiation damage

Due to the small distance to the interaction point severe radiation damage is foreseen in the VELO sensors [54], with doses $\sim 0.6 \times 10^{14}\text{MeVn}_{\text{eq}}$ cm^{-2} per accumulated fb^{-1}. The increase of the leakage current was measured as a function of the delivered luminosity (see Figure 5.4a). The periods with a decrease in the current corresponds to the annealing during shut-down periods or to occasional detector warm ups. The typical current increase is around 1.9 μA per 100 pb^{-1} delivered. The effective depletion voltage is measured with HV scans during dedicated data-taking periods. Figure 5.4b displays the results of these scans split by detector region and received dose. Most of the innermost parts of the n$^+$-on-n sensors have already passed through type inversion. Studies of the cluster finding efficiency have revealed a radiation induced charge loss in R-type sensors. For these sensors the mean of the collected charge is lower, and the distribution has experienced deformation due to a growing fraction of clusters with very small charge. The effect has been linked to coupling between routing lines in the second metal layer and the aluminium of the strips in the first metal layer. After irradiation, phantom signals in the inner strips (with readout through lines in the second metal layer) have been detected when the particles cross the outer strips. In the case of the ϕ sensors the effect is mitigated because lines in both metallizations are collinear. The exact mechanism and the relationship with radiation damage is under study. For more information about radiation damage in the VELO, see [55, 56].

5.2 The VELO upgrade

5.2.1 The LHCb upgrade

As it was explained, LHCb is running above design parameters, recording around 2 fb^{-1} per year, expecting up to 9 fb^{-1} by the end of 2017. In that moment LHCb will be able to cover its primary physics goals, namely the search for New Physics via the measurement of CP asymmetries and rare decays of b and c quarks. Nevertheless, many physics channels will still be statistically limited. An upgrade is planned for 2018 and the luminosity will be increased up to 2×10^{33} cm^{-2}s^{-1}, reaching 10 fb^{-1} per year.

Luminosity by itself will not improve hadronic event yield since the current bottleneck is the hardware trigger. Currently the LHCb trigger is implemented in two stages (see Figure 5.5). The first level is a hardware implemented trigger, carried out with information from the Muon and Calorimeters detectors. The next step is the High Level Trigger (HLT) where more refined selections are made in a CPU-farm using data from the others detectors, like the displaced vertices information provided by the VELO. The hardware trigger was implemented to filter the event rate from 40 MHz to a maximum of 1 MHz so the HLT can process them. Thus the effective readout rate for the current VELO is ≤ 1 MHz.

After the upgrade, all the detectors will be readout at 40 MHz, providing data to a fully flexible software trigger, which will select events of interest according to information like the reconstructed vertices. This trigger-less system will raise the bandwidth needs by a factor of 40, promoting the LHCb to the category of a general purpose experiment in the forward direction. This implies that all the front-end electronics must be redesigned or adapted to cope with the new data rate requirements, implementing new functionalities like zero suppression in order to reduce the bandwidth.

The LHCb experiment will record around 1-2 fb^{-1} of data per year until end 2017, accumulating in excess of 5 fb^{-1}. Afterwards many of the physics channels will still be statistically limited. The LHC is already capable of delivering much higher luminosity to the experiment than the current one, therefore the LHCb has planned an upgrade for 2018 which is independent, but compatible with, the LHC upgrade. After the upgrade the experiment will operate at luminosities up to 2×10^{33} $cm^{-2}s^{-1}$ and will readout collisions at 40 MHz. In these new conditions we expect to collect more than 5 fb^{-1} per year, with improvements of up to a factor 2 in the efficiencies in hadronic channels.

5.2.2 The VELO upgrade

It is a big challenge for the VELO to cope with the requirements of the LHCb upgrade, specially in terms of radiation damage and data bandwidth [57, 52]. These new conditions must be satisfied keeping, or improving, the performance of the current VELO in terms of precision, pattern recognition and impact parameter resolution. The radiation dose will reach up to 230 MRad or 5×10^{15} 1 MeV n_{eq}/cm^2 in the inner regions of the sensors. The radiation dose will be extremely non-uniform as can be appreciated in Fig. 5.6a. Preliminary simulations shows an average rate of 26 tracks per sensor per bunch crossing, giving an output rate above 2 Tbit/s from the whole VELO, Fig. 5.6b.

Many systems of the current VELO detector, such as the motion system, the vacuum, the power systems (LV/HV) and the evaporative CO_2 cooling system, will be reused.

On the sensor side two options are under consideration, pixel sensors with an ASIC based on Medipix/Timepix family (Figure 5.7a), and strips sensors with a new and more advanced ASIC (Figure 5.7b). Both options imply a completely new module and RF foil design.

Requirements One of the main constraints for the VELO upgrade is the bandwidth associated to a triggerless experiment, specially with the increase of the luminosity. The total data rate coming out from the detector will be around 2.4 Tbit/s for the strip option, or 2.8 Tbit/s for the pixel option. The other main issue is the radiation damage, as the upgraded VELO must be able to withstand radiation levels above 400 MRad or 10^{16} 1 MeV n_{eq}/cm^2.

Table 5.1: Main Velopix features

Pixel array	256 x 256
Pixel size	55 μm $\times$ 55μm
Minimum threshold	$\sim$ 500 e^-
Peaking time	$<$ 25 ns
Time walk	$<$ 25 ns
Measurements	Time-of-Arrival & Time-over-Threshold
ToT range	4 bit (1-2 MIP)
ToA resolution / range	25 ns / 12 bit
Count rate	Up to 500 Mhit/s/chip
Readout	Continuous, sparse, on-chip clustering
Output bandwidth	$>$ 12 Gbit/s
Power consumption	$<$ 3 W/chip
Radiation hardness	$>$ 500 MRad, SEU tolerant

FE Electronics

Pixel option The baseline choice for the upgraded VELO is a pixel ASIC called Velopix, which is based on the Timepix3 [58]. Some of the Velopix characteristics are summarized in Table 7.1. The ASIC will integrate local intelligence at the pixel level for time-over-threshold measurement and sparse readout, on-chip zero suppression and packet-based readout. In addition, Velopix must be immune to single-event upsets in its digital logic. The main difference between Timepix3 and Velopix is that the latter should cope with higher particle flux, hence the bandwidth must be 6 or 7 times greater. The Medipix3 family was designed to be radiation hard, and the Velopix chip will inherit this feature to cope with radiation conditions of the upgraded VELO.

Strips option The conservative proposal is the strip sensor with an enhanced design and readout chip. The development of the ASIC is ongoing in synergy with other silicon detectors in LHCb. It will implement embedded solutions such as clustering, sparsification, common mode suppression and pedestal subtraction. A strip design results in a lower material budget than a pixel based solution.

Sensors The baseline option for the sensor is planar silicon with n^+ type readout [59]. The challenges for both pixels and strips include coping with a large and very non uniform radiation dose, reducing the material budget and incorporating as narrow as possible guard rings.

For the strip option, sensors should have a minimum pitch of 30 μm or below (currently 40 μm), 200 μm thickness (currently 300 μm), *n-on-p* type, and with a variable pitch in order to keep the same occupancy per strip. For this option,

several prototypes with R and ϕ design were produced by Hamamatsu, and are currently under characterization in the University of Santiago de Compostela.

In the case of the pixel option, other alternatives than planar sensors are under consideration, like 3D sensors [60] and diamond sensors. Several 3D sensors from CNM were studied during last testbeam campaigns (Figure 5.8).

Mechanics and cooling As it was explained in section 5.2.2 the cooling system for the VELO upgrade will be based on the same evaporative CO_2 system that is installed in the current VELO. However, two main techniques are being investigated in order to cool the module sensors.

CVD Diamond A proposed solution (Figure 5.9a top), and consists of a chemical vapor deposition (CVD) diamond support plus a thermal pyrolitic (TPG) cooling block. The diamond support guarantees a high thermal conductivity, highly robust and low material budget. For this solution the R&D is currently centered on diamond metalization.

Micro-channel Through etching processes, a set of micro-channels are developed into a silicon substrate [61, 62]. The coolant (CO_2) is forced to circulate through them at a pressure of $\sim$ 60 bar (Figures 5.9a-bottom and 5.9b). It is an attractive solution because the channel layout can be adapted to the heat dissipation needs.

RF-foil The RF-foil is the aluminium box which encloses the VELO in a secondary vacuum. It allows overlap between the halves of the detector and shields the front end electronics from the RF noise pick-up and from beam currents. Depending on the module technology, a custom RF-foil must be manufactured. A new technique will be used, milling the 250 μm thick box from a solid aluminium block by a 5-axis milling head. The milling process is better than the pressing method used in the current VELO because it can manufacture sharp corners needed for the pixel option and allows a better thickness control. A large R&D is under way to manufacture a full scale prototype within the required specifications.

5.2.3 The testbeam program

We have built a testbeam telescope with 9 Timepix sensors [65, 66], 8 in ToT[1] configuration and the last one in ToA[2]. This telescope has a point resolution at the Device Under Test (DUT) level of $\sim$ 1.5 μm, a time tag resolution of $\sim$ 1 ns and handles a track rate $\approx$ 10 kHz. The Timepix hybrids are connected to an innovative system called RELAXed which is based on FPGAs and can read 4 hybrids in parallel sending the data through an Ethernet connection.

[1] **T**ime **o**ver **T**hreshold provides a value proportional to the deposited energy.
[2] **T**ime **o**f **A**rrival provides the time-stamping of the track

Up to 8 different DUTs were analyzed with this telescope such as irradiated Medipix2 chips, thinned planar sensors (150 μm thick) or 3D sensors [64]. In Figure 5.11a a comparison between two planar sensors of 150 μm and 300 μm thickness is shown. The residual value inform us about the resolution of the reconstructed cluster in the DUT with respect to the extrapolated track given by the telescope, and it changes with the angle and the thickness as expected. In 3D sensors polarization is made between n-type and p-type columns etched into the silicon. Due to this particular geometry, a certain loss of efficiency is expected when a particle crosses the sensor trough a polarization column, as it can be seen in Figure 5.11b.

Figure 5.11c shows a resulting plot from the 2012 testbeam campaign. The device under test was an n-on-n edgeless sensor, 150 μm thick, bump bonded to a Timepix chip. It can be seen how the sensor efficiency remains near the 100% beyond the last sensitive cell, reaching the physical edge of the sensor.

5.2.4 Schedule

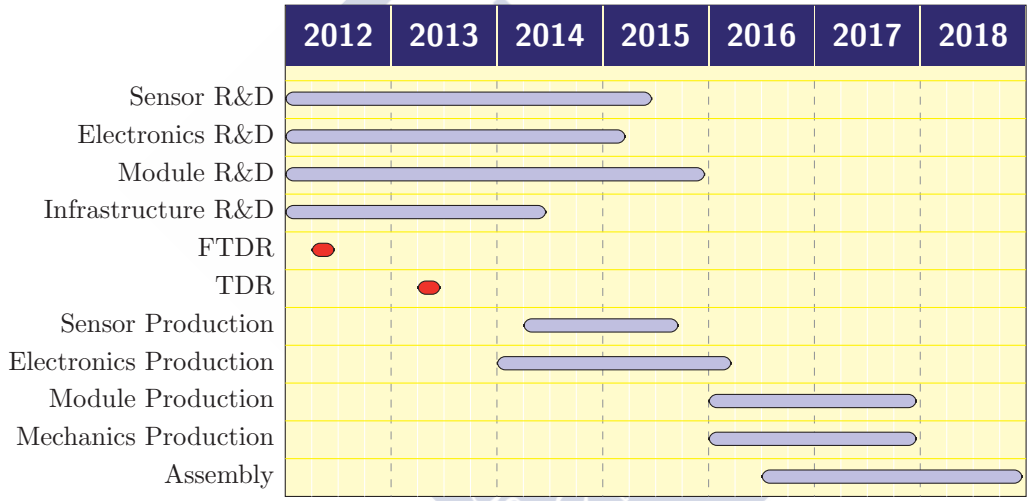

The upgraded VELO will be installed during the Long Shutdown 2, starting in 2018. A Letter of Intent [67], and a Framework Technical Design Report [68] were already published describing the LHCb Upgrade. To be ready for the production stage, an intense R&D program is underway providing useful information to choose the most suitable technology on the different aspects detailed previously. That decision will be made in the second quarter of 2013, when the Technical Design Report will be published.

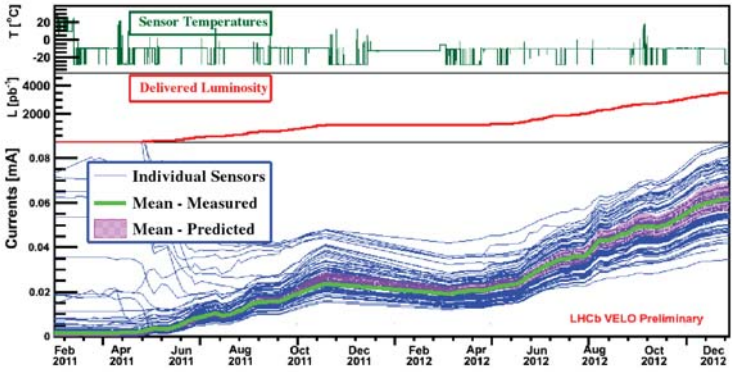

(a) Leakage current versus delivered luminosity

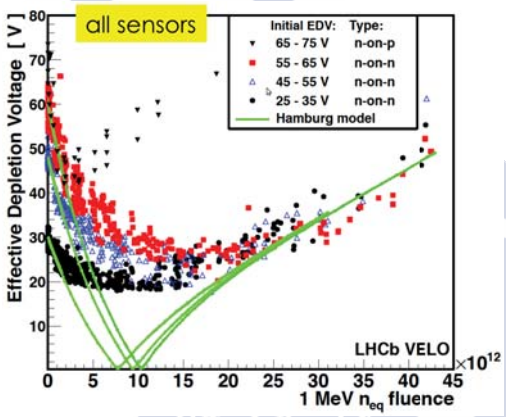

(b) Effective Depletion Voltage (EDV)

Figure 5.4: Radiation effects on VELO. Plot (a) shows the measured leakage current at -8^{o}C as function of the luminosity. Each blue line corresponds to a single sensor, the green curve is the mean current value excluding those sensors with initial high currents, and the pink band corresponds to predicted currents. Figure from Ref. [52]. The effective depletion voltage (EDV) for sensors with different initial EDV is shown in plot (b). EDV initially decreases with fluence for all radius. After type inversion, EDV increases with fluence. Type inversion starts at inner radius. Figure from Ref. [53].

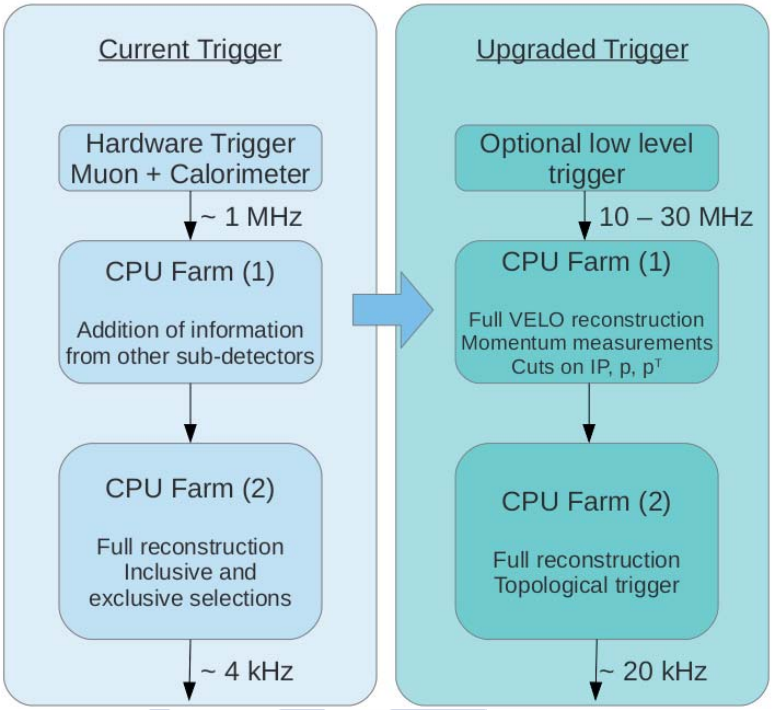

Figure 5.5: Comparison between the current LHCb trigger scheme and its corresponding in the upgraded LHCb

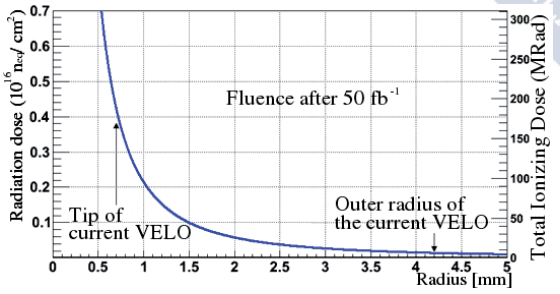

(a) Radiation dose as function of the distance to the beams

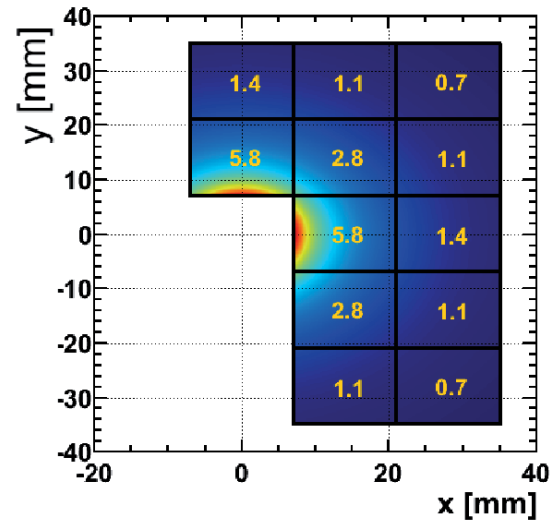

(b) Rate of tracks per bunch crossing in a pixel based module

Figure 5.6: Expected values of radiation and track rate per bunch crossing for the upgraded VELO. Figure from Ref. [52].

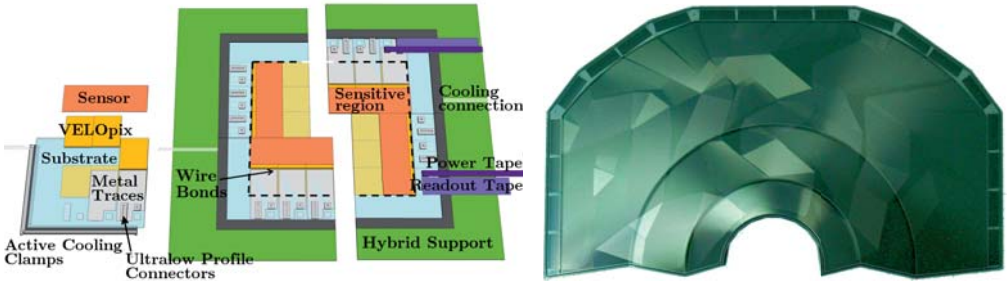

(a) (b)

Figure 5.7: L-shape module for the pixel prototype 5.7a, and prototype of ϕ strip sensor produced by Hamamatsu 5.7b

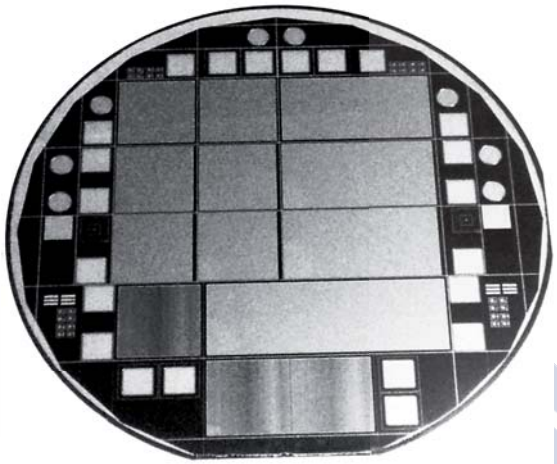

Figure 5.8: Wafer produced by CNM with tiles of 1, 2 and 3 Medipix ASICS

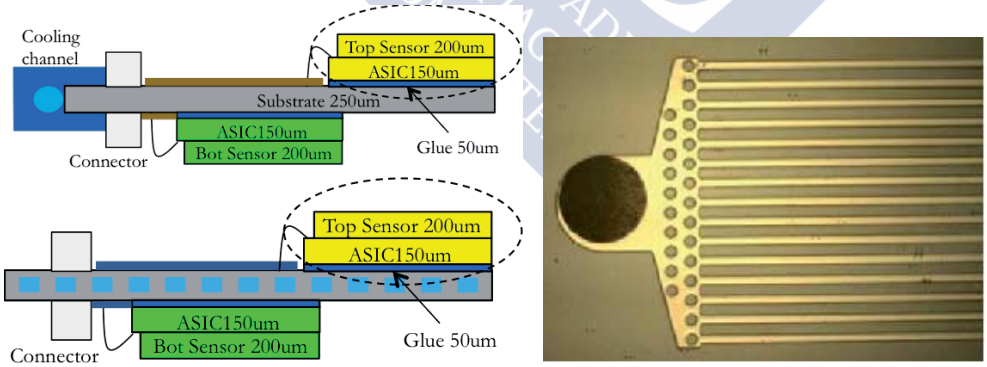

(a) CVD Diamond support and TPG block (top) and Micro-channel (bottom)

(b) Micro-channel Cooling: substrate outlet

Figure 5.9: The two options under consideration for module cooling. Figure (a) (top) is the baseline solution based in a diamond support. Figures (a) (bottom) and (b) show the alternative solution based on microchannels etched into the silicon module's support. Microchannels dimensions are 200 μm $\times$ 70μm.

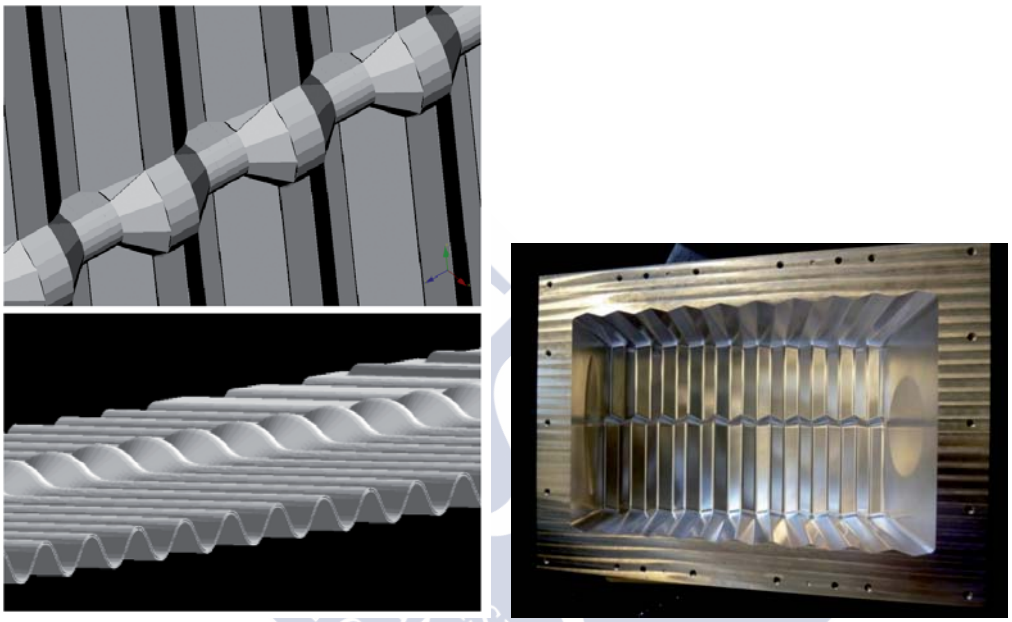

(a) RF-foil description in XML language (top) and in GDLM (bottom)

(b) RF-foil milled from an aluminium block

Figure 5.10: In Figure 5.10a a comparison is show between the current software description of the RF-foil using XML language, and the future object described with GDML language. On Figure 5.10b a picture of a prototype of an RF-foil is show after the milling process.

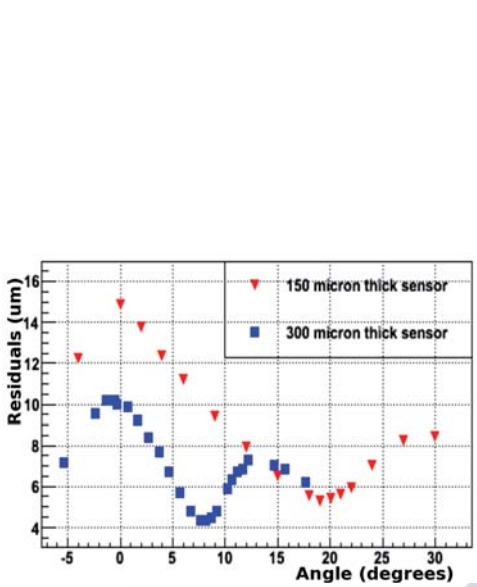

(a) Residuals of different planar sensors

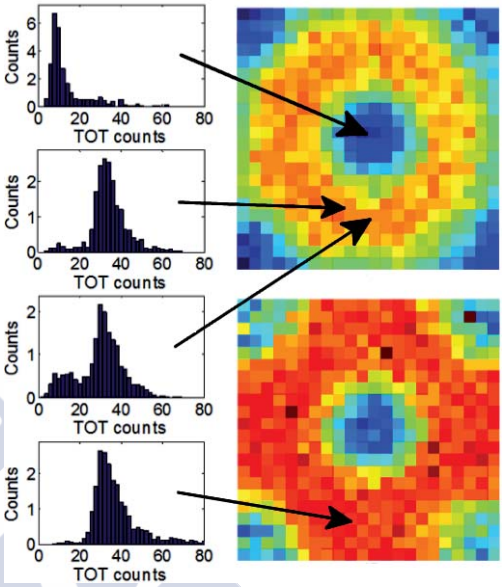

(b) Efficiencies in column region measured for a 3D sensor

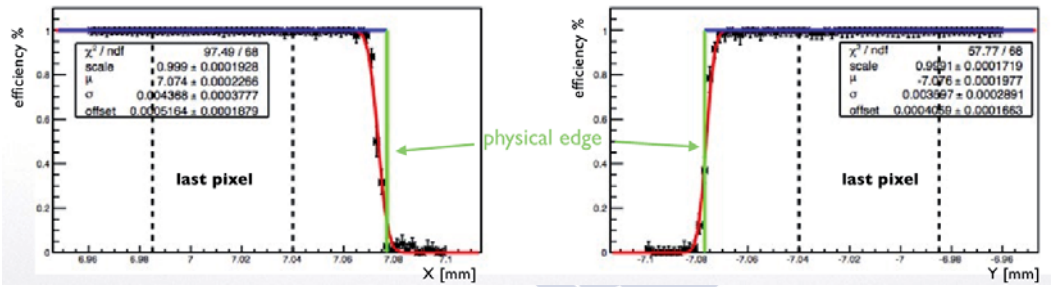

(c) Efficiency in an edgeless Timepix device

Figure 5.11: Figure (a) shows a comparison between two planar sensors of different thickness. Figure form Ref. [63]. Figure (b) shows the energy collected for a 3D sensor in a column neighborhood. Figure from Ref. [64]. Figure (c) shows the efficiency in an edgeless device. The sensor is sensitive beyond the pixel cell, until the physical edge. Credits Panagiotis Tsopelas

6

Theory of Silicon Detectors

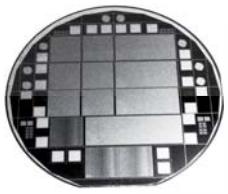

In this chapter some theoretical background is introduced in order to understand the principles of the silicon detectors.

Silicon crystals and the PN-junction are briefly described in first place, to continue then with the fundamentals of the interaction of radiation with matter and how we can build a detector able to register a ionizing particle.

The chapter will finalize with a short description of the different roles that the silicon detectors plays in the actual High Energy Physics experiments.

Most of the information for this chapter, as well as most of the figures, were obtained from [69, 70, 71, 72].

6.1 Principles of Silicon Semiconductors

Silicon is an element with 14 electrons, four of them in its outermost shell. Silicon atoms can join to another atoms through covalent bonds by sharing their four valence electrons, reaching a configuration equivalent of a full outer shell. Under certain conditions a silicon crystal can be grown, in such a way that all the silicon atoms are arranged making a periodic structure.

6.1.1 Silicon Crystal Structure

Spatial atomic distribution in a silicon crystal is shown in Figure 6.1. Into a cell, atoms are linked by covalent bonds and each atom shares 4 electrons with the neighbours. The distance between atoms is around 2.35 Å and size of a unit cell is 5.43 Å. The cell structure is repeated periodically all through the crystal, making a lattice.

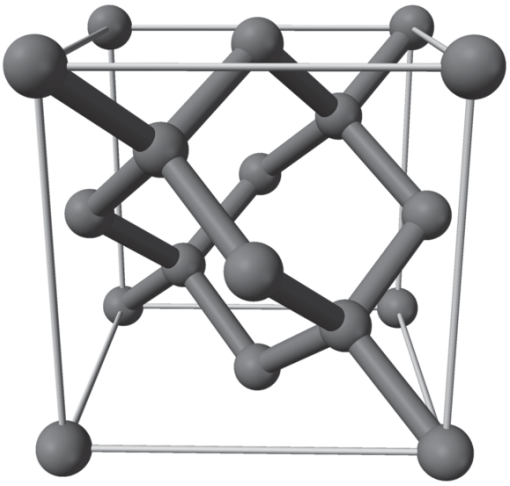

Figure 6.1: Structure of a crystal unit cell like the ones that you can find in diamond, Si and Ge crystals.

At low temperature (below 50 K) all the electrons are in their covalent bonds, but at higher temperature some electrons can scape from the cell and travel through the lattice. When an electron is released, a *hole* with positive charge is leaved behind and it can be occupied by another electron. Consequently, when a electron is released both the electron and the hole can travel through the net.

6.1.2 Energy bands

According to quantum mechanics electrons can only reach a discrete number of energy level into an atom. When two atoms are bonded, each quantum level is split, and when the atoms are arranged in a crystal lattice the quantum energy levels forms a quasi-continuum energy band (see Figure 6.2). In silicon, when the atoms are at the equilibrium distance of 5.43 Å electrons can be in either be in the conduction band or in the valence band according to their energy, but there is a forbidden band of energies in between (gap).

Materials can be organized according to their gaps in the energy band as follows:

- Isolators: those materials where the band gap is $\lesssim 9$ eV, meaning that all the electrons are strongly linked to the covalent bond.
- Conductors: those materials where the band gap is so small that the conduction band is partially filled, even both bands can overlap.
- Semiconductors: those materials where the band gap is ~ 1 eV, so it is not difficult for an electron to reach enough energy to jump from the valence band to the conduction band. This extra energy can be supplied by thermal excitation or by radiation absorption.

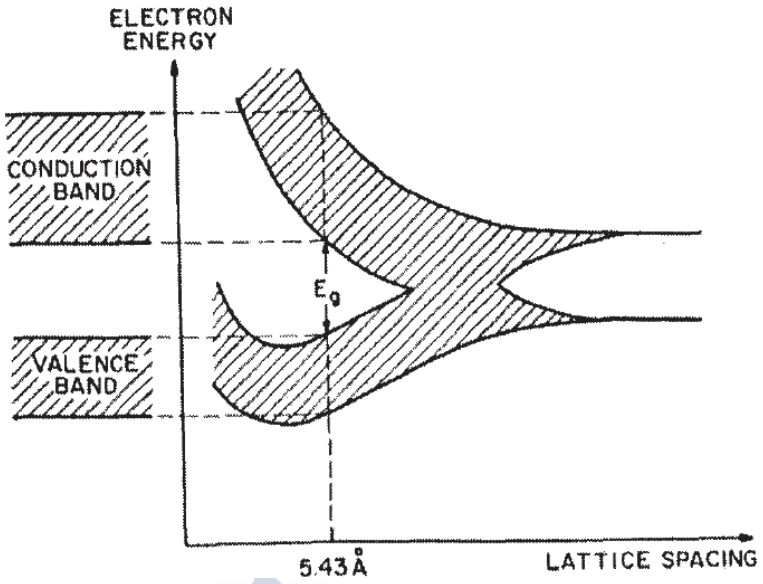

Figure 6.2: Distribution of the conduction and valence band in silicon with lattice spacing, remarking the equilibrium distance.

In silicon, the band gap energy is $E_g = 1.12$ eV at 300 K, and varies with temperature like:

$$E_g(T) = 1.17 - \frac{(4.73 \times 10^{-4}) \cdot T^2}{T + 636} \tag{6.1}$$

with E_g in eV. Note that when the temperature rises is easier for an electron to reach the conduction band because of the thermal excitation, and consequently the E_g decreases.

6.1.3 Direct and indirect band gaps

A remarkable point is that the energy bands are dependants of the crystal direction. Therefore, it could happen that the maximum of the valence band and the minimum of the conduction band are not at the same value of the electronic momentum. To get a complete model we need to consider the relationship of both, the energy and the momentum as a function of the lattice direction. Thus we can distinguish between *direct* and *indirect* semiconductors. Direct semiconductors (Figure 6.3a) are those where the maximum of the valence band and the minimum of the conduction band are coincident in momentum. In indirect semiconductors (Figure 6.3b) the maximum and minimum are not coincident, therefore to excite an electron from the valence band to the conduction band a transference of energy *and* momentum is required. That is the reason why the silicon (which is an indirect semiconductor) needs 3.6 eV to create a pair electron-hole whereas the E_g is 1.12 eV.

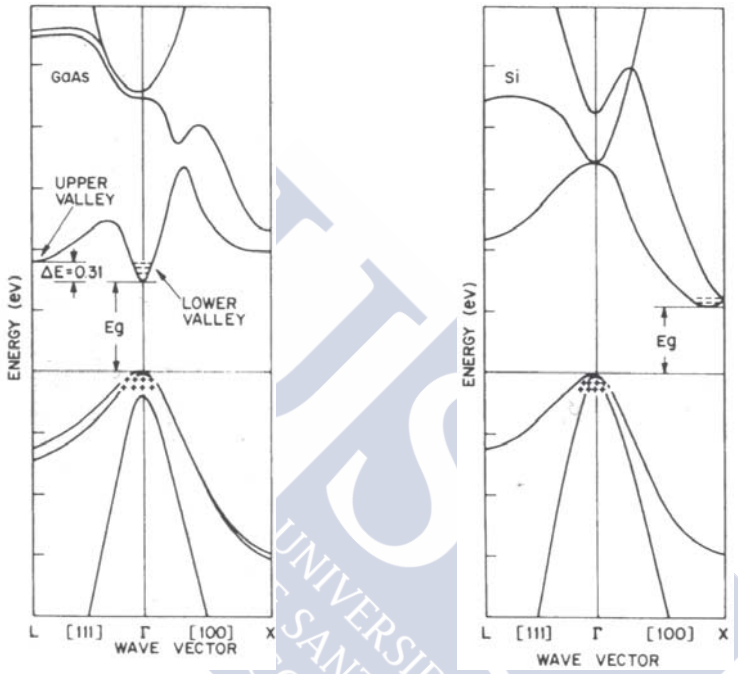

(a) Direct semiconductor (b) Indirect semiconductor

Figure 6.3: The band structure *vs.* the wavevector (momentum) depends on orientation. In Si (indirect) the minimum bandgap is associated with non-zero momentum, while in GaAs (direct) the transition occurs with zero momentum. (From [71])

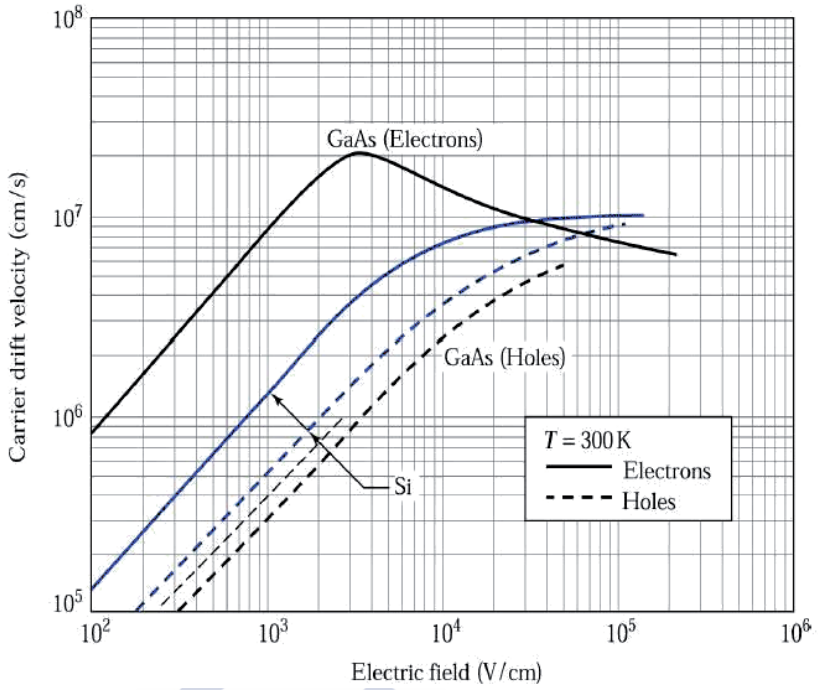

Figure 6.4: Drift velocity versus electric field in GaAs and Si

6.1.4 Doping and carriers

In semiconducting devices most of the devices are doped, that means that atoms of other elements (impurities) are added into the crystal lattice. Depending on the type of added material, one obtain n-type semiconductors (with an excess of electrons in the conduction band) or n-type (with an excess of holes in the valence band). The extra atoms must be placed instead of silicon atoms into the lattice, in order to preserve the behaviour of the device. Only atoms with the same size that silicon atoms can be introduced into the lattice without significant changes in the unit cell, for this reason only a small number of elements are used as dopers.

In the energy band model, the introduction of doper can be described as the creation of localized energy levels in the band gap. If donor (n-type) level is close to the conduction band the new atoms will be ionized at room temperature, and the excess of electrons will be transferred to the conduction band. The same happens when the acceptor (p-type) level is close to the valence band, then the excess of holes will be transported to the valence band.

It may be said that the number of donor or acceptors does not necessarily equal the number of impurity atoms, since the impurities must be placed correctly in the crystal lattice to become electrically actives.

Drift

The electrons in the conduction band and the holes in the valence band can be considered as free particles with a kinetic energy equal to $\frac{3}{2}$kT, which is

$\sim 10^7$ cm/s. Imperfections in the lattice drives to scattering process, so the average displacement of a mobile charge will be zero. However, in the presence of an electric field the charge carriers will be accelerated in between random collisions, reaching a mean drift velocity which is dependant of the temperature, the imperfections of the lattice, and the electric field. At moderate electric fields the drift velocity υ is proportional to the electric field ε as follows:

$$\upsilon_n = -\mu_n \varepsilon \qquad \upsilon_p = \mu_p \varepsilon \tag{6.2}$$

where μ_{n} and μ_{p} are the mobility values for electrons and holes and are dependant of the temperature and doping concentration. Typical mobility values for silicon at 300 K under a are:

$$\mu_n = 1415 \pm 46 cm^2/(Vs) \qquad \mu_p = 480 \pm 17 cm^2/(Vs) \tag{6.3}$$

At very high electric fields, the drift velocity become independent of the field, reaching a saturation value as can be seen in Figure 6.4.

Diffusion

When the carriers are not equally distributed (f.i. due to different doping concentrations) and no external electric field is applied, we can guess that the carriers will diffuse from the regions with higher concentrations towards regions with lower concentrations. Although the average displacement of an individual carrier is zero, the probability of carriers crossing form the side showing higher concentration to the other is larger than the probability of carriers crossing in the opposite direction. The diffusion effect is proportional to the temperature, as the velocity of the carriers will be greater, and decreases with the lattice imperfections as the number of random collisions will be larger.

The diffusion and the mobility are related by the Einstein relation:

$$D_{n,p} = \frac{kT}{q} \mu_{n,p} \tag{6.4}$$

6.1.5 The p-n Diode Junction

The p-n diode is the basic building block of silicon sensors. A p-n junction means that we got a semiconductor with two separate regions, one n-doped and one p-doped. In the transition region carriers will diffuse into the differently doped side and they will recombine producing a region which is depleted from free charge carriers. In the depletion zone, donor and acceptor atoms are ionized generating a local electrical field, counteracting the diffusion process.

A p-n Diode with the Application of an External Voltage

When a reverse external voltage is applied it will remove further majority carriers from either side and will extend the depletion region. The width of

the depletion voltage can be calculated by solving the one-dimensional Poisson equation, obtaining:

$$W = \sqrt{\frac{2\varepsilon_0\varepsilon_{Si}}{e}\left(\frac{1}{N_A} + \frac{1}{N_D}(V + V_{bi})\right)} \tag{6.5}$$

where:

W is the total width of the depletion zone

V is the external voltage

V_{bi} is the so-called built-in voltage (~ 0.7 V in Si)

N_A **and** N_D are the concentration of acceptors and donors

ε is the dielectric constant ($\varepsilon_{\mathrm{Si}} = 11.9\varepsilon_0$)

When the doping concentration is highly uncompensated (f.i. $\mathrm{N_A} \gg \mathrm{N_D}$), and as $\mathrm{V_{bi}} \ll \mathrm{V}$ equation 6.5 can be approximated as:

$$W \approx \sqrt{\frac{2\varepsilon_0\varepsilon_{Si}}{eN_D}V} \tag{6.6}$$

The full depletion voltage $\mathrm{V_{depl}}$ is the voltage needed to extend the depletion zone over the complete thickness d of the device. It is one of the most important sensor parameters and defines the minimum operating voltage. If the applied reverse bias voltage is greater than the depletion voltage, the sensor is overdepleted and a constant field of $(\mathrm{V} - \mathrm{V_{depl}})$ is present all through the sensor. During operation the sensor is biased at the operation voltage, which is typically 30-40 Volts above the depletion voltage to ensure that the sensor is fully depleted.

Leakage current

In absence of radiation a steady leakage current is always present. The leakage current is mainly coming from thermal generated carriers in the generation-recombination centers, at the surface of the device and in the depleted volume. The volume generation current (J_{vol}) per unit area is proportional to the depleted region, and given by:

$$J_{vol} \approx -e\frac{n_i}{\tau_g}\sqrt{\frac{2\varepsilon_0\varepsilon_{Si}}{eN_D}V} \tag{6.7}$$

The temperature dependence of the volume generation current can be approximated by:

$$J_{vol} \propto T^2 e^{-\frac{E_g(T)}{2kT}} \tag{6.8}$$

The ratio of currents at two temperatures $\mathrm{T_1}$ and $\mathrm{T_2}$ is:

$$\frac{J_{vol2}}{J_{vol1}} = \left(\frac{T_2}{T_1}\right)^2 e^{-\frac{E}{2k}\left(\frac{T_1 - T_2}{T_1 T_2}\right)} \tag{6.9}$$

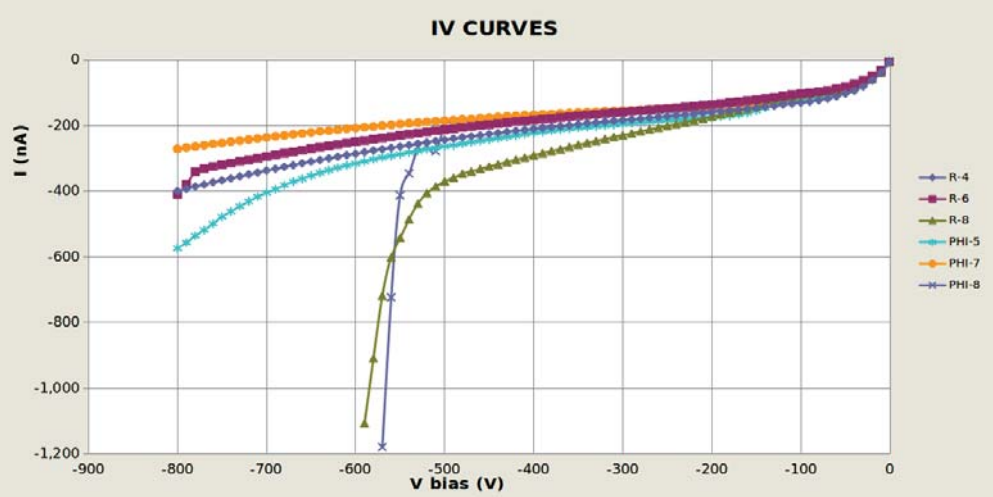

Figure 6.5: IV-Curves for 200 μm thick sensors. Note that two sensors shows a smaller breakdown voltage than the "good" ones.

A rule of thumb for rough estimations is to assume that the volume currents around 273 K doubles every 4 K, so if the leakage current measurements are accurate enough we can even use it as indication of the sensor temperature.

IV Curves

Measuring the leakage currents as function of the reverse bias voltage is a very powerful tool for sensor testing. In Figure 6.5 some IV-curves are shown for practically identical sensors, and it is clear from this plot that two sensors had a problem during production process. As it can be seen in the plots, for voltages below full depletion the current increases with the square root of V, according to Equation 6.7. After full depletion the IV-curve displays a plateau region in which the current increases very slowly before reach the electrical breakdown. If the voltage is increased beyond the breakdown point current increases dramatically and eventually the device can be destroyed. It is not generally possible give a strict rule to know where the breakdown occurs, so usually an individual IV-curve must be measured for each sensor.

CV Curves

As it was mentioned, the depletion voltage is a very important parameter of a silicon sensor. The usual procedure to determine the depletion voltage is with a CV-curve. IV-curve is not a good way to obtain the depletion voltage because the transition from the region where the current increases with the square root of the voltage, and the region where the current is almost constant is not accurate. The capacitance per unit area of a pn-diode is calculated as two conductive plates

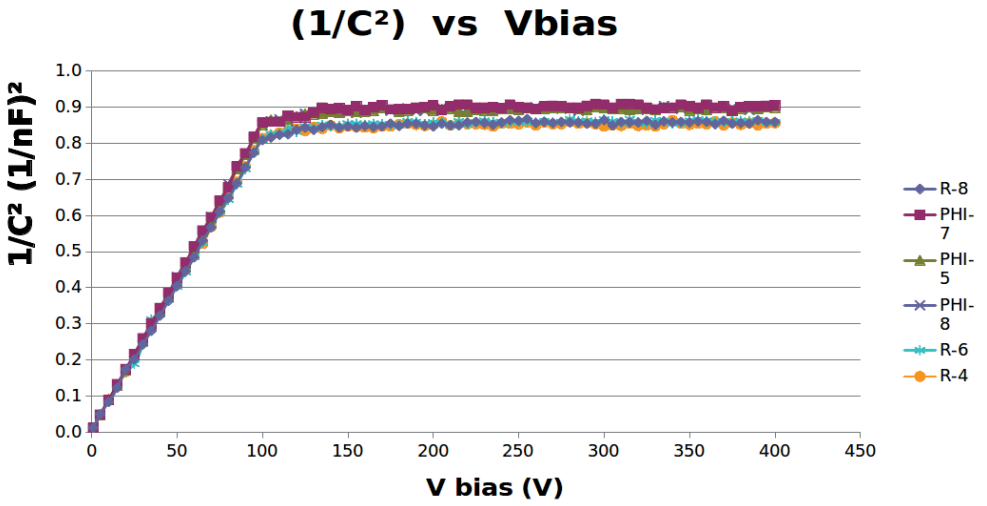

Figure 6.6: CV-Curves for 200 μm thick sensors.

separated by the depletion zone of width W(V):

$$C(V) \approx \sqrt{\frac{\varepsilon_0 \varepsilon_{Si} e N_D}{2V}} \quad for\ V < V_{depl} \tag{6.10}$$

$$C(V) \approx \frac{\varepsilon_0 \varepsilon_{Si}}{d} \quad for\ V > V_{depl} \tag{6.11}$$

where d is the sensor thickness.

The full depletion voltage can be determined by plotting $1/C^2$ versus V because then both branches can be fitted by a straight line (see Figure 6.6).

6.1.6 Charge Generation and Recombination

Silicon based devices are widely used in high energy physics because of the interaction of ionizing particles with the silicon of the sensor. When a ionizing particle reach the silicon, a part of the energy absorbed is used to generate electron-holes pairs that can be detected as electrical signals. The fundamental process behind the generation of pairs is different for charged particles and for photons.

Generation by Charged Particles

The basic theory describing the interaction between charged particles passing through material was developed by Bethe (1930), Bloch (1933) and Landau (1944). The Bethe-Block formula gives the rate of ionization loss of a charged particle in matter due to scattering process with the electrons of the material:

$$-\langle \frac{dE}{dx} \rangle = K z^2 \frac{Z}{A} \frac{1}{\beta^2} \left(\frac{1}{2} ln \left(\frac{2 m_e c^2 \beta^2 \gamma^2 T_{max}}{I^2} \right) - \beta^2 + \cdots \right)$$

where:

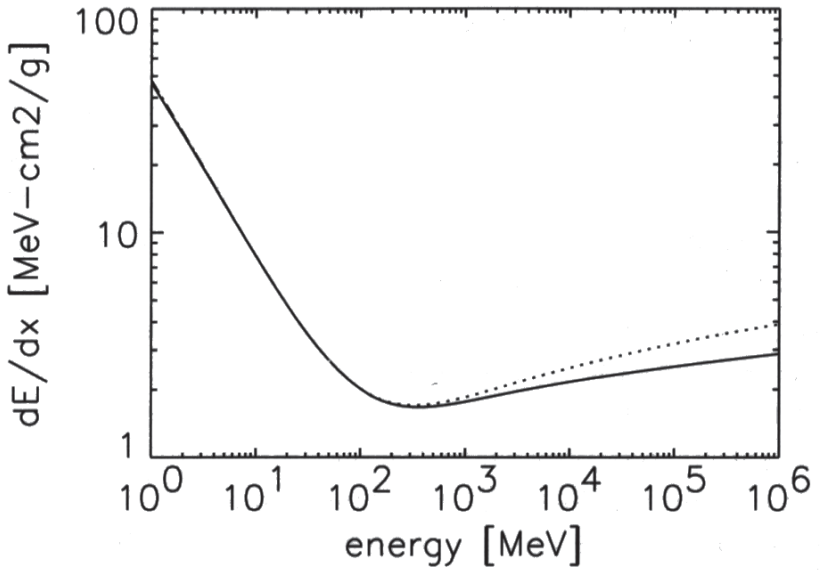

Figure 6.7: Rate of energy loss due to ionization as a function of the kinetic energy of a charged pion traversing silicon (dotted line corresponds to corrections). Image obtained from [69]

$\frac{dE}{dx}$ energy loss of the particle usually given in $\frac{eV}{g/cm^2}$

K $= 4\pi N_{Av} r_e^2 m_e c^2 = 0.307075$ MeV cm^2

z charge of the traversing particle in units of the electron charge

Z atomic number of the absorption medium (14 for silicon)

A atomic mass of the absorption medium (28 for silicon)

$m_e c^2$ rest energy of the electron (0.511 MeV)

β velocity of the traversing particle in units of the speed of light

γ Lorentz factor $(1/\sqrt{1-\beta^2})$

I mean excitation energy (137 eV for silicon)

Additional terms can be added like the density correction for high particle energies and the shell correction for lower energies. The energy loss rate as a function of particle energy is shown in Figure 6.7. The minimum of the energy lost curve is called *Minimum ionizing particle* (MIP).

Occasionally the ionising particle will interact with a more tightly bound electron than the silicon valence electrons and as a result create an electron with a significant amount of kinetic energy. This electron can cause secondary ionisation of the silicon. The energy deposited for this interaction is therefore higher than a MIP. As a result, the deposited energy spectrum in the silicon detector is not

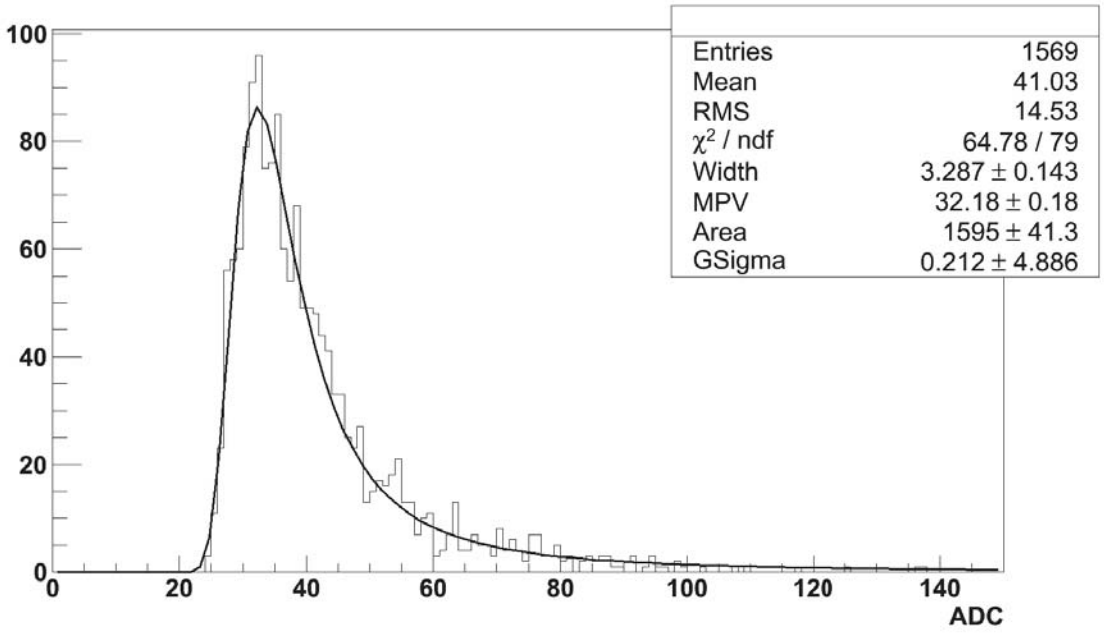

Figure 6.8: Energy spectrum in a 300 μm thick micro-strip detector.

a symmetric distribution, but a convolution of a Gaussian distribution with a Landau. Figure 6.8 shows a typical energy spectrum.

Due to the non-symmetric distribution, the mean value is higher than the most probable value. For a MIP the mean energy loss is 116 keV for a 300 μm of silicon, while the post probable energy loss is ~ 0.7 times this value or 81 keV. As in silicon takes 3.6 eV to create a pair electron-hole, the mean number of charge carriers created by a MIP is 108 per micrometer, and the most probably value is 72 per micrometer. This results in a mean signal of 32000 electrons or a most probably value of 22500 electrons for the same 300 μm thick sensor. It is the most probably energy that is used for calculations of collected charge from a silicon detector. Figure 6.9 shows the number of electron-hole pairs as a function of the energy of the incident particle, and two different particles are taken into account, protons and muons.

Generation by Electromagnetic Radiation

Silicon detects photons from the infrared up to the X-ray, however in high energy physics most of the photons are much more energetic and the probability of interaction with the detector is very low.

Electromagnetic radiation interacts with the silicon mainly via three processes:

Photoelectric effect: an electron absorbs the incident photon and gain energy enough to be released by the atom and jump to the conduction band

Pair production: when the photon is highly energetic, it can be absorbed by the atom nucleus and an electron and a positron are produced

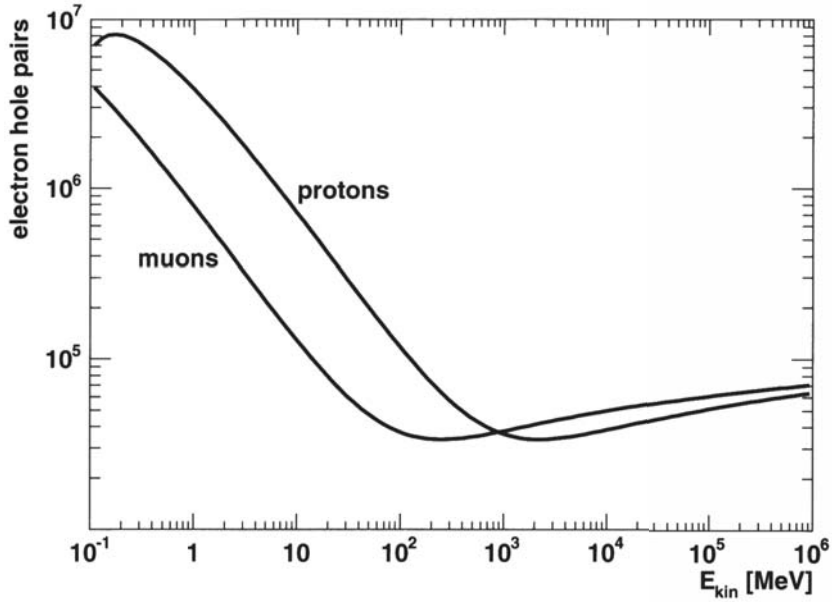

Figure 6.9: Number of electron-hole pairs generated in 300 μm thick silicon layer. Image obtained from [70]

Compton effect: the incident photon interacts with an electron via an inelastic scattering. Part of the momentum of the photon is transferred to the electron, thus the wavelength of the photon will change proportionally to the scattering angle

In Figure 6.10 the probability of interaction of an incident photon with a 300 μm thick silicon sensor is plotted as a function of the photon energy. To manifest the relationship of the interaction probability with Z, the absorption for cadmium telluride is also plotted.

The photoelectric effect is the dominant at low energies, and it is very strongly dependent on the nuclear charge Z of the absorbing material:

$$\sigma_{photon} \propto Z^n \tag{6.12}$$

with n varying between 4 and 5 depending on the photon energy. That's why materials like CdTe are preferred for X-ray detection.

Recombination

In thermal equilibrium the concentration of carriers is constant due to the compensation between generation and recombination process. In the case of a low level injection the concentration of majority carriers is practically unchanged, so the recombination process is limited by the minority carriers. The recombination rate is proportional to the concentration of the minority excess carriers.

The recombination process is quite different in direct and indirect semiconductors. As silicon is an indirect semiconductor the direct band-to-band recombination is forbidden because holes in the valence band and electrons in the conduction

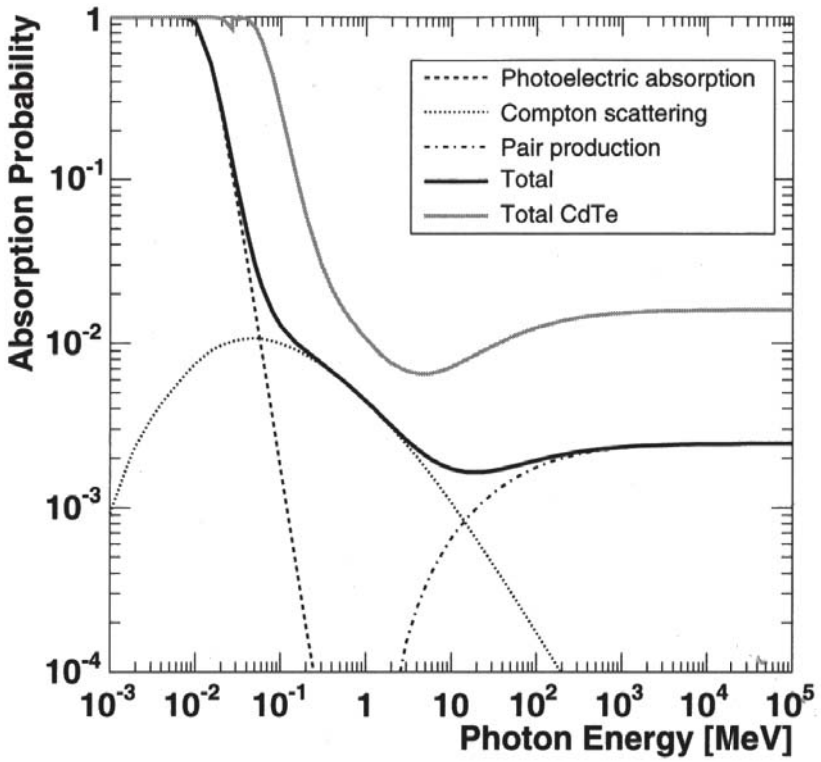

Figure 6.10: Probability of photon absorption for 300 μm silicon as function of the photon energy. Contributions from different processes are indicated. Same curve for 300 μm CdTe is give for comparison. Image obtained from [70]

band carry different crystal momentum. Actually, recombination process involves crystal imperfections or unwanted impurities as intermediate steps, becoming recombination centers. The carriers lifetime is thus inversely proportional to the number these recombination centers and the temperature.

6.2 Radiation Damage

Radiation induced effects are usually divided into bulk and surface defects. The former are caused by atoms displaced from their positions into the crystal lattice while the latter include all effects in the covering dielectrics and the interface region. Since the sensors in High Energy Physics experiments are reverse biased and have a large depletion region they are especially sensitive to bulk damage.

6.2.1 Bulk damage

When a highly energetic particle crosses the sensor, by a inelastic scattering process it could move an atom from its position in the crystal lattice. As a consequence, a crystal imperfection will appear and it can take the role of a generation-recombination center. An important point to keep in mind is

that different particles interact different ways with the crystal lattice. Charged particles scatters via electromagnetic interaction and are partially screened by the electrons in the atom's cloud, generating more point defects. However, neutrons only feel the nuclear producing more cluster defects. To compare the damage caused by different type of particles with different energies, radiation damage is scaled with the *non-ionizing energy loss* (NIEL). Neutrons of 1 MeV are used as reference. The experimental determination of the hardness factors is done via the normalization of the leakage current. In this document all fluences will be given in units of 1 MeV neutron equivalent fluence, 1 $\mathrm{MeVn_{eq}/cm^2}$.

Displacement damage manifest in three different ways:

- Formation of energy levels in the band gap, facilitating the transition of electrons from the valence to conduction band. In the depletion region this leads to an increase in the leakage current and the consequent increase of the shot noise. The increase of the leakage current can be sorted out as the leakage current also has a strong dependency with the temperature, as it was introduced in eq. 6.7. Therefore, by reducing the operational temperature we can extend the life of the sensor despite the radiation damage.

- States close to the band edges facilitate trapping, where charge is captured and released after some time. When electron-hole pairs are produced in the depletion region, trapping centers will reduce the signal amplitude.

- A change in the effective doping. The predominant charge states formed in Si are acceptors-like, and in severe irradiated devices the voltage required for a full charge collection will change. If the bulk is n-type the EDV will decrease following the fluence dose until the number of acceptor centers exceed the number of donors reaching the type inversion point, after which the EDV increases with the fluence. Nevertheless the behaviour of the bulk after type inversion is not the same as conventional p-type bulks, as annealing and temperature dependent effects are different.

6.2.2 Surface defects

Electron-hole pairs are also produced in the oxide region between the metallization layer and the implants. Holes mobility is rather low in the oxide, which increases the probability of being trapped. They can be trapped also by interface traps in the oxide-silicon interface. In sensors with n-type implants, the positive charge build-up at the silicon interface requires that the gate voltage be adjusted to more negative values to maintain the electric field in the depleted region. To keep in mind that holes are not permanently trapped, so benefits from annealing process is also expected here.

6.2.3 Annealing

Defects caused by irradiation are able to move through the crystal. This movement can lead to an annealing if defects meet during their migration through the crystal, and the leakage current will decrease as a consequence. However, when irradiation defects meet already present point defects, they became static and can create new energy level in the band gap region. Thus, as the mobility is strongly temperature-dependent then radiation-induced changes of sensor properties show a complex annealing behaviour.

6.3 Silicon Detectors in High Energy Physics

Currently silicon is used in high energy physic detectors for the detection of ionizing particles and for visible photons. Only when large volumes or areas need to be equipped, gaseous detectors are preferred because they are cheaper.

Main vantages of silicon detectors over gaseous are:

- Lower energy loss: 3.6 eV in silicon versus 15 eV in argon and even higher for other gases.
- Higher ionization: 8×10^5 electron-hole pairs per cm in silicon, versus 100 electrons in argon.
- Amplification electronic can be embedded in the silicon sensor without the need of huge electric fields.
- Better resolution thanks to photolithography technology.
- Faster readout.

6.3.1 Sensor doping

As was already mentioned, sensor's bulk can be either n-type or p-type, and the electrode can be doped also with acceptor or donors, given four possible sensor types:

p^+-on-n: is a single-sided process, widely employed in industry. Can be operated partially depleted as the depletion zone grown starting in the electrode. After an irradiation dose of 10^{12} n_{eq}/cm^2 the bulk will convert to p-type, and the depletion zone grows from both sides but leaving the edge region of the sensor not depleted any more.

p^+-on-p: double-sided process, expensive and without advantages over p^+-on-n. Same problems with irradiation than p^+-on-n.

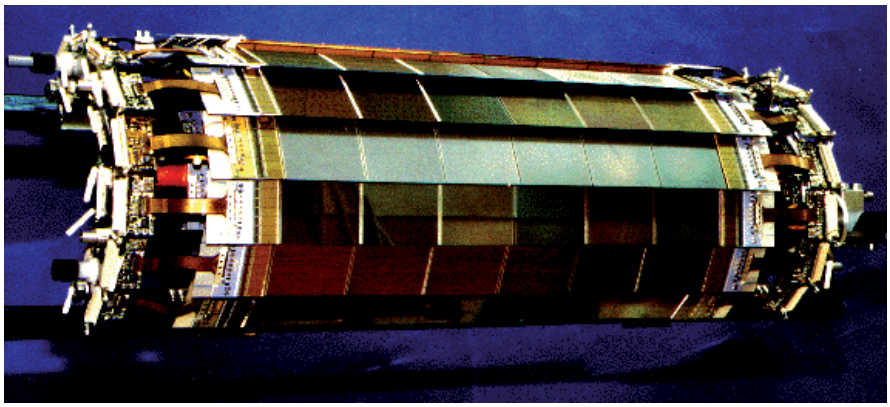

Figure 6.11: Vexter detector (VDET) of the ALEPH experiment. Installed in 1991, was made of two concentric silicon layers at radii 6.3 cm and 10.8 cm around the beam pipe. Strip's pitch was 25 μm, although the effective pitch was 50 μm. The CAMEX64 amplifier chips were bonded directly to the strips and mounted at the end of the layer. The VDET was the first silicon detector with VLSI electronics installed at CERN.

n^+-on-n: double-sided process, twice expensive than p^+-on-n. After type inversion depletion zone is growing from the segmented n^+-side allowing to operate the sensor under-depleted. Currently is being used in radiation hard devices. Another advantage is that allows to keep all sensor edges at ground potential, avoiding sparks between neighbouring sensors.

n^+-on-p: single-sided process. Collects electrons, which has higher mobility and less prone to trapping. The disadvantages are more sensitivity to external magnetic fields (Lorentz angle) and the need of an insulating structure around the n-implants. Not industrially developed yet. Could be cheaper than n^+-on-n in future.

6.3.2 Charge collection

According to the Ramo's theorem [73] moving charges induce currents in the readout electrode. Thus, the signal is due to the change of electrostatic flux lines which end on the electrode, not the amount of charge received by the electrode per second. If the integration times of the readout electronics is faster than the collection time, if the sensor is partially depleted or if trapping process has become relevant then the signal readout will be only a fraction of the deposited energy.

6.3.3 Vertexing and Tracking

Silicon detectors began its role in high energy physics in the eighties because of their good resolution ($\sim$ 10 μm) and the ability to cope with large data rates. The NA11/NA32 experiments at CERN were the first to use silicon strips detectors. At that time, the main handicap of the silicon detectors was the lack of

integration with the front end electronics. The introduction of VLSI (Very Large Scale Integration) made it possible to construct compact detectors which could be installing in colliding beam experiments, like the MICROPLEX chip developed for MARKII experiment at SLAC or CAMEX for the ALEPH experiment at CERN (see Figure 6.11). LEP experiments bet strongly for silicon technology, ALEPH and DELPHI installed vertex silicon detectors from the very beginning, while OPAL and L3 added such technology in later upgrade programs.

The first silicon detectors were single side micro-strips detectors, providing measurements in one direction per layer. By rotating the strip direction in different sensor planes, a two dimensional track reconstruction can be achieved. The disadvantage of such arrangement is the ambiguity if more than one particle crosses the sensor at the same time.

Pixelized detectors do not suffer from this problem, so they can be used in high density environments. The first pixel detectors were again installed in NA32 and SLD detector at SLAC. Both detectors were based in CCDs (Charge Coupled Devices) technology, but the interest has shifted towards hybrid pixel detectors like the installed in ATLAS and CMS at the LHC. In future these hybrid devices may be replaced by monolithic detectors with integrated electronic[1].

Originally silicon detectors were exclusively used for vertexing, placed very close to the interaction point so with a few centimetres they could cover almost all the acceptance. This is different in the tracking detectors, where to reach a good momentum resolution several measurements along the track are needed. Tracking detectors, thus use to be large and for cost reasons silicon sensors are an excluded technology. In experiments with a high rate of tracks, like the LHC ones, gaseous detectors can not cope with the occupancy and radiation levels, so again silicon strip detectors were the solution, and taken advantage of the best resolution, a more compact (and therefore more cost saving) detector could be installed. For instance, CMS has installed a silicon tracking detector with a total surface of 200 m^2.

[1]In **hybrid** pixel devices the ASIC is made on a highly resistive silicon wafer, while the sensor is low resistivity silicon. Highly resistive wafers are used in commercial silicon chips, and achieves a higher integration level. In the **monolithic** devices, the sensor and the ASIC are integrated in the same (low resistivity) silicon substrate. The integration techniques suitable for monolithic devices allows only very simpler circuitry.

USC
UNIVERSIDADE
DE SANTIAGO
DE COMPOSTELA

7

Microstrip prototypes

The VELO Upgrade program was already introduced in Chapter 5. As part of the program, three micro-strip prototypes were tested with a beam of 120 GeV pions at the CERN SPS facility. The first sensor to be tested was the PR01 in 2010, which is a R-sensor with 40 and 60μm pitch. In 2011 it was tested the DØ, which has intermediate strips (that means that the readout pitch is the double than the strip pitch). Finally in 2012-2013 a new R-type sensor with variable pitch was designed in Santiago, manufactured by Hamamatsu and tested with a laser beam and a beta source in Santiago. A complete description of the sensors is given in this chapter, together with the measured efficiency and resolution.

7.1 The PR01 sensor

The 1998 PR-01 prototype detector was manufactured by Hamamatsu Photonics (HPK). It is a n-on-n sensor, 300 μm thick, with quasi-circular shape and an aperture of 72º. The 1006 strips ran over the R-coordinate, arranged in 4 different regions of constant pitch as can be seen in Figure 7.1.

The PR01 detector is divided into 4 regions, Regions 1 and 2 consist of 40 μm pitch half-length strips, Region 3 of 40 μm pitch full-length strips and Region 4 of 60 μm pitch full-width strips; the pitch between the last strip of region 3 and the first of region 4 is 50 μm.

The detector is divided into eight areas of consecutive routing line read-out, these are shown on Figure 7.2. The routing lines are implemented in a second metal layer in order to connect the inner strips to the outer readout pads.

The 1006 strips are uniquely identified by the strip and region number, the

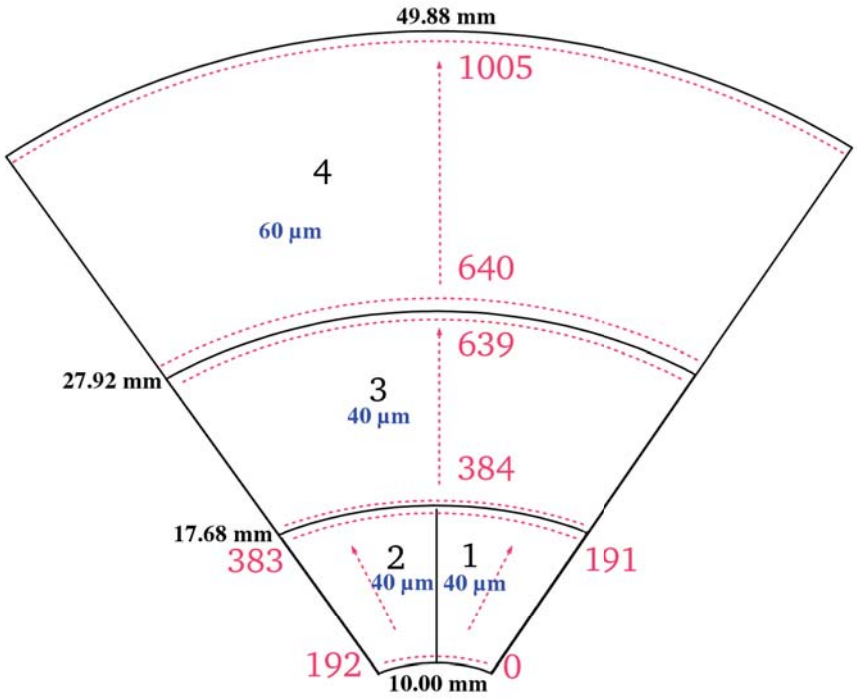

Figure 7.1: The division of the 1998 Hamamatsu PR-01 prototype R detector into regions with strips of constant pitch (in blue). The strip number is written in red, ranging from 0 to 191 in Region 1 (in total 192 strips), Region 2 has also 192 strips, from 192 up to 383, Region 3 has 256 strips, from 384 up to 639, and finally Region 4 has 366 strips, from 640 up to 1005. The radius of the first strip of each region is written in black. The sketch shows the front surface of the detector.

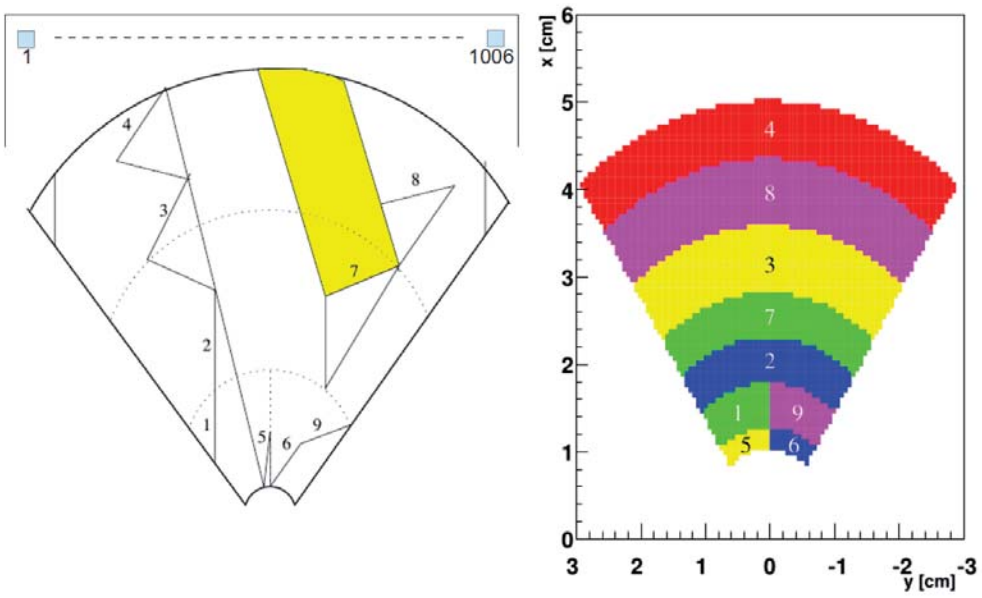

Figure 7.2: The routing line read-out scheme of the PR-01 sensor. The marked numbers indicate the division into routing line areas. The lines next to the numbers in leftmost plot represent the contact points between the strips and the routing lines. As an illustration, the shaded area shows the path of the routing lines that read the outer strips in the 40 micron pitch region. In the rightmost plot the strips that are read out by each routing line area are shaded in bands. Area 4 contains 110 strips, areas 5 and 6 each have 64 strips, all other areas have 128 strips. Routing line number 1 is linked to bonding pad at the top left and number 1006 is linked to bonding pad at the top right.

strip numbering starts from 0 within each region. The routing line numbers run from 1 to 1006, and are marked on the silicon. These routing line numbers run in ascending order from left to right of the detector with respect to Figure 7.2. Table 7.1 is provided as a reference guide to the strip layout of the detector.

7.1.1 Readout Electronics

The PR01 sensor was bonded to an IT hybrid with 3 Beetles [50] as can be appreciated in Figure 7.3. As each Beetle has 128 readout channels, only a small fraction of the sensor strips were instrumented. In Table 7.2 a relationship between the Beetle channels and the strip number is given. Note that consecutive routing lines are bonded to consecutive Beetle pads.

Unfortunately, not all of the 128×3 Beetle channels could be successfully bonded due to several reasons (dirty pads, bonding failures or for testing purposes), given a total of 338 instrumented strips. Table 7.3 prints a relation of all of them.

As we got so few instrumented strips, and they are spread in 4 regions, it is not feasible to provide an accurate value of the efficiency of this sensor.

Strip Number	Detector Region	Routing Line	Routing Area	R (cm)
0	1	559	6	1.002
63	1	622	6	1.254
64	1	879	9	1.258
191	1	1006	9	1.766
192	2	495	5	1.002
255	2	558	5	1.254
256	2	1	1	1.258
383	2	128	1	1.766
384	3	129	2	1.77
511	3	256	2	2.278
512	3	623	7	2.282
639	3	750	7	2.79
640	4	257	3	2.795
767	4	384	3	3.557
768	4	751	8	3.563
895	4	878	8	4.325
896	4	385	4	4.331
1005	4	494	4	4.985

Table 7.1: Relationship between strip number and routing lines in the PR01 sensor. Color code is the same than the used in Figure 7.2

Beetle Number	Beetle Channel	TELL1 Channel	Routing Line	Strip Number	Detector Region
1	0 to 105	1536 to 1641	773 to 878	790 to 895	4
1	106 to 127	1642 to 1663	879 to 900	64 to 85	1
2	0 to 53	1920 to 1973	441 to 494	952 to 1005	4
2	54 to 117	1974 to 2037	495 to 558	192 to 255	2
2	118 to 127	2038 to 2047	559 to 568	0 to 8	1
3	0 to 18	1792 to 1810	109 to 128	364 to 383	2
3	19 to 127	1811 to 1919	129 to 236	384 to 491	3

Table 7.2: Instrumented strips

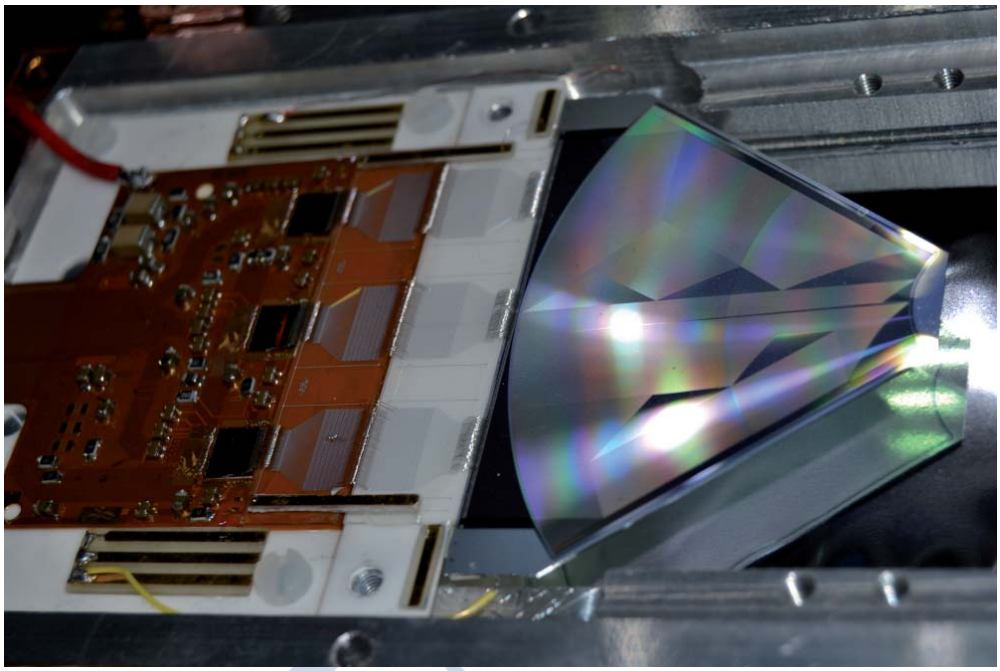

Figure 7.3: Assembly of the PR01 sensor. The hybrid with 3 Beetles can be appreciated in the picture.

Once the data is sent out from the hybrid it goes to a *repeater* board were the analog signal is amplified and sent to a TELL1 board through a 10 meters long cooper cable. The TELL1 board that we use is similar to the one described in 3.2.3 with the only difference that the input is directly the analog signal, and not an optical input. The TELL1 is designed to deal with a VELO module and can process up to 16 Beetles. The relationship between the TELL1 channels and the instrumented Beetle channels is described in Table 7.2.

7.1.2 Electrical characterization

The PR01 sensor was electrically characterized in the USC-GAES facilities. The IV curve (Figure 7.4) was taken into a clean room class 10.000 using a SUSS PM5 probe station.

The IV curve was carried out before the assembly of the sensor, with a picoammeter/voltage source Keithley 487. The environment variables were a temperature of 20 °C and a relative humidity of 40%. The measured values shows that the sensor breakpoint is above 350 V.

7.1.3 Testbeam setup

The PR01 was characterized with particles in the SPS 120 GeV/c pion beam at CERN, with the help of the Timepix telescope. The telescope was built with 6 Timepix devices in ToT mode plus another Timepix in ToA to associate a time-

Beetle Number	Routing Lines	Reason
1	798, 799, 802, 803	Dirty pads
1	779, 783, 796, 808, 809, 827, 830, 857, 854, 872, 896, 897, 898	Bonding failures
1	879, 880, 881, 882, 883, 884, 885, 886	Testing
2	443, 456, 461, 471, 495, 548, 550, ,552, 557	Bonding failures
2	487, 488, 489, 490, 491, 492, 493, 494	Testing
3	224, 189, 148, 123	Bonding failures

Table 7.3: Not bonded strips

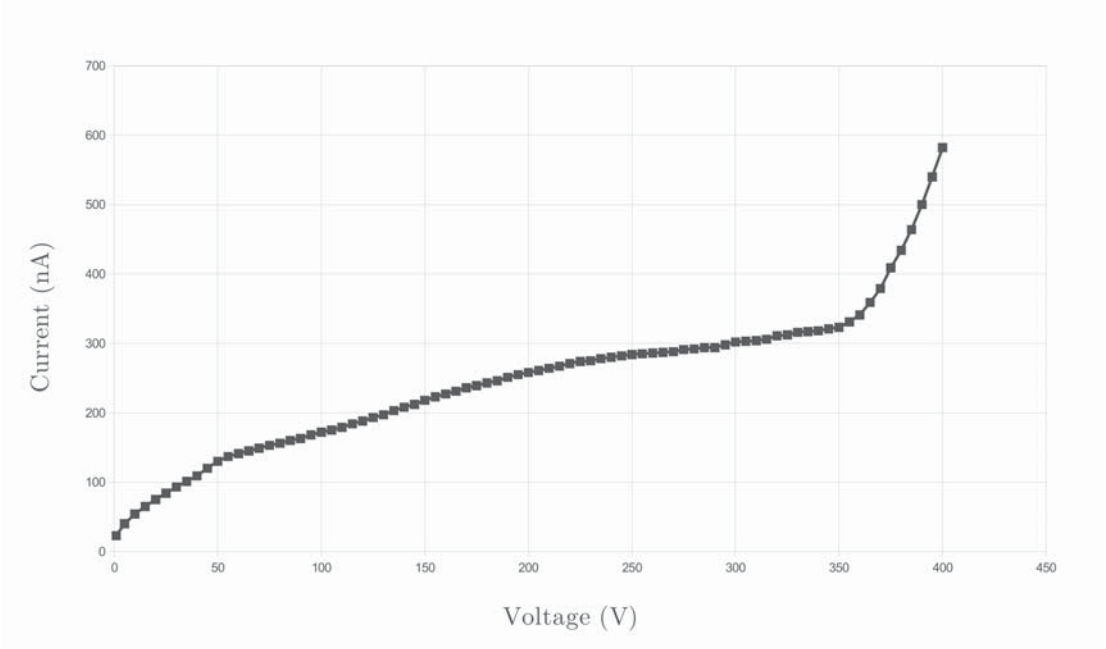

Figure 7.4: PR01 IV curve.

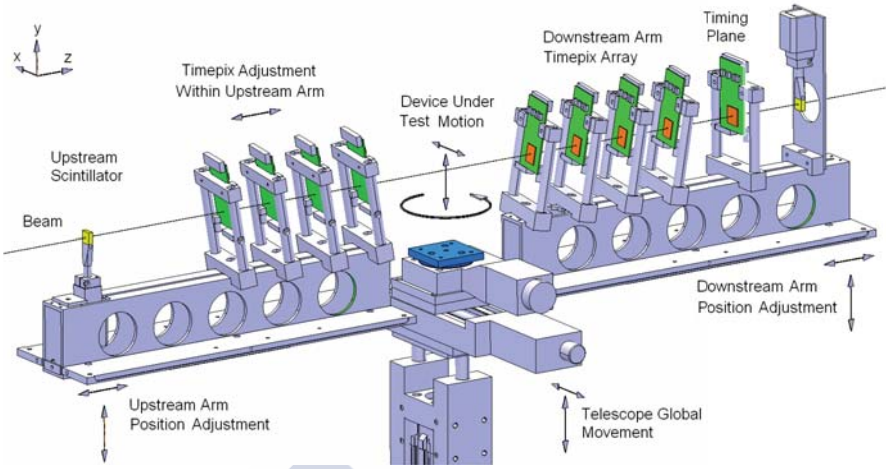

(a) Testbeam stand

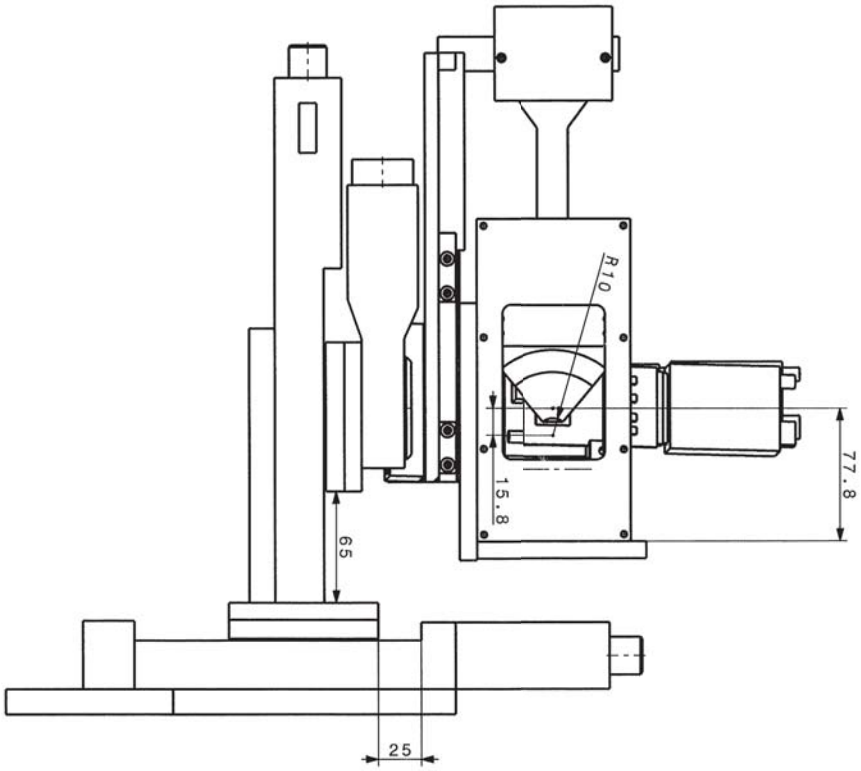

(b) PR01 DUT

Figure 7.5: PR01 module mounted in the DUT position

Device	Position	Telecope's arm	Mode
I08-W0092	z=0 mm	left	TOT
I04-W0092	z=150 mm	left	TOT
H07-W0082	z=300 mm	left	TOT
PR01	z=450 mm	DUT	
H03-W0092	z=600 mm	right	TOT
H05-W0082	z=750 mm	right	TOT
J09-W0092	z=900 mm	right	TOT
D04-W0015	z=1000 mm	right	TOA

Table 7.4: Telescope's planes

stamp to each track[1].

The Timepix devices and their positions are described in Table 7.4. As can be appreciated in Figure 7.6b all the planes are rotated in x and y coordinates, the reason is that the angle at which the best resolution is achieved (optimal angle) for these devices is 9 degrees.

An external trigger system has been set up, with two small scintillators at the front and back of the telescope. Within each beam fill (once every 50 seconds), about 40 Timepix frames were taken. The gate time of the frames was determined by the external trigger system. The shutter of each frame was closed either after 300 particles or after 300 μs. A delay of 150 ms was introduced after each frame before the next gate start time, to readout the chip and send the data to disk.

The readout of the Timepix chips was done with the USB2 interface. The output files of Pixelman are zero-compressed, which fastened the conversion into ROOT files for analysis. PR01 data is readout by the TELL1 board, and eventually, both the PR01 and the Timepix information were written into one ROOT file.

The run program of the first beam period in June 2010 was angle scans with the PR01 as device under test.

June 2010 test-beam campaign

From 4$^{\text{th}}$ to 6$^{\text{th}}$ of June, the PR01 was installed, calibrated and exposed to the SPS pion beam. Several runs were taken at different angles and different positions. A summary of the runs is given in Table A.1. From July 1$^{\text{st}}$ to 5$^{\text{th}}$ the sensor was installed again in the test-beam area, but due to huge common mode noise problems the data obtained was not valid for analysis. Detailed information of the runs taken can be obtained in Table A.3.

[1]The **T**ime **o**ver **T**hreshold (ToT) provides the charge deposited in a pixel, while the **T**ime **o**f **A**rrival (ToA) provides the time-stamp. A detailed description of the Timepix chip is given in Section 8.2.2.

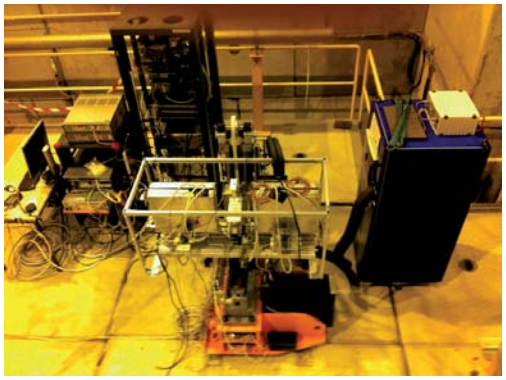

(a) Test-beam setup in June 2010. The blue box is a CO_2 cooling plant available for irradiated sensors. Note the rack with the power supplies and the trigger logic behind the telescope.

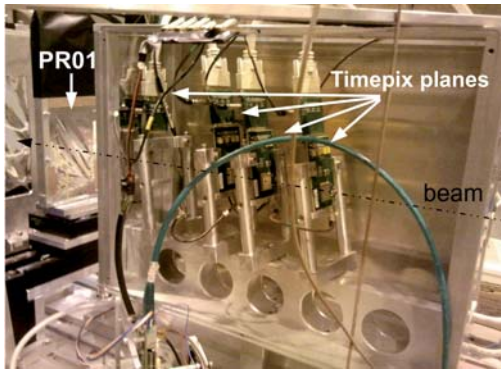

(b) Right arm of the telescope opened with four planes where the Timepix sensors were placed. In the leftmost side the PR01 assembly can be appreciated.

Figure 7.6: Test-beam setup in 2010

August 2011 test-beam campaign

After the analysis of the 2010 data, some problems came up to light like the apparently low signal collected by the sensor. One possible explanation is that the sensor were not fully depleted, so a new data taking run was scheduled on the 2011 test-beam campaign. Unfortunately, we could not find any correlations (nor spatial or temporal) between the telescope's data and the PR01's data. Furthermore, taking a look directly to the raw data is clear to see that the PR01 sensor does not see any beam and all the data can be explained as noise.

As a conclusion, it seems that the PR01 assembly suffer any kind of damage and in the current situation is not working any more.

7.1.4 Analysis software

The processing and posterior analysis of the data involves several steps:

1. **Pedestal subtraction:** this is the first analysis process carried out by Vetra software[2]. By default the value of each channel is not zero, but a number around the middle of the dynamic range of the Beetle. This value is calculated as the mean value of the channel without beam, and is subtracted in the analysis.

2. **Common Mode subtraction:** this is the second step in the Vetra software. The common mode is an effect of the external (low frequency) electrical noise. Typically it shifts all the channels up or down their pedestals

[2] *Vetra* is the software package used in the installed VELO. Instead of re-write the program needed to decode the TELL1 data, it was decided to use this package, although its functionalities and complexity are far beyond the required in a test-beam.

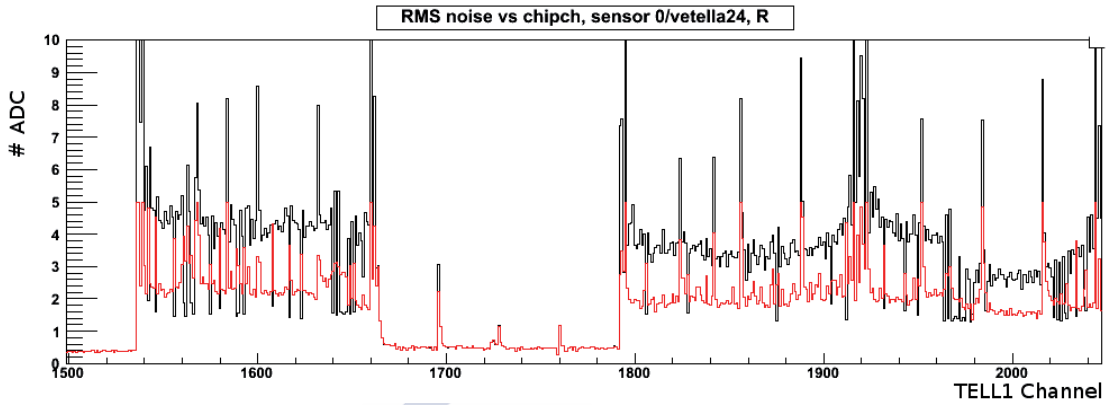

(a) Noise value for each TELL1 channel before (black) and after (red) common mode subtraction

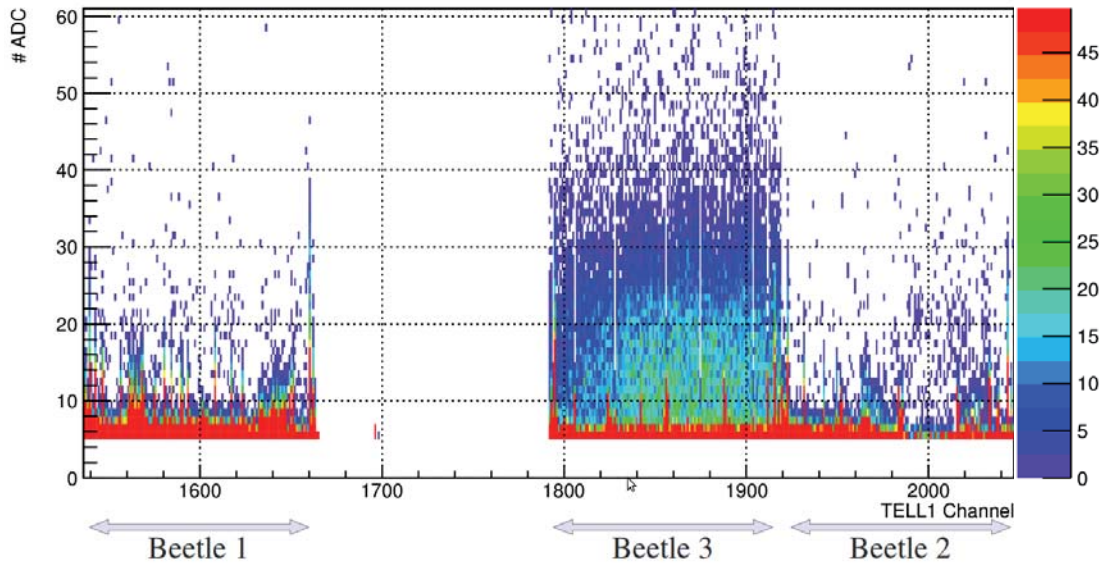

(b) ADC histogram for TELL1 channels after the pedestal and common mode subtraction

Figure 7.7: Output data from the Vetra analysis software. This data is used by the Amalgamation algorithm to be matched with telescope's data attending to time-stamping information

by a few ADC counts. This shift varies from event to event, and the way to calculate is by fitting the data after the pedestal subtraction to a straight line, and then subtract that fit to move all the channels to zero. The resulting data and noise values can be seen in Figure 7.7.

3. **Amalgamation:** here the PR01 data and the telescope data are joined together attending to the time-stamp information. This is the first analysis step carried out by the Timepix Test-beam software

4. **Mapping:** before the clustering, we must reorder all the channels in order to get the PR01 data sorted by strips and not by TELL1 channels. This is carried out following the scheme described in Table 7.2.

5. **Clustering:** described in subsection 7.8.

Clustering Algorithm

When a particle crosses through a sensor, the pairs generated will be collected by one or more strips. Thus, the energy deposited by the particle is proportional to the sum of the ADC values in all the strips which collected charge. The target of the clustering algorithm is to translate hits in strips into clusters.

Clustering parameters To perform the clustering a few parameters have to be defined:

Noise threshold: as can be seen in Figure 7.7a, some strips are more noisy than other. By choosing a noise threshold value we can reject these noisy strips to avoid fake hits.

Seeding strip: To identify a cluster a first strip individual threshold is applied. A strip must have an ADC value above the seed threshold to be considered a seed. Clusters are grown looking in the neighbourhood of the seed strips, thus at least one strip of each cluster accomplish the seed requirement. The seed threshold is an individual value for each strip as far as is weighted by the strip noise (which is obtained from Figure 7.7a). Typical value of seed threshold is 6 times the noise of the strip.

Low threshold: With a comparison to a low threshold one left and one right neighbour to a seeding strip(s) can also be included in a cluster. This allows to find a small signal in the neighbourhood of a large ADC value of a seeding strip. The low threshold is also an individual value, weighted by the noise of the strip. Typical low threshold value is 2 times the noise of the strip.

Sum threshold To accomplish with this requirement, the total charge of the cluster must be greater than a certain threshold. The total cluster charge is calculated by summing the ADC values of all strips in a cluster. This allows to reject single strip clusters with very few charge stored, which probably

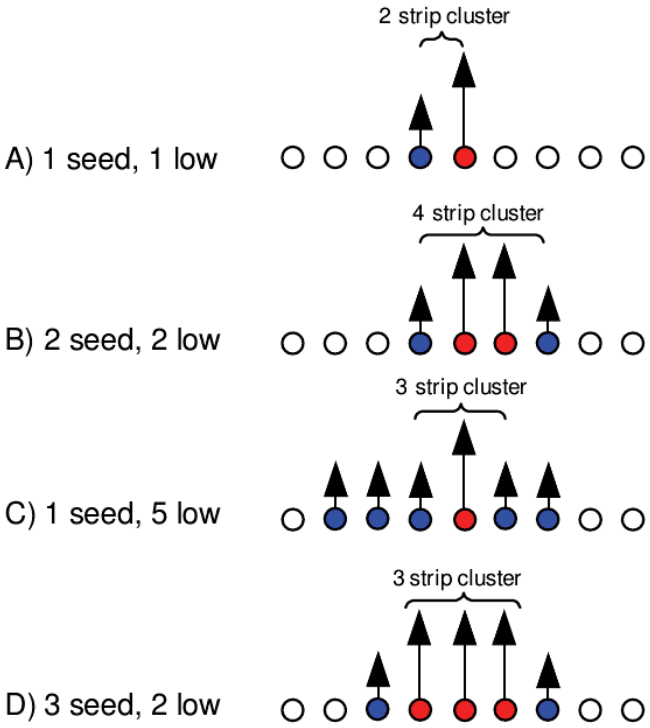

Figure 7.8: This figure shows all the possible cluster types built using a seeding (red) and a low threshold (blue): A) Cluster with one seeding and one strip over the low threshold resulting in a two strip cluster. B) Two seeding strips in one 4 strip cluster. C) One seeding strip and too many low threshold strips, only one left and one right neighbour is used for one 3 strip cluster. D) The 3 seeding hit cluster does not get any low strip hits in the cluster.

are fake or incomplete clusters. The sum cluster threshold is a fixed value, typically equal to 10.

The algorithm to grow the cluster around the seed is graphically described in Figure 7.8.

The centre of the cluster is determined by weighting the position of a hit by its ADC value:

$$x_{centre} = \frac{\sum_{i=1}^{N} ADC_i \cdot x_i}{\sum_{i=1}^{N} ADC_i} \tag{7.1}$$

where N is the cluster size, and i are the strips in the cluster. This centre of gravity method assumes that the position depends linearly on the charge ratio in the strip and it results in analog position reconstruction.

Implications of the asynchronous trigger

The Beetle chip was designed with a synchronous trigger because in the LHC environment collisions occur each 25 ns, or at least in agreement with a 40 MHz

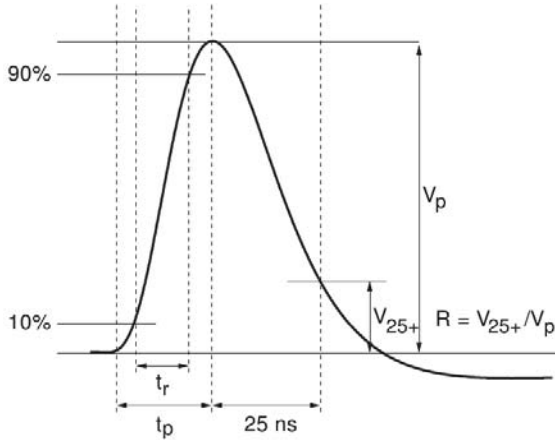

Figure 7.9: Beetle output signal is characterized by three parameters: peaking time (t_p), peaking voltage (V_p) and remainder (R), which is the ratio between the signal voltage 25 ns after the peak (V_{25+}) and V_p.

clock. The response curve of the Beetle chip to a signal follows a curve like the shown in Figure 7.9. In a LHC experiment, the Beetle chip will sample the signal always at the peaking voltage because all the delays involved in the trigger electronics and signal propagation are fixed for all the collisions and can be fine tuned.

However, in a test-beam environment this is not the case as the particles will arrive randomly. We can tune the delay settings in the TELL1 board to be sure that the peaking time falls into our sampling window, and then select a-posteriori all the particles which, by change, arrived at the peaking time. Only the charge of the clusters associated to particles which arrived at the proper time will be proportional to the whole deposited charge, while the rest will reflect a fraction of the charge. We can select the *good* particles because we have a TDC system which provides nanosecond resolution, and that information is attached to the strip hits data together with a 40 MHz clock time-stamp. Then, subtracting the asynchronous time-stamp from the synchronous time-stamp we know when the particle arrived into the sampling window. This is exactly what we see in Figure 7.10. From now on, all the data shown will be after selecting the clusters from a window of 5 ns around the peak of the mean charge distribution.

Rejected clusters

Once the clustering process is finished, two algorithms were developed to remove suspicious clusters and keep only crystal clear ones.

Attending to the division of the PR01 in 4 different regions, it could happen than consecutive strips should not belong to the same clusters because they are in different regions (for instance strip 383 is in Region 2 so its length is one half of strip 384 which is in Region 3). Those clusters with strips in the boundaries of a division region were rejected.

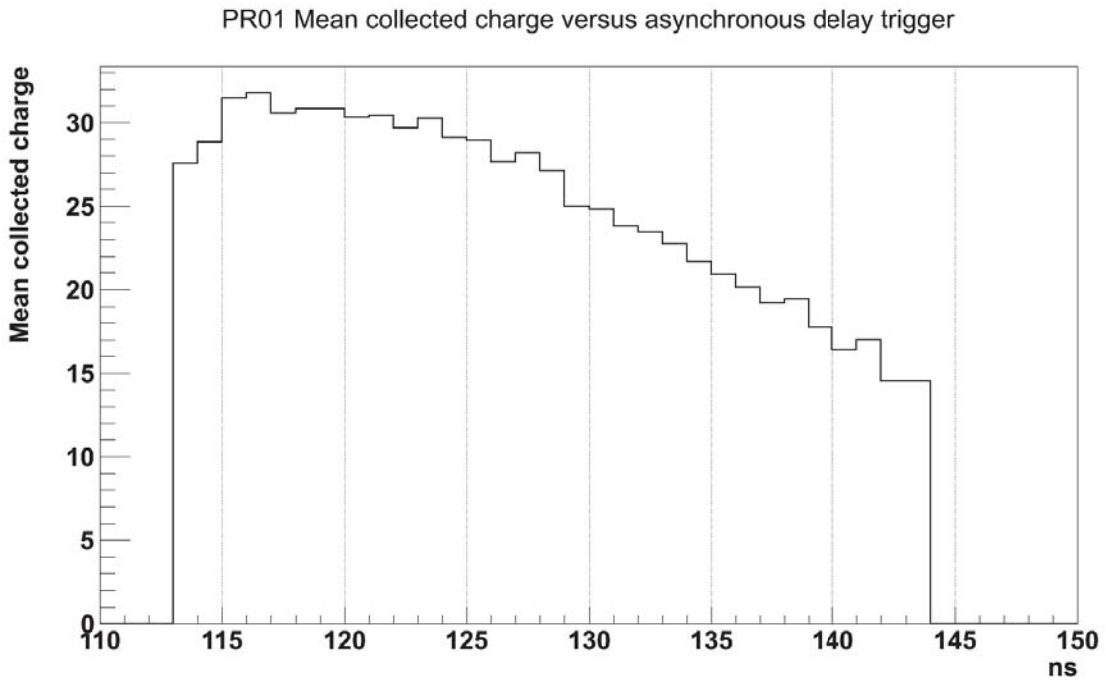

Figure 7.10: Mean charge collected in the PR01 sensor as function of the delay between the asynchronous and the synchronous (40 MHz) trigger.

The second consideration is related to noisy strips. It could happen that some pairs generated by the crossing particle will be collected by a noisy strip. That strip will never be a member of a cluster, but the total charge of the cluster in that specific case will be less than it should. As a safety rule we decided to reject all the clusters neighbouring to a rejected strip.

Tracks reconstruction

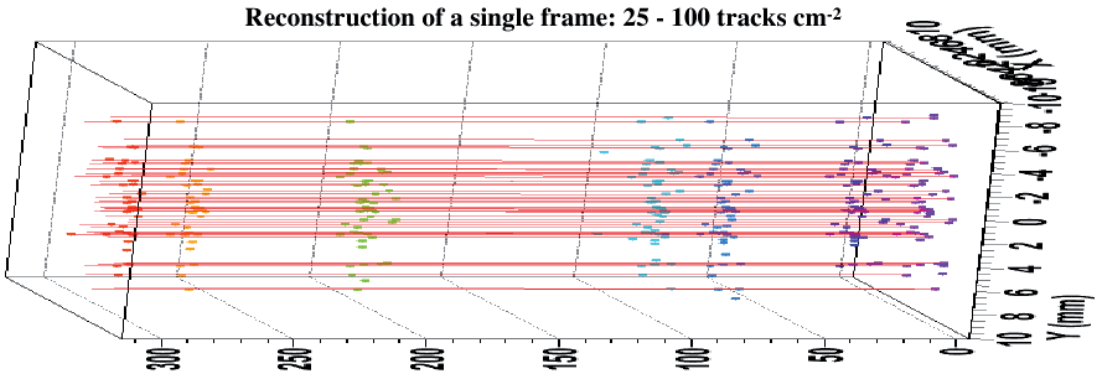

Figure 7.11: Track reconstruction (red) from the clusters of 6 telescope's planes. Plot from [74].

Tracks are reconstructed using a straightforward extrapolation along z (beam)

axis. Only straight tracks which were correctly measured in all the telescope planes were considered. Multiple scattering in the telescope can be ignored because of the high momentum of the pions in the beam (120 GeV). The clusters per plane are used as input to the track fit. In each iteration, the proto-track is extrapolated to the next telescope plane, then it looks for clusters in the vicinity and finally the closest valid cluster is added to the fitting algorithm to update the proto-track. From montecarlo simulations including scattering and single plane resolution, the pointing resolution of the telescope at the DUT plane is $< 2\mu$m.

The final situation is similar to the one showed in Figure 7.11, although that plot corresponds to a configuration of the telescope with only 6 planes.

Alignment

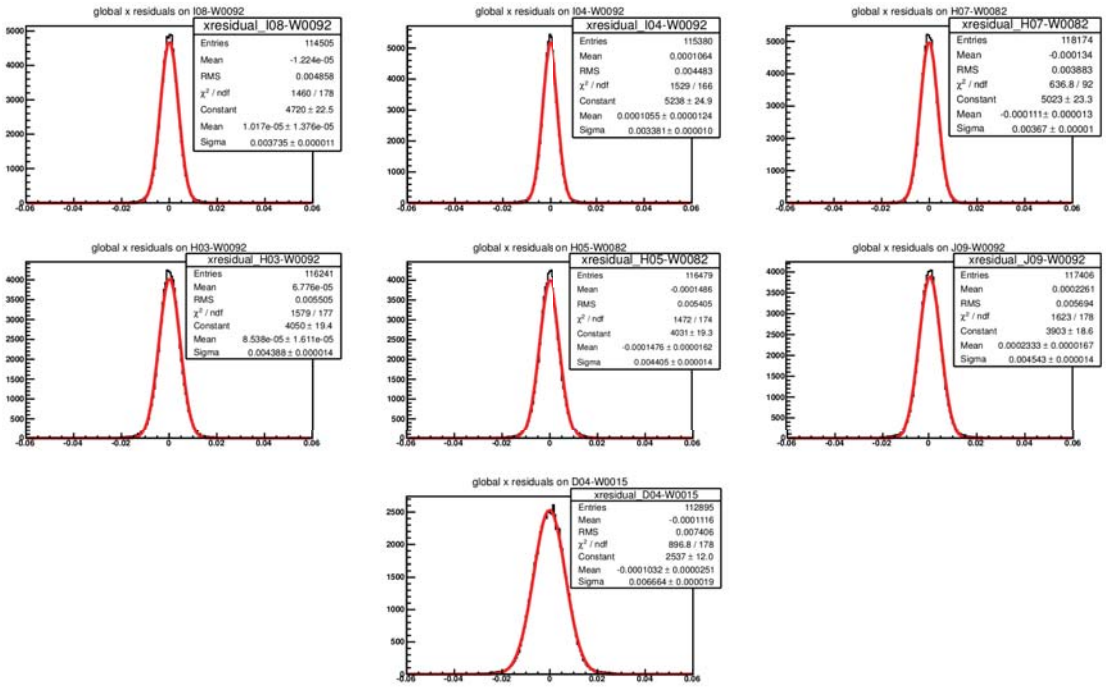

Figure 7.12: Resolution of the telescope's planes. The planes are shown sorted by their z positioning as can be seen in Table 7.4. Note how the resolution for each plane increases with z, due to scattering process.

Since the positioning of the seven detector planes is a crucial parameter for precise measurements, the alignment of the planes is essential for the fine reconstruction of the tracks. The DUT needs to be aligned after every run (after DUT rotation, or any other possible movement of the detector planes), so is useful to have a software-based alignment which could be reprocessed every data run.

The alignment of the telescope is based on minimising the chi-squared function of straight tracks through the different telescope planes.

Figure 7.12 shows the resolution of all the telescope planes after the alignment process.

7.1.5 Energy loss distribution

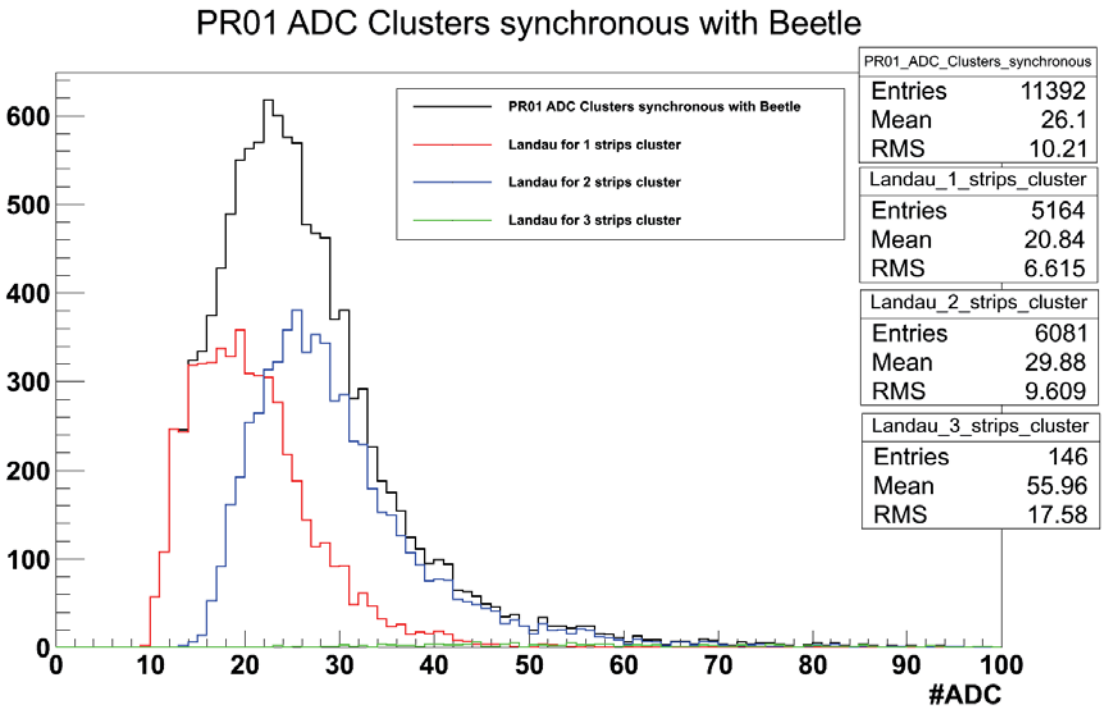

Figure 7.13: Charge collected in the PR01 sensor.

The expected energy loss distribution has a Landau shape as described in Section 6.1.6, and follows the distribution of a Gaussian convoluted with a Landau. Figure 7.13 shows the ADC distribution of the charge collected by the PR01, which indeed follows the Gaussian $\otimes$ Landau distribution.

The most probable value (MPV) is 26 ADC counts, which should correspond to a MIP particle. This MPV is lower than expected, and that is the reason why the PR01 was installed again in the test-beam facility in 2011 although unsuccessfully.

7.1.6 Spatial resolution

The spatial resolution is calculated by measuring the distance between the projection of the telescope track in the DUT plane with the center of gravity of the associated cluster. The whole group of distances, also know as residuals, follows a Gaussian distribution and the width of the fit provides the unbiased resolution of the DUT. As the PR01 has different regions with different pitch, the analysis must be separated for each pitch.

The binary resolution for the PR01 is:

40μm pitch regions:

$$\sigma_{binary} = \frac{40\mu m}{\sqrt{12}} = 11.5\mu m \tag{7.2}$$

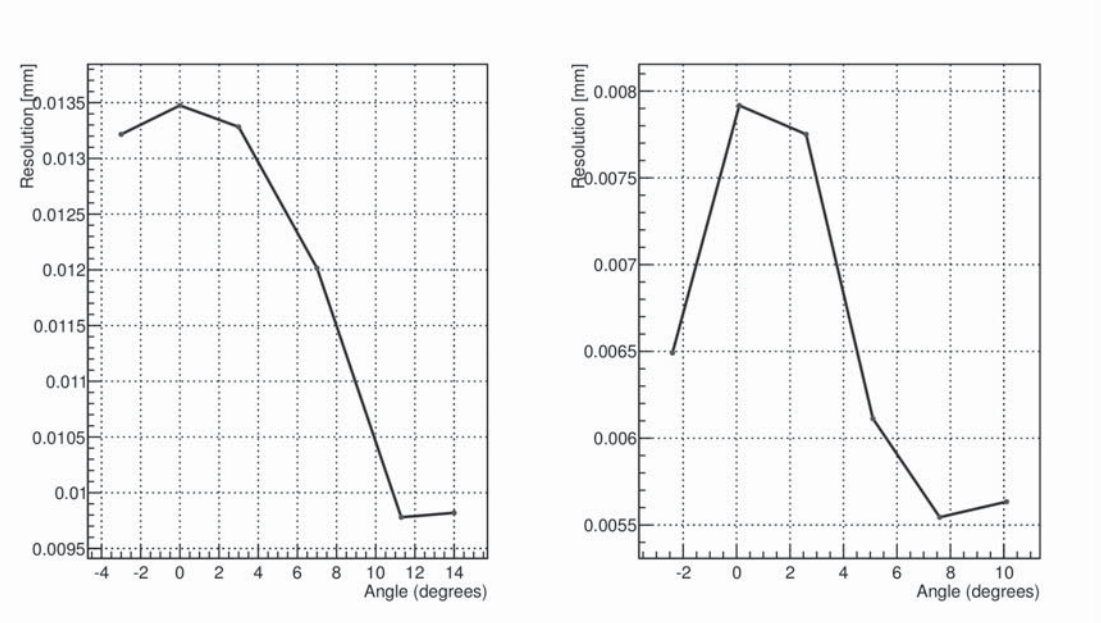

Figure 7.14: PR01's resolution as function of the angle between the sensor and the incident particle.

60μm pitch region:

$$\sigma_{binary} = \frac{60\mu m}{\sqrt{12}} = 17.3\mu m \tag{7.3}$$

Spatial resolution versus angle

In Figure 7.14 the relationship between the resolution of the PR01 sensor and the angle with respect to the incident particle is shown. It is clear to see that in both cases the pattern is the same, giving the worst resolution around 0 degrees and then improving as far as the angle increases up to reach a minimum. This minimum corresponds to the optimal angle, which can be calculated as the angle at which the x-component of the particle trajectory through the silicon is equal to the readout pitch. Using Figure 7.15 as reference, the optimal angle will be that at which $d = pitch$. Numerically:

$$tan(\alpha) = \frac{d}{thickness} \tag{7.4}$$

$$\alpha_{optimal} = tan^{-1}\left(\frac{pitch}{thickness}\right) \tag{7.5}$$

Thus, the optimal angle depends of the pitch, and for the PR01 sensor in the 40 μm region is:

$$\alpha_{40} = tan^{-1}\left(\frac{40}{300}\right) = 7.6^o \tag{7.6}$$

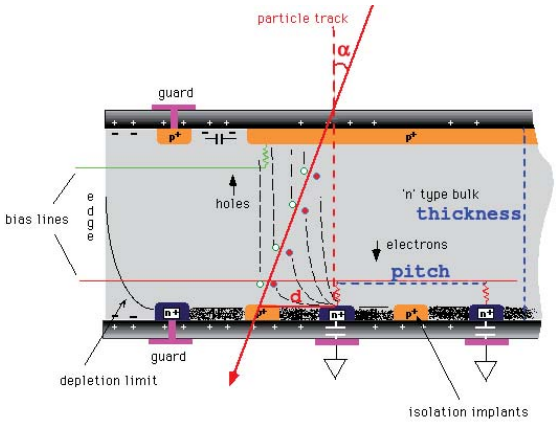

Figure 7.15: The electron-hole pairs are collected by the strips of the detector and the charge spreads along with the incident angle (α).

and in the 60 μm region is:

$$\alpha_{60} = tan^{-1}\left(\frac{60}{300}\right) = 11.3^{o} \tag{7.7}$$

which is in good agreement with what we see in Figure 7.14. Finally, it must be said that the reason of the asymmetric around 0^{o} is that the angle calibration was done roughly (by eye) and it corresponds to the angle motion system value, but this motion motor could be a bit rotated with respect to the beam line. Furthermore the sensor itself it could be a bit rotated inside the assembly.

As we could expect, the cluster size will always increase with the angle, as can be seen in Figure 7.16.

7.2 The D0 sensor

The DØ [75] was a sensor ordered for the DØ upgrade experiment at the Fermilab Tevatron collider. The DØ experiment was proposed in 1983 to study proton-antiproton collisions at a center-of-mass energy of 1.8 TeV at the Fermilab Tevatron collider. The Tevatron RunI cover from 1992 to 1996, lead to the discovery of the top quark [76] and measurement of its mass, a precision measurement of the mass of the W boson, among many other accomplishments. In Run IIa, which began in March 2001, the Tevatron was operated with an increased center-of-mass energy of 1.96 TeV. The instantaneous luminosity was increased by more than a factor 10 to greater than 10^{32} cm^{2}s^{-1}. In RunIIb, 2006, a new innermost layer (L0) was introduced in the vertex system in order to improve the vertex resolution and the other silicon layers were replaced. The sensors for the outer layers were purchased to Hamamatsu (HPK) with the characteristics that are described in Table 7.5. The silicon sensor is p-on-n type, single sided and AC coupled, with a single guard ring designed by Hamamatsu in order to improve the high voltage stability after irradiation.

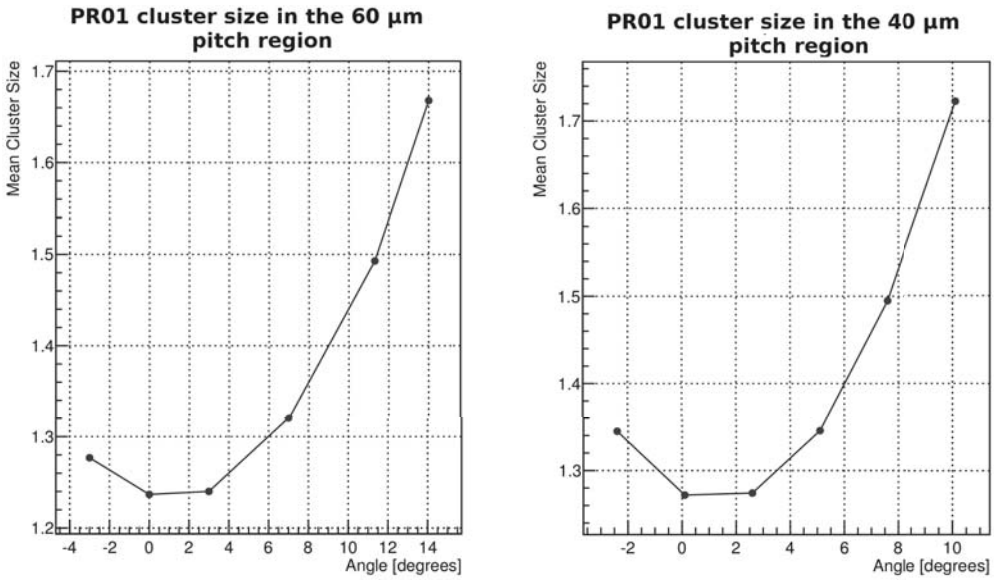

Figure 7.16: The cluster size increases with the angle because the generated electron-hole pairs will be spread in a greater number of strips.

Wafer thickness	320 ± 20 μm, sensor warp less than 50 μm
Depletion voltage	V $<$ 300 V
Leakage current	< 100 nA/cm^2 at RT and FDV+10%V, total current < 16 μA at 350 V
Junction breakdown	$>$ 350 V
Implant width	8 μm
Al width	$2-3$ μm overhanging metal
Al strip resistivity	< 20 Ω/cm
Coupling capacitance	$>$ 12 pF/cm
Coupling capacitor breakdown	$>$ 100 V
Interstrip capacitance	$<$ 1.2 pF/cm
Polysilicon bias resistor	0.8 ± 0.3 MΩ
Not working strips	$< 1\%$
Active Length (mm)	98.33
Active Width (mm)	38.34
Cut Length (mm)	100.00
Cut Width (mm)	40.34
Strip Pitch (μm)	30
Readout Pitch (μm)	60
# of Readout strips	639
Not working strips	$< 1\%$

Table 7.5: DØ specifications sent to Hamamatsu

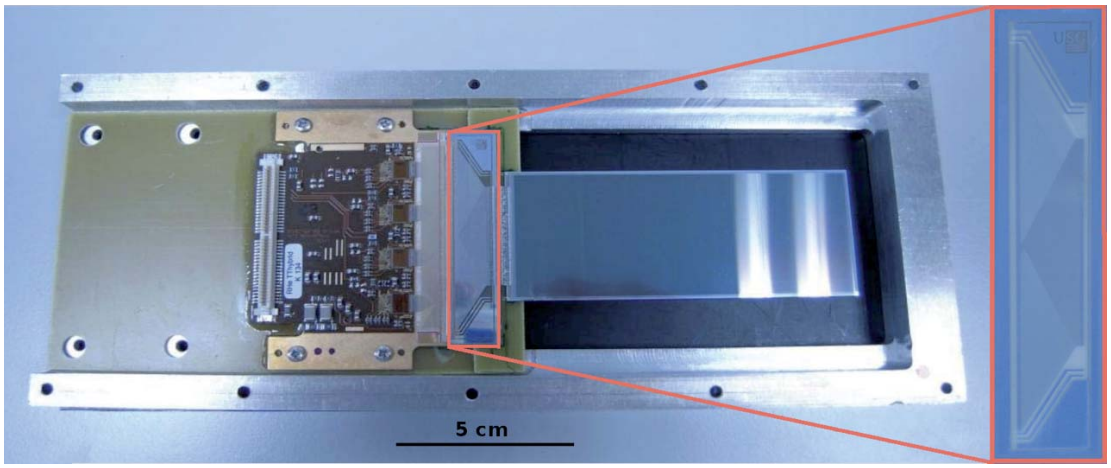

Figure 7.17: Assembly of the DØ sensor. The hybrid with 4 Beetles can be appreciated in the picture as well as the pitch adapter (zoom at the right) between the sensor and the hybrid.

These sensors were readout by the SVX-4 chips, which was designed to cope with a maximum interaction rate equal to 132 ns.

In 2011, a DØ sensor was bonded in the USC-GAES facilities to a TT hybrid which integrates 4 Beetles. The Beetle chip can handle a 25 ns bunch crossing rate, therefore it is much faster than the SVX-4 chip. This was the first time that the DØ sensor was readout by a faster front-end chip.

Besides the sensor, the hybrid is the only difference between the electronics of the DØ setup and the PR01 setup.

7.2.1 The Pitch Adapter

A novel technique was developed in the University of Santiago de Compostela to produce a custom designed pitch adapter (PA) for the DØ sensor. The technique was so successful that it was improved to build more PAs with tighter requirements. This project was a collaboration between the Experimental High Energy Physics Group [77] and the Microoptics and GRIN Optics [78] of the same university. A more detailed review of the process is given in [79].

The current method in the industry to manufacture pitch adapters is the photolithographic process. This photolithographic process implies the manufacturing of one or more masks and several steps, including resin deposition and chemical etching, among others. This is thus a slow and expensive method, for prototyping stage. We tried to fabricate PA with this technique (see Figure 7.18a) but the quality of the result was below specifications. Instead of the use of the current photolithographic process, searching for faster and cheaper preparative alternatives, a laser-ablation micromachinning process, performed on a previously metal-coated substrate was developed (Figure 7.18b). This process removes Al particles from a metal-on-glass substrate following a specific pattern structure, generated by CAD-like software, producing high-density pitch adapters.

(a) PA fabricated with photolithographic technique

(b) Francisco Rey working in a new PA with the laser machine

Figure 7.18: Photolithographic technique is more precise than laser, but involves much more steps becoming a very slow and very expensive process. Thus, for prototyping, laser allows a higher slope in the design curve.

The fabrication process begins with the deposition of a thin layer of chromium oxide between 3-4 nm on a 300 μm thick commercial borosilicate glass, in order to improve the adherence of the following layer. This step is carried out under a very low air pressure (2×10^{-4} mbar) in order to control the oxidation of the deposited chromium. The next step is the deposition of a Cr layer of 0.2 μm at a rate of 1 nm/s and at a higher vacuum (2×10^{-5} mbar) and the oxidation is negligible. The third layer is a thicker (1.0 μm) Al layer that must be accomplished in several steps. This layer is deposited under the same vacuum condition than the previous one, and at a rate of 5 nm/s. The purpose of the Cr layer is just to increase the adherence of the Al to the glass. The Al layer is deposited to ease the wire-bonding between the metal-on-glass substrate and the Al wire. Finally the metallized substrate is heated at 200ºC during 2 hours to harden enough the metallic layers to support the wedge bonding process.

Customized PA were prepared by laser ablation of the metal-on-glass substrates described above. Figure 7.19 shows a section of the PA design and a picture of the result. These substrates were irradiated with a quasi-perpendicular nanosecond Nd : YVO_4 laser, emitting 9.90 J/cm^2 with a repetition rate of 100 kHz at a wavelength of 1064 nm. The laser apparatus is fitted with a galvanometer beam steering system and a flat-field lens of 160 mm focal distance. This lens allows scanning the substrate within the XY plane.

The expected effect from this process is to pull off metal ions and particles from the metal-on-glass target without causing any cracks or visible damage, as long as the laser emission characteristics are adjusted to avoid negative consequences on the substrate surface.

Although the laser equipment used provides CAD-like software, this tool is not appropriate for the design of a PA because it does not allow to copy patterns

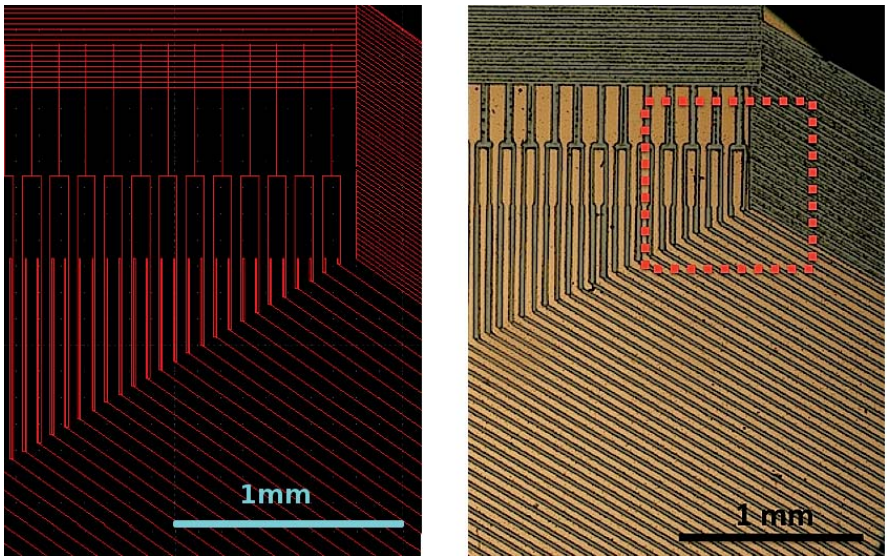

Figure 7.19: Pitch adapter CAD-like design (left) compared with a micrograph (right). The red square indicates the region studied by confocal microscopy (Figure 7.21).

with the introduction of small changes in each copy. A PA has several hundred channels, each slightly different from its neighbours, so drawing trace by trace in the CAD-like software becomes unfeasible. A different approach based on DXF (Drawing Exchange Format) files was chosen. DXF files are AutoCAD data files, with an ASCII format that allows interoperability between CAD programs. Following the format requirements these files can be generated using an external program, where the pattern coordinates are accurately computed and the output DXF file is filled. Introducing changes in the design is thus very fast and simple, which is very convenient in the prototyping phase of the PA manufacturing. The use of DXF format files together with Open Source programs: emacs (developing environment), g++ (compiler) and librecad (CAD software for visualization), makes this solution platform independent from commercial products. An example of a generated DXF file can be seen in Figure 7.19.

Laser ablation is a very flexible and fast technique for this purpose, allowing testing improvements in a couple of minutes. Therefore, we could perform extensive tests of the involved parameters like different metallization, mechanics planarity, design limits and laser parameters. Around 300 different test were done so far, allowing to improve the technique up to the very limit of the laser machine reaching traces down to 13 μm. Many parameters must be tuned to reach such precision, balancing the power of the laser to remove only the desired traces as it can be seen in Figure 7.20.

A Nikon Sensofar Plμ2300 confocal microscope was employed to perform the topographic analysis of the different regions in the pitch adapter. The profile of the structures obtained reproduces with high accuracy the CAD-like designs, and shows the existence of a debris area due to the laser ablation collateral effects

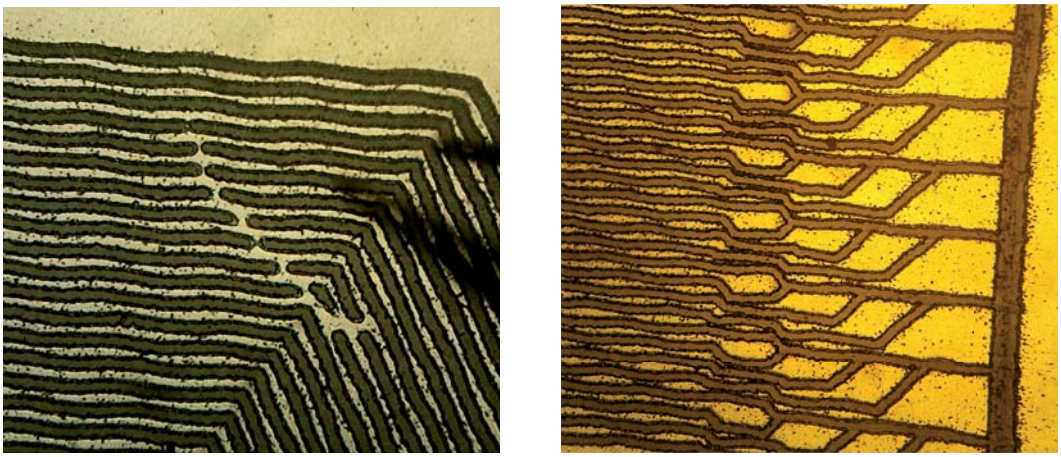

(a) Short between strips (b) Discontinuity (open) in strips

Figure 7.20: This figure shows the kind of problems that laser ablation technique must cope. Depending on the pulse frequency, the intensity, the speed and the lens, the metallization layer it could be not completely removed (left) or too much (right).

placed at the border of the pads and some grooves in which the laser ablation process damages the substrate (Figure 7.21). In these places the depth of the laser-cleaned inter-strip region is higher ($\pm 3\mu$m) than the thickness of the metallic layer ($\pm 1.5\mu$m).

All the strips of the PAs produced following this technique were tested electrically using a SUSS PM5 probe station looking for open circuits and shortcuts. Our acceptance criterion was less than 1% defective channels per PA that led to a 20% yield.

We measured metal conductivity and inter-strip capacitance. Resistances of the order of 34 and 25 Ω and inter-strip capacitances of 1.3 and 0.75 pF at 100 KHz were measured for the longer and shorter strips respectively, see Figure 7.22a. The inter-strip resistance was measured to be always larger than 1 GigaΩ.

In order to prove good pad bondability, tests were performed on a final pitch adapter with a Kulicke & Soffa 8060 wedge-bonding machine using a 25 μm Al/Si (1%) alloy wire. Wire bond pull tests were performed following standards and pulling the wires at their center with a Dage 3000 series pull tester obtaining an average force of 8.9 ± 0.51 grs as shown in Figure 7.22b.

These values are compatible with high quality PAs produced with the standard photolithography technique.

7.2.2 Electrical characterization

The DØ sensor was electrically characterized with the IV and CV curves (Figure 7.23). These curves were measured in a clear room class 10.000, using a SUSS PM5 probe station.

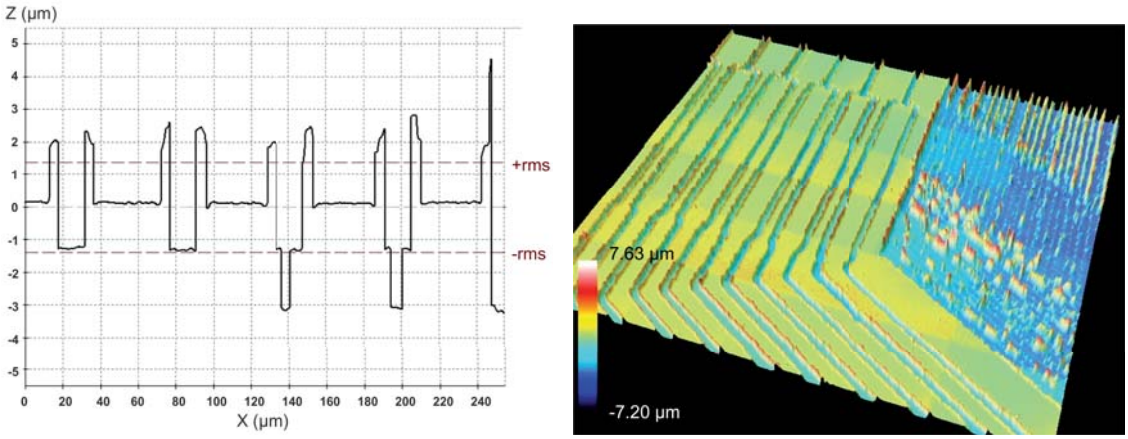

Figure 7.21: Profile of the metal strips and laser-cleaned inter-strips regions. The profile was obtained by a Leica TCS-SP2 spectral confocal microscope (40x). The border of the pads presents an important amount of debris due to the laser ablation process.

The IV curve was carried out before the assembly of the sensor, with a picoammeter/voltage source Keithley 487. The environment variables were a temperature of 21 ºC and a relative humidity of 37%. The measured values shown in Figure 7.23a are in good agreement with the IV curves measured originally in the DØ experiment for the same bunch of sensors (see [80]).

The CV curve was performed with the same picoammeter and a LCR Agilent E4980A, with a signal of 1 mV of amplitude and a frequency of 1 kHz. The environment variables were again a temperature of 21 ºC and a relative humidity of 41%. Representing the $1/C^2$ versus the voltage; the depletion voltage of the sensor can be obtained as the point where the plateau begins. In this case, Figure 7.23a shows that the depletion voltage was ≈ 120 V.

7.2.3 Testbeam setup

The Timepix telescope [66] was installed in the mentioned SPS 120 GeV pion beam at CERN. The telescope was built with 8 Timepix devices in ToT mode plus another Timepix in ToA to associate a time-stamp to each track[3]. The Timepix devices and their positions are described in Table 7.6. The main difference between the 2011 setup and the 2010 (PR01), was that the USB readout links from the telescopes planes were joined in a FPGA based board called RELAXD. The RELAXD [81] readout systems are linked to a single DAQ PC via dedicated UDP Gigabit Ethernet links.

Besides the RELAXD system, the rest of the setup was the same than the described for the PR01 test-beam, as can be appreciated in Figure 7.24.

[3]The **T**ime **o**ver **T**hreshold (ToT) provides the charge deposited in a pixel, while the **T**ime **o**f **A**rrival (ToA) provides the time-stamp. A detailed description of the Timepix chip is given in Section 8.2.2.

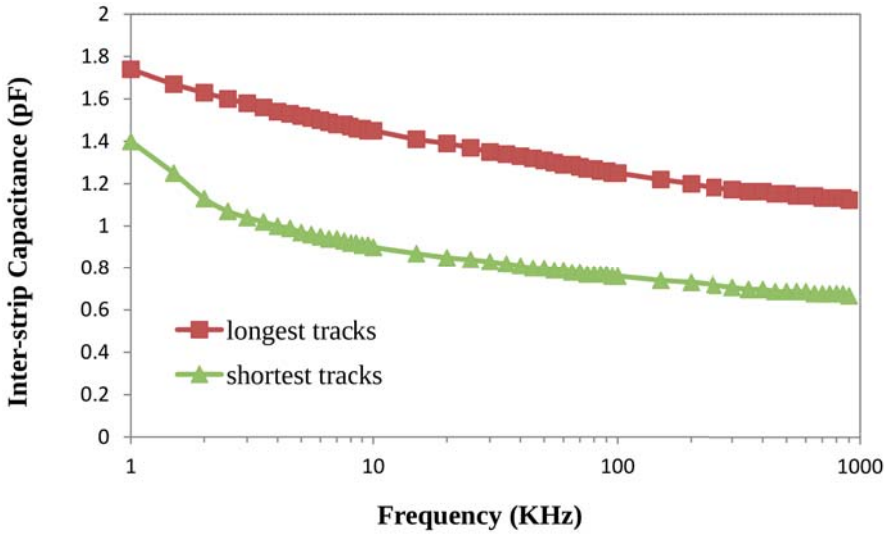

(a)

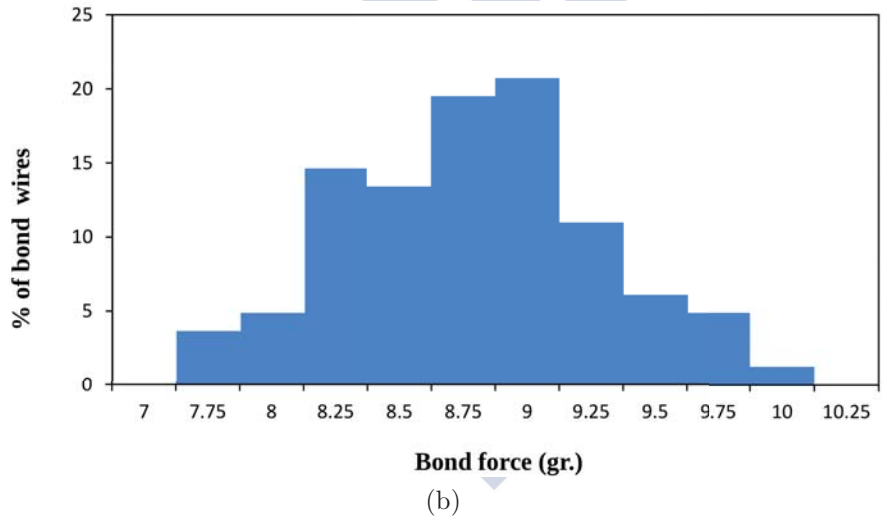

(b)

Figure 7.22: a) Inter-strip capacitance as a function of sampling frequency and strip length. b) Measurements of the bond pull test forces for the final pitch adapter.

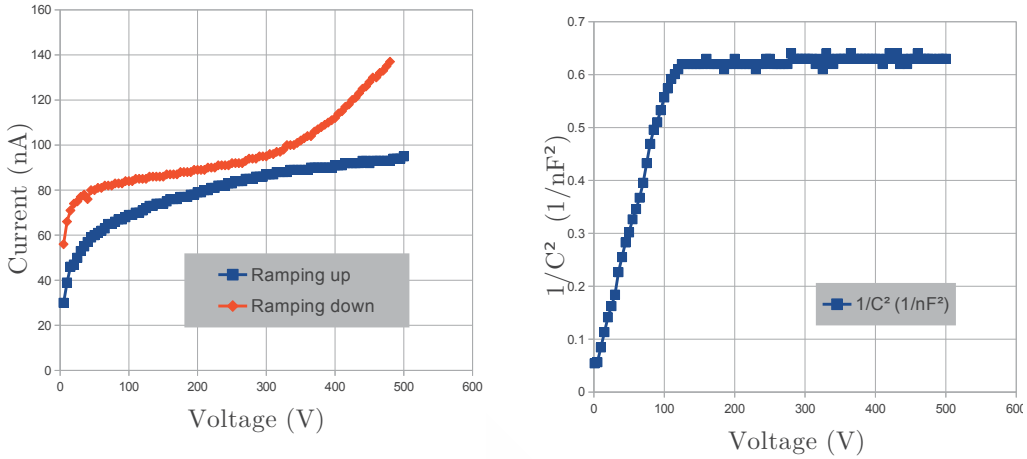

(a) DØ IV Curve

(b) DØ depletion voltage

Figure 7.23: DØ IV curve and CV curve. Instead of representing directly the CV curve, it was decided to show $1/C^2$ versus Voltage, which is useful to obtain de depletion voltage.

(a) The author placing the DØ in the DUT position

(b) Santiago's team in the 2011 test-beam campaign. Starting from the left: Abraham Gallas Torreira, Eliseo Pérez Trigo and the author.

Figure 7.24: DØ module mounted in the DUT position

Device	Position	Telecope's arm	Mode
H03-W0092	z=0 mm	left	ToT
I06-W0092	z=25 mm	left	ToT
H03-W0092	z=50 mm	left	ToT
J08-W0087	z=50 mm	left	ToT
DØ	z=373.5 mm	DUT	
I08-W0092	z=556.5 mm	right	ToT
H09-W0082	z=582.5 mm	right	ToT
I09-W0092	z=606.5 mm	right	ToT
I08-W0087	z=623.5 mm	right	ToT
D04-W0015	z=686.5 mm	right	ToA

Table 7.6: Telescope's planes

August 2011 test-beam campaign

Three different sets of runs were taken with the DØ sensor grouped as an angle scan, a bias scan and a displacement scan (see Table A.2). The angle scan allow us to measure the resolution and the bias and position scan provide us data to know the efficiency of the sensor.

The DØ sensor has two main features to take into account during the data analysis:

1. As the sensor is p-on-n type it will collect electrons instead of holes. As the typical VELO sensors are n-on-p or n-on-n[4] then the readout electronics will provide a signal with the sign inverted, as can be seen in Figure 7.25.

2. DØ is a 30 μm pitch sensor with intermediate strips. That means that the effective readout pitch is 60 μm, and thus the amount of readout charge will be about one half than in a similar sensor. This feature can be clearly confirmed in Figure 7.26 where the MPV of the Landau is below 20 ADC counts.

7.2.4 Spatial resolution

As it was introduced in the PR01 spatial resolution section, the binary resolution of the a sensor is given by the formula:

$$\sigma_{D\emptyset} = \frac{pitch}{\sqrt{12}} = \frac{60\ \mu m}{\sqrt{12}} = 17.3\ \mu m \tag{7.8}$$

The optimal angle of the DØ sensor is:

$$\alpha_{D\emptyset} = tan^{-1}\left(\frac{pitch}{thickness}\right) = tan^{-1}\left(\frac{30}{320}\right) = 5.3^{o} \tag{7.9}$$

[4]n-on-p and n-on-n are radiation hard, that's the reason why they are preferred in the VELO upgrade program.

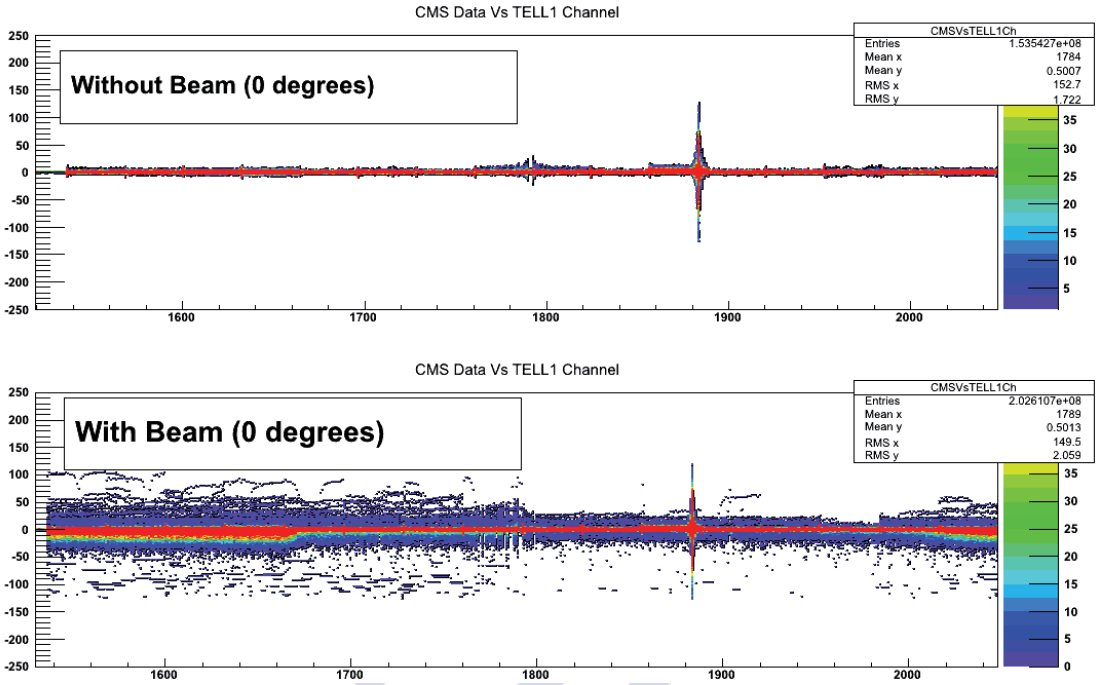

Figure 7.25: DØ raw data. Top plot corresponds to pedestal and common noise suppress data without beam, and bottom with beam. Note that as the sensor is p-on-n type, the sign of the readout signal is the opposite than in the PR01 sensor.

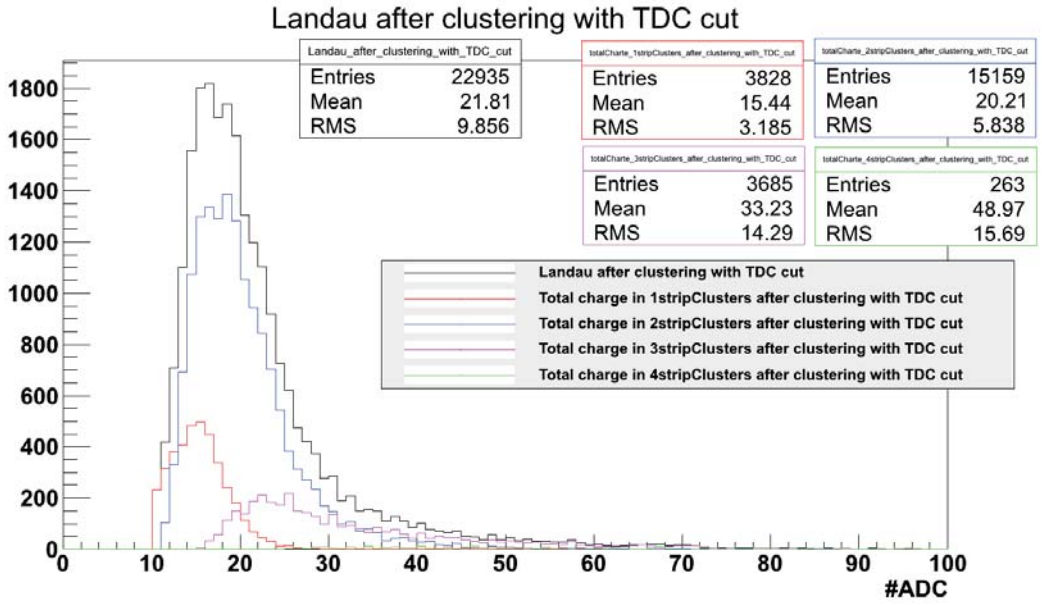

Figure 7.26: DØ energy loss distribution.

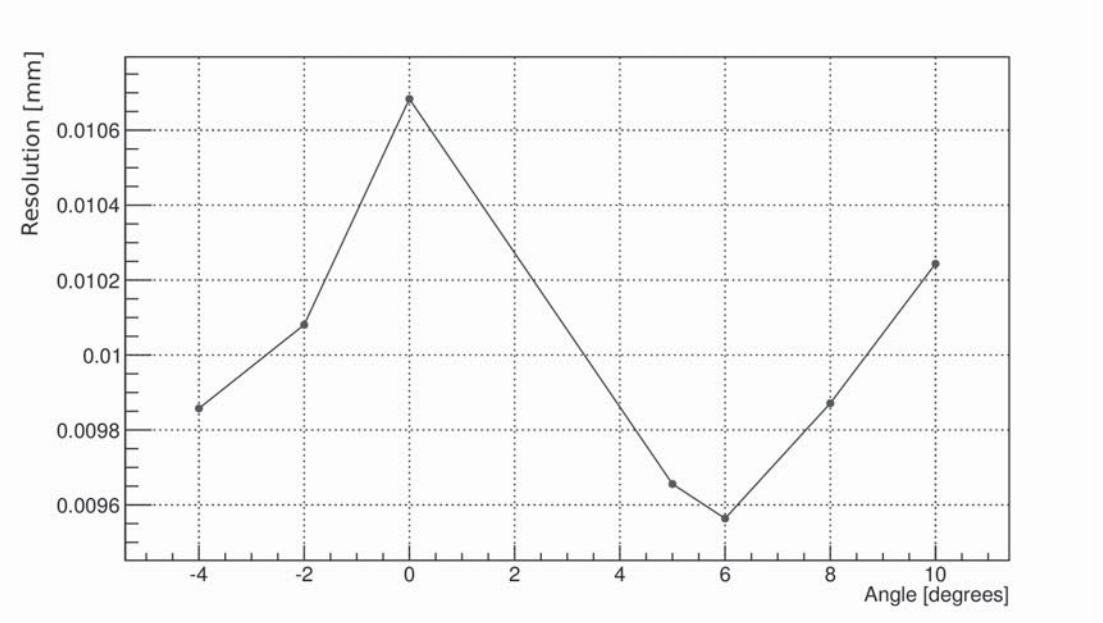

Figure 7.27: DØ resolution versus angle. The measured optimal angle is around 5 degrees, as predicted.

Both values are in agreement with the results shown in Figure 7.27[5].

7.2.5 Efficiency

In order to know the sensor efficiency we look for clusters in the DUT into a certain window around the tracks. Clearly the percentage of tracks with an associated DUT cluster will be function of the window size.

As it can be appreciated in Figure 7.28, the efficiency of the DØ is above 99% when the size of the window around the track is equal to the readout pitch (60 μm).

There are two runs not present in the plots, corresponding to bias voltage 50 V and 70 V, the reason is that at such bias voltage the DØ sensor was so under-depleted that no cluster could be created.

In concordance with expected, when we increase the bias voltage the number of strips per cluster (cluster size) will increase. The reason is that at low bias voltage the sensor is not fully depleted, so not all the electron-hole pairs are readout. However, if we continue increasing the bias voltage far beyond the depletion point, the electric field inside the sensor will be much higher and the drift velocity will be increased accordantly. As a consequence, the spread of the generated pairs will be lower and thus the cluster size will be also lower. At certain point, the drift velocity will reach a maximum and the cluster size will asymptotically tend

[5]These results were obtained setting the clustering algorithm with a seed threshold of 6 times the noise, an inclusion threshold of 3 times the noise and a sum threshold of 9 times the noise. For more information see 7.1.4

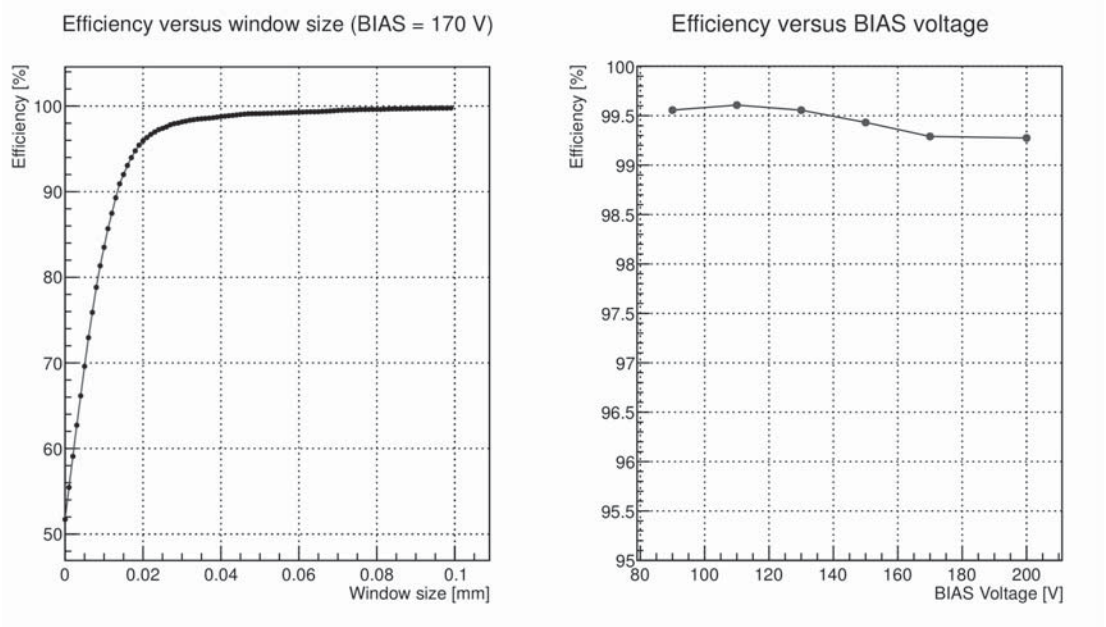

Figure 7.28: Left plot shows the DØ efficiency measured as the percentage of tracks with an associated cluster into a given window size. Right plot is the efficiency value as function of the bias voltage. These values correspond to a window of 60 μm around the tracks.

to a certain value. This behaviour is clearly represented in Figure 7.29 where the cluster size is represented as a function of the bias voltage.

7.2.6 Charge spread problem

A problem was detected during the analysis of the DØ data. As it can be seen in Figure 7.30a the residual distribution does not match a Gaussian curve as it should. Also the Figure 7.30b shows a lack of charge at the left side of the η distribution[6]. The explanation is that the charge injected in the analog readout link is non-homogeneously spread during the transmission. As a result, some charge is added to the next readout channel and thus the distribution in 2-strip clusters is non-homogeneous.

There is a way to solve this problem which is the use of the Finite Impulse Response (FIR) algorithm. This algorithm can calculate the spread factor for each channel and add a correction factor in order to recover the homogeneous situation. Unfortunately the FIR algorithm needs an special run called *test pulse* which was not taken in 2011 test-beam and thus it could not be applied.

[6]The η distribution shows the probability of charge distribution in 2-strip clusters.

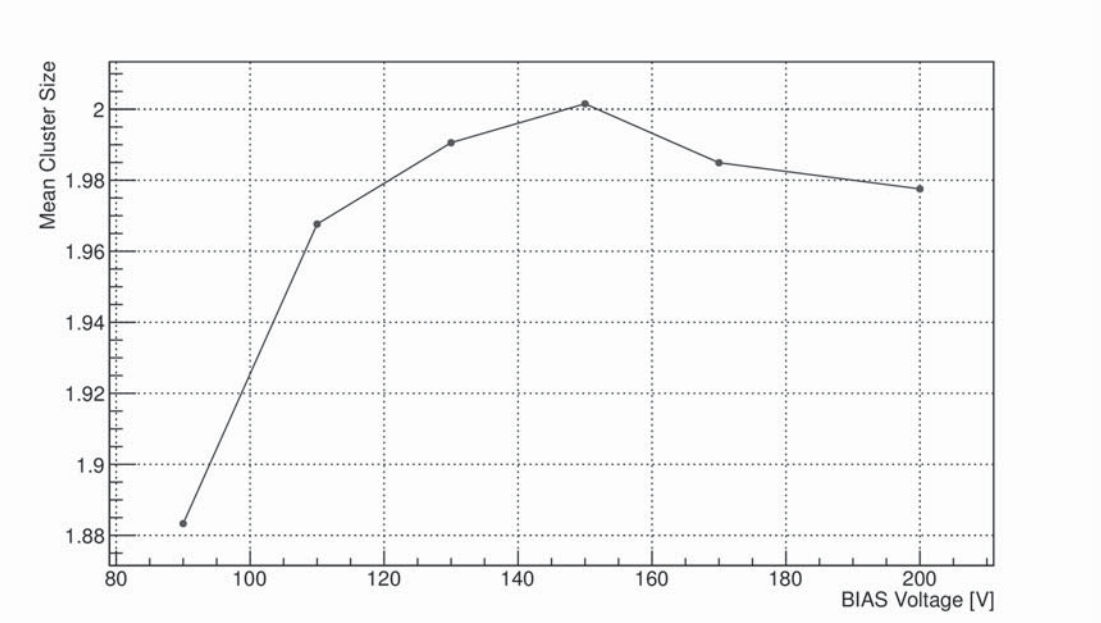

Figure 7.29: Evolution of the DØ mean cluster size as function of the bias voltage.

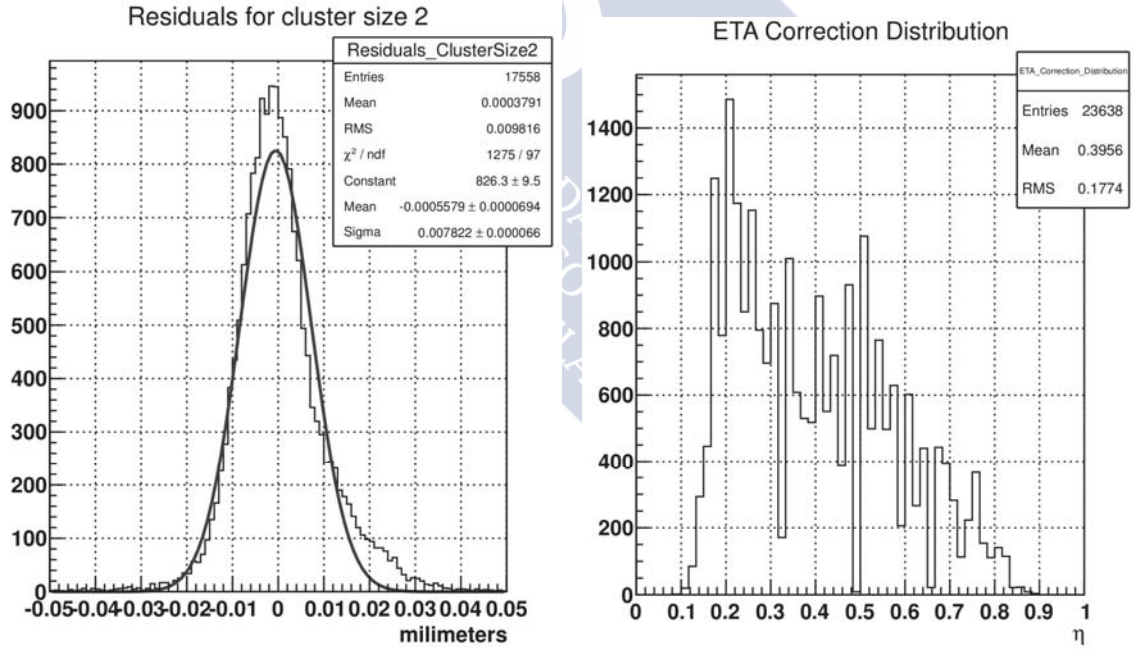

(a) DØ resolution for 2-strip clusters

(b) DØ eta distribution

Figure 7.30: The resolution distribution and the η are clearly non-symmetric and the reason is that the charge is spread in the analog readout link.

7.3 The Hamamatsu sensor

Silicon micro-strips is the chosen technology for current VELO, and taking into account the demanding specifications for the VELO upgrade, a new silicon micro-strip sensor was developed to confirm if the requirements can be met.

The new micro-strip ASIC will be developed in synergy with other LHCb silicon detectors. It will include embedded complex algorithms to implement clustering, sparsification, common mode suppression, pedestal subtraction and more in order to reduce the data rate. Such ASIC is not yet available, so the micro-strip prototypes have to be bonded to current Beetle chip [50].

As part of the VELO upgrade program, several n^+-on-p micro-strip sensors were purchased to Hamamatsu and were served on the second half of 2012. Unfortunately, they could not be instrumented on time to be ready for the 2012 test-beam campaign, so instead of a 120 GeV pions beam, they were tested in Santiago's laboratory with a ^{90}Sr β^- source and laser beams. Readout chain was also different from previous sensors, as this time an Alibava motherboard was used instead of the TELL1.

7.3.1 Sensor design

As it was already mentioned, 12 n-on-p micro-strip sensors were purchased to Hamamatsu and delivered on the second half of 2012. Each micro-strip sensor has 2560 strips, which are intended to be readout by a total of 20 Beetle chips. A sketch of both prototypes are shown in Figure 7.31. The main characteristics of the R-type sensors are:

- 6 uds: 4 μm and 2 $\times$ 150 μm thick.
- 5 sectors in every sensor
- $\sim$512 strips per sector
- pitch ranges from 30.0 (inner radius) to 106.0 μm (external radius) for every sector
- strip radius from 7.5 (inner radius) up to 37.2 mm
- implants length from 5 (inner radius) to 25 mm

The main characteristics of the ϕ-type sensors are:

- 6 uds: 4 μm and 2 $\times$ 150 μm thick.
- 3 sectors in every sensor
- $\sim$768 strips per sector
- pitch ranges from 30.0 (inner radius) to 120.0 μm (external radius) for every sector

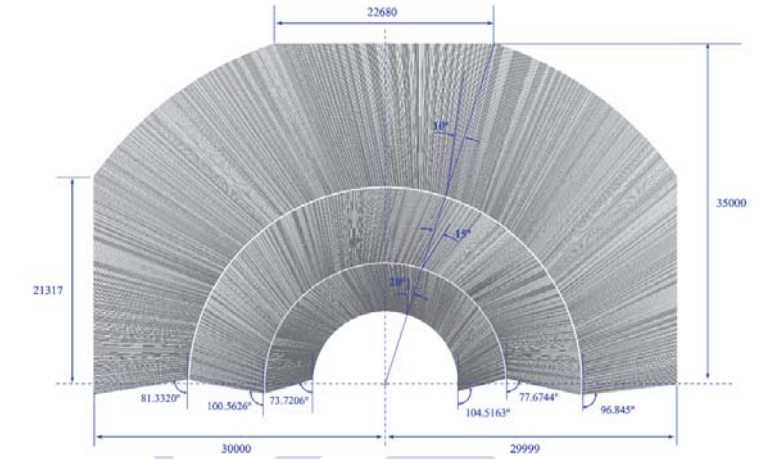

(a) ϕ-type sensor

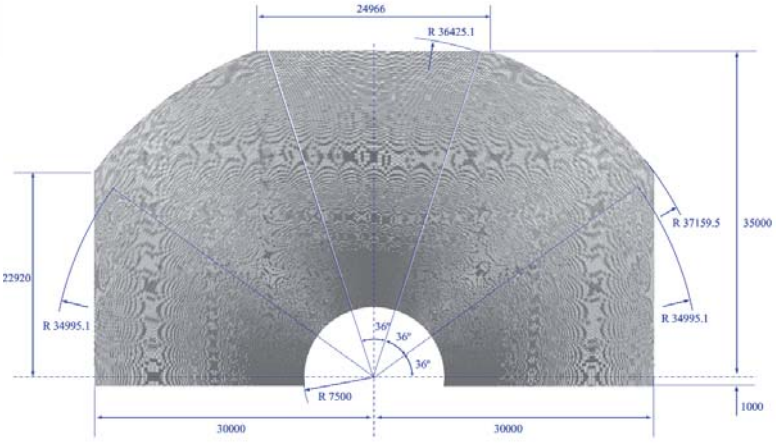

(b) R-type sensor

Figure 7.31: Sketch and dimensions of the Hamamatsu ϕ-type and R-type microstrip sensors.

- implants lengths are approximately: 5, 8 and 17.5 mm for inner, middle and outer region respectively.
- Stereo angles are: 20^o, -15^o and 10^o for the inner, middle and outer region respectively.

The GAES group at the University of Santiago de Compostela, took the responsibility of the electrical characterization and metrology of the sensors. Together with Eliseo Pérez [82], we performed the metrology, the electrical characterization, the pitch adapter manufacture, the wedge-bonding to a TT hybrid and S/N ratio measurements with Laser beams and ^{90}Sr β^- source.

7.3.2 Electrical characterization

The electrical characterization was carried out in the clean room class 10.000 available at the USC. The instruments used are the same than for the PR01 and DØ sensors characterization:

- Keithley 487 picoammeter/voltage source
- Two Keithley 2410 source meter, 1100V
- Probe station Karl Suss PM5 & probe heads PH100
- LCR Agilent E4980A, 2Mhz
- Decoupling card to do CV measurements

According to tender document, the sensors should be able to withstand an reverse bias voltage of -800 V. Following the standard procedure to obtain the break point, our measurements showed that the current through the sensor quickly went out of safety margin at only -110 V. Several iteration steps were followed together with Hamamatsu, until a new procedure was determined which differs from the previous one in the need of isolate the chuck which holds the sensor from the sensor itself. Unfortunately, during this process two sensors (one R-type and one ϕ-type) were damaged and could not be used any more. For that reason only 10 sensors were measured. More detailed information about the sensor status can be found in Table 7.7.

IV curves

To perform the IV curve, all the sensors were isolated from the chuck with a *Kapton*® foil, and biasing was applied through top surface pads. The resulting IV curves are displayed in Figure 7.32.

According to the tender document, several conditions must be fulfilled by the IV curves of the sensors. These conditions are summarized in Table 7.8 and it shows that two 200 μm thick sensors did not cope with the specifications. As the tender document did not mention 150 μm thick sensors, the only thing that we can

ID	Thickness	Location	Status	Comments
PHI_1	200 μm	Japan	Damaged	Dummy sensor damaged during IV investigation
R_2	200 μm	Japan	Damaged	Dummy sensor damaged during IV investigation
PHI_5	200 μm	USC	OK	-
PHI_7	200 μm	Glasgow	OK	Wedge-bonded to TT-hybrid
PHI_8	200 μm	USC	Damaged	Damaged during CV curves. Can not be fully depleted
R_4	200 μm	Glasgow	OK	-
R_6	200 μm	USC	OK	Bonded to TT-hybrid
R_8	200 μm	USC	OK	-
PHI_15	150 μm	USC	OK	-
PHI_16	150 μm	USC	OK	-
R_13	150 μm	USC	Damaged	Damaged between IV and CV curves
R_15	150 μm	USC	OK	-

Table 7.7: Status of the Hamamatsu prototypes at June 2013

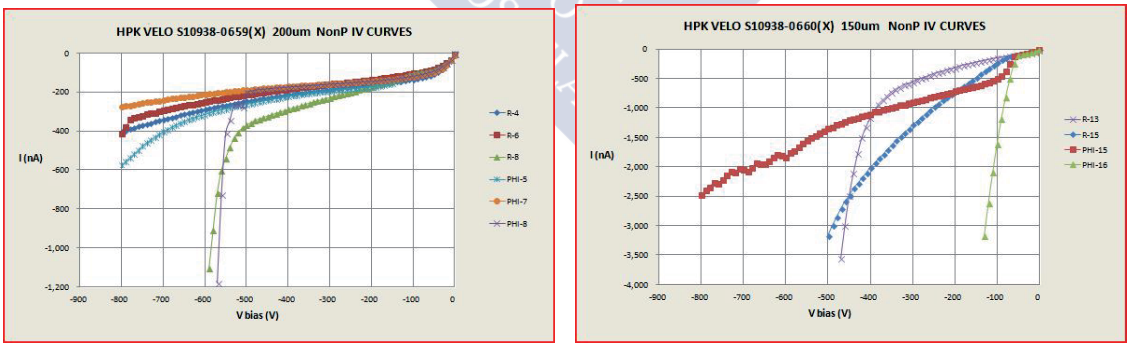

Figure 7.32: Left plot corresponds to IV curves for 200 μm thick sensors, and right plot belongs to 150 μm thick sensors.

Sensor ID	Cond_1	Cond_2	Cond_3	Cond_4
PHI_5	√	√	√	√
PHI_7	√	√	√	√
PHI_8	√	X	X	X
R_4	√	√	√	√
R_6	√	√	√	√
R_8	√	√	X	X
PHI_15	√	√	√	√
PHI_16	X	X	X	X
R_13	√	X	X	X
R_15	√	X	X	X

Table 7.8: Sensors behaviour according to working conditions written in the tender document, where **Cond_1:** $I_{leak} < 5$ μA [300 V]; **Cond_2:** $I_{leak} < 10$ μA [600 V]; **Cond_3:** $I_{leak} < 20$ μA [750 V]; **Cond_4:** $\frac{\triangle Ileak}{\triangle V} < 100$ nA/V [750-800 V]

say is that 75% of the 150 μm thick sensors did not cope with the specifications for 200 μm sensors. It is not clear yet if they were somehow damaged during the investigation previously mentioned. In either case, all the sensors could be fully depleted at a reasonable current during this test.

CV curves

In this case all the sensors showed a fine behaviour, and the resulting CV curves are displayed in Figure 7.33. Sensor R_13 is not listed because it could not be fully depleted while keeping the current between safety margins (Table 7.7). As expected, 200 μm thick sensors are fully depleted at -100 V, and 150 μm thick sensors at -60 V. Both values are well below the limit written in the tender document, which is 150 V for 200 μm thick sensors.

Total strip capacitance

The total strip capacitance per length unit is covered by the tender document, and it should be lower than 1 pF/cm at depletion voltage, where the strip length is the sum of the implant and routing line length. This capacitance is defined as the sum of the inter-strip capacitance to the two neighbouring strips on each side and the capacitance to the backplane ($C_{tot} = C_{int} + C_{back}$). We could not measure the second parameter because the needed setup was not available, however its value is usually lower than the C_{int}, so we can provide a good approximation to know if the requirements are fulfilled.

To measure the capacitance between strips the probe needles were placed in contact with the AC strip pads. The values showed in Figure 7.34 are capacitance per cm, and the measured length is the sum of the strip length plus the routing lines length. As the length of the routing lines and the strips is quite different depending on the sensor sector, it was decided to measure three different sectors,

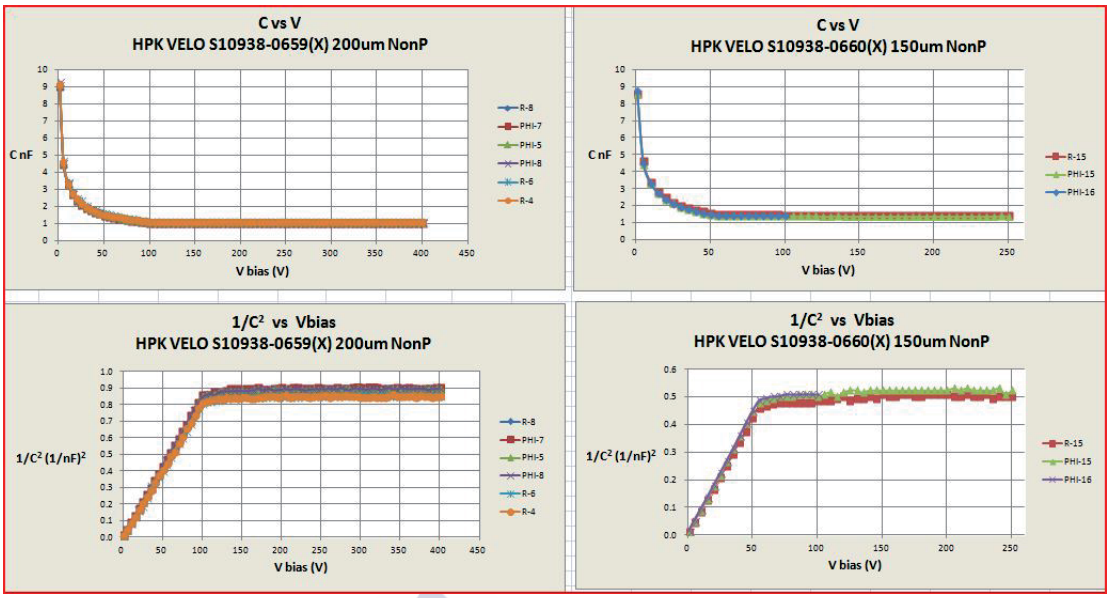

Figure 7.33: CV curves for 200 μm and 150 μm thick sensors. Bottom plots shows $1/C^2$ instead of C because it results more clear the point where the fully depletions is achieved.

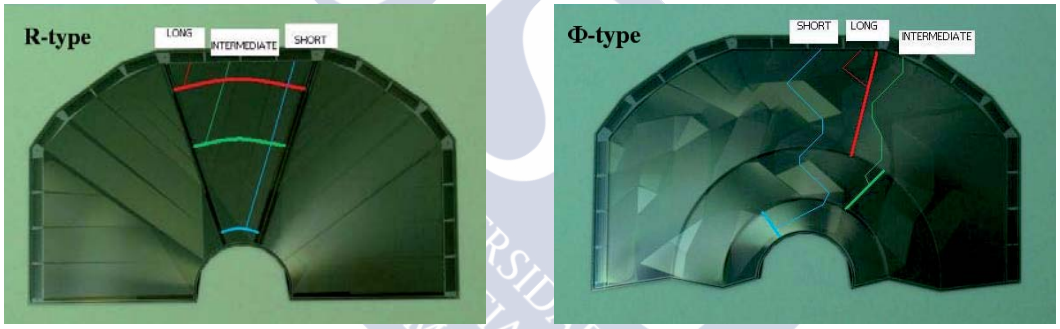

(a) Measured routing lines and strip lengths in a R-type sensor

(b) Measured routing lines and strip lengths in a ϕ-type sensor

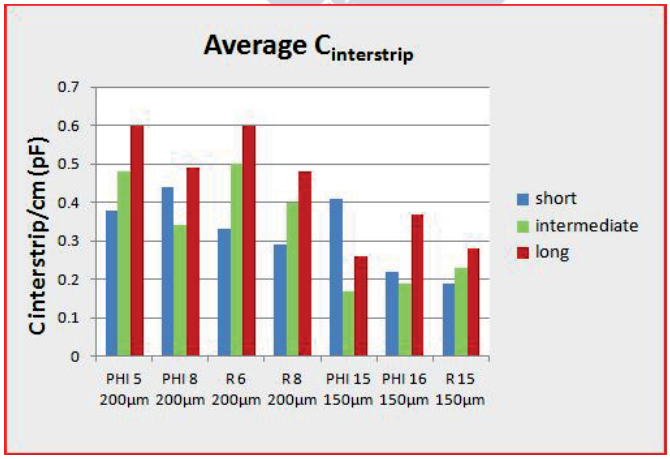

Figure 7.34: Capacitance per centimetre between neighbouring strips.

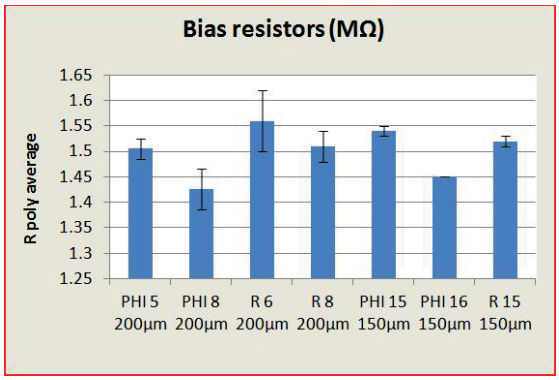

(a) R_{poly}

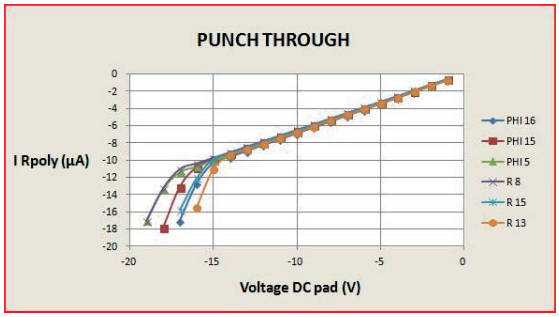

(b) Punch Through

Figure 7.35

and into each sector 4 consecutive strips were measured. Therefore, the values of the Figure 7.34 are the average of these four strips.

The inter-strip capacitance to first neighbour strip (left and right) was measured, resulting ∼0.6 pF/cm in the worst case, so is reasonable to think that the sensors were built according to specifications in terms of total strip capacitance.

Resistivity of the polysilicon bias resistors

The polysilicon resistors are between the strips implants and the bias ring. To measure the resistivity the sensor must be previously polarized, and then a small voltage is applied between the DC strip pad and the bias ring pad. Measuring the current provided by the voltage source, and fitting the IV curve to a straight line, the resistivity of the polysilicon can be determined.

According to the tender document, the resistivity of the polysilicon must be 1.5 ± 0.5 MΩ, and measured values are well within this tolerance.

Punch trough voltage

This test measures the isolation between the strip implant and the bias ring. To perform this test, the setup is the same than the used to calculate the polysilicon bias resistor, but the voltage applied is increased until the current begins to circulate, not only through the polysilicon, but also between the strip implant and the bias ring.

The punch through voltage is calculated as the voltage at which the current starts to grow exponentially, meaning that the equivalent resistivity between the strip and the bias ring starts to drop from the polysilicon resistor value. The measured values can be seen in Figure 7.35b, giving an average value of:

$$V_{pt} = -16.7 \pm 1.2\ V$$

7.3.3 Metrology

Figure 7.36: Leica microscope and linear stages used in the metrology process

The purpose of the metrology measurements was to confirm that the dimensions of the sensor, the flatness and the thickness were according to specifications.

To perform the metrology of the Hamamatsu sensors, the methodology followed was to measure X and Y coordinates with linear stages, and Z coordinate with a microscope. The used linear stages were two Newport ESP300, driven by Labview, which were screwed in 90º to an optical table. These linear stages provide the X and Y coordinates with sub-micron precision. To measure the Z coordinate a Leica M205A microscope was used. This microscope is equipped with a motorized column, which provides the Z coordinate by focusing a given point. In this case, the precision depends on the operator, as far as he must decide when a point is well focused. To minimize the error each point was measured 5 times, thus the Z coordinate was calculated as the mean value and the error as the standard deviation. To minimize systematic errors, the focusing process was carried out from lower focus and from higher focus towards the measuring point alternatively. A picture of the setup can be seen in Figure 7.36.

To perform the metrology of the sensors, 14 points in the R-type and 16 points in ϕ-type sensors were chosen. These points are shown in Figure 7.37 and they provide an accurate profile of the sensor surface. These measurements were carried out in a clean room class 10.000, at controlled temperature of 20ºC.

Metrology calibration

A way to ensure the metrology measurements is to use a previously calibrated sample. Unfortunately, the available calibrated samples are around a few microns, much thinner than our requirements. Therefore we decided to create a new sample and calibrate it with a perfilometer. The available perfilometer is a *Veeco/Sloan* Dektak^3 which can be seen in Figure 7.38. It provides a vertical resolution of 10 Å in optimal conditions, which was relaxed to ~ 1 μm in our setup.

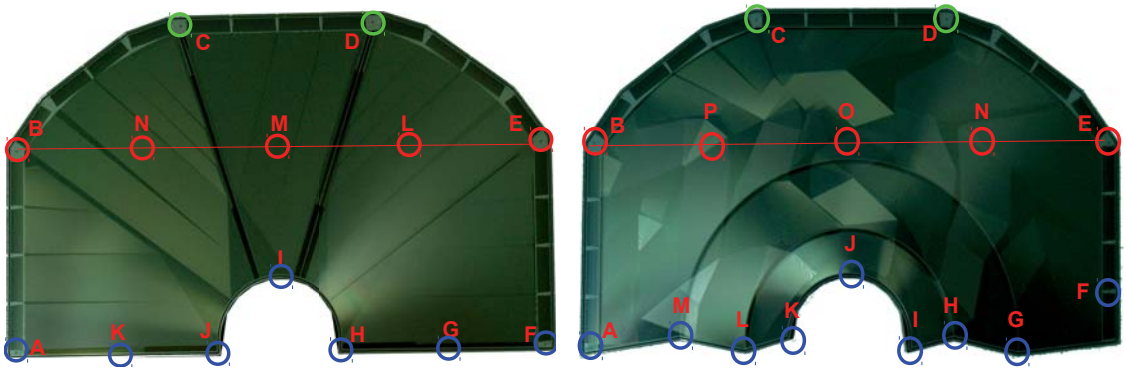

(a) R sensor (b) ϕ sensor

Figure 7.37: R and ϕ sensors. Colour circles show the chosen points to measure the planarity of the sensors.

As the perfilometer uses a diamond stylus with a diameter of 12.5 μm, brushing against the surface, the sample must be strong enough to resist that process without being damaged. For that reason a ceramic pitch adapter was chosen as sample. The pitch adapter was glued to a ceramic base with a small slope, guaranteeing that the vertical range was in the same order than our sensors ($\sim$ 300 μm).

Once the sample was measured with the perfilometer, we used the same setup that is used for the metrology to measure the sample. Both values matched into the incertitudes given by the Leica microscope (see Figure 7.39), validating the metrology methodology.

Thickness

One of the main purposes was to measure the sensor thickness. To obtain these values, we measured the Z-coordinate of 6 fiducial marks at the sensor's periphery (A, B, C, D, E and F in Figure 7.37) as well as the corresponding Z-coordinate of the base plate in the nearest points. Taking into account that some points could not be in touch with the base, the sensor thickness value must be determined by the minimum distance in height between a fiducial mark and its correspondent point at the base. The summary of the data taken is shown in Figure 7.40. Thickness tolerance is defined in tender document, being $\pm$20 μm for 200 μm thick sensor. As 150 μm thick sensors are not covered by the available tender document, we assumed the same tolerance values. Both limits are printed in Figure 7.40 as horizontal dashed lines.

According to the tolerance values defined, all the sensors but one are in agreement with the specifications. The one that is not, named PHI_1, is currently in Hamamatsu central offices at Japan, and it could not be measured again to be sure that the thickness is the one showed in the plot.

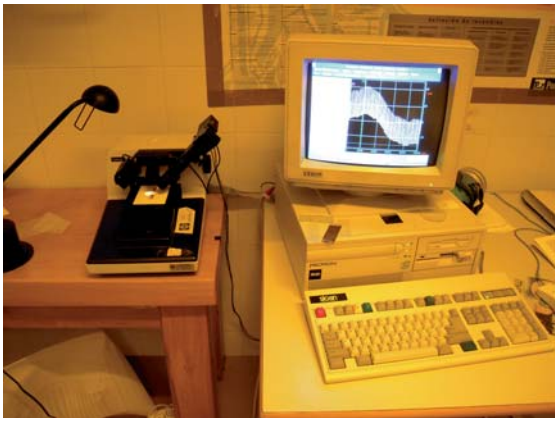

(a) Perfilometer and control system

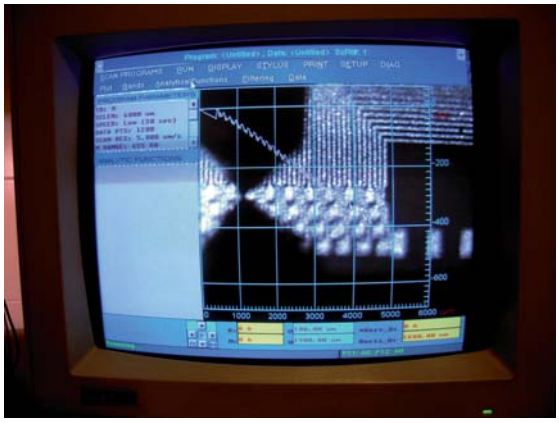

(b) Perfilometer's software

Figure 7.38: Veeco/Sloan Dektak^3 perfilometer. In Figure 7.38b the stylus can be appreciated as a dark cone (top) which meets its shadow (bottom) at the pitch adaptor surface. The pitch adapter profile is overprinted, and the bonding pads are clearly visible as individual peaks.

Flatness

During the wafer manufacture, several dicing processes were carried out until the sensor was ready for shipment. Dicing process introduces mechanical stress in the silicon lattice, and consequently is expected some kind of warping in the sensor. Also, warping will presumably increase with sensor size and decrease with thickness.

The flatness value for a given sensor is calculated as the maximum distance in height between two points at the sensor surface. The resulting values are showed in Figure 7.41. Again, dashed line corresponds to tolerance value written in the tender document, however this time no assumption is made for 150 μm thick sensors. Measured values for 200 μm thick sensors are this time just in the limit of the specifications. As expected, 150 μm thick sensors are more bend than 200 μm, and the data shows that their deviation from flatness is $\sim 75\%$ greater.

Another remarkable result is that all the sensors have the same convex shape, and the supporting points are in all the cases the sectors A-B and E-F. This result can be easily visualized in 3D plots shown in Appendix B.

2D dimensions

The points selected for metrology measurements at the periphery of the sensor correspond to fiducial marks. Technical sheets show several distance values between these fiducial marks, so we used the values obtained from the linear stages to compare.

Figure 7.42 shows the difference between measured distances between fiducial and the theoretical distance. It can be seen that the difference appears only in the B-E and C-D directions, but not in A-B, which is compatible with the fact

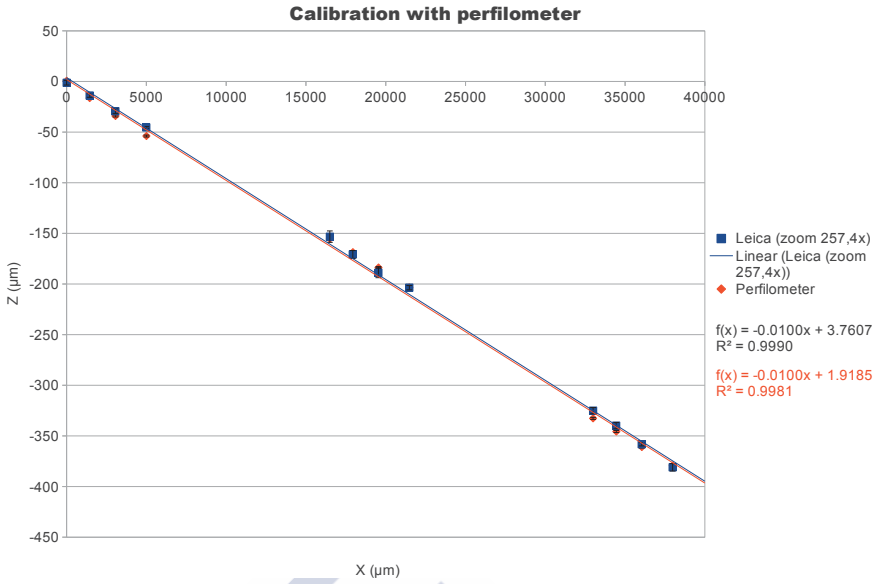

Figure 7.39: Linear fit of the perfilometer data (red) and the microscope data (blue). Note that the reconstructed slope of the pitch adapter is the same in both cases, and the offset is 2 μm, well below of the microscope's precision.

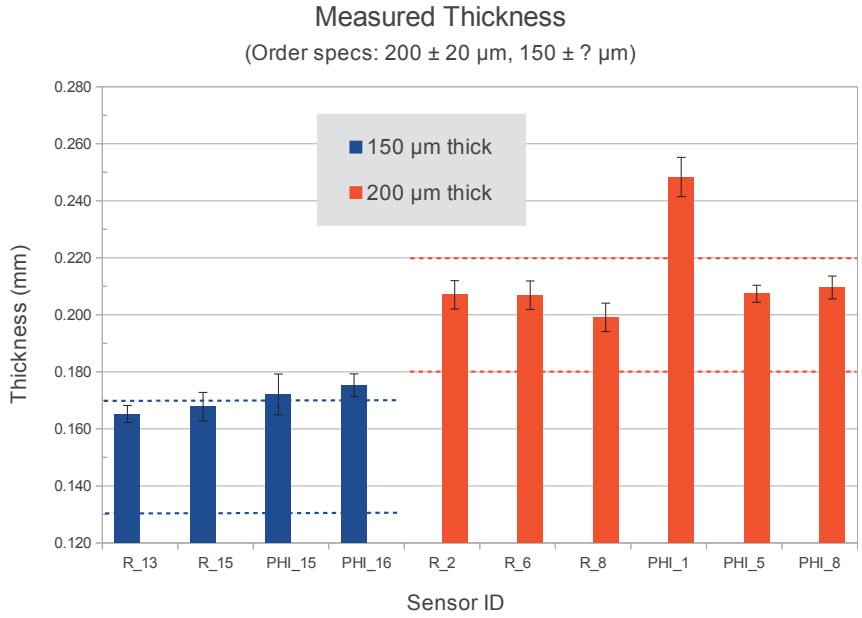

Figure 7.40: Hamamatsu sensor's thickness. Dashed lines are the tolerance values written in the tender document.

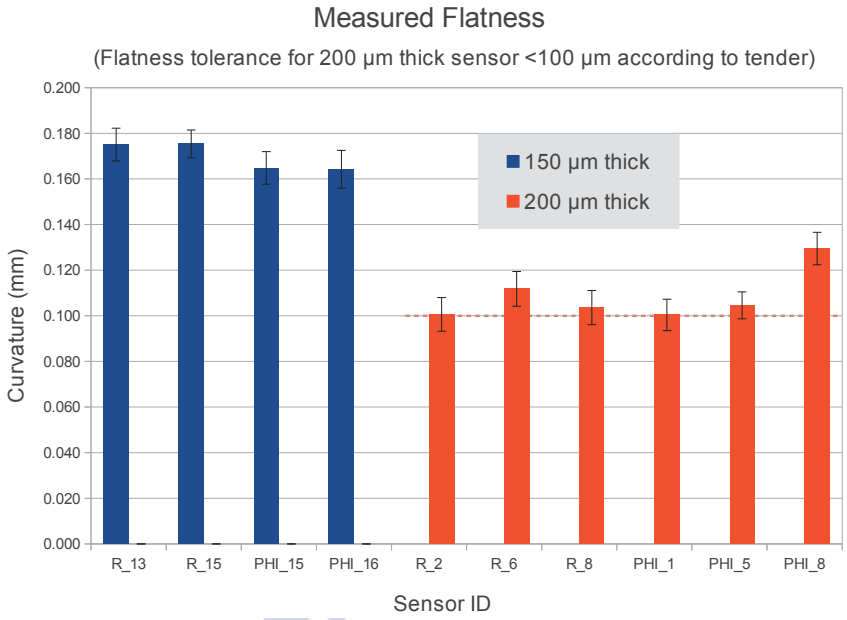

Figure 7.41: Hamamatsu sensor's flatness. Dashed line is the tolerance value for 200 μm thick sensors written in the tender document.

that the sensor is bent along that axis.

7.3.4 Alibava setup

In order to test a Hamamatsu sensor we used an Alibava's board [83]. This system provides a portable acquisition system made of a motherboard and the software. The software package implements pedestal subtraction, common mode subtraction and clustering (up to 8 strips per cluster). An interesting feature of the Alibava's motherboard is that it implements connectors to read directly the Beetle's output. This way, with an oscilloscope we could see the Beetle signals *live*, both the headers and the 128 channels.

Alibava's output files are written in binary format, however some example functions are available in order to be able to read them with some minor changes. Some capabilities like masking are implemented but disabled, so some work in the code had to be done. Another features like limits in clustering (to avoid clusters with too much or too few charge) were implemented.

Originally the Alibava motherboard was designed to readout 2 Beetles, with I^2C address `0x20` and `0x22`. As we wanted to use a TT hybrid, which has 4 Beetles, some adaptations had to be done. On one hand, a set of two firmwares were developed to address the Beetles with addresses `0x10` and `0x12` or The Beetles `0x14` and `0x16`. On the other hand, a custom made board was designed and manufactured in the USC which allows to send the I^2C signals to the proper Beetle. This feature is implemented with selector switched, as it can be seen in Figure 7.44. The TT hybrid also implements filters for the bias lines which were probed to be indispensable.

Figure 7.42: Hamamatsu sensor's dimensions. Dashed lines are the values written in the technical sheets.

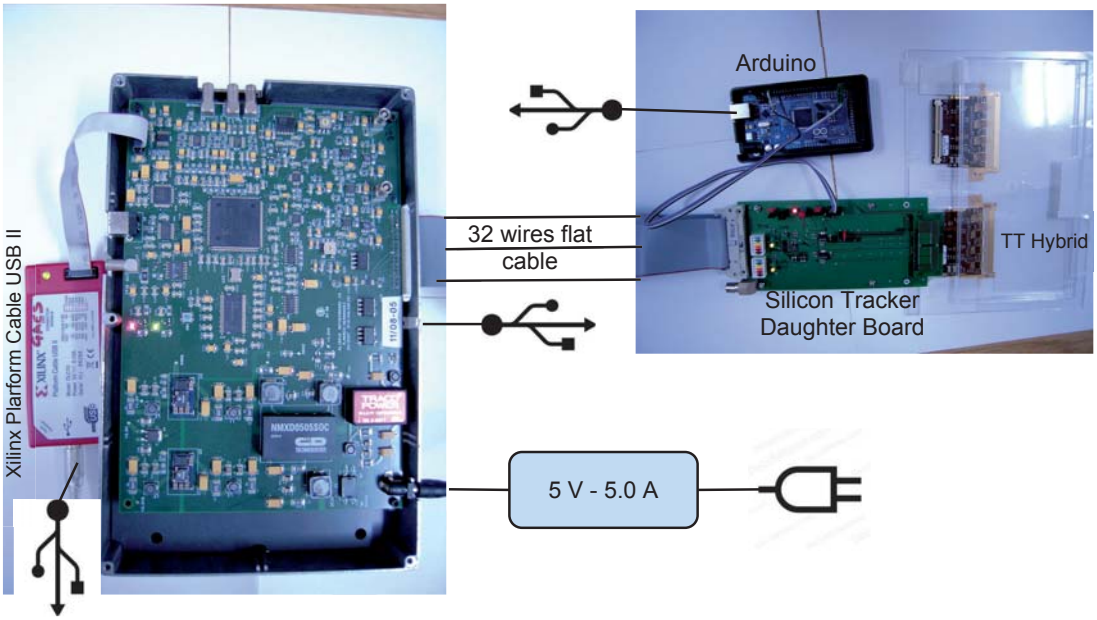

Figure 7.43: From left to right: Xilinx Platform Cable to flash Alibava's firmware; Alivaba's motherboard; adaptor board which allows to choose the pair of Beetles that we want to read; Arduino's board to program the Beetles when necessary; TT hybrid with 4 Beetles, the sensor was wire bonded to this hybrid.

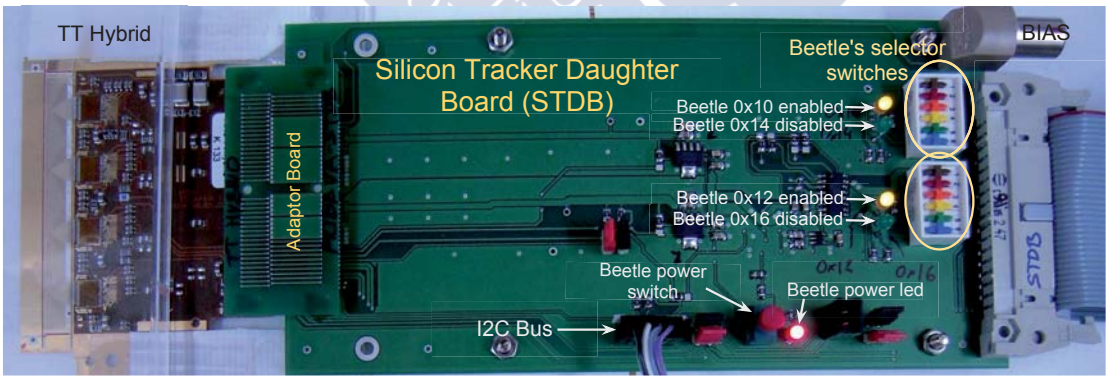

Figure 7.44: Adaptor board built to select the pair of Beetles of the TT hybrid that we want to read. Moving the selector switchers we will select `(0x10 & 0x12)` or `(0x14 & 0x16)`. Two leds will indicate the address selected. I^2C connectors are used by Arduino to program `0x16` when we want to read `(0x10 & 0x12)`.

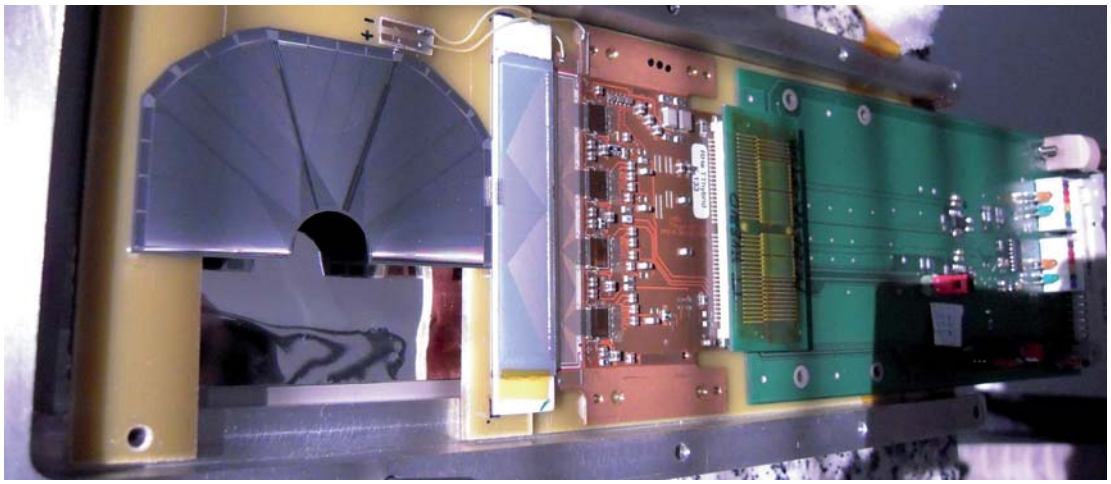

Figure 7.45: Hamamatsu R_6 prototype wire bonded to TT hybrid. Only one Beetle was wire bonded in this case and bonds can be seen in the picture between the sensor and the pitch adapter.

A 200 μm thick, R-type sensor tagged with the ID: R_6 (see Figure 7.45) was wire bonded to a TT hybrid. As the other prototypes, R_6 is a n-on-p sensor, thus the readout signal is negative. The main reason to choose such a sensor was that bonding one side of the sensor we could read a complete set of strips, from the inner to the outer ones.

A new pitch adapter was designed and manufactured with the dimensions required for this sensor. The procedure followed to build the pitch adapter was the same than in 7.2.1, however in this case the equipment capabilities were taken to their limit, resolving lines below 14 μm wide.

Two different sources were used to induce signal in the sensor, laser beam (see Section 7.3.5) and a ^{90}Sr β^- source (see Section 7.3.6). With the β^- source, a single silicon avalanche photo-detector (APD) was placed below the sensor to generate the trigger signal. No coincidence logic was implemented because the majority of the β^- particles are stopped in the photo-detector.

The purpose of the setup is to probe its feasibility and to gain expertise with the Alibava's system which is planned to be used extensively in the future.

7.3.5 Test with Laser beams

Using a laser beam to test sensor properties is a common procedure in instrumentation. In this setup, two laser beams (1060 and 660 nm) were used. The laser was driven by an optical fibre from the source up to a lens which focalize the beam on top of the instrumented strips. The lens was mounted in a square support to guarantee a perpendicular incidence and to keep constant the distance to the sensor surface.

Alibava's system is well suited for laser studies and allows to send a trigger signal to the Beetles and another one to the laser. Also the delay between both

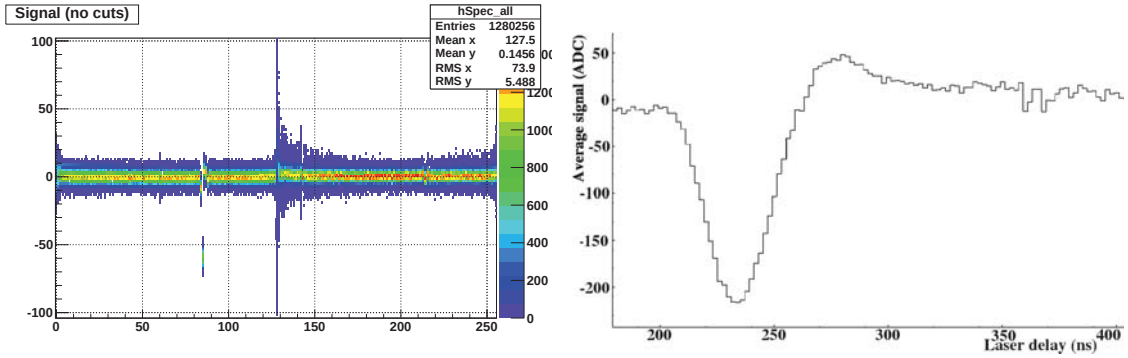

(a) (b)

Figure 7.46: Figure (a) shows the data after pedestal and common mode subtraction. The impinged strip is clearly visible with a signal around -50 ADC counts. Vertical line around strip 128 is due to cross talk. Figure (b) shows the Beetle pulse-shape reconstructed by changing the delay between the laser pulse and the trigger signal.

signals can be configured with Alibava's software. Actually delay scans can be performed automatically obtaining figures like the showed in 7.46. However, several parameters can not be configured with the Alibava software, like the amplitude and the width of the laser trigger. These parameters are very important because they parametrize the laser pulse and the laser intensity. The turnaround followed was to use a pulse generator as intermediate step. Alibava's generated signal was used as input trigger for the pulse generator, and the output was a customized pulse signal. This way we could configure the laser intensity in such a way that the laser beam will impinge one single strip, as it can be seen in Figure 7.46, and it will not saturate the Alibava's ADCs.

When a laser beam crosses a reverse polarized diode, photons generate a certain number of electron-hole pairs depending on its energy. As the laser is monochrome, all the photons has the same energy, thus all the pulses will generate essentially the same amount of charge. In our readout system this will be seen as a narrow signal as the one displayed in Figure 7.47b.

Laser source characterization

The laser pulse is controlled by the input signal, which is generated in a pulse generator and triggered by the Alibava's motherboard. It was decided to keep constant the pulse width to a value of 32 ns. Due to the limitations of the pulse generator it was not possible to get a shorter pulse with a flat top signal

The 660 nm laser was characterized with a *Stellar Line EPP2000* spectrometer, and a *Newport 1835C* optical meter which allow us to get an estimation of the number of photons sent by the laser. The spectrometer shows that the laser wavelength when the laser is biased with a 800 mV signal (Figure 7.48) has its peak

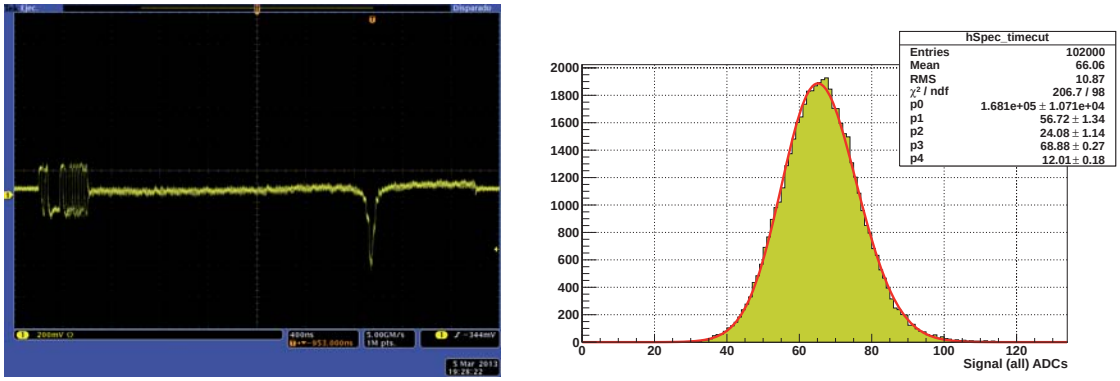

(a) (b)

Figure 7.47: Figure (a) is an oscilloscope screenshoot of the Beetle's signal. The group of peaks at the left belongs to the headers of the communication package, and the narrow peak of the right is the laser induced signal. The recorded Laser spectrum with Lorentzian multiplied by a Gaussian fit is showed in (b).

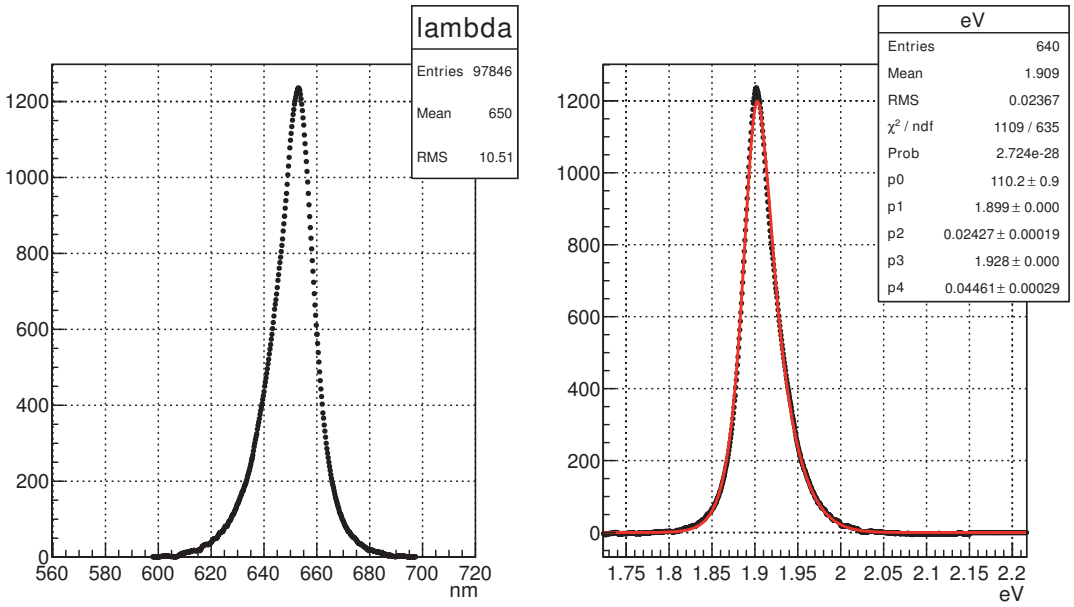

Figure 7.48: Left plot shows the laser spectrum measured by *Stellar Line EPP2000* spectrometer when the laser diode was biased with a 800 mV signal. Right plot is the same data in energy units. Red curve is the Lorentzian with a Gaussian fitting function, where p0 is the scale factor, p1 and p2 are the Lorentzian MPV and sigma, p3 and p4 are the Gaussian MPV and sigma.

in 653 nm, and the FWHM[7] is 15 nm, which represents a spread of ∼2%. This value is coherent with 655 nm, which is the value provided in the laser technical sheet.

The measured power of the laser is shown in Figure 7.49 and it clearly shows the two regions where the laser can work. The region where the applied voltage is lower than 1300 mV is called *spontaneous emission region*, or LED zone. In this region, emitted photons are not coherent but the beam is quite monochrome as it was confirmed with the spectrometer. Above 1300 mV, the diode starts working in the *stimulated emission region*, or laser zone. Here the emitted photons are coherent and collimated and the power is much higher than in the LED zone. For that reason is necessary to use splitters to reduce the laser power, otherwise the readout electronics will saturate.

During the measurements with laser pulses, most of the data were taken with the laser working in the LED zone, that means that the beam was not coherent. For our purposes that was not a problem, and this way we can avoid to use splitters.

A detailed exposition of the different studies carried out with both laser beams is detailed below. In this particular case, no resolution studies were carried out because it was not feasible to install the laser fibre in a linear stage.

S/N ratio with Laser beams

Laser amplitude scan When the laser diode is working in spontaneous emission zone, it behaves like a LED and its output power is linearly proportional to drive current. In a diode, drive current grows exponentially with the applied voltage:

$$I_o = I_s \cdot \left(e^{\frac{eV}{kT}} - 1\right)$$

We could confirm experimentally that the power of the laser grows exponentially with the applied voltage in the LED zone. Figure 7.49 shows the 660 nm laser power measured with a *Newport 1835C* optical meter. Unfortunately, the optical meter was not calibrated, so the Y-axis absolute values should not be taken in consideration. The same exponential relationship between the laser bias voltage and the readout signal in the Hamamatsu R_6 sensor was obtained (Figure 7.49). In this case the laser power, i.e. the number of photons sent per second, is proportional to the signal recorded.

Strip position scan

As it was already mentioned, R_6 prototype has a pitch between strips which varies continuously from 30 μm to 106 μm, therefore it was reasonable to investigate if the variable pitch has some measurable impact in the recorded signal.

To perform such study the laser lens was manually moved upon the aluminium foil which protects the sensor. A small window was opened in the aluminium to

[7] **F**ull **W**ith at **H**alf **M**aximum.

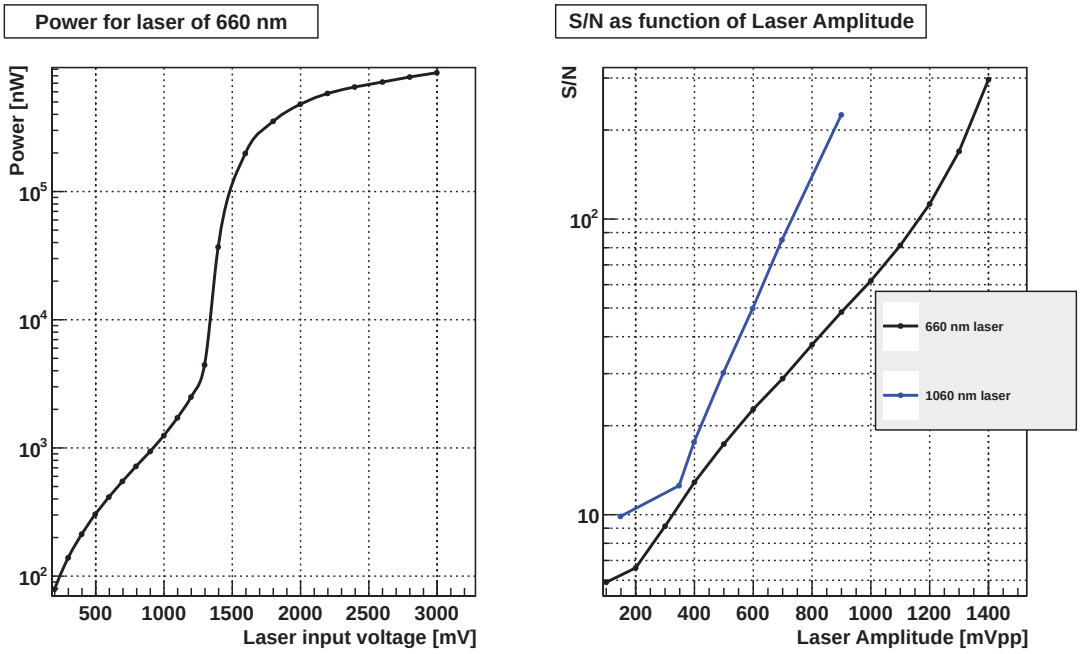

Figure 7.49: Left plot corresponds to the power for 660 nm laser measured with a Newport 1835C optical multimeter. Right plot shows the signal over noise value measured with the Hamamatsu R_6 sensor when the laser is working in the LED zone. In both cases, the relationship is exponential and they can be fitted to a straight line when they are represented in logarithmic scale.

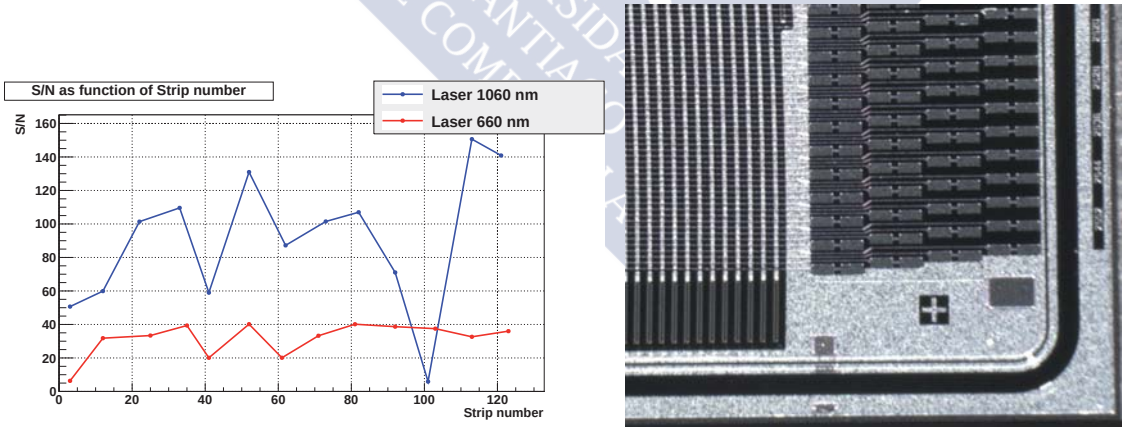

(a) (b)

Figure 7.50: Figure (a) shows the recorded signal as function of the strip number with two different laser beams. The discrepancy of the data can be explained by reflections in the metallization lines (b). These reflections can not be controlled with the current setup.

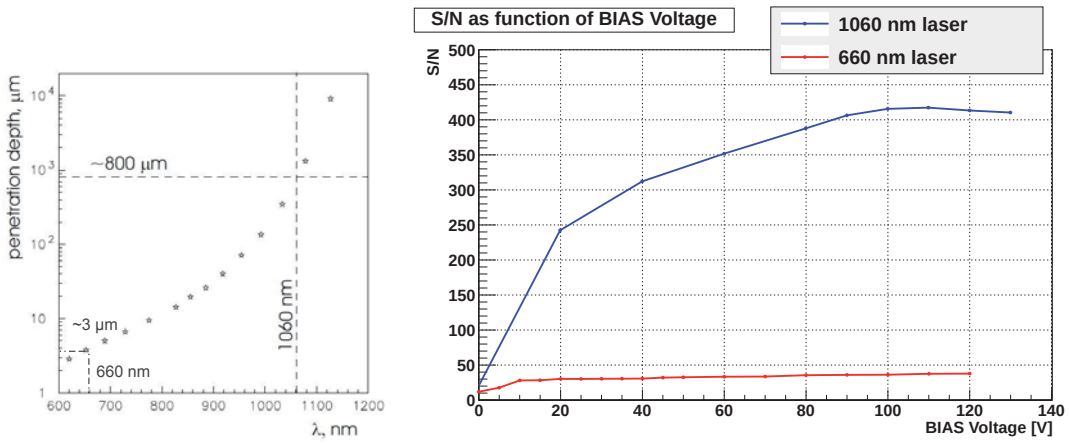

(a) (b)

Figure 7.51: Figure (a) shows the penetration depth for both lasers used. The 660 nm laser will be absorbed in the first microns of the sensor. Figure (b) shows the signal induced in sensor as function of the laser input voltage

allow the laser to hit the instrumented strips, without any noticeable impact in the electromagnetic noise isolation capabilities (Faraday box). With the help of an oscilloscope, the lens was moved until the laser beam hits one single strip. When such situation is achieved, the oscilloscope's display looks like Figure 7.47a.

Two scans were carried out, one with each laser, and the results are shown in Figure 7.50a. It is immediate to notice the huge discrepancy in the data which is not possible to explain attending to strip properties like the pitch. One possible explanation is the reflections of the laser beam in the two metallization lines and in the backplane. Two levels of metallization lines can be seen in Figure 7.50b, horizontal thin lines coming from the readout pads are the routing lines, while the strips are the vertical lines. This picture was selected because both lines are clearly recognizable, but along the sensor the angle between both can take any value from 0 to 90º.

Therefore, no conclusion about the S/N ratio dependence with the strip pitch can be taken with this setup. For future setups, is encourage the use of linear stages to move in a controlled way the sensor or the laser lens, so the reflections in the metallized lines could be avoided.

Sensor bias scan with laser source

BIAS scan is a very interesting test because it provides information about the full depletion voltage, which was introduced in 6.1.5, but summarizing we can say that a sensor is basically a collection of p-n junctions and at the full depletion voltage the sensor is free of mobile carriers. It is a very important parameter because it defines the voltage at which the sensor must be operated (typically the operational voltage is +40 V above the full depletion voltage). When the sensor is fully depleted, the electron-hole pairs generated by a ionizing radiation will not

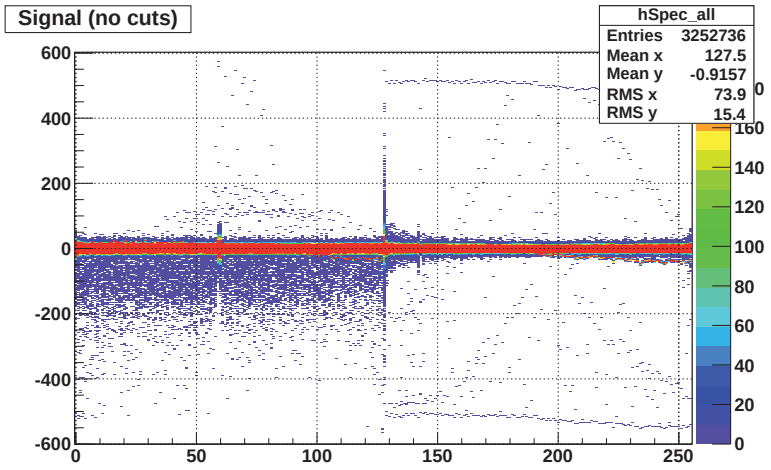

Figure 7.52: The plot shows the recorded raw data of the R_6 prototype. Only first 128 channels are instrumented, and channels 59 and 60 were masked for analysis purposes because they proved to be very noise. It can be seen the cross talk effect in channels 129 and 130.

suffer recombination with the mobile carriers, and they will move towards both sides of the sensor due to the applied electrical field. That diffusion movement takes a few nanoseconds and it will induce a signal in the readout strips of pixels.

In High Energy Physics, usually the ionizing radiation consists in relativistic (or highly energetic) charged particles, but we can obtain also compatible measurements when we use a laser beam. As in the case of charged particles, the probability of passing through the sensor depends on the beam energy, which in the laser beam case means that it depends on the laser frequency. Figure 7.51a shows the penetration depth as function of the photon's energy. The penetration depth is defined as the depth at which the beam intensity is equal to 1/e of the original (about 37%), and it can be seen that a 660 nm laser will be fully absorbed in the first ten microns, while the 1060 nm laser beam will pass through the sensor.

The relationship of the penetration depth with the laser frequency is relevant when we perform a bias scan of the sensor, because while we rise the applied bias voltage the depletion zone of the sensor will increase (Section 6.1.5). As a consequence, the full depletion voltage can be only measured with the 1060 nm laser, as the response of the sensor to the bias voltage with the 600 nm laser will be constant once the depletion zone reach the first 10 microns.

The analysis results are shown in Figure 7.51b and from these plots it can be concluded that at -10 V the first $\sim$ 10 μm are depleted, and the full depletion voltage is achieved at -100 V, which is consistent with the value obtained during the electrical characterization with the CV curve.

Figure 7.53: Setup used to measure the signal deposited by β^- particles from ^{90}Sr source. The source was placed over the window opened in the Faraday box which surrounds the sensor (in the picture the window is covered with a plastic plate for safety). The scintillator is placed below the sensor, and in between there is the aluminium foil from the Faraday box.

7.3.6 Test with ^{90}Sr source

The prototype was characterized also with a β^- source. ^{90}Sr was chosen because is an almost pure β^- source, with relatively low levels of gamma emission. The ^{90}Sr decays to ^{90}Y emitting a β^- with an end-point energy of 0.546 MeV and the ^{90}Y decays to ^{90}Zr (which is stable) emitting a β^- with an end-point energy of 2.28 MeV.

Figure 7.52 shows the raw data recorded by the R_6 prototype. As it was already mentioned, the sensor is n-on-p type and when is reverse biased the electrons will move towards the strips, giving a readout signal with negative sign. It can be seen that the signal is homogeneously distributed trough the 128 instrumented strips. The noisy strips, like the 59 and 60, were masked offline before the analysis.

Experimental Setup

The setup used to test the HPK R_6 prototype is showed in Figure 7.53. The ^{90}Sr source was placed on top of the window opened on the Faraday box, and aligned with the instrumented strips and the scintillator in order to obtain the maximum trigger rate. To build the trigger system, an APD scintillator was used to generate the primary trigger signal. The signal coming out from the APD is a pulse of 100 mV and 4 ns wide. The second step was to use a LeCroy 623A discriminator, in order to get a valid NIM-level signal which can be accepted

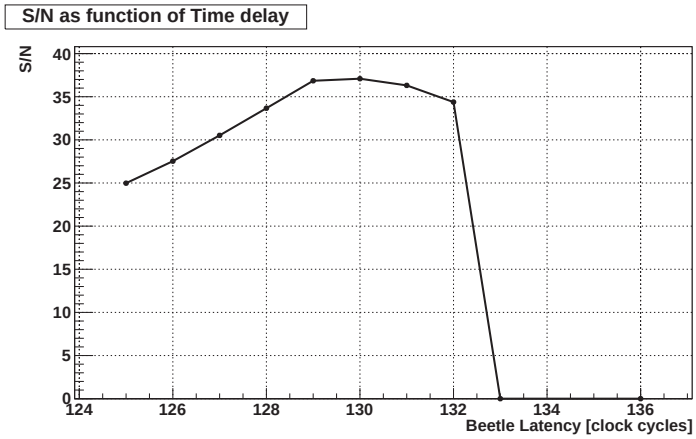

Figure 7.54: MPV cluster charge as a function of the latency parameter. That parameter compensates the propagation time of the trigger through the cables, and using this plot it was decided to use a latency value of 129.

by the Alibava motherboard. The generated NIM signal is a square pulse with an amplitude of 800 mV and 166 ns wide. The parameters of the signals were measured with a Tektronix MSO4104 oscilloscope.

The activity of the ^{90}Sr source was measured in 2001 giving a value of 0.38 kBq. The area of the source, the instrumented strips and the active area of the scintillator were all around 1 cm^2, obtaining a maximum trigger rate of 4.2 Hz.

Coarse delay: propagation signal delay

The Beetle chip was designed for the LHCb experiment and implements some features which are characteristic of the LHC beam, like the 40 MHz bunch crossing rate. That rate is fixed and it is provided by a common LHCb clock. Therefore the Beetle chip samples the signal each 25 ns and then the analog charge is stored in a 160 position pipeline. The L0 trigger signal arrives several clock cycles after the particle, but that latency is always the same and depends on the propagation time through the cables from the L0 electronics to the Beetle. The latency value is thus a parameter that must be configured for each Beetle. In our setup, in order to know which is the correct latency value, a scan around the central value was done and the results are showed in Figure 7.54. The Beetle was configured in such a way that the amplifier discharge will last several clock cycles, and that was achieved by setting the Vfs parameter to 1.96 V. More information about Beetle parameters can be found in [50]. The chosen latency value was 129 because is the value at which the MPV of the cluster has a greater S/N ratio.

Fine delay: asynchronous-synchronous trigger

Each Beetle accepts a 40 MHz synchronous trigger and to optimize the readout signal an independent fine delay is implemented for each one. When the trigger signal is intrinsically asynchronous, like in a test-beam or with a β^- source,

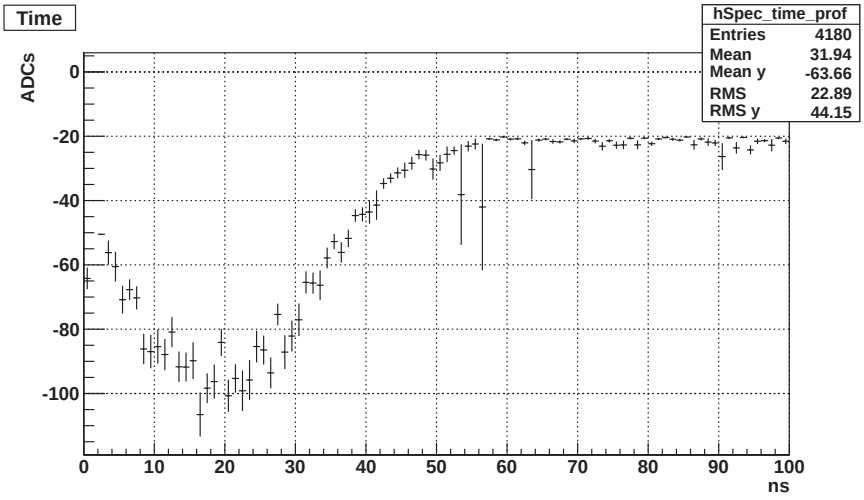

Figure 7.55: Mean cluster energy as function of the delay between the particle arrival and the Beetle sampling time

the Beetle delay has no meaning, and the generated signals are unequally amplified. The only way to solve this problem is to make an offline selection and use only these triggers which are quasi-synchronized with the Beetle sampling. The synchronous triggers can be determined by plotting the readout signal as a function of the delay between the synchronous and asynchronous triggers. Figure 7.55 shows that relationship. It was decided to use all the triggers with a delay between 12 and 24 ns with respect to the synchronous trigger.

BIAS scan with ^{90}Sr source

As well as it was done with the Laser setup, is interesting to measure the full depletion voltage of the sensor with β^- source. In order to reduce the time needed for each run, the Beetle chip was configured in such a way that the time needed to discharge the amplifier reaches ~ 0.5 μs. As the rate of triggers is 4 Hz, the overlap probability between two consecutive triggers is very low. The advantage of this configuration is that all the triggers are valid and the time needed for each run can be reduced in a factor 6. On the other hand, the S/N ratio obtained should not be compared with test-beam results because in the second case the Beetle parameters must be the same than in the VELO.

Up to 10 runs were taken with the ^{90}Sr source at different bias voltages, and the results are plotted in Figure 7.56. The behaviour is the expected, the signal rise when the bias voltage is increased, as the depletion zone is bigger and the number of electrons which are not recombined grows. When the full depletion voltage is achieved, around -100 V, the signal remains constant. This value is consistent with the FDV obtained from the IV-CV curves which were described in 7.3.2 and the one obtained with the laser beam.

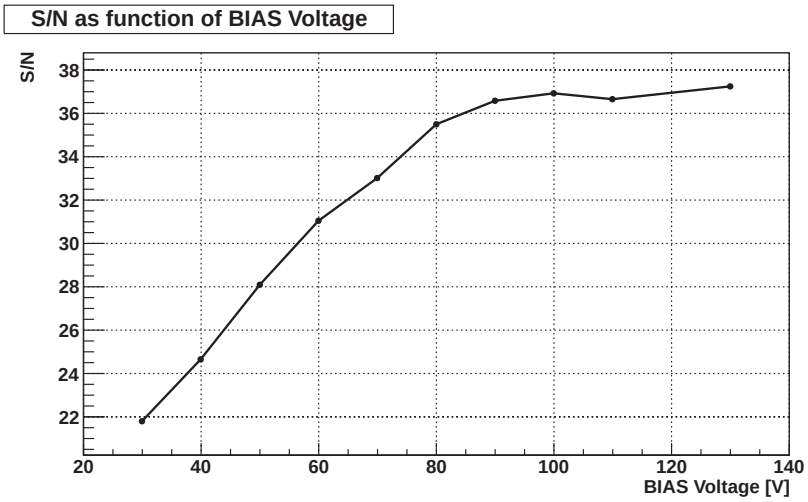

Figure 7.56: S/N ratio as function of the bias applied to the sensor. It can be seen that above 100 V the S/N ratio remains approximately constant.

S/N ratio with ^{90}Sr source

The signal-noise (S/N) ratio is a crucial parameter for a detector, and it depends not only of the sensor, but also on the readout chain. The signal value that we can obtain with the ^{90}Sr source is similar to a MIP, so is reasonable to foreseen similar values in future test-beams.

The S/N ratio was obtained from the triggers which passed the fine delay cut, in this particular case, all the triggers inside a window of ± 6 ns around the peak of the Figure 7.55. That means that we are discarding $\sim 90\%$ of the triggers, for instance it took 5 hours to obtain 2700 events which passed the fine delay cut. The value of the signal is the MPV of the ADC spectrum readout by the sensor, once is fitted to a Landau convoluted with a Gaussian function. The signal value has also a direct relationship with the Beetle parameters, as they define the amplification of the signal. The parameters used to calculate the signal are very similar to the ones used currently in the VELO, and they are listed in Table 7.9. To calculate the noise value, the strips with a noise value above 2.6 ADC counts were excluded, and the rest of the values were fitted to a Gaussian function. Both fitting functions are plotted in Figure 7.57 resulting in a S/N ratio of 33.

S/N dependence with strip length

The noise of a micro-strip sensor is a critical parameter, and it depends on many factors like the strip capacitance or the electronics. The electronic noise is common for all the strips of the sensor, but this is not the case of the strip capacitance as it depends of the strip and routing line lengths. In the R-type prototype, the inner strips are shorter, but their routing lines are longer. It is not clear to see if both contributions are compensated, keeping the noise constant for all the strips. Furthermore, as the pitch also varies all along the sensor, the signal readout in

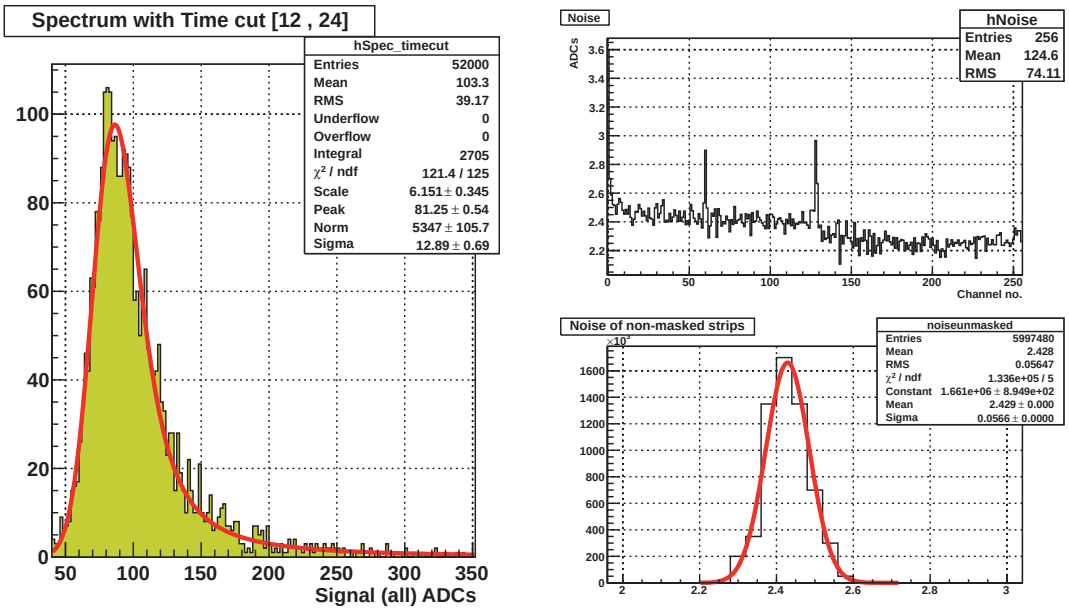

Figure 7.57: ^{90}Sr spectrum measured with the Hamamatsu R_6 sensor bonded to a TT Hybrid. The S/N ratio is the ratio between the most probably value of the signal and the average noise, giving a value of 33.

Parameter	Beetle Setting	Step	Value
CompCtrl	9	-	-
Ibuf	10	7.8 μA	78 μA
Icurrbuf	114	7.8 μA	889 μA
Ipipe	13	7.8 μA	101 μA
Ipre	75	7.8 μA	585 μA
Isf	29	7.8 μA	226 μA
Isha	10	7.8 μA	78 μA
Itp	0	7.8 μA	0 μA
Ivoltbuf	20	7.8 μA	156 μA
Latency	130	25 ns	3250 ns
ROCtrl	26	-	-
RclkDiv	0	-	-
Vd	130	9.8 mV	1274 mV
Vdcl	105	9.8 mV	1029 mV
Vfp	15	9.8 mV	147 mV
Vfs	71	9.8 mV	696 mV
Vrc	0	9.8 mV	0 mV

Table 7.9: Beetle parameters used to obtain the S/N ratio of the R_6 prototype with ^{90}Sr source.

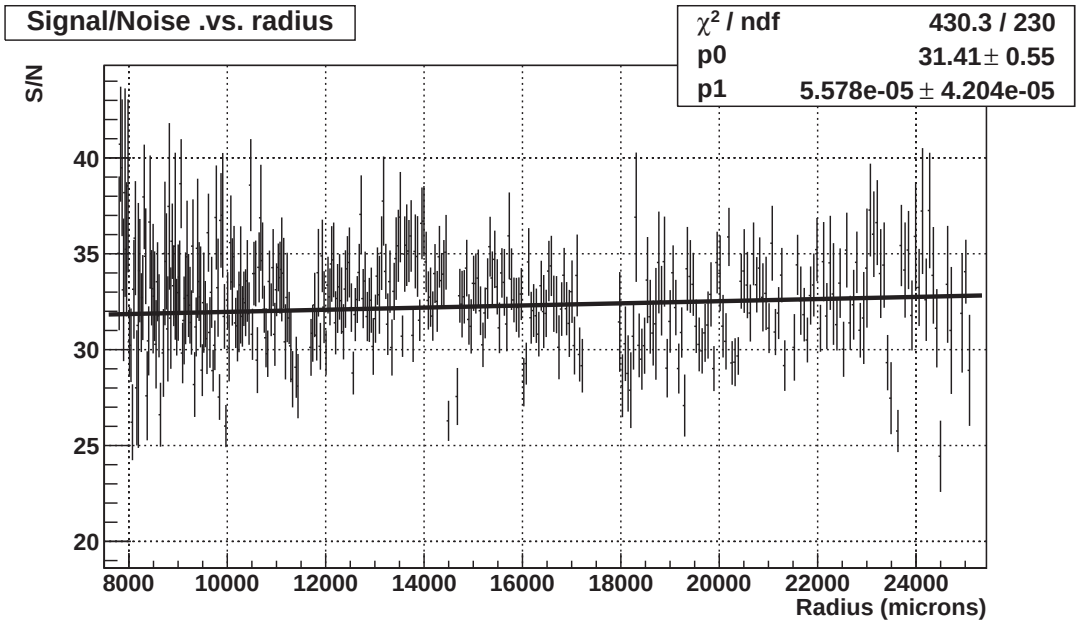

Figure 7.58: S/N ratio as function of the strip radius, with a linear fit. Note that the slope (p1) is compatible with 0 as is of the same order than the error.

each strip can also be different. For these reasons, is important to plot the S/N ratio as function of the strip radius in order to characterize the sensor response. Figure 7.58 shows how the S/N ratio remains quite stable through the sensor, so it can be concluded that the R-type prototype has an homogeneous response to ionizing particles.

8

Pixel Detectors

Pixel technology is one of the two options for the upgraded VELO. The pixel option is based on a new radiation hard ASIC dubbed VeloPix, from the Medipix/Timepix family, bump bonded onto a n^+-on-p or n^+-on-n sensor. The VeloPix, as well as the Medipix and Timepix ASICs, has a matrix of 256×256 pixels of 55×55 μm. As part of the VELO upgrade program, several Medipix3 and Timepix devices were tested in test-beam. In this chapter, an introduction to the pixel proposal and the Medipix/Timepix chips is given, together with the results of one Timepix and two irradiated Medipix3 devices which were tested in the test-beam of 120 GeV/c pions at the CERN SPS facility.

Most of the Medipix and Timepix information is taken from [58].

8.1 The VeloPix option for the VELO upgrade

As it was already said in Section 5.2.2, the vertex detector for the LHCb upgrade must cope with a very demanding list of requirements in terms of radiation hard, occupancy and specially data rate. One of the proposals is to replace the current micro-strip solution with pixel sensors.

The Medipix collaboration is developing an ASIC that will meet the requirements of the VELO upgrade. The proposed chip, named VeloPix, is based on the TimePix3 chip which, in itself, is based on the MediPix2 chip. VeloPix is a hybrid pixel detector, where the sensor and the ASIC are manufactured independently and bump bonded at the end of the fabrication process. The disadvantage of the hybrid sensors are the additional bump bonding step and the total thickness of the device. On the other hand, they allow to test a wide range

Pixel array	256 × 256
Pixel size	55 μm × 55μm
Min. threshold	$\sim$ 500 e^-
Peaking time	$<$ 25 ns
Time walk	$<$ 25 ns
Measurements	ToA & ToT
Count rate	500 Mhit/s/chip
Readout	Continuous, sparse, on-chip clustering
Output bandwidth	$>$ 12 Gbit/s
Power consumption	$<$ 3 W/chip
Radiation hardness	$>$ 500 MRad, SEU tolerant

Table 8.1: Main VeloPix features

of sensor parameters like doping, thickness, guard-rings designs, distance to edge or radiation tolerance. Even more important, in hybrid pixel devices the ASIC is made on a low resistive silicon wafer, while the sensor uses highly resistive silicon. Low resistive wafers are the same than for commercial silicon chips, allowing to use mature techniques achieving a higher integration level and a greater number of vendors is available. The contrary happens in the monolithic devices, where the sensor and the ASIC are integrated on the same silicon substrate. Nowadays only simple circuitry can be implemented in monolithic devices, and this will not be enough to cope with the requirements of the VELO upgrade. The main characteristics of the VeloPix ASIC are presented in Table 8.1, while MediPix2 and TimePix3 are introduced in Section 8.2.

8.2 The Medipix/Timepix family

8.2.1 The Medipix collaboration: historical approach

Hybrid pixel detectors are excellent devices in tracking systems especially in high multiplicity environments where excellent spatial resolution is combined with extremely high signal to noise ratio. The Medipix collaboration was formed in 2002 to exploit the knowledge gained in the design and fabrication of hybrid pixel detectors to make a single photon counting system for X-ray radiography, thus it was an ASIC designed for a medical applications. The Medipix1 was a hybrid photon counting pixel detector with a 64 × 64 square pixels with 2 metal layers, and the dimensions of each cell were 170 μm × 170 μm. This chip had two working modes, in *acquisition mode* each pixel has a shift register counter with a dynamic range of 8001 counts, so basically each hit in the sensor above a certain threshold is converted into a count. In *read mode* the data was shifted from pixel to pixel towards the readout electronics placed at the periphery. The working modes were defined by a bit called *Shutter*, so the device was in acquisition mode when the

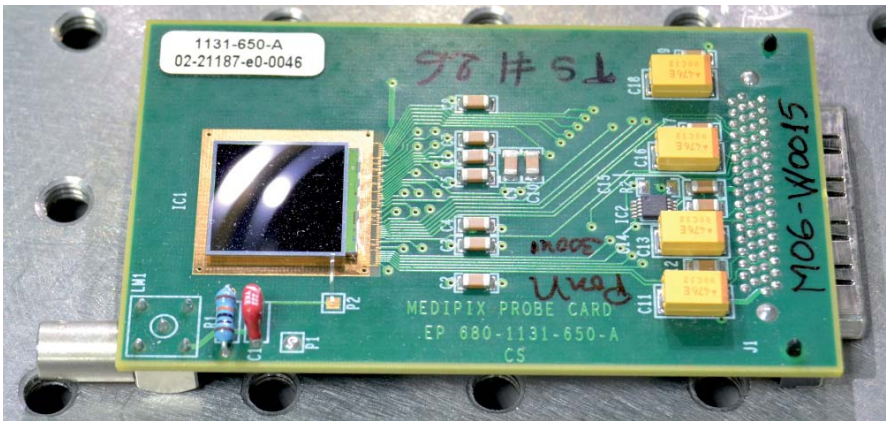

Figure 8.1: Timepix device with a square window open in the backplane metallization to allow laser injection tests.

shutter was low and in read mode when the *shutter* was high.

Medipix2 was completely redesigned at CERN from the Medipix1 chip, and introduced the pixel matrix of 256×256 with cells of 55×55 μm^2. It is designed in a commercial 0.25 μm CMOS technology while the Medipix1 was designed in the SACMOS 1 μm process.

Another improvements are a front end sensitive to both polarities, a fast readout and a layout where the last pixel is as close as possible to the edge of the chip in order to minimize dead areas and allowing tiling. The Medipix2 suffered a redesign (Mpix2MXR20) to bring more functionality and robustness to the chip, specially to become a radiation hard chip.

8.2.2 The Timepix chip

Following the successful results of the Medipix2 and Mpix2MXR20, a new collaboration was formed to provide arrival time information in each pixel with a time resolution of 10 ns. This new chip was called Timepix (Figure 8.1), and it could be presented as an evolution of the Mpix2MXR20. In the Timepix chip each pixel can be configured independently in three different operation modes:

Time of Arrival (ToA): when the amplified signal in a given pixel is above a certain (and individually adjusted) threshold, a shift registers start to count clock cycles until the shutter changes from acquisition to read mode or until the counter reach 11810 counts which is the limit of the dynamic range of the 14-bit counter. Thus the data stored in the pixel give us a time-stamp information of the particle in clock cycle units. A sketch of the ToA mode can be found in Figure 8.2a.

Time over Threshold (ToT): while the amplified signal remains above the defined threshold, the shift register counts clock cycles. The data is stored and read out at the end of the shutter period and is proportional to the amplitude of the signal, and consequently to the deposited charge. The

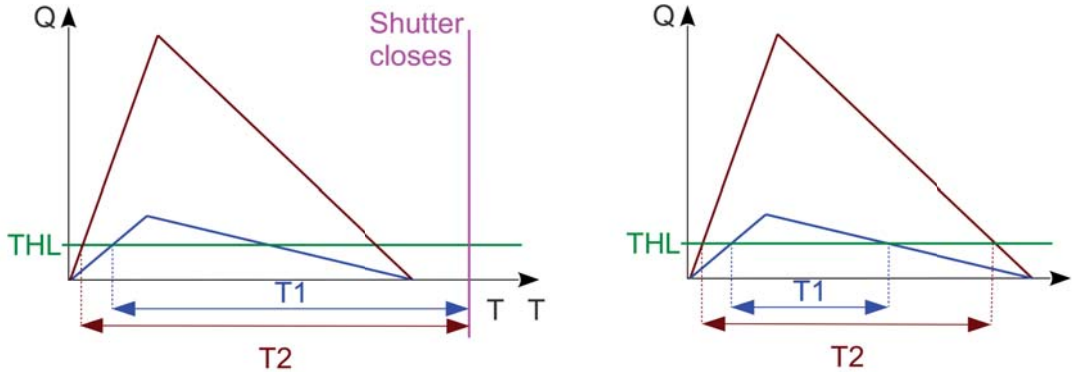

(a) Time of Arrival (b) Time over Threshold

Figure 8.2: The time of arrival mode will give us information of the time-stamp of the particle, while the time over threshold will tell us the amount of deposited charge in the sensor.

threshold parameter determines the height of the threshold, and therefore the width of the pulse. A typical threshold is about 50 ADC ($\approx 1250e^-$) above the noise mean. The ToT range is 14 bits or 11810 counts and the resolution is determined by the frequency of the counting clock, which can be up to 100 MHz. The ToT mode is sketched in Figure 8.2b.

Medipix mode: the shift register simply counts the number of times that the amplified signal passes the threshold. It is the same acquisition mode than in the Medipix chip, hence its name.

8.2.3 The MediPix3

The Medipix3 [85] chip is built in 0.13 μm CMOS technology. It has been built in a 8-metal layer and introduces a new inter-pixel architecture, which aims to improve the energy resolution by mitigating the effects of charge sharing between channels. Charges are summed in all 2×2 pixel clusters on the chip and a given hit is allocated locally to the pixel with the biggest total charge. This is a way of maintaining the 55 μm spatial resolution, while eliminating the spectral distortion due to charge diffusion in the sensor. The chip allows to choose whether pixels use charge summing or not. In the single pixel mode each pixel works in photon counting mode independently of its neighbour while in the charge summing mode the summing circuits and arbitration logic are used. Also, its design is expected to be more radiation hard that its predecessor Medipix2.

At the hardware level the Medipix3 allows also dicing variations depending of the requirements. The periphery of the chip at the top of the pixel matrix contains only power pads, but in systems which require 3-side buttable chips this top periphery can be diced off (B line in Figure 8.3a).

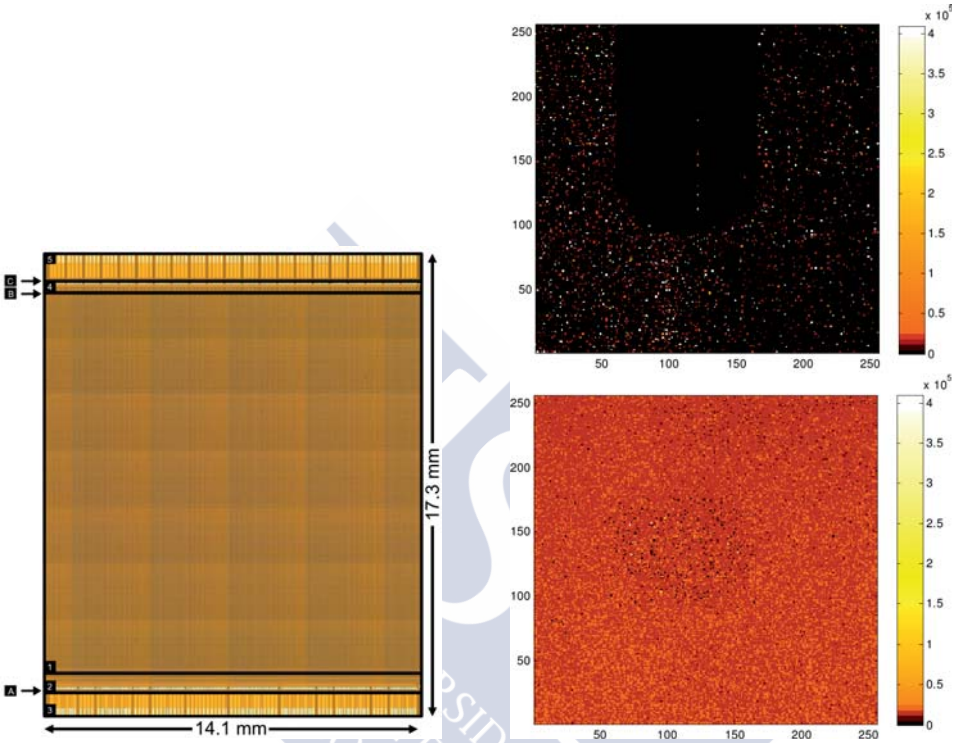

(a) Medipix3 chip

(b) Medipix3 chip 25 days after being irradiated

Figure 8.3: In Figure 8.3a can be appreciated (1) 256×256 Pixel matrix, (2) chip periphery and TSV, (3) bottom wire-bonding extension, (4) top TSV power pads and (5) wire-bonding extensions. A, B and C shows the different in-chip dicing options. In Figure 8.3b shows a recovery of the individual pixels. Top figure corresponds to the detector efficiency the same day of the irradiation and bottom one after 25 days. Both pictures are presented in [84]

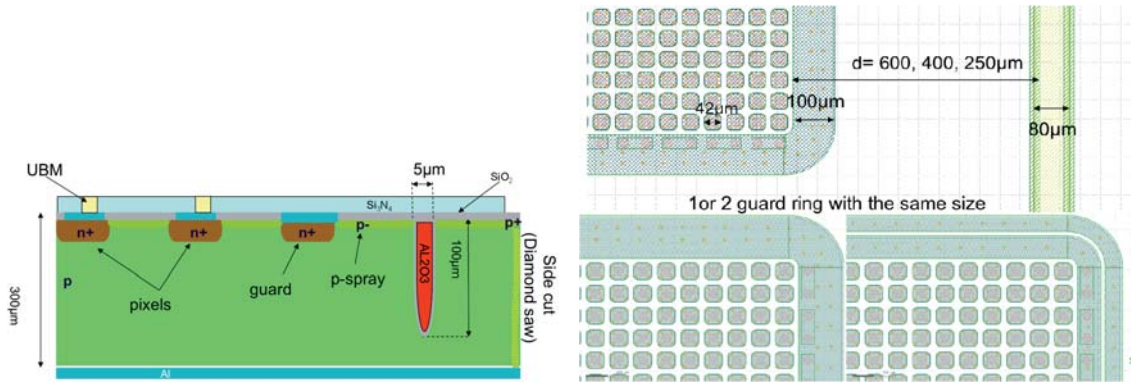

(a) Implant layout (b) Design parameters

Figure 8.4: Figure 8.4a shows the implant layout of the sensors manufactured at CNM. Several sensors were manufactured with different Pixel-To-Edge and guard rings designs, as is showed in Figure 8.4b

Another important feature of the chip is that the data acquisition and readout can be performed either sequentially or continuously. In the sequential acquisition mode, each discriminator output increments one counter. There are therefore two thresholds and two binary counters per pixel. In continuous count-read mode, only the low level threshold discriminator output increments one counter, while the other is being read out. Unfortunately a race condition has been found in the transitions between counting and reading out from the pixel counters 8.3a. This race condition prevents the continuous count-read mode to perform as designed.

The Medipix3 has been proven to be radiation hard [84] when the device was irradiated with 15 keV photons with a resulting dose rate of 13.8 kGy/s and a total dose of 1.8 MGy. After the detector irradiation and the recovery time (25 days), the detector linearity was identical to that shown by the detector before irradiation.

8.3 Sensors

It was already mentioned than operational parameters like the primary vertex resolution are quickly degraded by scattering process, thus to minimize the material in the acceptance of the experiment is a golden rule that must be pushed to the limit. As the pixel detectors shows a much better signal to noise ratio, the sensor can be thinner than in micro-strips sensors. One of the test-beam program goals was to determine the minimum sensor thickness which can be instrumented by a Timepix/Medipix ASIC while keeping the resolution and efficiency values. Two main vendors (VTT and CNM) supplied sensors for the test-beam program, with thickness of 100, 150, 200 and 300 μm.

Guard ring is also a key element in sensor design because of several reasons:

- The number of guard rings, and their placement, has a fundamental impact in the behaviour of the electrical fields inside the sensor when is depleted. As the sensors will be highly irradiated, the depletion voltage must be increased with time and guard rings have a key role avoiding a degradation in the behaviour of the sensor.

- The trigger algorithms of LHCb rely on an impact parameter cut, hence the impact parameter resolution is an excellent benchmark performance number for the detector. The presence of the r_1^2 term in the impact parameter resolution equation[1] indicates that the first measured point should be as close to the interaction point as possible, which is achieved by designing the minimum possible inner dimensions by reducing the size of the guard rings.

- The guard rings area is non sensitive, thus to avoid dead zones the devices must be overlapped, with the consequent increase in material.

These reasons, among others like the distance from the last pixel to the sensor edge, made that the impact of the number and design of the guard rings can not be fully predicted. Several combinations of the number of guard rings (1 or 2), distance to edge (50, 100, 250, 400 and 600 μm) and irradiations (0 or 2.5×10^{15} n_{eq}/cm^2) were tested. These parameters are showed over a mask designed by CNM in Figure 8.4.

In this work three different devices manufactured at CNM facility in Barcelona are analysed, one Timepix and two Medipix3. The main characteristics of the three devices are presented in Table 8.2.

8.4 Electrical characterization

The IV curves of the analysed pixel devices are shown in Figure 8.5. Unlike the sensors showed in previous chapters, these were characterized at CERN by Heinrich Schindler. Note that for W20_D6 (Medipix3), several curves are shown to indicate the temperature and the annealing dependence. These curves indicate that the behaviour of the irradiated Medipix W20_F6 is much worse than W20_-D6, as the leakage currents are always higher even when the W20_F6 sensor is cooled at -11 °C and W20_D6 is at room temperature.

[1] The impact parameter resolution is well described to first order by the following expression:

$$\sigma_{IP}^2 = \frac{r_1^2}{p_T^2\sqrt{2}}\left(0.0136\sqrt{\frac{x}{X_0}}\left(1+0.038\,\ln\left(\frac{x}{X_0}\right)\right)\right)^2 + \frac{\Delta_{02}^2\sigma_1^2+\Delta_{01}^2\sigma_2^2}{\Delta_{12}^2} \quad (8.1)$$

Where r_1 is the radius of the first measured point, p_T is the transverse momentum of the track, x/X_0 is the fractional radiation length before the second measured point, which includes the foil, any dead area of silicon traversed, and the material of the first measured point, σ_1 and σ_2 are the measurement errors on the first and second point respectively, and Δ_{ij} represents the distance between i and j, where i and j can be 0 (the interaction region), 1 (the first measured point), or 2 (the second measured point).

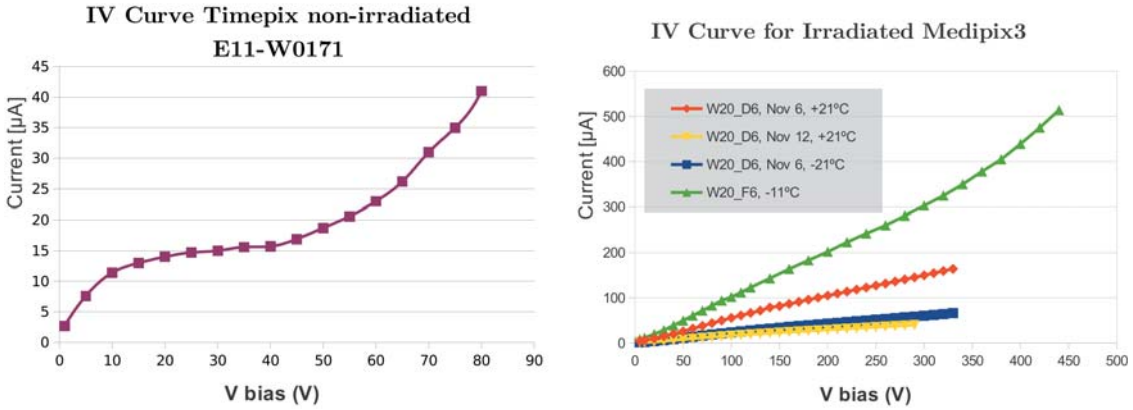

(a) E11_W0171 IV Curve

(b) W20_D6 and W20_F6 IV curves

Figure 8.5: Figure 8.5a corresponds to the IV curve for Timepix E11_W0171 device at room temperature ($\simeq$ +23ºC). Figure 8.5b is the IV curves for irradiated Medipix3 W20_D6 and W20_F6 at low temperature.

The IV curve is an early indicator that tell us that W20_F6 has severe damage. Unfortunately the sensors were not characterized before irradiation, so it can not be said for sure that the radiation damage is the only responsible of the W20_F6 behaviour.

8.5 2012 Test-beam Setup

The 2012 test-beam setup was basically the same than in 2011, with the only difference of the sensors in the telescope planes. In this work, three different n^+-on-p DUTs are analysed: one n^+-on-p, non-irradiated Timepix and two n^+-on-p, irradiated Medipix3. Table 8.3 shows the telescope's planes and their relative positions.

The main purpose of the test-beam was to measure the efficiency of a Medipix3 device after irradiation levels around the expected in the VELO upgrade after 5 years of operation. A comparison between the two Medipix3 devices provides information about the impact of the distance to edge parameter (Figure 8.6).

The Timepix device could be used as a reference for the non-irradiated situation as its sensor is the same than one of the Medipix3. A bias and an angle scans were taken for the Timepix device, and the meaningful values are showed in Appendix A, Table A.3. To characterize the behaviour of the irradiated Medipix3 chips, threshold scans were carried out as shows Table A.4 and Table A.5. The poor signal obtained of the W20_F6 device indicates, as the IV curve did, that this device shows worse performance than W20_D6.

ID	ASIC	Sensor Thickness	Distance to Edge	Fluence
E11_W0171	Timepix	200 μm	400 μm	None
W20_D6	Medipix3	200 μm	400 μm	2.5×10^{15} n_{eq}/cm^2
W20_F6	Medipix3	200 μm	250 μm	2.5×10^{15} n_{eq}/cm^2

Table 8.2: Main characteristics of the DUTs analysed. All the devices were produced by CNM with a n^+-on-p doping and 2 guard rings.

Device	Position	Mode
C09-W0108	0	ToT
C10-W0108	23	ToT
J08-W0087	46	ToT
F11-W0108	69	ToT
E11-W0171	263	DUT
D09-W0108	461	ToT
H03-W0092	484	ToT
G08-W0087	507	ToT
J03-W0089	530	ToT

(a) E11_W0171

Device	Position	Mode
C09-W0108	0	ToT
C10-W0108	26	ToT
J08-W0087	46	ToT
F11-W0108	69	ToT
DUT	181	
D09-W0108	293	ToT
H03-W0092	319	ToT
G08-W0087	344	ToT
J03-W0089	369	ToT
I10-W0108	415	ToT

(b) W20_D6 and W20_F6

Table 8.3: Telescope planes

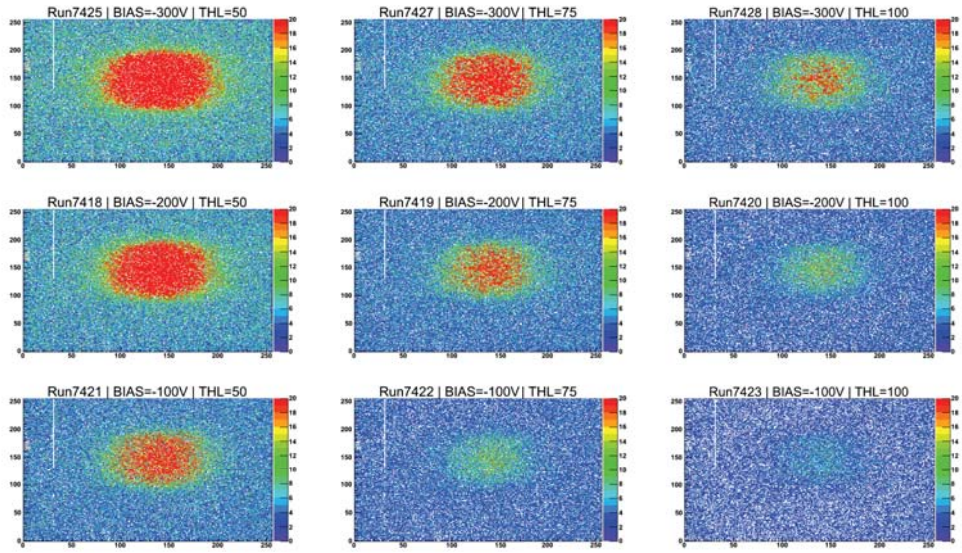

(a) W20_D6 Raw data

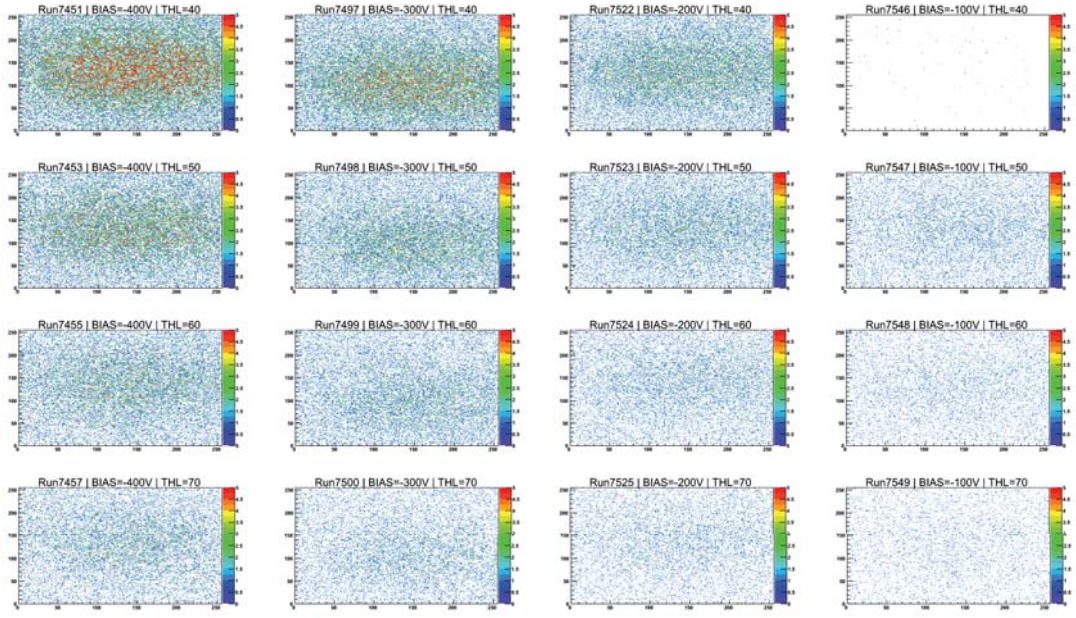

(b) W20_F6 Raw data

Figure 8.6: Hitmap for several threshold and bias configurations in the irradiated Medipix devices. From these plots is clear to see that the W20_F6 sensor has a worse efficiency than W20_D6. These plots were obtained with the same number of incident particles.

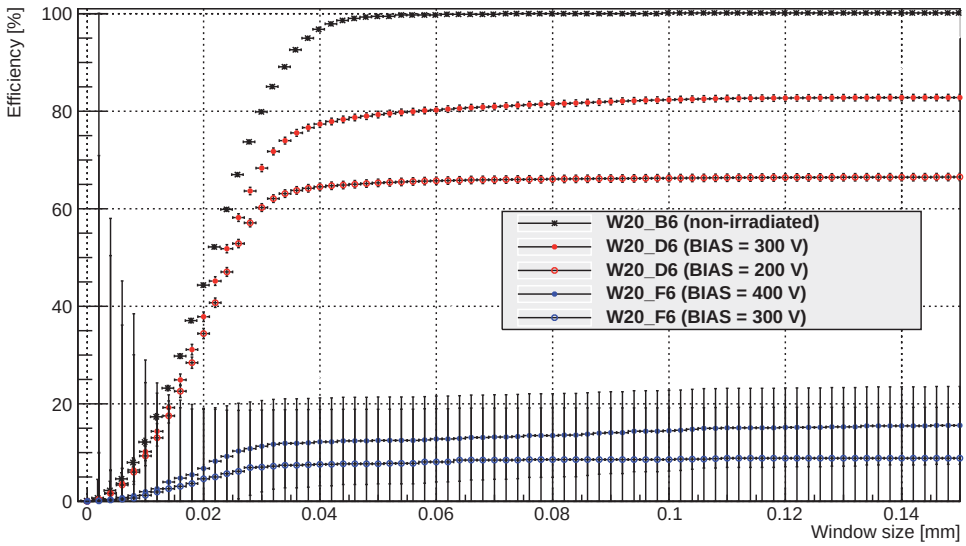

Figure 8.7: Efficiency of the irradiated Medipix devices W20_D6 and W20_F6 as function of the bias voltage. The device B6 is a non-irradiated Medipix and is showed as reference.

8.6 Cluster Finding Efficiency

The cluster finding efficiency is defined as the percentage of tracks with an associated cluster in the DUT over the total number of tracks. The efficiency value depends on the window size around the point where the track hits the DUT plane, as far as the alignment of the DUT is not perfect. Therefore the alignment is a critical procedure, but unfortunately the alignment algorithm did not provide optimal results in the irradiated sensors because of the poor statistic and the fake clusters. For that reason the efficiency of the irradiated devices is quite worse than the non-irradiated, specially the efficiency of W20_F6.

8.6.1 W20_D6 and W20_F6 efficiency

Both Medipix3 assemblies were irradiated with neutrons at the RD50 Ljubljana facilities up to a total dose of 2.5×10^{15} $1\text{MeVn}_{\text{eq}}/\text{cm}^2$, and bump-bonded to Medipix3 ASICs before the irradiation. As a consequence a degradation in the sensor and the ASIC is foreseen, although the Medipix3 chip was designed to deal with doses even greater than that. However fake clusters were found homogeneously distributed all along the sensors, as it can be appreciated in Figure 8.6. The suspicion is that the fake clusters comes from betas emitted by the Tantalum in the chip, which became activated during the irradiation campaign.

The efficiency value for the W20_D6 sensor was calculated for different bias voltages and different threshold values[2]. Figure 8.7 shows the efficiency of the

[2]The **THL** value corresponds to the threshold value setted to distinguish between signal and

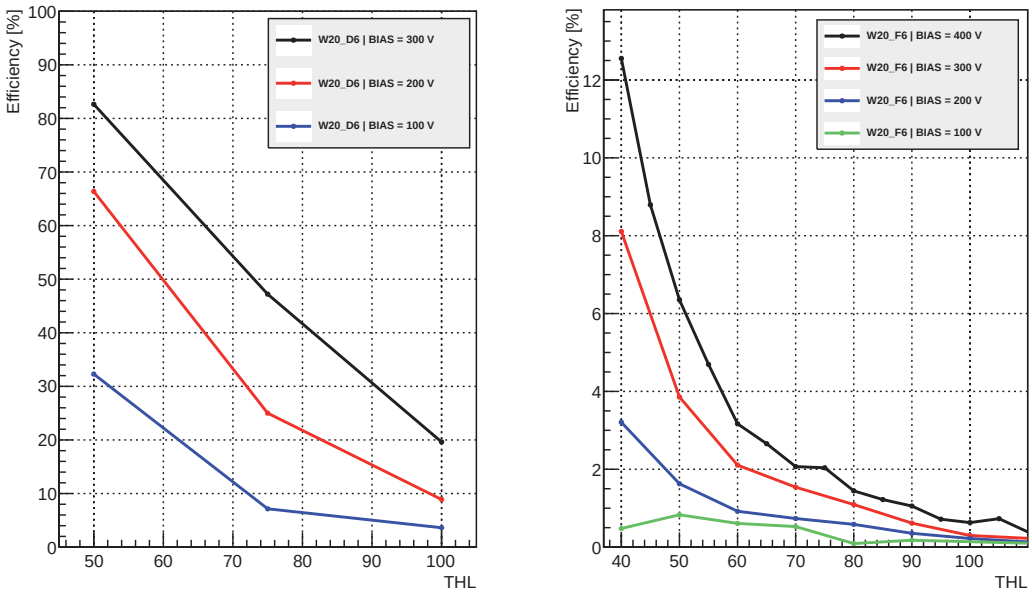

Figure 8.8: Efficiency of the irradiated Medipix devices W20_D6 and W20_F6 as function of bias voltage and the threshold cut.

W20_D6 sensor, taking into account all the tracks which hits the sensor. B6 sensor is a non-irradiated Medipix3 with similar characteristics. It was used as cross-check to validate the analysis and is showed for comparison. The W20_F6 sensor is also showed in Figure 8.7 although its efficiency values are quite small, around 15%. The error bars are unusually big because they are proportional to the statistic of the sample, and due to the poor efficiency the number of clusters associated to beam tracks is very low.

As it was already mentioned, the efficiency of the device depends of the bias applied and the threshold value. The results for the irradiated devices can be seen in Figure 8.8.

Efficiency and charge sharing

We investigated where the inefficiency of the irradiated devices comes from, and found out a correlation between the efficiency and the track intercept within the pixel cell. The resulting plot is showed in Figure 8.9, and it clearly shows than the efficiency is between 90 to 100% in the inner region of the pixel cell. The explanation is that when the track hits a pixel in the very center, then all the generated electron-hole pairs are collected by a single pixel, and the signal-noise ratio is greater. The opposite case happens when a track hits in a corner of a pixel cell, then typically a cluster of 3 pixels is created, with the charge spread between the three pixels, and as a consequence the read out signal could not be enough to

noise. Increasing the THL value we will discard clusters with lower signal.

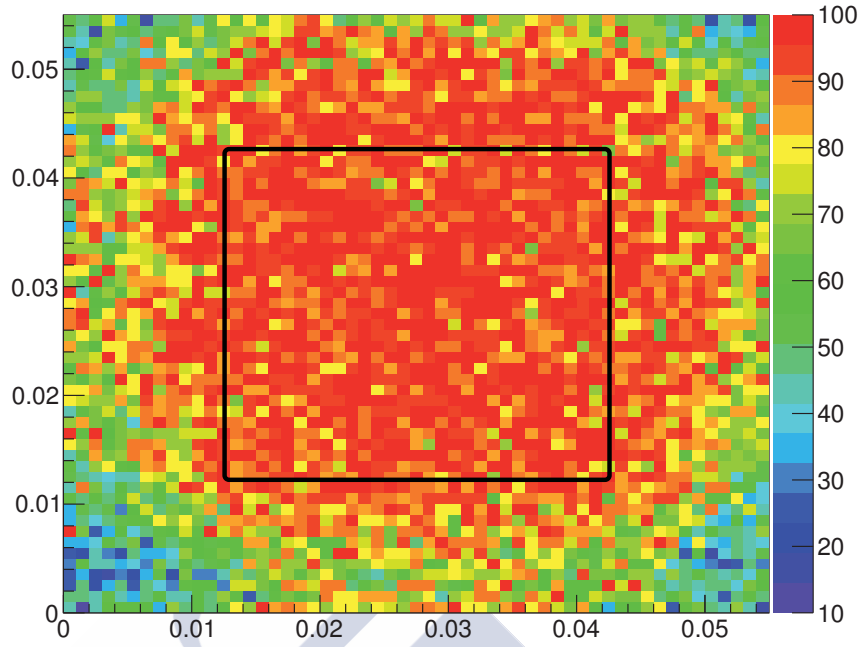

Figure 8.9: Efficiency of the irradiated Medipix W20_D6 as function of the hit of the track inside the pixel cell. The binning is a square of 1 μm side.

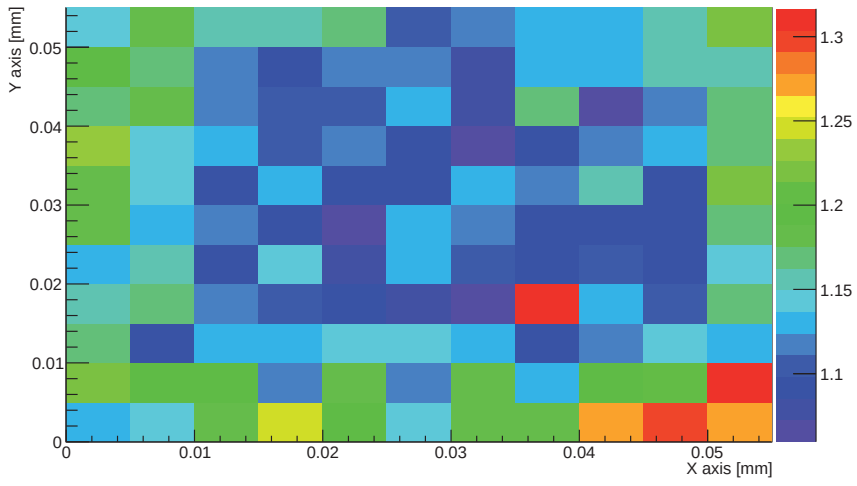

Figure 8.10: Mean cluster size according to where the track hits the pixel cell.

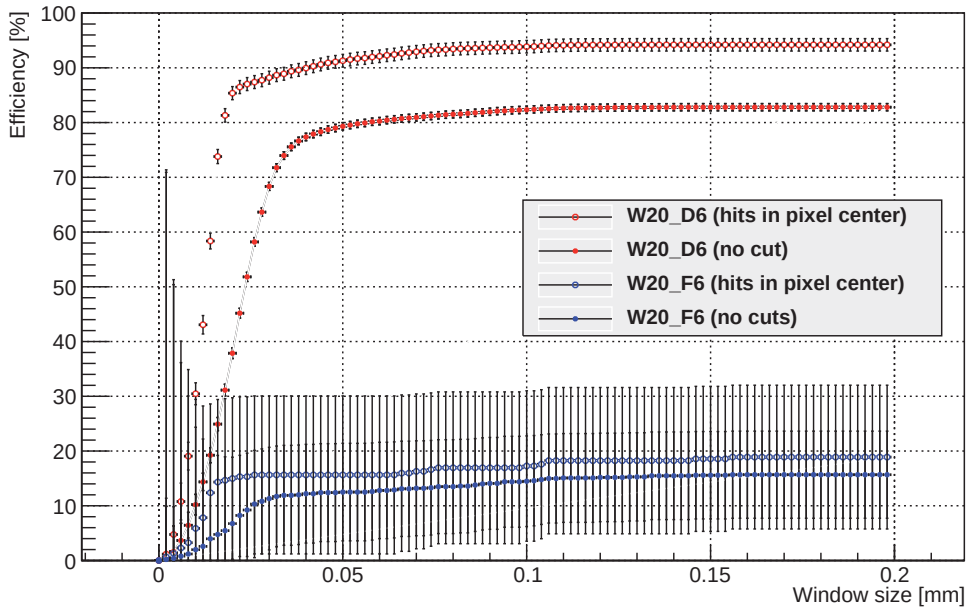

Figure 8.11: Efficiency of the irradiated Medipix W20_D6 and W20_F6 with different cuts.

reach the threshold. This assumption is confirmed in Figure 8.10, where the mean size of the cluster is showed according to where the tracks hits the pixel cell. In that figure we can see how the mean cluster size is minimum at the center of the pixel cell, and greater at the corners.

By selecting those tracks which hits the center of the pixel cell (black rectangle in Figure 8.9) we should obtain a much better efficiency. The resulting plot is showed in Figure 8.11, and indeed the efficiency was improved, reaching a 94%.

8.7 Resolution

Figure 8.12 shows the resolution for the E11_W0171 Timepix (which provides information about the deposited charge) and the W20_D6 Medipix (which provides binary information).

The optimal angle for Medipix/Timepix devices at which the best resolution is achieved is:

$$\alpha = tan^{-1}\left(\frac{pitch}{thickness}\right) = tan^{-1}\left(\frac{55}{200}\right) = 15.3^{o} \tag{8.2}$$

This value is consistent with Figure 8.12 where a resolution of 6 μm is achieved at 14 degrees. The plot shows that the resolution of the E11_W0171 Timepix device at 40 V is slightly better than at 60 V at low angle. The reason is that the charge sharing is higher at low bias voltage, and thus the cluster size is higher. Higher

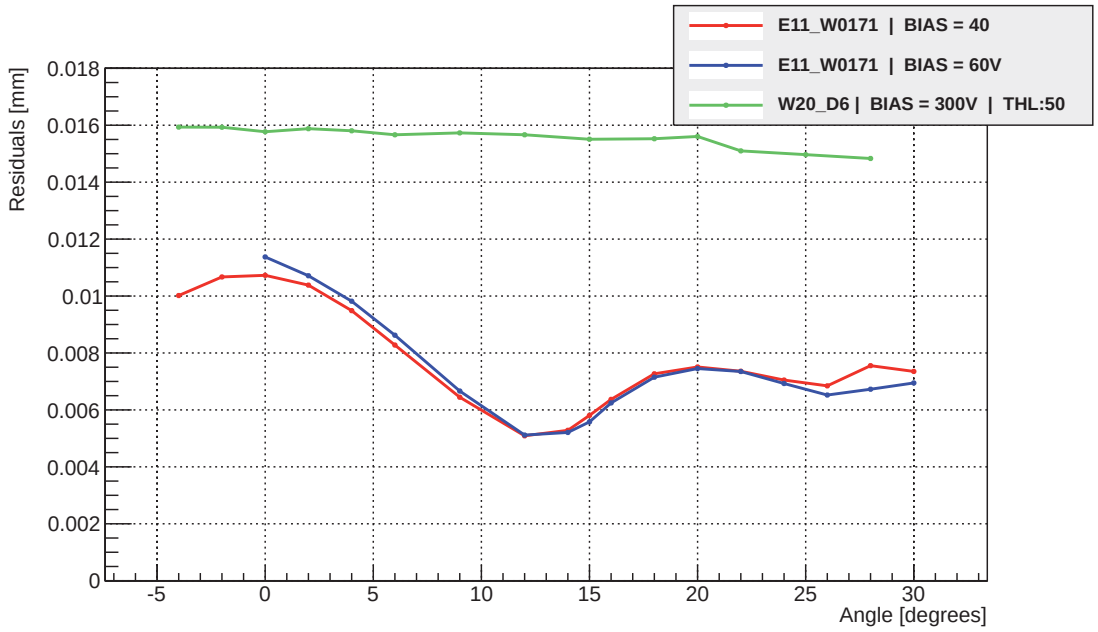

Figure 8.12: Resolution of the E11_W0171 and W20_D6 sensors as function of the angle.

cluster sizes improves the resolution because more pixels in the clusters allows a better center of gravity calculation.

The binary resolution for a 55 μm pitch sensor is 15.8 μm, which is consistent with the resolution achieved for the W20_D6 irradiated device.

Figure 8.13 shows that the average cluster size of the Timepix sensor increases linearly with incident angle, which is consistent with what we expect.

8.8 Energy loss distribution

As Medipix devices did not provide ToT information the information of the deposited energy can not be easily recovered, that's why Figure 8.14 only shows curves for E11_W0171.

As it was already explained, the energy loss distribution follows a Gaussian $\otimes$ Landau distribution. Fitting the ToT values recorded in each run with a Landau convoluted with Gaussian distribution, the Most Provable Value (MPV) can be obtained. Figure 8.14 shows the fit, which matches pretty well the ToT distribution. It can be observed that the MPV value changes with the angle, reaching a minimum at 0 degrees. The reason is that the ToT is proportional to the deposited charge, and the number of electron-hole pairs generated increases with the silicon thickness. Therefore, at bigger angles the particles crosses more silicon and more charge is generated.

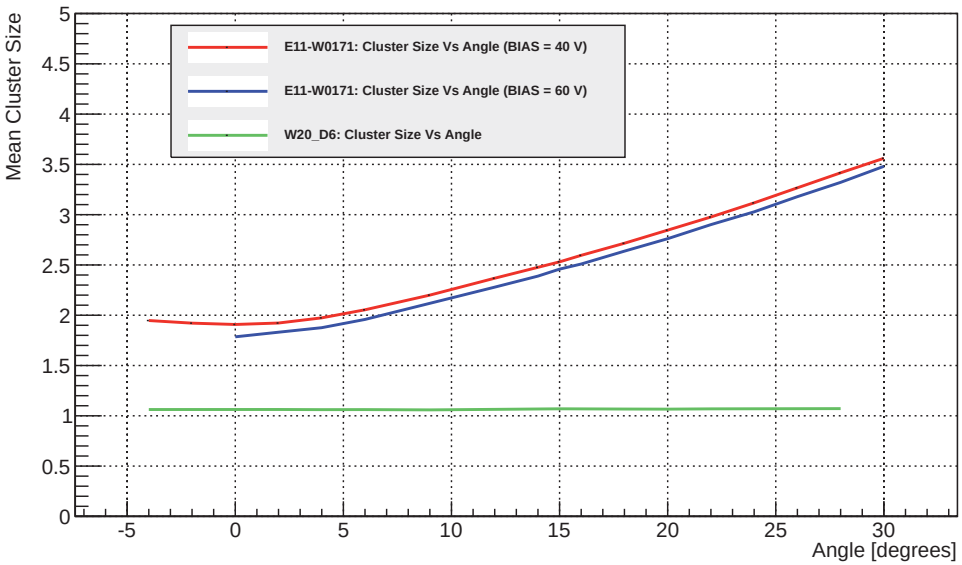

Figure 8.13: ClusterSize vs angle

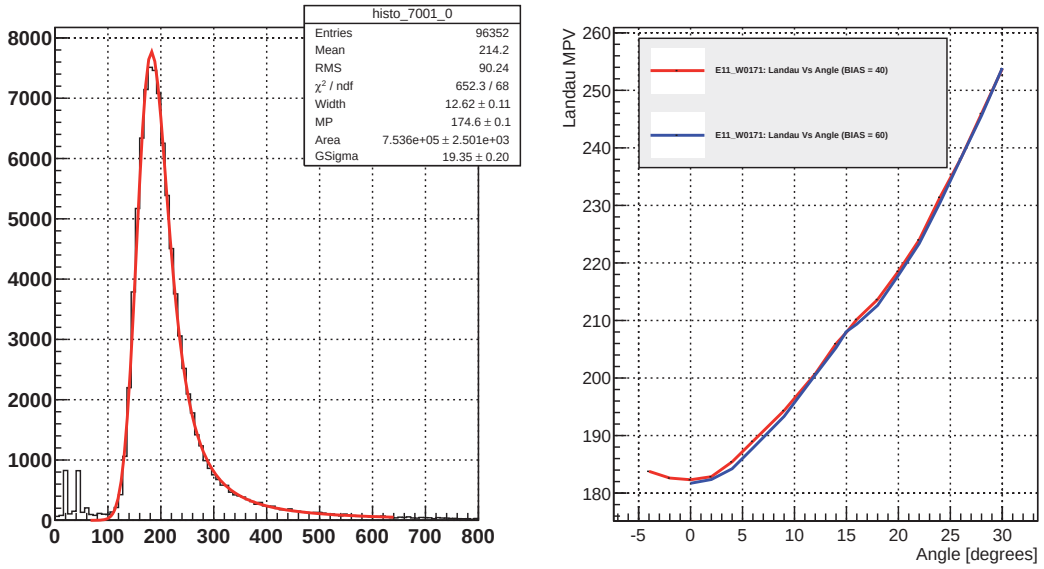

Figure 8.14: Left plot shows the energy of the clusters recovered in E11_W0171 fitted with a Landau convoluted with Gaussian function. Rigth plot corresponds to the peak of the fit as function of the angle of the incident particles for two different bias voltages.

9 Conclusions

This thesis covers most of my research from 2007 to 2013 as member of the High Energy Physics group in the Particle Physics department at the University of Santiago de Compostela. The LHCb experiment was the common topic during these years. At first, I was involved in the installation and commissioning of the *Silicon Tracker* detector. The ST is a silicon micro-strip detector which provides precise momentum measurements. The sensitive area is approximately 12 m^2 placed around the beam line, with a total of 272.600 electronic readout channels. Afterwards I joined the *VELO* upgrade project in the research and development of new sensor technologies for the LHCb upgrade. The VErtex LOcator is placed inside the beam pipe surrounding the LHCb interaction point, at only 7 mm from the beams, enclosed in a secondary vacuum box. The role of the VELO is critical in the overall performance of LHCb, providing excellent vertex and impact parameter resolution, high efficiency, and fast pattern recognition for triggering purposes.

At the beginning of 2007 the production of the *Silicon Tracker* modules was finished and I got involved in the detector installation in the LHCb cavern. For the next three years I worked in the design and development of the detector control system (DCS). At the same time I helped in the detector commissioning with LHC particle beams. These activities allowed me to gain a detailed knowledge of the detector, as the DCS controls all the aspects related to the detector performance. The DCS tasks involves the power-up, sensor biasing, control and configuration of the electronics and monitoring of the environmental variables to ensure safe operation of the detector.

The LHCb's IT team provided guidelines for the experiment control system that we should follow in order to allow a proper integration and synchronization

with the experiment. However we found some additional issues related to the detector safety that were not covered. For that reason we implemented a parallel control tree called *Safety Tree* which look after the detector status and take automatic actions if a problem is detected. The *Safety Tree* is made of a set of hierarchical rules which evaluates the nature of the problem and decides if is necessary to shut down, in a controlled way, the smallest partition possible. Thus the *Safety Tree* anticipates the *DSS* actions, which would take a much more sudden shutdown of the whole detector. We also implemented alarm services that send emails and SMS to the experts responsible of the detector safety. The control system was completed in time for the LHCb commissioning in 2009, but the work continued in the code maintenance and improvement one more year, until Sandra Saornil took the responsibility of the project.

In 2010 I joined the *VELO* upgrade project. The upgraded *VELO* will be installed in 2018. It will be placed closest to beam, at 5.1 mm instead of the current 7 mm. Therefore it will have to cope radiation conditions and data bandwidth much more demanding than the current ones. For the upgraded *VELO* sensors two possible technologies were under consideration: silicon micro-strips and pixels. The first option is an evolution of the current *VELO* sensors, taking advantage of technological progress that have appeared since the construction of the detector. For this option, I was responsible for the assembly and characterization of prototypes to address different issues of the micro-strip technology.

The first micro-strip prototype in which I was involved was built in 2010. It was made of a micro-strip sensor, called PR01, wire bonded to a *Silicon Tracker* hybrid. The PR01 sensor was manufactured by Hamamatsu on a n^+-on-n basis. It follows a radial geometry with quasi-circular shape and an aperture of 72º. The sensor has two different regions: the innermost one has a pitch of 40 μm, while the outermost one has a pitch of 60 μm. I carried out the prototype characterization with a 120 GeV/c pion beam in the CERN SPS North area facilities. One of my responsibilities was to develop the analysis code for the PR01. Such code was used later to analyse all the micro-strip sensors that were tested in the following test-beam campaigns, and it was integrated into the larger test-beam software package. The data collected during the test-beam showed that the sensor could achieve a resolution of 5.6 μm for particles at the optimum angle of $\sim 7^o$.

In 2011 I worked in the assembly and test of a new sensor, the DØ, which is a p^+-on-n type with parallel micro-strips manufactured by Hamamatsu. The DØ sensor has the particularity of including intermediate strips that are not instrumented, i.e. not connected to the readout electronics. In this case the pitch was 30 μm, although being instrumented alternately, so the distance between readout strips is 60 μm. The resolution achieved with the DØ during the test-beam at the SPS facility was 9.5 μm. This is a much better resolution than the theoretical (binary) 17.6 μm. The prototype efficiency is greater than 99.5%.

During the construction phase of the DØ prototype I developed along with Eliseo Pérez and Francisco Rey a novel process for manufacturing pitch adapters by laser ablation. This procedure proved to be very flexible and robust, and allow

us to design, fabricate, test and implement improvements in a single day. Thanks to it, we successfully produced pitch adapters for the DØ sensor and many other micro-strip prototypes.

With the accumulated knowledge and experience of these and other sensors, new micro-strip sensors were designed in order to withstand the radiation of the LHCb with high luminosity while keeping, if not improving, the performance of the current *VELO*. Such sensors were manufactured by Hamamatsu with an R and ϕ geometries, and delivered in mid-2012. The sensors were built on silicon wafers of 150 and 200 μm thickness. They are n^+-on-p type, and the pitch increases continuously from the inner region (30 μm) to the periphery (114 μm). Once the sensors were received in our facilities at Santiago, together with Eliseo, I proceeded with the electrical characterization to ensure that they achieve the manufacturing requirements. I developed a procedure to check that the metrology of the sensors met the specifications. I found out that the warp of the 150 μm thick sensors is 50% higher than their counterparts in 200 μm, as expected. Finally we built a prototype with a radial sensor, which was characterized with two laser beams of 660 nm and 1060 nm and a beta source of 2 MeV betas (^{90}Sr). The sensor was instrumented with a readout hybrid developed for the *Silicon Tracker*, with a new pitch adapter developed by the procedure mentioned above, and read out by the Alibava system. After developing the analysis code it was demonstrated that the sensor signal to noise ratio is above of 30, and it is kept constant throughout the sensor, and independent of the pitch.

In addition, I was involved in the pixel technology within the *VELO* upgrade. In late 2012 we tested in the SPS area a pixel sensor bump-bonded to a Timepix chip, and two sensors bump-bonded to Medipix3 chips. These Medipix3 assemblies were designed in Santiago and manufactured by CNM-Barcelona. Afterwards they were irradiated to a dose of 2.5×10^{15} 1MeVn$_{\text{eq}}$/cm^2 at Ljubljana Neutron Irradiation Facility. The purpose was to analyse different guard ring structures and test two different thickness of the sensor. We need to ensure that they can withstand full bias voltage after irradiation levels similar to the expected for the *VELO* upgrade conditions.

The irradiated sensors were identical but the distance from the last pixel to the edge of the sensor. In one case it was 250 μm and in the other it was 400 μm. The test-beam data showed that the efficiency could reach 94% when we discard charge sharing issues (particle hitting the center of the pixel), and fell to 82% when we consider all the particles hitting the assembly. The sensor with less distance between the last pixels to the edge of the sensor had a efficiency below 20%.

These results, among others and the result of simulations, were part of the evidence supporting the decision taken in June of 2013 to choose 200 μm thick pixel sensors for the future *VELO* for the LHCb with high luminosity.

USC
UNIVERSIDADE
DE SANTIAGO
DE COMPOSTELA

Part III

Summary

USC
UNIVERSIDADE
DE SANTIAGO
DE COMPOSTELA

10 Summary

This thesis covers most of my research from 2007 to 2013 as a member of the High Energy Physics group in the Particle Physics department at the University of Santiago de Compostela. Most of this work was performed on the LHCb experiment. At first, I was involved in the installation and commissioning of the *Silicon Tracker* (ST) detector. The ST is a silicon micro-strip detector which provides precise momentum measurements of ionizing particles coming from the collisions. Afterwards I joined the VErtex LOcator (*VELO*) upgrade project in the research and development of new sensor technologies for the LHCb upgrade.

10.1 Context

The Standard Model (SM) of Particle Physics is the most reliable theory which explains the structure and interactions of the fundamental particles of nature. The SM asserts that the material in the universe is made up of elementary fermions interacting through fields. The particles associated with the interaction fields are bosons.

Although the SM is probably one of the most predictive and heavily tested of all physics theories, it suffers from several issues that hint at a more complete underlying theory. One question that the SM can not answer is the asymmetry between matter and antimatter. After the Big Bang, for a short time there was a perfect balance between matter and antimatter. As the Universe expanded and cooled it went through a series of changes in its composition; particles acquired their characteristic masses, and matter and antimatter revealed differences which caused asymmetry between the two.

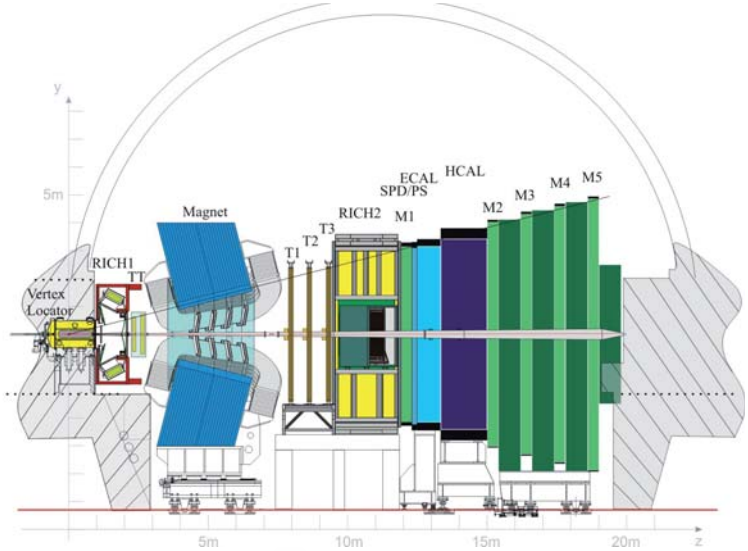

Figure 10.1: Side view of LHCb.

The LHCb experiment (Figure 10.1) uses the energy density provided by the LHC to attempt to probe asymmetries between particles and antiparticles that can not be explained by the Standard Model, and thus provide evidence that would allow us to build a new model of fundamental physics.

10.2 The LHCb Silicon Tracker

The LHCb Silicon Tracker detector is a silicon micro-strip detector which provides precise momentum measurements. The sensitive area is approximately 12 m^2 with a total of 272.600 readout channels.

From 2007 to 2010 I was involved in the commissioning of the ST detector with LHC beams, as well as the development of its control system.

10.2.1 The Silicon Tracker detector

The ST consists of two sub-detectors as shown in Figure 10.2. The *Tracker Turicensis* (TT) is located upstream of the 4 Tm dipole magnet and covers the full acceptance of the experiment. The *Inner Tracker* (IT) covers the region of highest particle density closest to the LHC beam pipe in the three tracking stations (T1-T3) located downstream of the magnet.

10.2.2 The Silicon Tracker control system

The LHCb's Control System is a hierarchical and distributed system which controls the whole LHCb experiment. To build a common, consistent and integrated control system for the whole experiment, the development teams are required to work with the same technologies and devices:

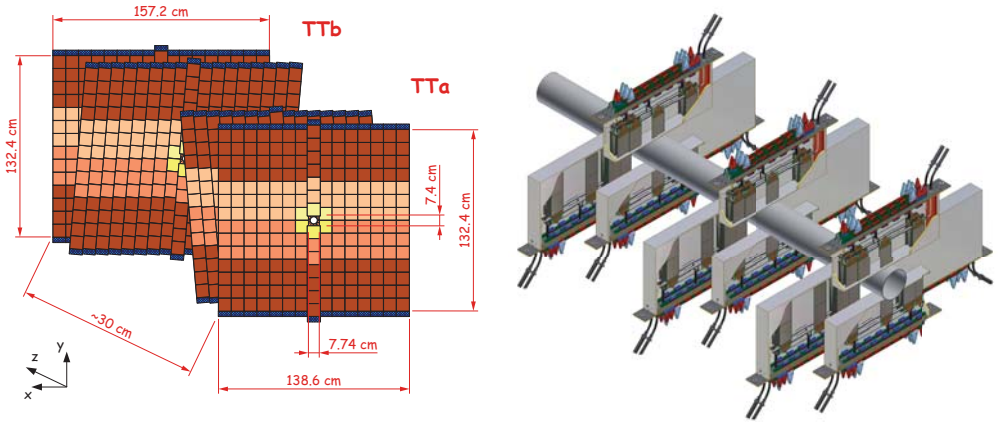

(a) TT's XUVX layers

(b) The 12 boxes (3 stations) of the IT

Figure 10.2: ST Sketches.

- The software tools and protocols used by the development teams are common for all the detectors. One of the major agreement points is the use of the PVSS SCADA (now SIMATIC WinCC Open Architecture) by all LHC experiments.

- Each team follows a set of guidelines for building the hierarchical distributed control system of each detector, which were defined at the conception of the control system.

- Common hardware developments such as the SPECS and systems such as the power supplies have been accepted by each sub-detector.

- The network infrastructure is common to every sub-detector and system, and is isolated from the outside world.

The Silicon Tracker collaboration was in charge of the design, development and maintenance of the control system directly linked with the ST hardware. From the detectors point of view, the main task of the DCS is to enable the proper and safe operation of the detector and provide a link to the general LHCb Experiment Control System (Figure 10.3). The tasks that the DCS has to fulfill can be summarized as follows:

- It has to control, configure and monitor the status of the detector electronics and the environmental variables.

- It has to implement functionalities to perform calibration runs on the detector.

- It has to perform exhaustive tests of individual modules.

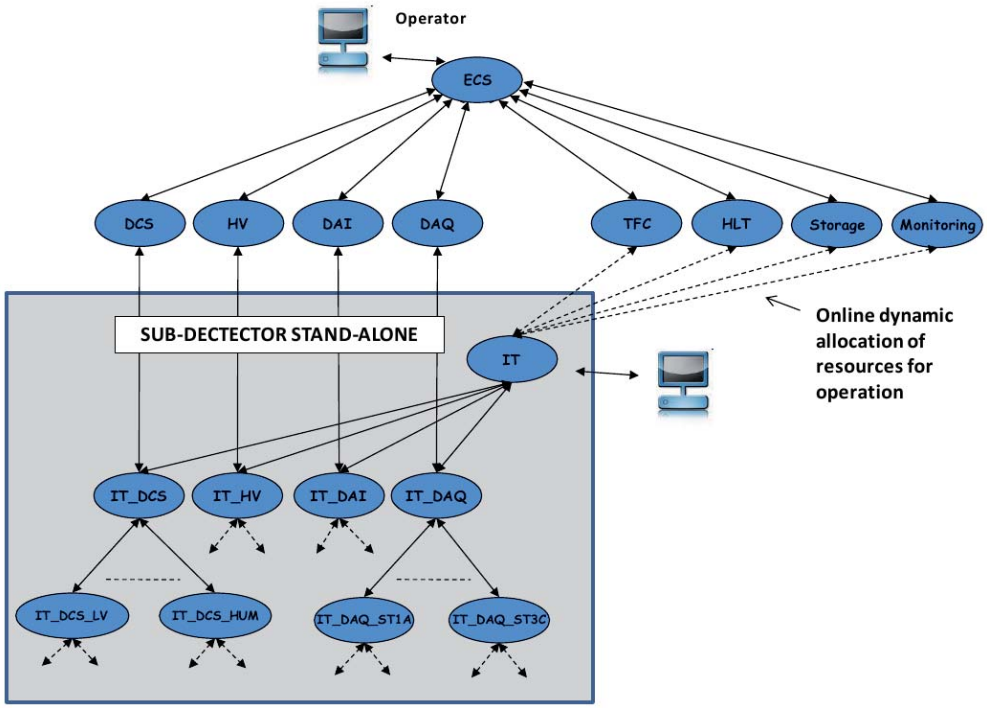

Figure 10.3: ST interconnection with LHCb.

- It has to interface to external systems such as databases, the DSS system, the LHCb higher level control units and the TFC system.

For safety purposes, a parallel tree or *Safety Tree* was conceived and implemented to link several parts of the control tree together, which were not otherwise connected. The idea behind the Safety Tree is to use the monitoring signals in order to prevent a DSS action. If necessary, the *Safety Tree* will perform a controlled switched off of the affected half station, leaving the rest of the detector operational. Otherwise, the DSS alarms will switch off the affected subsystem without hesitation. This could have catastrophic consequences for such delicate hardware, and must be avoided as much as possible.

10.3 The LHCb VELO upgrade project

The VErtex LOcator is the silicon detector surrounding the LHCb interaction point. The role of the VELO is critical in the overall performance of the LHCb experiment, providing excellent vertex and impact parameter resolution, high tracking efficiency, and fast pattern recognition for triggering purposes.

An upgrade of the LHCb experiment is planned for 2018, where the operational luminosity will be increased to 2×10^{33} cm^{-2}s^{-1}, allowing data taking at a rate of 10 fb^{-1} per year. The trigger will be upgraded towards a fully software trigger,

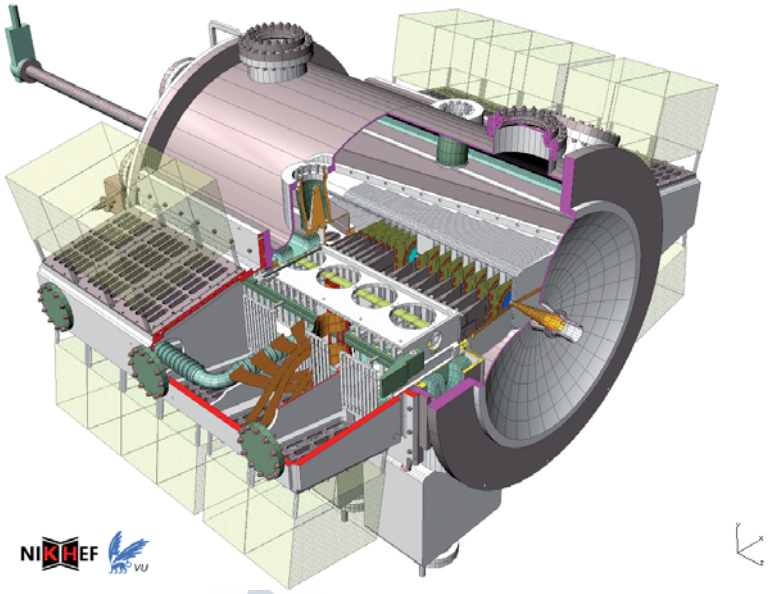

Figure 10.4: CAD image of the VELO detector. The beam passes through the center of the detector where the collisions occur.

and as a result the detectors will be upgraded to allow full event readout at the 40 MHz bunch crossing frequency.

The upgraded VELO will have to cope radiation levels and output bandwidth far more demanding than the current ones, not only due to the new LHCb requirements, but also because it will be placed even closer to the interaction point.

10.3.1 The current VELO detector

The current VELO consists of an array of 42 modules surrounding the interaction point, mounted on two retractable halves. Every module has two micro-strip sensors, providing R and ϕ coordinates. Unlike other detectors at the LHC, there is no pipe between the VELO sensors and the beam, and these sit within a large vacuum vessel to allow them to reach distances of only 7 mm from the beam. The LHC vacuum is preserved by means of a corrugated foil which additionally protects the sensors from RF pickup from the beam.

The main purposes of the VELO (Figure 10.4) can be summarized as follow:

- Distinguish between the collision and the disintegration points.
- Hits in the silicon are used to reconstruct straight track segments within the detector. Those tracks segments are used as seeds for the LHCb track reconstruction software.
- As Pile-Up detector in the first-level L0 trigger.

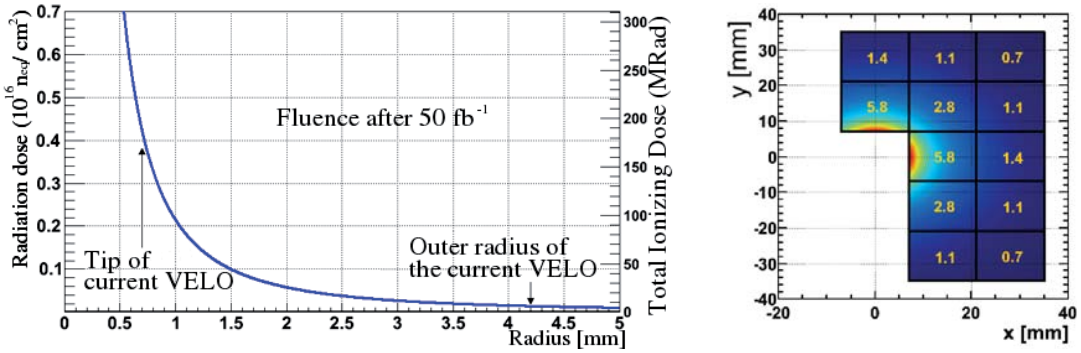

(a) Radiation dose as function of the distance to the beams.

(b) Rate of tracks per bunch crossing in a pixel based module.

Figure 10.5: Expected values of radiation and track rate per bunch crossing for the upgraded VELO. Figure from Ref. [52].

- The VELO is also used in the software High Level Trigger (HLT), together with the other LHCb detectors.

10.3.2 The VELO upgrade project

The LHCb upgrade places many challenges on the design of a new VELO, particularly in terms of radiation damage and output bandwidth. Placed even closer to the beam, at only 5.1 mm, the radiation dose will be extremely non-uniform reaching up to 200 MRad or 8×10^{15} 1 MeV n_{eq}/cm^2 in the inner regions of the sensors (Figure 10.5).

For the upgraded VELO sensors two technologies were under consideration: silicon micro-strips and pixels. For the first option, I was responsible for the assembly and characterization of several prototypes to address different issues of the micro-strip technology. For the second, we tested in the SPS area a pixel sensor bump-bonded to a Timepix chip, and two irradiated sensors bump-bonded to Medipix3 chips with the purpose of investigate different guard ring structures.

10.3.3 Micro-strip prototypes for the VELO upgrade

As part of the VELO upgrade project, three micro-strip prototypes were tested with a beam of 120 GeV/c pions at the CERN SPS facility.

The PR01 prototype

The PR01 sensor was manufactured by Hamamatsu Photonics. It is a n^+-on-n sensor, 300 μm thick, with quasi-circular shape and an aperture of 72°. The 1006 strips ran over the R-coordinate, arranged in different regions of constant pitch: 40 μm in the inner region and 60 μm in the outer.

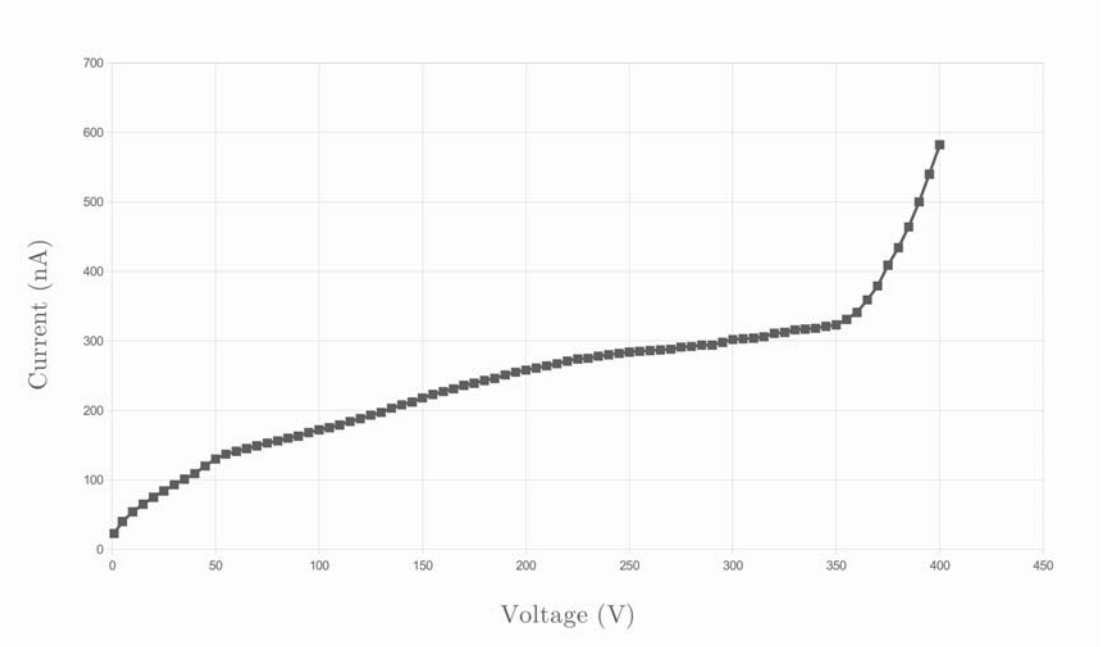

Figure 10.6: PR01 IV curve.

The PR01 sensor was bonded to an IT hybrid with 3 Beetles, although not all the channels could be successfully bonded due to several reasons (dirty pads, bonding failures or for testing purposes).

As so few strips were feasible for bonding, and were spread over several regions, it was not not possible to make an accurate measurement of the efficiency of this sensor.

The PR01 sensor was electrically characterized in the USC-GAES facilities. The IV curve (Figure 10.6) was carried out before the assembly of the sensor. The measured values shows that the sensor breakpoint is above 350 V.

Afterwards, the PR01 was characterized with particles in the SPS pion beam with the Timepix telescope. In Figure 10.7 the relationship between the resolution of the PR01 sensor and the angle of the incident particles is shown. In the 40 μm region the optimal angle is 7.6º and in the 60 μm region is 11.3º. The results shows a resolution of 5.6 (9.7) μm in the 40 (60) μm pitch region at optimal angle, being the binary resolution 11.5 (17.3) μm.

DØ prototype

The DØ silicon sensor is p^+-on-n type, single sided and AC coupled, with a single guard ring designed by Hamamatsu. It additionally includes intermediate strips which are not connected to readout pads. The pitch is 30 μm, although being instrumented alternately, so the distance between readout strips is 60 μm. In 2011, a DØ sensor was bonded in the USC-GAES facilities to a TT hybrid which contains 4 Beetles.

During the construction phase of the DØ prototype I developed along

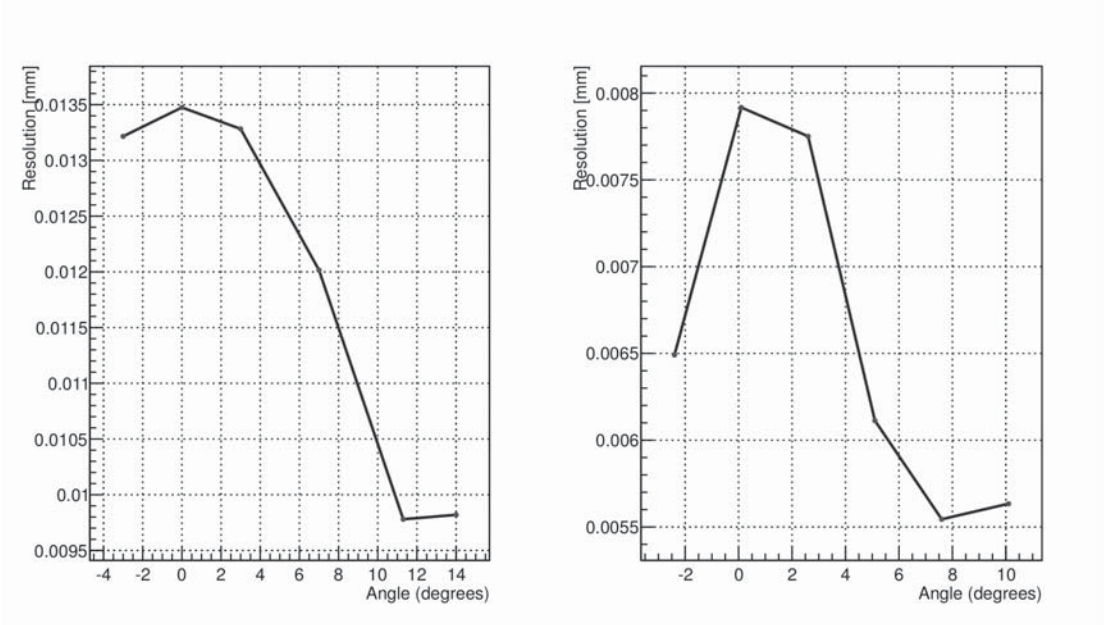

Figure 10.7: PR01's resolution as function of the angle between the sensor and the incident particle.

with Eliseo Pérez and Francisco Rey a novel process for manufacturing pitch adapters by laser ablation. Searching for faster and cheaper alternatives to the photolithographic process, we developed a laser-ablation micromachinning process, performed on a previously metal-coated substrate. This process removes Al particles from a metal-on-glass substrate following a specific pattern generated by CAD-like software, producing high-density pitch adapters. Figure 10.8 shows a section of the pitch adapter design and a picture of the result.

The DØ sensor was electrically characterized in Santiago, with the measurement of both the IV and CV characteristics (Figure 10.9). By plotting the inverse squared capacitance against the applied bias voltage, the depletion voltage of the sensor can be obtained as the point where the plateau begins, in this case was ≈ 120 V.

The DØ prototype was characterized with a particle beam facility as the PR01 testbeam (Figure 10.10). The result of the angle scan taken during the test-beam is shown in Figure 10.11. The resolution of the DØ prototype at optimal angle (5.3°) was found to be around 9.55 μm, while the binary resolution is 17.3 μm.

As can be appreciated in Figure 10.12, the efficiency of the DØ is above 99% when the size of the window around the track is equal to the readout pitch (60 μm).

As expected, it was shown (Figure **??**) that the number of strips per cluster followed the evolution of the bias voltage. Once the detector bias was far beyond depletion, the generated electron-hole pairs did not have time to spread themselves in several strips, and therefore the cluster size decreases.

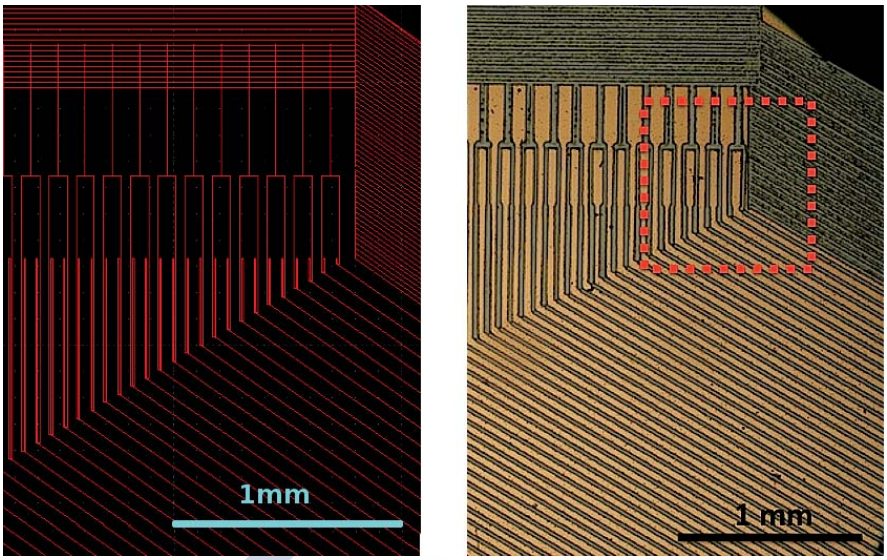

Figure 10.8: Pitch adapter's CAD-like design (left) compared with the manufactured piece (right).

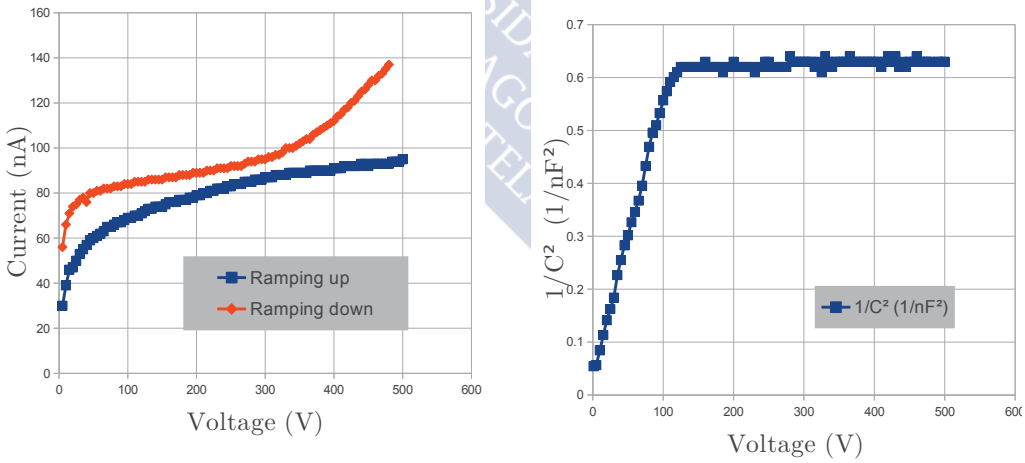

(a) DØ IV Curve

(b) DØ CV Curve

Figure 10.9: Measured voltage-current and voltage-capacitance for the DØ device.

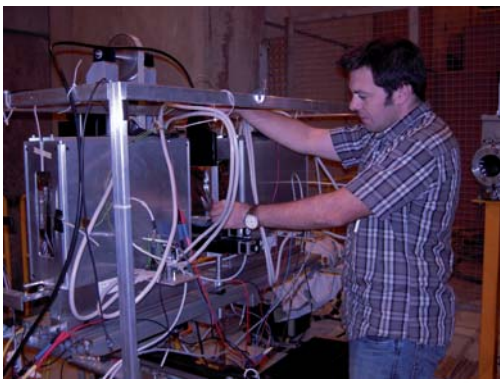

(a) The author placing the DØ in the DUT position.

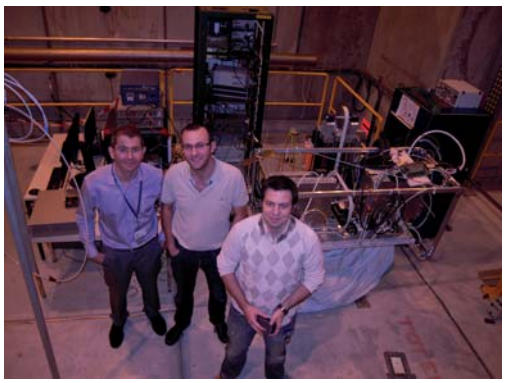

(b) Santiago's team in the 2011 test-beam campaign. Starting from the left: Abraham Gallas Torreira, Eliseo Pérez Trigo and the author.

Figure 10.10: DØ module mounted in the DUT position.

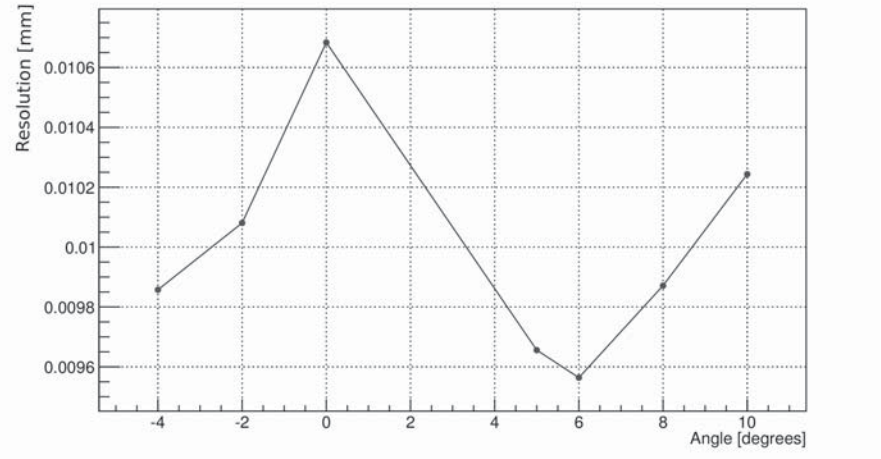

Figure 10.11: DØ resolution versus angle.

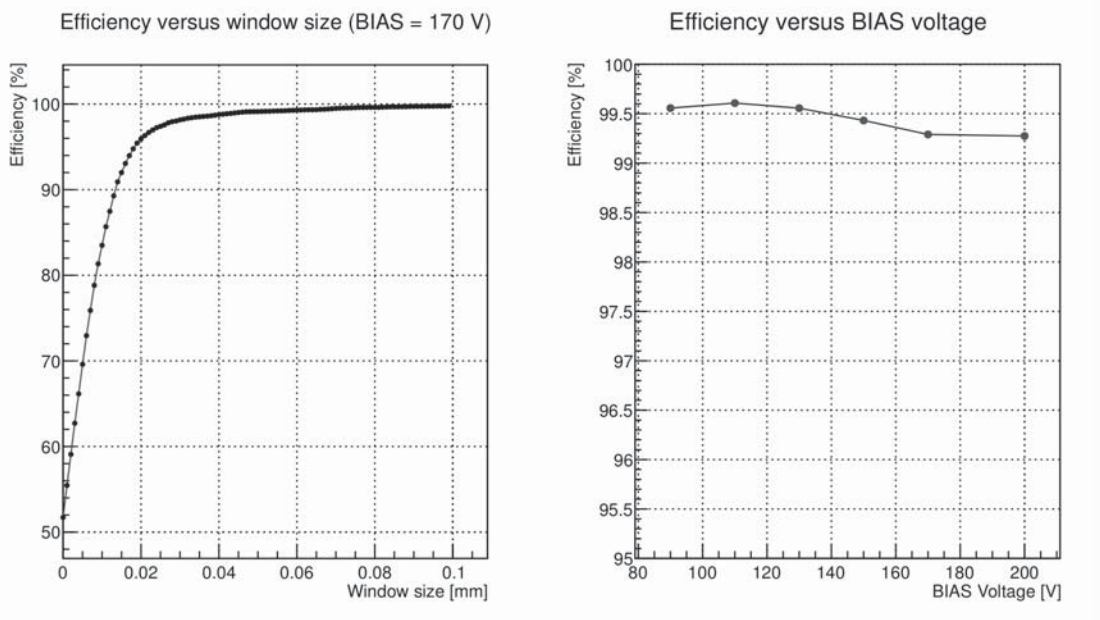

Figure 10.12: Left plot shows the DØ efficiency measured as the percentage of tracks with an associated cluster in a given window size. Right plot is the efficiency value as function of the bias voltage. These values correspond to a window of 60 μm around the tracks.

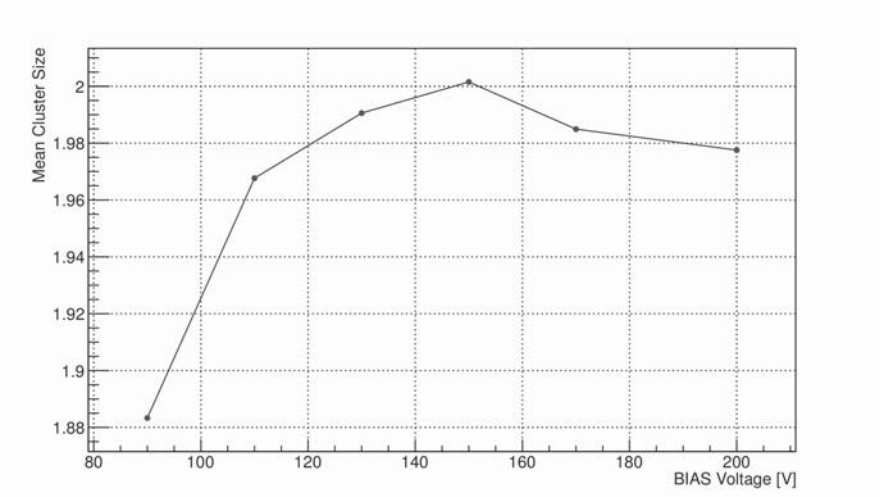

Figure 10.13: Evolution of the DØ mean cluster size as function of the bias voltage.

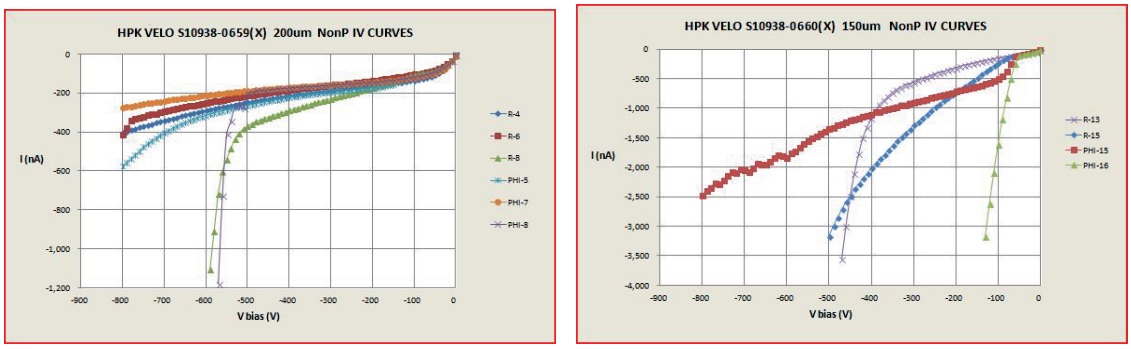

Figure 10.14: Left plot corresponds to IV curves for 200 μm thick sensors, and right plot belongs to 150 μm thick sensors.

The Hamamatsu sensor

As part of the VELO upgrade program, several n^+-on-p micro-strip sensors were purchased from Hamamatsu and were delivered in the second half of 2012. Each micro-strip sensor has 2560 strips, to be readout by a total of 20 Beetle chips. The sensors were built with R and ϕ geometry, and two different thickness were produced: 150 and 200 μm.

Together with Eliseo Pérez, we performed the metrology, the electrical characterization, the pitch adapter manufacture, the wedge-bonding to a TT hybrid and S/N ratio measurements with laser and ^{90}Sr β^- source.

To perform the IV curve, the sensors were isolated from the chuck with a *Kapton*® foil, and biasing was applied through top surface pads. The resulting IV curves are displayed in Figure 10.14, and the CV curves in Figure 10.15. As expected from the bulk resistivity, the 200 μm thick sensors are fully depleted at -100 V, and 150 μm thick sensors at -60 V.

Metrology of the sensors was carried out to measure the sensor thickness and flatness. A summary of the data taken is shown in Figure 10.16 and in Figure 10.17. According to the tolerance values defined, all but one of this sensors is in agreement with the specifications (dashed line). As expected, 150 μm thick sensors are more warped than the 200 μm ones.

Lasers are commonly used in instrumentation to test sensor properties. In this case, two laser beams (1060 and 660 nm) were used to characterize a 200 μm thick module with radial strips. Figure 10.18a shows the penetration depth as function of the photon's energy. It can be seen that a 660 nm laser will be fully absorbed in the first ten microns, while the 1060 nm laser beam will pass through the sensor, so the later was chosen to measure the depletion voltage.

The full depletion voltage can be obtained looking at the S/N ratio as function of the applied bias voltage. The analysis results are shown in Figure 10.18b. It can be concluded that at -10 V the first tens microns are depleted, and the full depletion voltage is achieved at -100 V. This value is consistent with the value obtained in the CV curve during the electrical characterization.

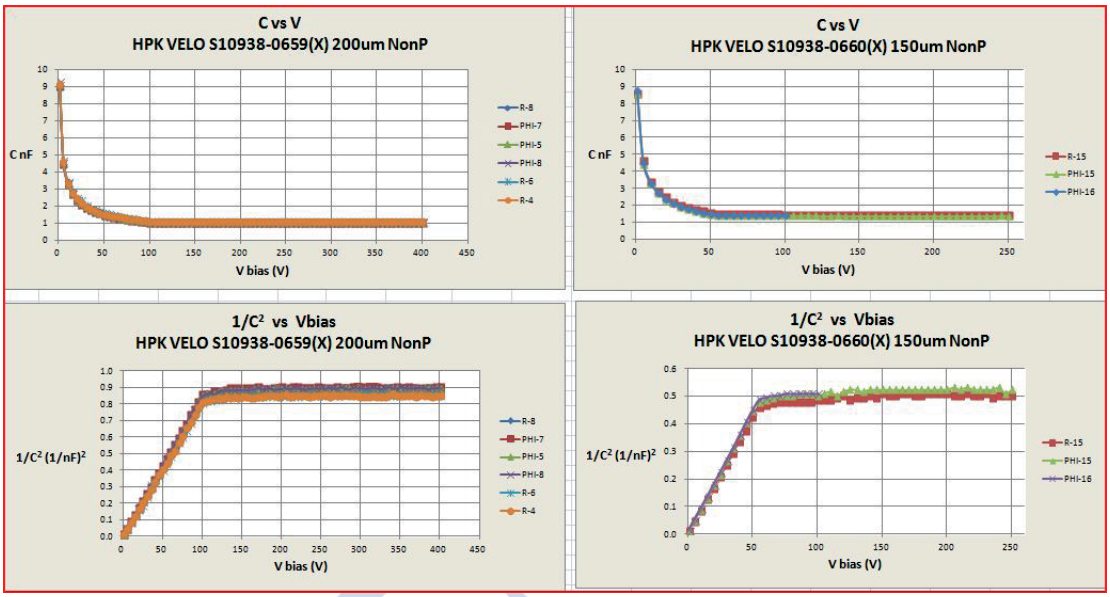

Figure 10.15: CV curves for 200 μm and 150 μm thick sensors.

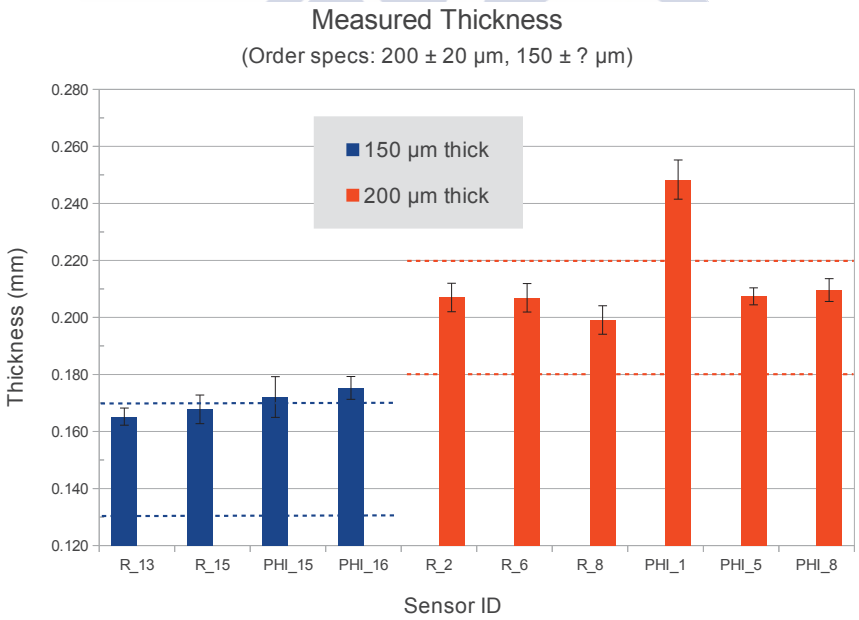

Figure 10.16: Hamamatsu sensor's thickness. Dashed lines are the tolerance values written in the tender document.

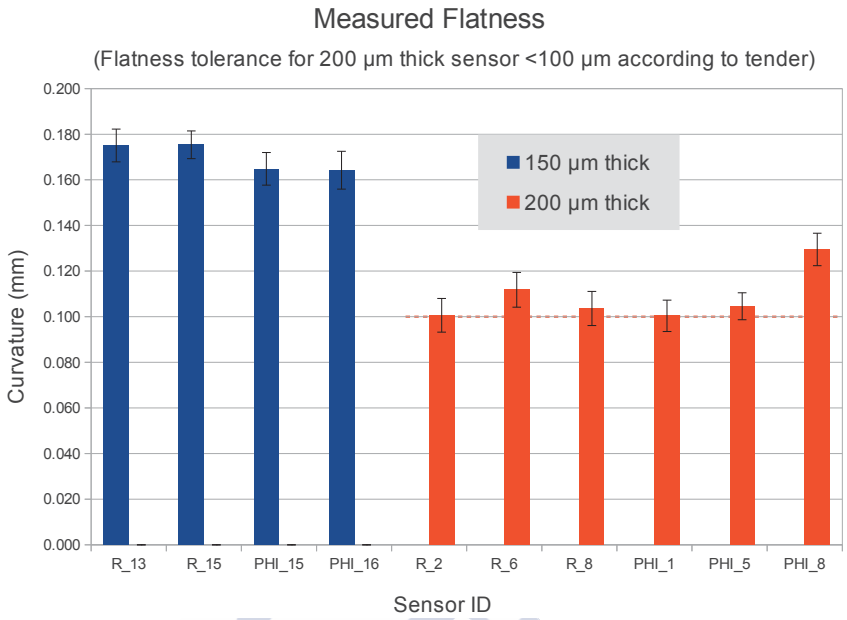

Figure 10.17: Hamamatsu sensor's flatness. Dashed line is the tolerance value for 200 μm thick sensors written in the tender document.

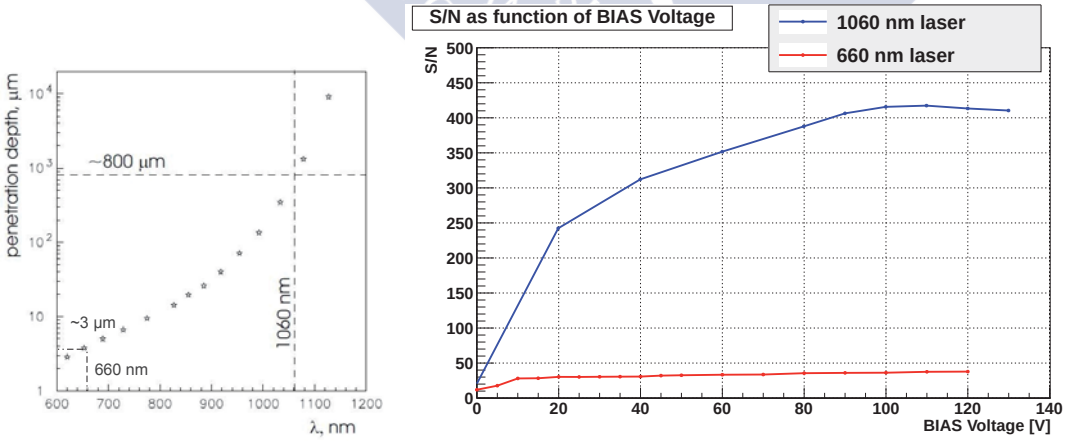

Figure 10.18: Left plot shows the penetration depth for both lasers used. The 660 nm laser will be absorbed in the first microns of the sensor. Right plot shows the signal induced in sensor as function of the laser input voltage

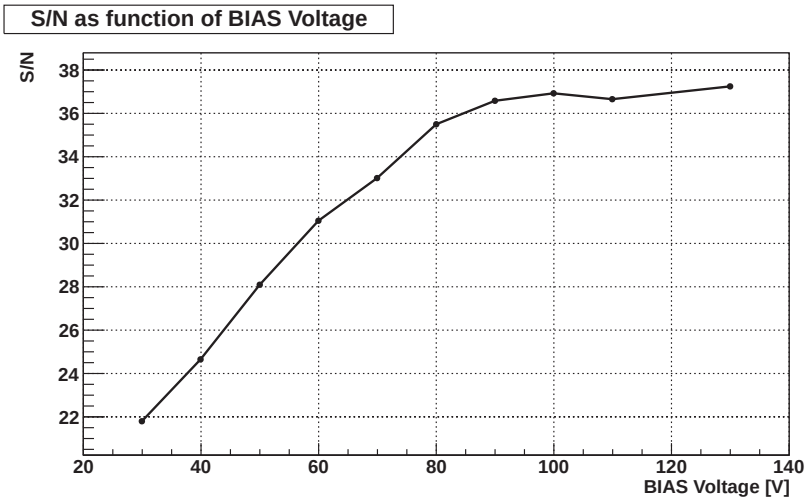

Figure 10.19: S/N ratio as function of the bias applied to the sensor using a ^{90}Sr source. It can be seen that above 100 V the S/N ratio remains approximately constant.

ID	ASIC	Sensor Thickness	Distance to Edge	Fluence
E11_W0171	Timepix	200 μm	400 μm	None
W20_D6	Medipix3	200 μm	400 μm	2.5×10^{15} n_{eq}/cm^2
W20_F6	Medipix3	200 μm	250 μm	2.5×10^{15} n_{eq}/cm^2

Table 10.1: Main characteristics of the DUTs analyzed. All the devices were produced by CNM with a n^+-on-p doping and 2 guard rings.

The prototype was characterized also with a β^- source. ^{90}Sr was chosen because is an almost pure β^- source, with relatively low levels of gamma emission.

Several runs were taken with the ^{90}Sr source at different bias voltages, and the results are plotted in Figure 10.19. The full depletion voltage is achieved around -100 V, which is consistent with the values obtained from the IV-CV curves and the 1060 nm laser measurements.

The signal and noise distributions are plotted in Figure 10.20 showing a S/N ratio of 33. The relationship between the S/N ratio and the strip length was studied, but no correlation was observed, suggesting that the noise is dominated by the electronics.

10.3.4 Pixel prototypes for the VELO upgrade

As part of the VELO upgrade program, several Medipix3 and Timepix devices were tested in the SPS North area. This work covers the analysis of three different devices manufactured at CNM facilities in Barcelona. Their main characteristics are presented in Table 10.1.

The IV curves of the analyzed pixel devices are shown in Figure 10.21. These

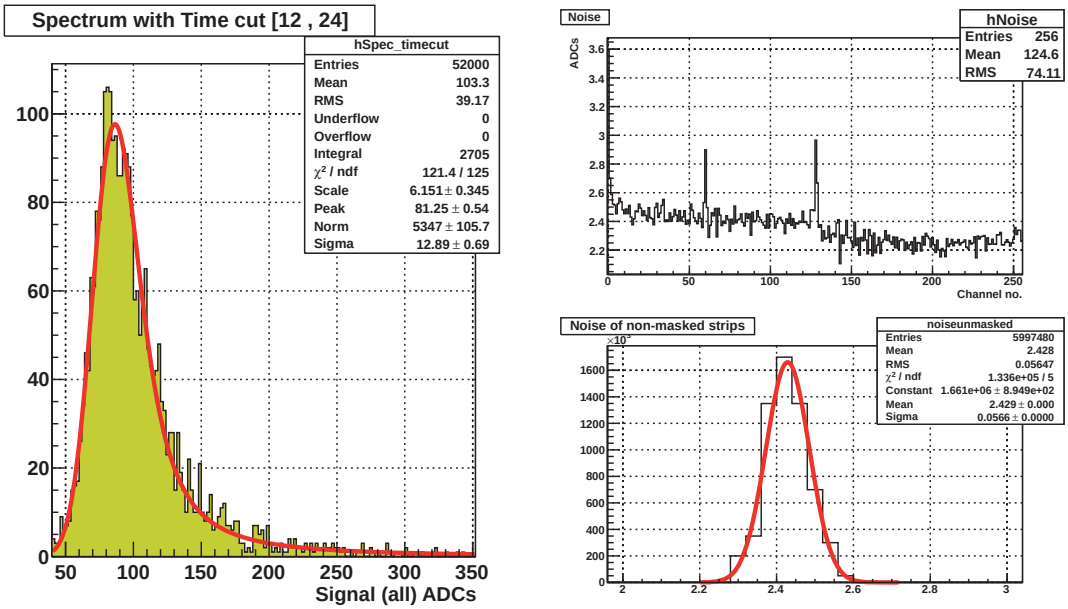

Figure 10.20: ^{90}Sr spectrum measured with the Hamamatsu R_6 sensor bonded to a TT Hybrid. The S/N ratio is the ratio between the most probably value of the signal and the average noise, giving a value of 33.

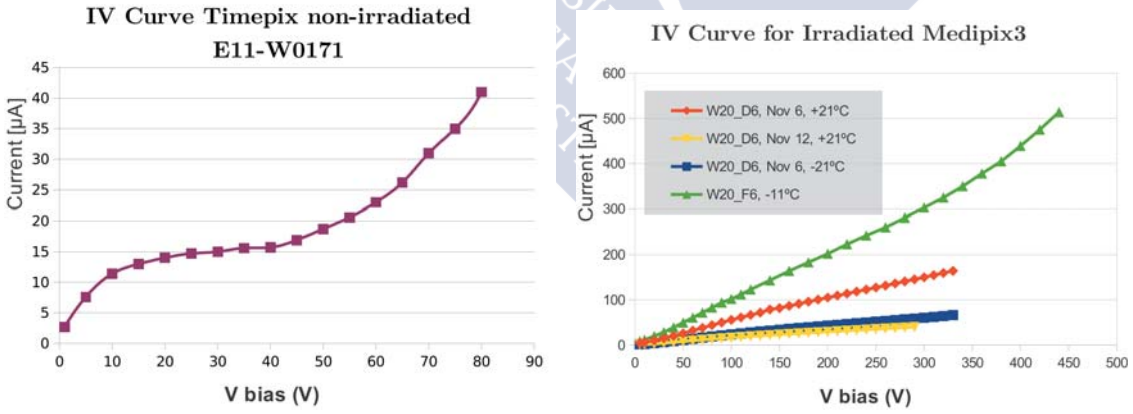

(a) E11_W0171 IV Curve

(b) W20_D6 and W20_F6 IV curves

Figure 10.21: Figure 10.21a corresponds to the IV curve for Timepix E11_-W0171 device at room temperature ($\simeq$ +23ºC). Figure 10.21b is the IV curves for irradiated Medipix3 W20_D6 and W20_F6 at low temperature.

curves indicate that the behaviour of the irradiated Medipix W20_F6 is much worse than W20_D6. The IV curve is an early indicator of the damage suffered by the W20_F6.

Both sensors were bump-bonded to Medipix3 ASICs which were designed according radiation hard techniques. Unfortunately the sensors were not characterized before irradiation, so it can not be said for sure that the radiation damage is the only responsible of the W20_F6 behaviour.

The main purpose of the test-beam carried out in November of 2012 was to measure the efficiency of the irradiated Medipix3 devices. Both assemblies were bump-bonded to Medipix3 ASICs and irradiated with neutrons at the RD50 Ljubljana facility up to a total dose of 2.5×10^{15} $1\text{MeVn}_{\text{eq}}/\text{cm}^2$. Figure 10.22 shows the raw data obtained. The poor signal obtained of the W20_F6 device indicates, as the IV curve did, that this device shows worse performance than W20_D6.

As can be seen in Figure 10.23, the efficiency of the irradiated devices is well below the non-irradiated. The analysis procedure was cross-checked using a non-irradiated Medipix3 device (W20_B6) which showed an efficiency close to the expected 100%.

The test-beam data showed that the efficiency of the irradiated devices increases with bias voltage, and decreases with threshold cut as shown in Figure 10.24. Trying to isolate the inefficiencies from charge sharing, the efficiency of the W20_D6 device was plotted as function of the track intercept within the pixel cell. The resulting plot (Figure 10.25) shows how efficiency dramatically drops when tracks hit the periphery of the pixel cell, where the charge sharing has a greater impact. Figure 10.26 shows that the efficiency reaches 95% once we remove the effects of charge sharing.

Figure 10.27 shows the resolution for the E11_W0171 Timepix (which provides information about the deposited charge) and the W20_D6 Medipix (which provides binary information). The optimal angle for Medipix/Timepix devices at which the best resolution is achieved is 15.3º. This value is consistent with Figure 10.27 where a resolution of 5 μm is achieved at 14 degrees. The plot shows that the resolution of the E11_W0171 Timepix device at 40 V is slightly better than at 60 V at low angle. The reason is that the charge sharing is higher at low bias voltage, and thus the resolution is improved because more pixels in the clusters allows a better center of gravity calculation. The binary resolution for a 55 μm pitch sensor is 15.8 μm, which is consistent with the resolution achieved for the W20_D6 irradiated device.

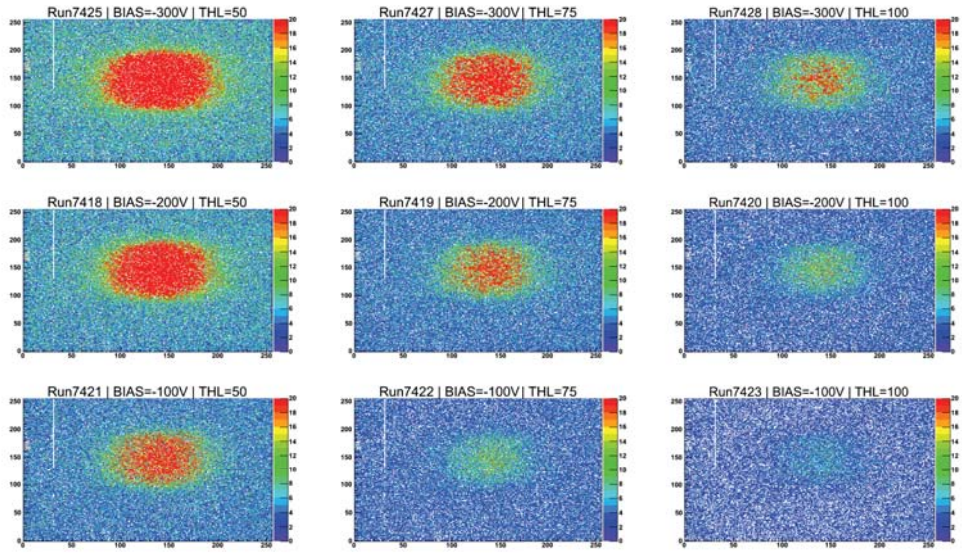

(a) W20_D6 Raw data

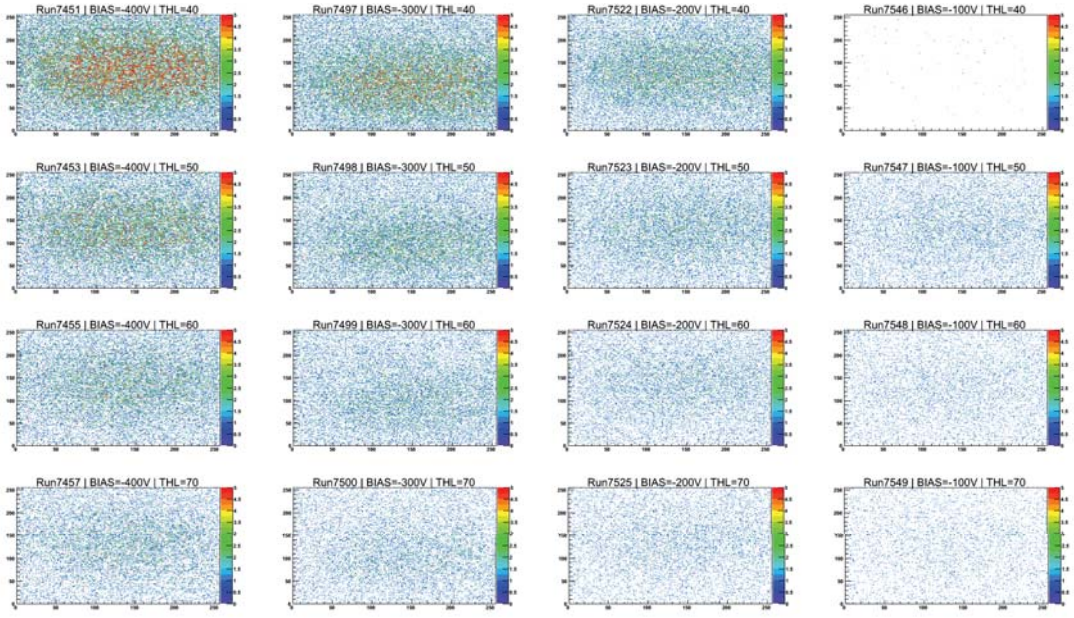

(b) W20_F6 Raw data

Figure 10.22: Hitmap for several threshold and bias configurations in the irradiated Medipix devices. From these plots is clear to see that the W20_F6 sensor has a worse efficiency than W20_D6. These plots were obtained with the same number of incident particles.

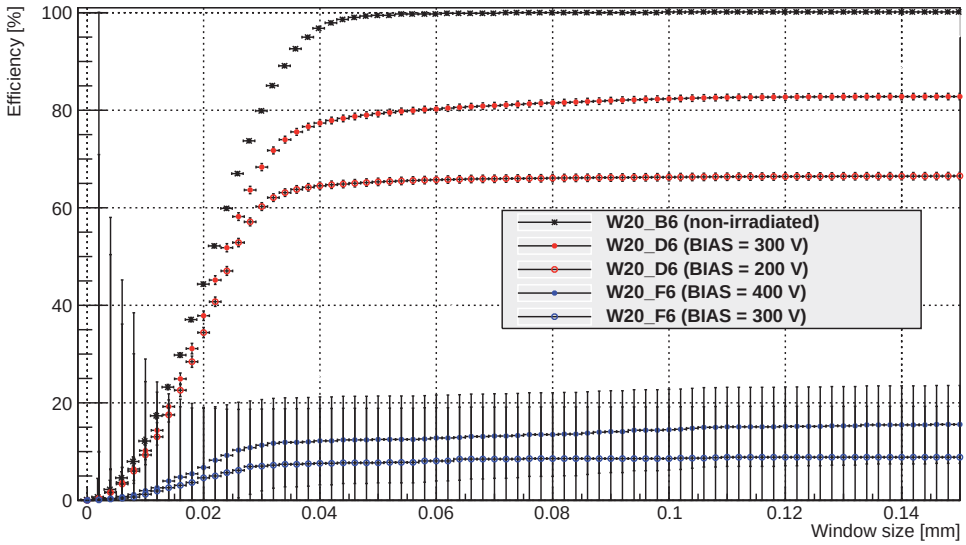

Figure 10.23: Efficiencies of the W20_B6 non-irradiated Medipix3 and the irradiated Medipix3 W20_D6 and W20_F6 with different bias voltages.

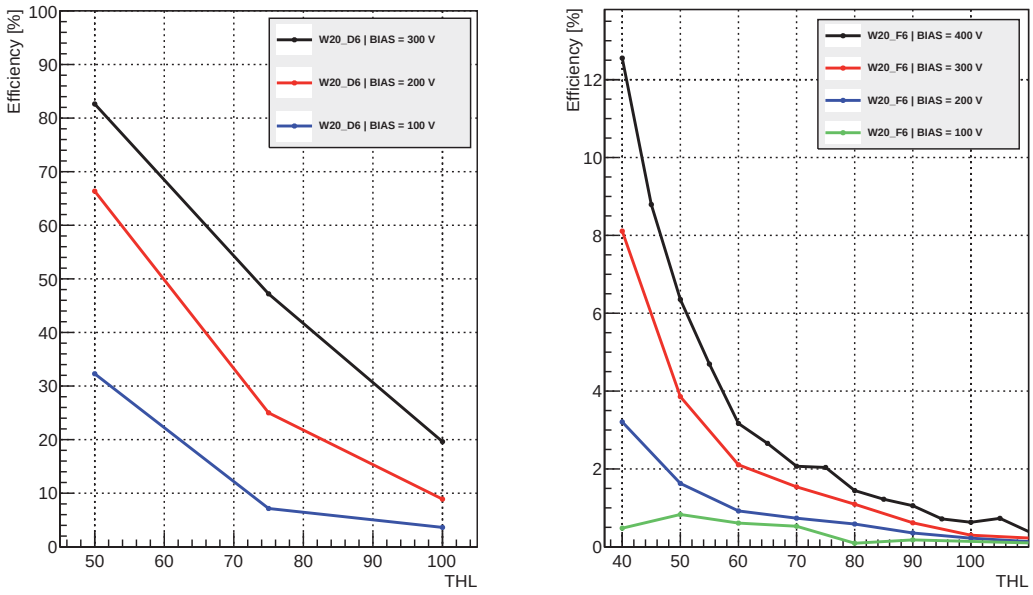

Figure 10.24: Efficiency of the irradiated Medipix devices W20_D6 and W20_F6 as function of bias voltage and the threshold cut.

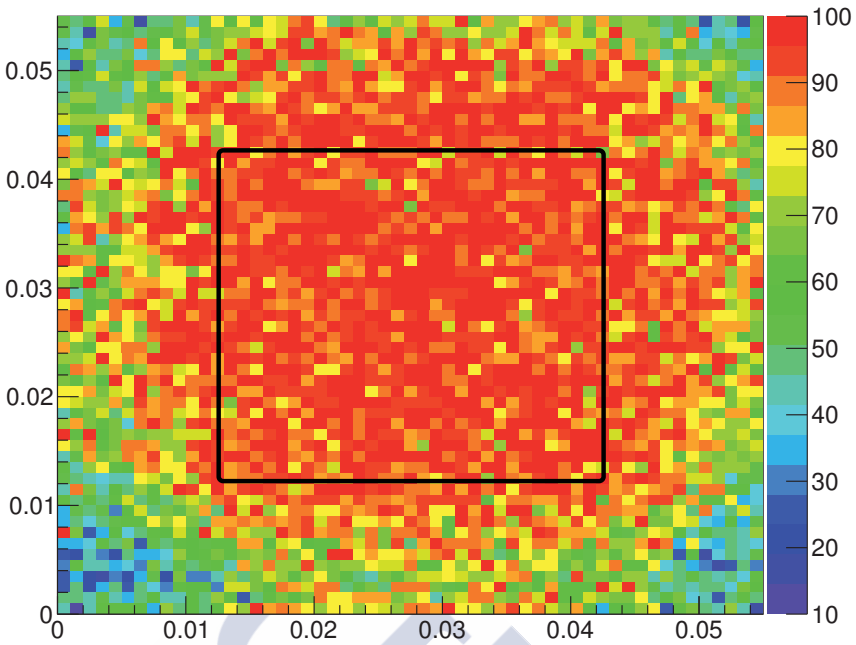

Figure 10.25: Efficiency of the irradiated Medipix W20_D6 as function of the hit of the track inside the pixel cell. The binning is a square of 1 μm side.

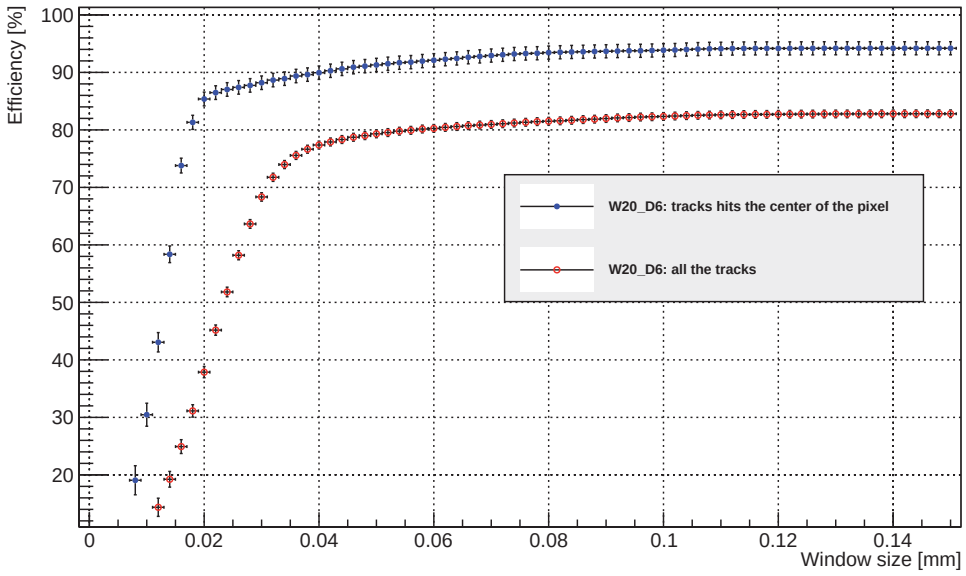

Figure 10.26: Efficiency of the irradiated Medipix W20_D6 and W20_F6 with different cuts.

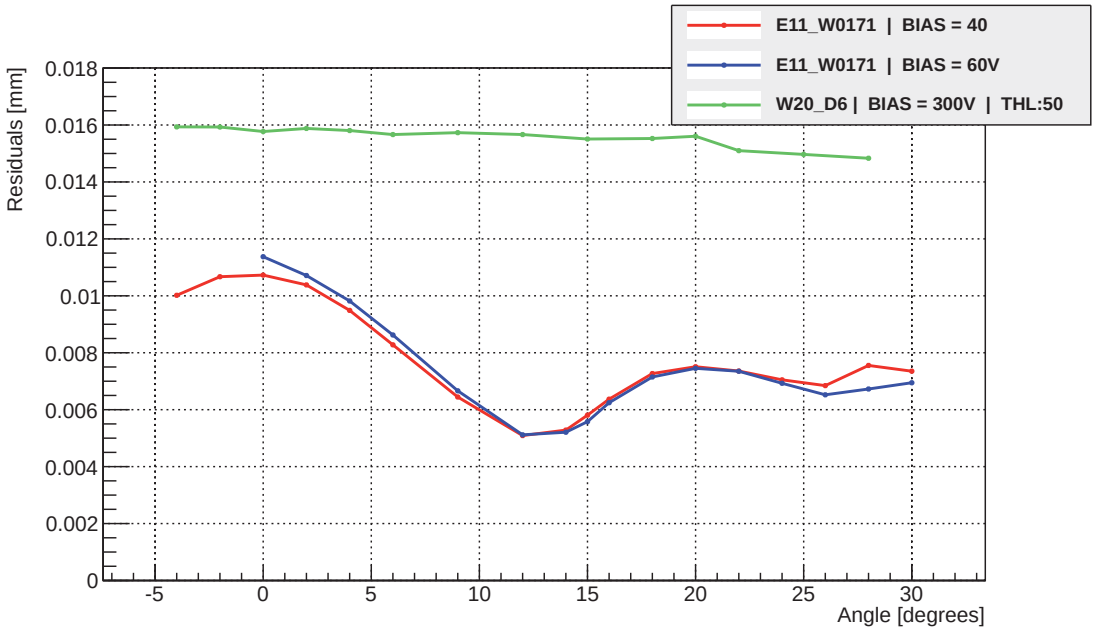

Figure 10.27: Resolution of the E11_W0171 and W20_D6 sensors as function of the angle.

USC
UNIVERSIDADE
DE SANTIAGO
DE COMPOSTELA

11 Resumo

Esta tese cobre a miña investigación entre 2007 e 2013 como membro do grupo de Física de Altas Enerxías no departamento de Física de Partículas da Universidade de Santiago de Compostela. O experimento LHCb é o tema común durante toda a tese. Cando comezei a investigación involucreime na instalación e posta en funcionamento do detector *Silicon Tracker* (ST). O ST é un detector de micro-pistas de silicio que proporciona medidas precisas do momento das partículas ionizantes procedentes das colisións. Despois uninme ao proxecto de actualización do detector *VErtex LOcator* (VELO) na procura e desenvolvemento de novas tecnoloxías para os sensores de cara ó LHCb de alta luminosidade.

11.1 Contexto

O Modelo Estándar (SM) da Física de Partículas resulta ser a teoría máis fiábel para explicar a estrutura e relacións de todas as partículas fundamentais. O SM xurdiu como a teoría que describe os compoñentes fundamentais da materia e as súas interaccións. O SM afirma que a materia do universo está composta de partículas elementáis chamadas fermións, que interactúan por medio de campos. As partículas asociadas cos campos de interacción son bosóns.

A pesar de que o SM é probabelmente a teoría máis preditiva e probada da física, adoéce dalgunhas lagoas que apuntan a necesidade dunha teoría subxacente máis completa. Unha cuestión que o SM non pode contestar é a asimetría entre a materia e a antimateria. Despois do BigBang, durante un curto espacio de tempo mantívose un equilibrio perfecto entre materia e antimateria. Cando o Universo comezou a expandirse e arrefriou pasou por unha serie de cambios na

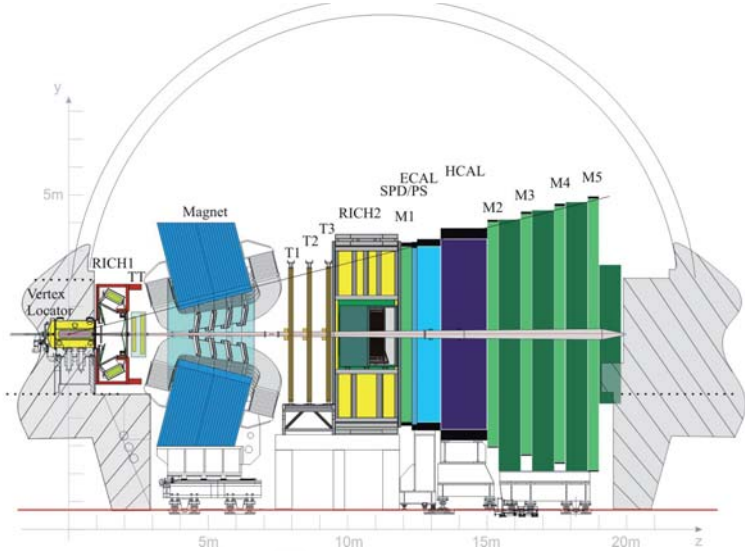

Figure 11.1: Side view of LHCb

súa composición. As partículas adquiriron as súas masas características e un fenómeno ocorreu que differenciou a materia da antimateria, causando asimetría entre as dúas. Este fenómeno denominado violación CP, está recollido no SM. Nembargantes a magnitude da violación CP predita non é suficiente para explicar o dominio de materia sobre antimateria no universo actual. O experimento LHCb (Figure 11.1) utiliza a densidade de enerxía proporcionada polo LHC para descubrir novas fontes de violación CP máis aló das predicciónss do SM.

11.2 O LHCb Silicon Tracker

O detector *Silicon Tracker* é un detector de micro-pistas de silicio que proporciona medidas precisas do momento das partículas producidas polas colisións no LHCb. A súa área sensible é aproximadamente de 12 m^2 cun total de 272.600 canles de lectura.

Dende 2007 ata 2010 estiven involucrado na posta en funcionamento do detector con feixes de partículas do LHC, así como no desenvolvemento do seu sistema de control.

11.2.1 O detector Silicon Tracker

O ST está formado por dous sub-detectores tal e como se amosa na Figura 11.2. O *Tracker Turicensis* (TT) está situado antes do imán de 4 Tm do LHCb e abrangue toda a aceptancia do experimento. O *Inner Tracker* (IT) abrangue a rexión arredor do tubo do LHC de maior densidade de partículas, e está situado nas tres estacións de seguimento que hai despois do imán.

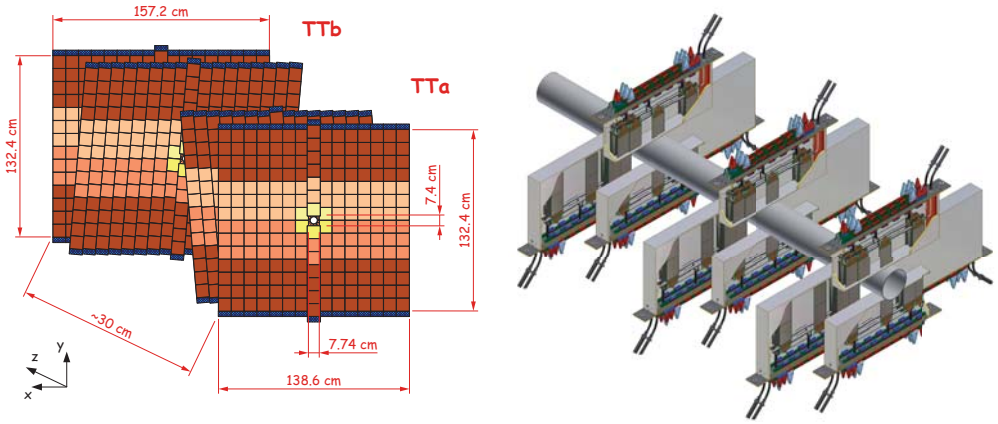

(a) TT's XUVX layers

(b) The 12 boxes (3 stations) of the IT

Figure 11.2: ST Sketches

11.2.2 O sistema de control do Silicon Tracker

O sistema de control do experimento LHCb (ECS[1]) é un sistema xerárquico e distribuído que controla tódalas máquinas relacionadas co LHCb. O ECS do LHCb ten ao seu cargo a configuración, control e monitorización de tódolos compoñentes conectados ao sistema. Esto inclúe tódolos dispositivos nas áreas de adquisición de datos, control de detectores, monitorización de detectores, sinais de disparo, sincronización e a interacción cos operadores.

A colaboración do *Silicon Tracker* ten a tarefa de deseñar, desenvolver e manter o sistema de control do detector (DCS[2]) que está relacionado directamente co equipamento do *Silicon Tracker*. Para facer un sistema de control común, consistente e que integre todo o experimento, os equipos que desenvolven os DCS teñen que traballar coas mesmas tecnoloxías e dispositivos:

- As ferramentas software e protocolos empregados polos equipos son comúns a tódolos detectores. Un dos máis importantes acordos foi o uso do PVSS SCADA (agora chamado SIMATIC WinCC Open Architecture) por tódolos experimentos do LHC.
- Tódolos equipos seguen un conxunto de liñas mestras a hora de construir o sistema de control xerárquico e distribuído de cada detector, as cales foron definidas na etapa inicial.
- Os compoñentes desenvoltos en común coma o SPECS, e sistemas tales como as fontes de alimentación, foron adoptadas de común acordo por tódolos detectores.
- A infraestrutura de rede tamén é común e está illada do mundo exterior.

[1] **E**xperiment **C**ontrol **S**ystem
[2] **D**etector **C**ontrol **S**ystem

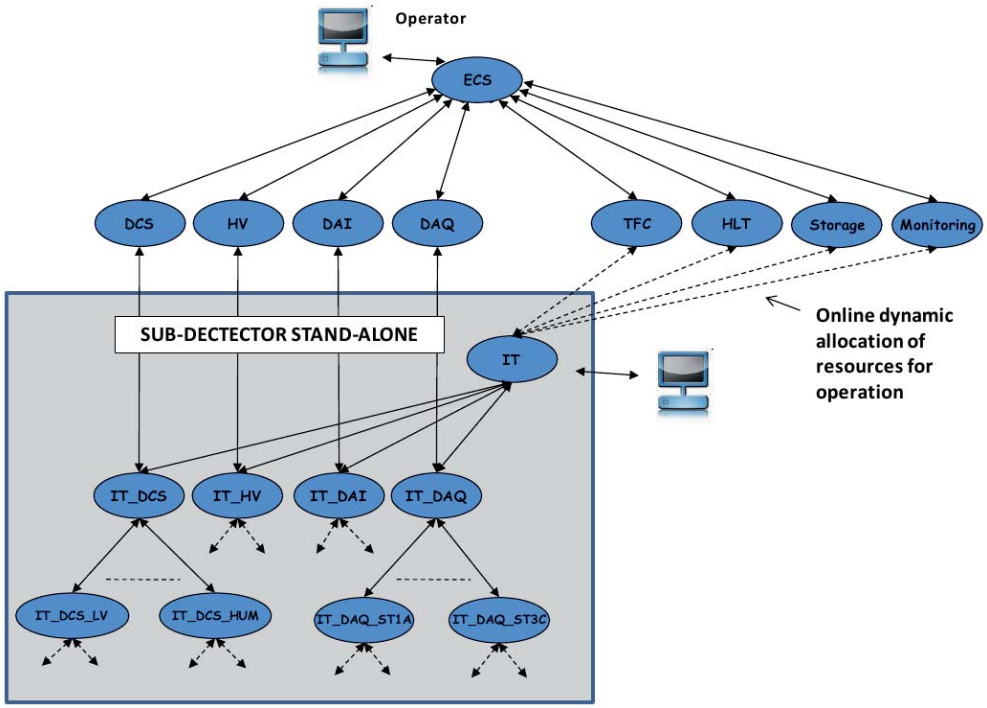

Figure 11.3: Interconexión do Silicon Tracker co LHCb.

Dende o punto de vista do detector, a tarefa principal do DCS é levar a cabo unha operación axeitada e segura do detector e prover a conexión co ECS xeral to LHCb (Figure 11.3). As tarefas que o DCS ten que levar a cabo pódense resumir la seguinte lista:

- Ten que controlar, configurar e monitorizar o estado da electrónica do detector, as temperaturas e a humidade.
- Ten que permitir realizar calibracións do detector con datos reais.
- Ten que realizar controis exhaustivos dos módulos de xeito individual.
- Ten que integrar accesos a sistemas externos como son as bases de datos, o sistema DSS[3], o nivel superior de lóxica de disparo do LHCb e o sistema TFC[4].

Adicionalmente e por razóns de seguridade, diseñouse e implementouse unha árbore paralela de control denominada *Safety Tree* que enlaza ramas da árbore de control que doutro xeito non estarían conectadas. O obxetivo do *Safety Tree* é empregá-las sinais de monitorización para adiantarse ás accións do sistema *DSS*, e se a situación o precisa, levar a cabo un apagado controlado da sección máis

[3]**D**etector **S**afety **S**ystem
[4]**T**ime **F**ast **C**ontrol

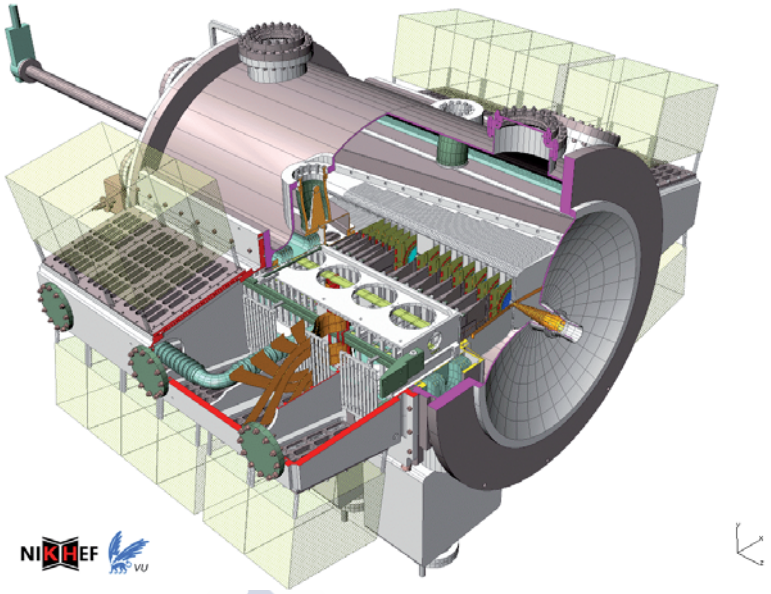

Figure 11.4: Imaxe xerada por ordenador do VELO actual. O feixe de partículas pasa polo centro do detector, e alí prodúcense as colisións.

pequena posible do detector. O motivo de tentar evitar no posible que o sistema *DSS* sexa disparado é que este sistema corta a alimentación dos sistemas afectados, o cal pode ter consecuencias non desexadas nuns equipos tan delicados.

11.3 O proxecto para construir o futuro LHCb VELO

O detector *VErtex LOcator* é o detector de micro-pistas de silicio instalado arredor do punto de colisións do LHCb. O papel do *VELO* é crítico no funcionamento xeral do LHCb, proporcionando unhas resolucións excelentes na determinación dos vértices de desintegracións, unha alta eficiencia e unha identificación rápida de trazas para as lóxicas de disparo.

O experimento LHCb vaise actualizar no ano 2018 e a luminosidade incrementarase ata 2×10^{33} cm^{-2}s^{-1}, alcanzando 10 fb^{-1} por ano. Os sistemas de disparo tamén serán actualizados. Tras esta actualización, tódolos detectores serán lidos a unha frecuencia de 40 MHz, entregando os datos a un sistema de disparo e selección totalmente configurable por software.

O futuro VELO terá pois que soportar doses de radiación e anchos de banda moi superiores ós do VELO actual debido as novas condicións do LHCb, pero tamén a que estará situado aínda máis preto do feixe de partículas.

11.3.1 O VELO actual

O VELO actual consiste nun conxunto de 42 módulos (ver Figura 11.4). Cada módulo ten dous sensores que proporcionan as coordenadas R-ϕ por onde pasaron

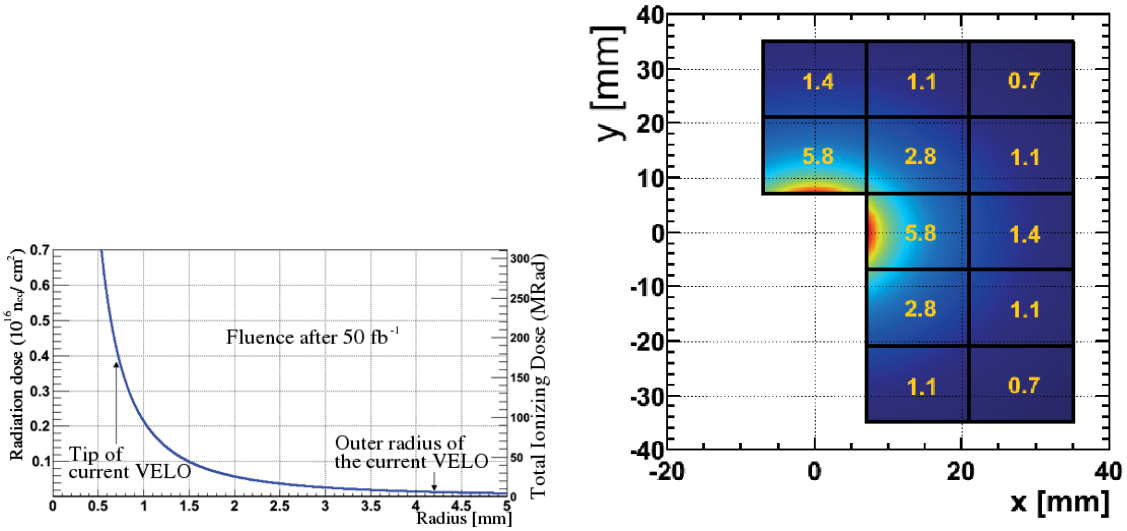

(a) Dose de radiación esperada en función da distancia ó feixe de partículas.

(b) Número de trazas por colisión esperadas nun módulo de píxeis.

Figure 11.5: Valores esperados de radiación e trazas por colisión nas condicións calculadas para o futuro VELO. Figura obtida de Ref. [52].

as partículas. Os sensores do VELO están instalados dentro da tubería de vacío, a só 7 mm do feixe, aínda que encerradas nunha caixa denominada *RF-foil*.

Os obxetivos principais do VELO pódense resumir nos seguintes puntos:

- Distinguir entre os vértices de colisión e de desintegración.
- Reconstruir segmentos de liñas rectas a partires dos impactos nos sensores de silicio do detector. Eses segmentos son empregados polo software do LHCb para reconstruir trazas completas.
- Descartar eventos nos que haxa demasiadas colisións dentro do primer nivel da lóxica de disparo.
- Emprégase no nivel superior de lóxica de disparo, xunto co resto de detectores, para determinar aquelas colisións interesantes e gardalas en disco.

11.3.2 O futuro VELO

O futuro VELO terá que lidar con condicións de radiación e de ancho de banda moito máis esixentes ca o VELO actual. Situado aínda máis cerca do feixe de partículas, a só 5.1 mm, a dose de radiación agardada será extremadamente non uniforme, chegando ata 200 MRad (8×10^{15} 1 MeV n_{eq}/cm^2) nas rexións interiores do sensor, e 3.2 MRad nas máis alonxadas (Figura 11.5).

Para os sensores do futuro VELO dúas tecnoloxías foron tidas en consideración: micro-pistas e pixeis. Para a primeira opción, fun responsable da construcción e

caracterización de varios prototipos co obxetivo de atopar solucións a diferentes inconvintes da tecnoloxía de micro-pistas. En canto a segunda, encargueime das probas de tres sensores da familia Medipix/Timepix que foron levadas a cabo nas instalacións do CERN. Dous destes sensores foran irradiados con neutróns co obxetivo de poder analizar o impacto de diferentes estructuras de aneis de garda nas eficiencias dos sensores.

11.3.3 Prototipos de micro-pistas para o futuro VELO

Como parte do proxecto para o futuro VELO, tres prototipos de micro-pistas foron testados con feixes de pións de momento 120 GeV/c nas área experimental do SPS[5] no CERN.

O prototipo PR01

O sensor PR01 foi fabricado por Hamamatsu Photonics. Trátase dun sensor n^+-sobre-n, 300 μm de grosor, con forma quasi-circular abarcando un arco de 72º. As 1006 pistas están dispostas de xeito radial, e distribuídas en diferentes rexións con distancia entre pistas constante: 40 μm na rexión interna do sensor e 60 μm na externa.

O sensor PR01 foi micro-soldado a un híbrido da IT que conta de tres chips de lectura (Beetles). Non tódolos canles de lectura dos Beetles puideron ser conectados a micro-pistas por múltiples causas: pes de soldadura sucios, faios nos fíos de soldadura ou porque foran usados para probas anteriores. En total únicamente puideron ser micro-soldados un total de 338 canles.

Dado o baixo número de micro-pistas lidas, e o feito de que están distribuídas por diferentes rexións, non foi posible facer medidas precisas de eficiencia neste sensor.

As propiedades eléctricas do sensor PR01 foron caracterizadas nas instalacións do grupo GAES[6] da USC. A curva IV (Figure 11.6) fíxose antes de soldar o sensor ó híbrido. Os valores medidos amosan que o punto de ruptura do sensor está por riba de 350 V.

Posteriormente o sensor PR01 foi caracterizado con partículas na xa mencionada área experimental do SPS, empregando un telescópio construído con dispositivos Timepix. Na Figura 11.7 amósase a relación entre a resolución do sensor PR01 e o ángulo que forma coas partículas incidentes. Na rexión de 40 μm o ángulo óptimo é 7.6º e na rexión de 60 μm é de 11.3º. Os resultados amosan unha resolución de 5.6 (9.7) μm na rexión de 40 (60) μm a ángulo óptimo, sendo a resolución binaria neses casos de 11.5 (17.3) μm.

[5] **S**uper **P**roton **S**ynchrotron
[6] **G**rupo de **A**ltas **E**nerxía**S**

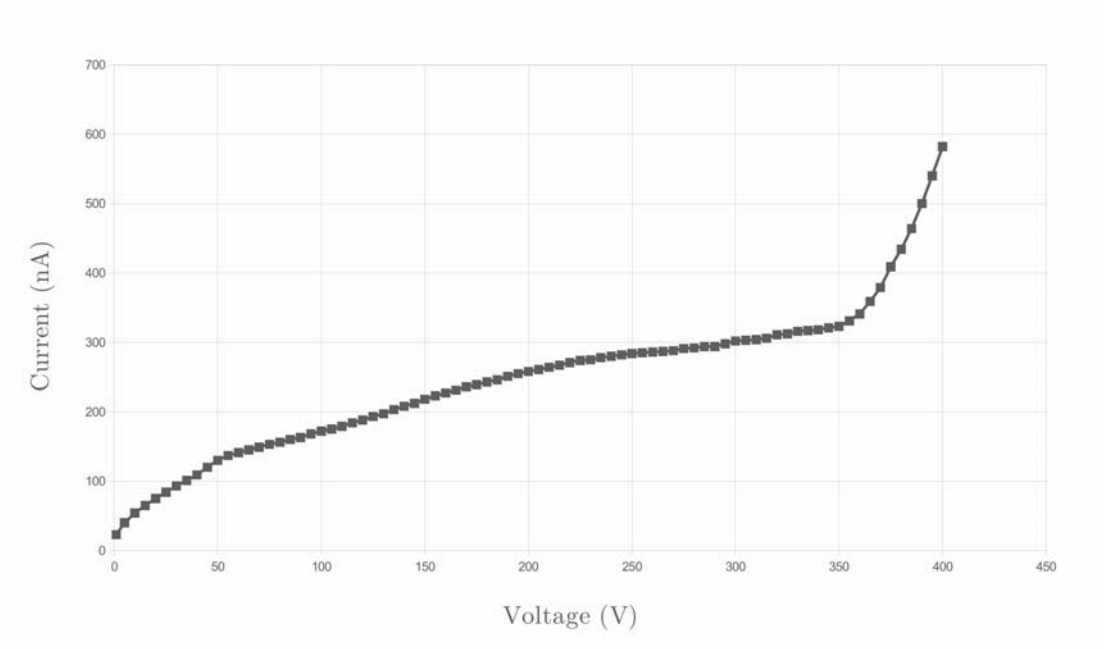

Figure 11.6: Curva IV do sensor PR01.

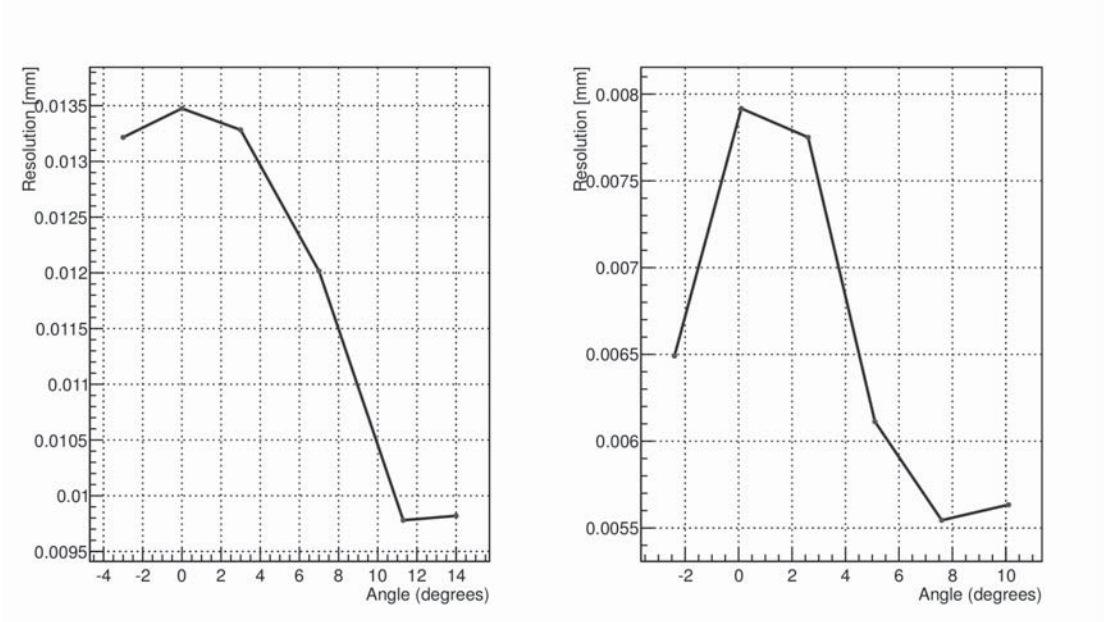

Figure 11.7: Resolución do sensor PR01 en función do ángulo das partículas incidentes ca perpendicular do sensor.

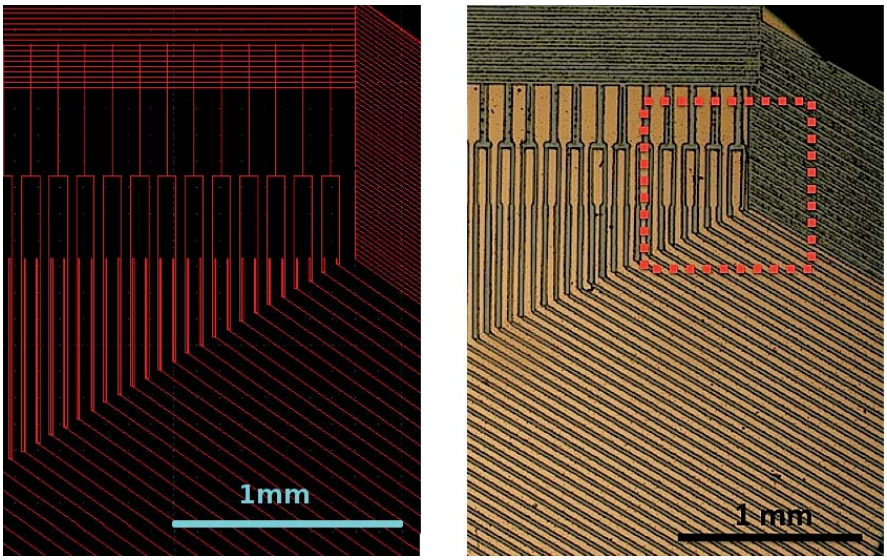

Figure 11.8: Diseño do adaptador de pistas (esquerda) comparado cunha microfotografía do resultado (dereita).

O prototipo DØ

O sensor DØ é un sensor de micro-pistas fabricado por Hamamatsu Photonics nunha oblea de tipo p^+-sobre-n e un único anei de garda. Ten a particularidade de incluir pistas intermedias que non están instrumentadas. A distancia entre pistas é de 30 μm, pero como están instrumentadas de forma alterna, a distancia efectiva entre canles de lectura é de 60 μm. No ano 2011 o sensor DØ foi micro-soldado nas instalacións do grupo GAES a un híbrido da TT con catro chips de lectura (Beetles).

Durante a fase de construcción desenvolvín xunto con Eliseo Pérez e Francisco Rey un método novedoso para fabricar adaptadores de pistas mediante a técnica de ablación por láser. A motivación para desenvolver un novo procedemento foi a procura dunha alternativa ao proceso fotolitográfico que fora máis rápida e económica. A ablación láser retira as partículas de aluminio dun substrato que previamente fora metalizado, seguindo o diseño xerado por un software tipo CAD, conseguindo fabricar adaptadores de pistas de moi alto nivel de integración e unha alta fiabilidade. A Figura 11.8 amosa unha sección do diseño do adaptador de pistas xunto co resultado final.

O sensor DØ foi caracterizado eléctricamente en Santiago coas curvas IV e CV (Figure 11.9). Representando $1/C^2$ fronte a voltaxe de polarización podemos obter máis claramente a voltaxe de deplexión, que sería o punto no que o valor de $1/C^2$ faise constante. Para o DØ determinouse unha voltaxe de deplexión arredor de 120 V.

O sensor DØ foi caracterizado con feixes de partículas nas mesmas instalacións que foran empregadas polo PR01 (Figura 11.10). Os resultados do barrido a diferentes ángulos móstranse na Figura 11.11. A resolución do DØ a ángulo óptimo (5.3°) resultou estar arredor de 9.55 μm, mentras que a resolución binaria é de

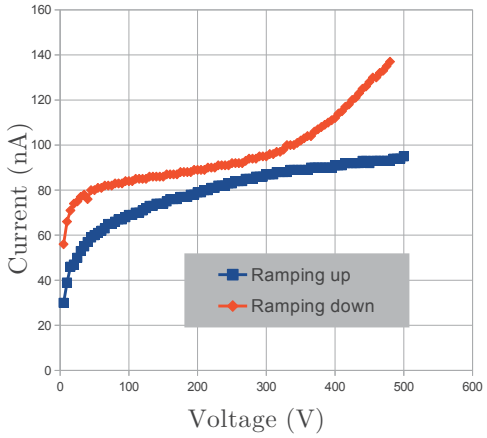

(a) Curva IV do sensor DØ

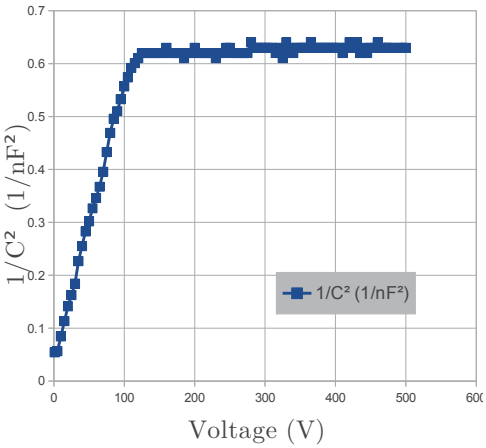

(b) Curva CV do sensor DØ

Figure 11.9: Curvas IV e CV do sensor DØ. En troques de representar directamenta a curva CV, sóese representar $1/C^2$ fronte a voltaxe, o cal amosa máis claramente cal é a voltaxe de deplexión.

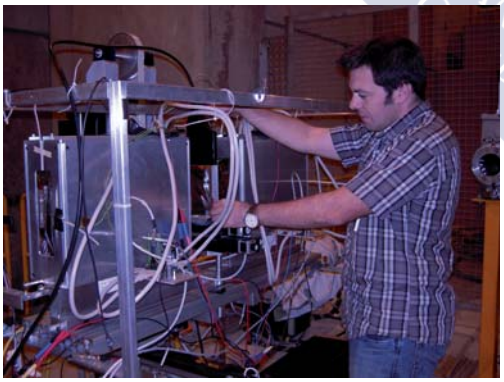

(a) Fotografía do autor durante a instalación do DØ na posición de probas en medio do telescópio Timepix

(b) Equipo de Santiago durante a campaña do 2011 de probas na área experimental do SPS. Comenzando pola esquerda: Abraham Gallas Torreira, Eliseo Pérez Trigo e o autor.

Figure 11.10: O DØ montado no telescopio Timepix.

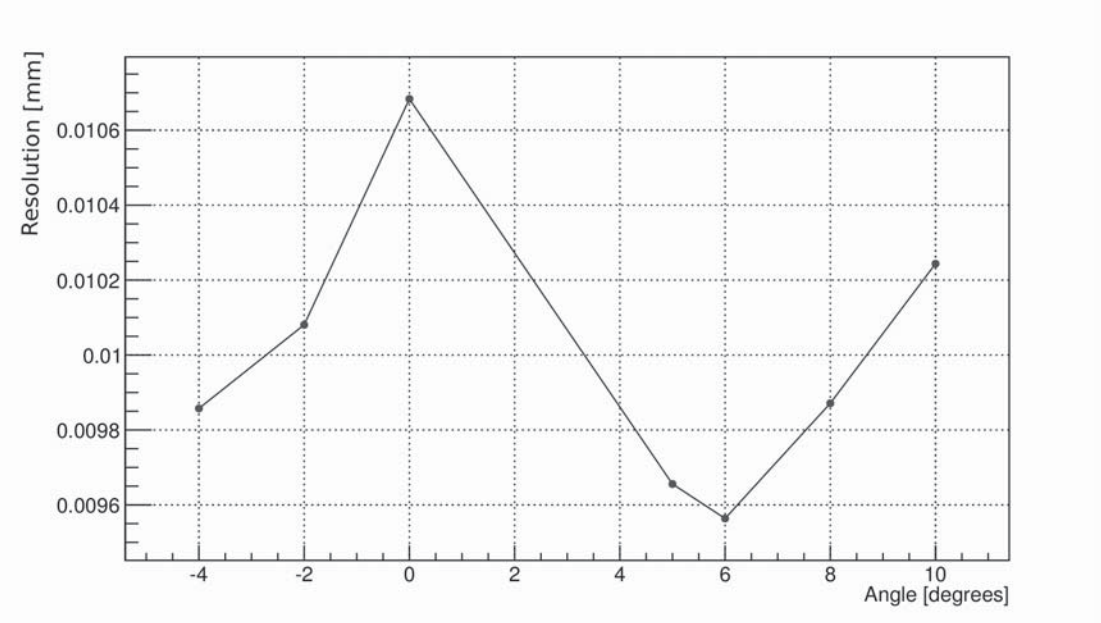

Figure 11.11: Resolución do DØ en función do ángulo.

17.3 μm.

Na Figura 11.12 pódese apreciar que a eficiencia do DØ está por riba do 99%.

De acordo co esperado, demostrouse que o número de micro-pistas que detectan una sinal (*cluster size* en inglés) aumenta conforme o fai a voltaxe de polarización. Cando sobrepasamos a voltaxe de deplexión, aumenta a velocidade de deriva dos pares electrón-hoco xerados e polo tanto redúcese a súa dispersión.

O prototipo de micro-pistas para o futuro VELO

Como parte do programa para desenvolver of futuro VELO, diseñáronse varios sensores n^+-on-n ca empresa Hamamatsu Photonics, que foron servidos na segunda metade to 2012. Cada un destes sensores ten 2560 micro-pistas que precisan dun total de 20 chips Beetle para ser lidas. Os sensores foron construídos seguindo dúas xeometrías, unha radial e outra angular, e con dous espesores distintos: 150 e 200 μm.

Xunto con Eliseo Pérez procedimos a facer a metroloxía dos sensores, a súa caracterización eléctrica, a fabricación do adaptador de pistas, a micro-soldadura cun híbrido da TT e medidas do cociente sinal-ruido tanto con feixes láser como con partículas β^- procedentes dunha fonte de ^{90}Sr.

Para realizá-las curvas IV os sensores foron illados do soporte metálico mediante unha lámina de *Kapton*®, e a polarización foi feita polos contactos a cara superior. As curvas IV resultantes amosanse na Figura 11.14, e as curvas CV na Figura 11.15. Tal e como se agardaba, os sensores de 200 μm de espesor atópanse totalmente deplexionados a un voltaxe de -100 V, mentras que os sensores de 150 μm só precisan -60 V.

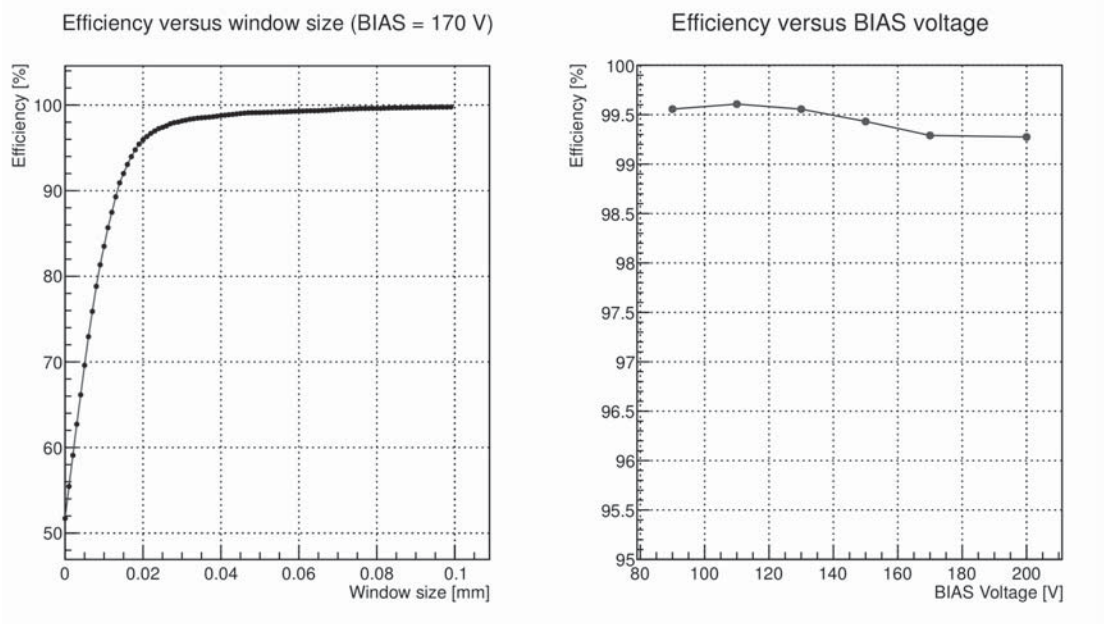

Figure 11.12: A figura da esquerda amosa a eficiciencia do DØ medida como a porcentaxe de partículas que teñen unha sinal asociada no detector dentro dunha distancia determinada. A figura da dereita amosa a eficiencia en función do voltaxe de polarización. Estes valores corresponden a unha distancia máxima de 60 μm entre partícula e sinal.

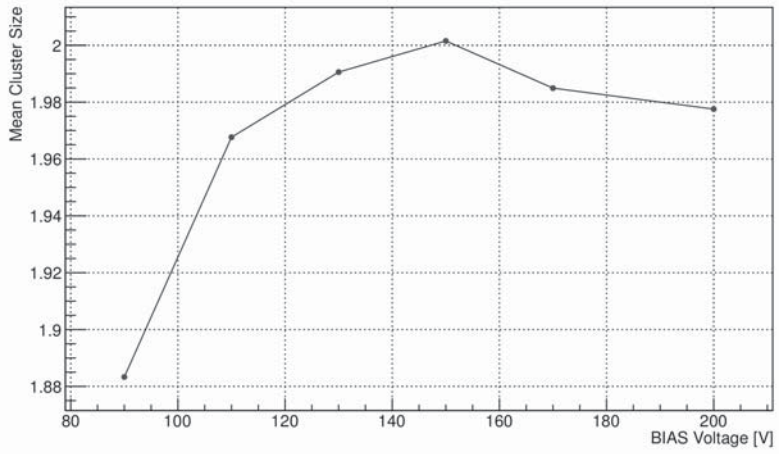

Figure 11.13: Evolución do número promedio de micro-strips do DØ con sinal en función do voltaxe de polarización.

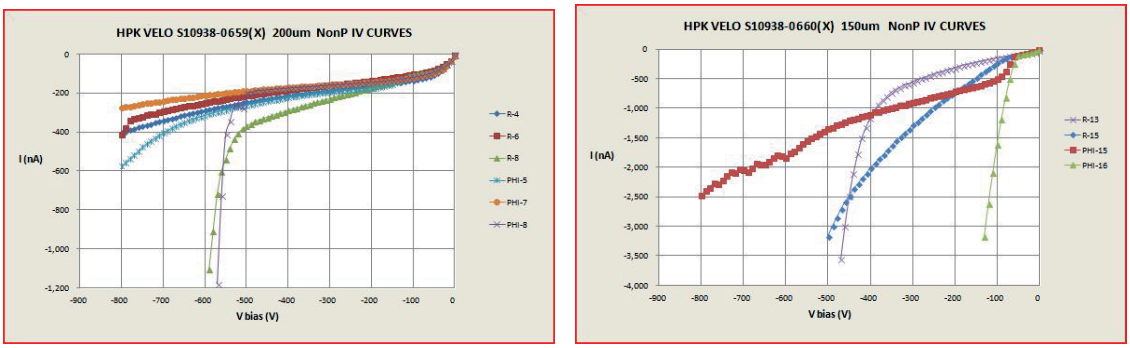

Figure 11.14: A figura da esquerda corresponde ás curvas IV dos sensores de 200 μm de espesor, mentras que os da dereita corresponden ós sensores de 150 μm.

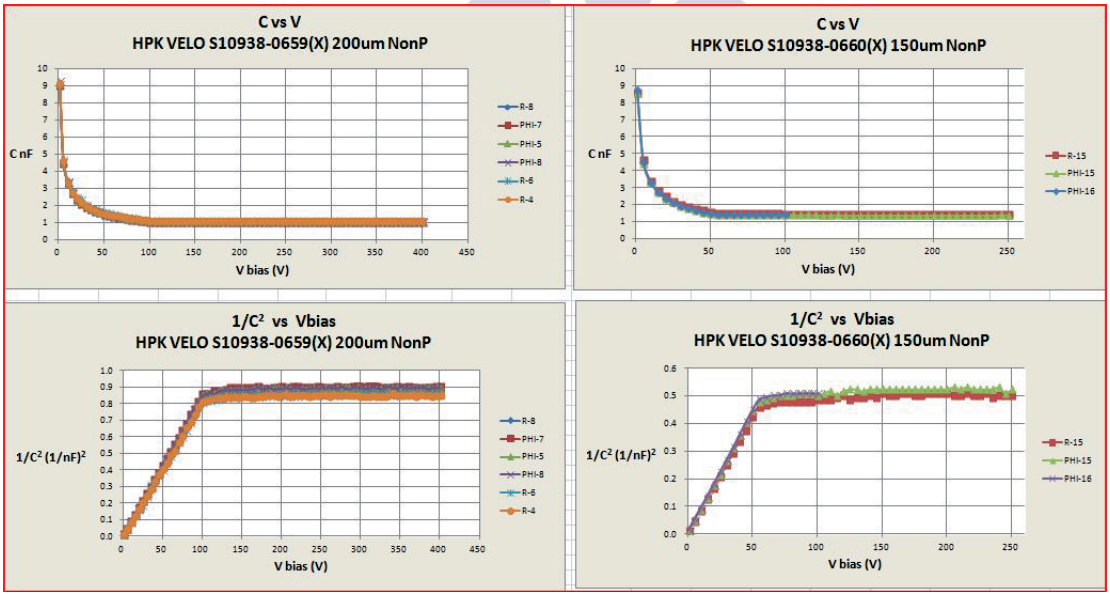

Figure 11.15: Curvas CV para os sensores de 200 μm e 150 μm. As figuras inferiores amosan os valores de $1/C^2$ en lugar dos da capacidade, xa que deste xeito resulta máis claro ver a voltaxe para a cal o sensor está completamente deplexionado..

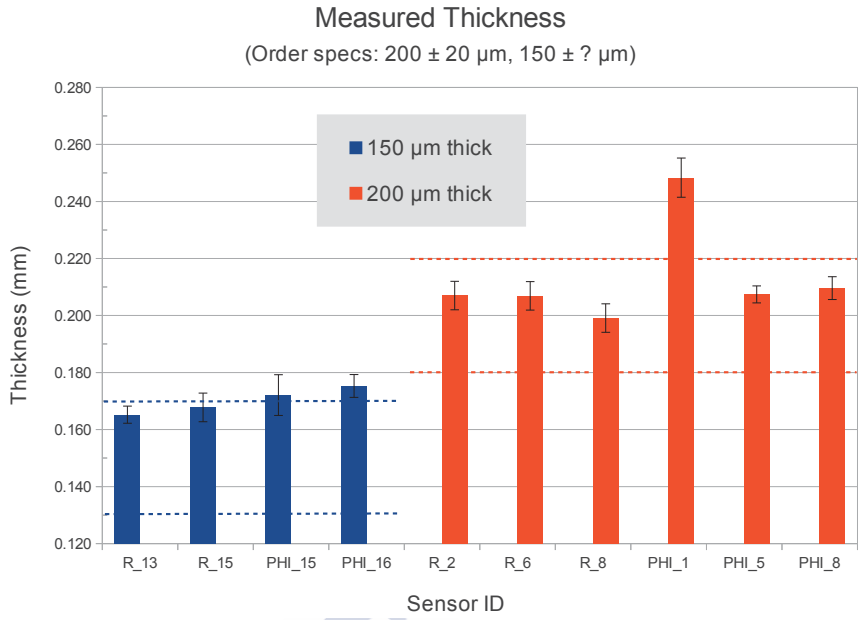

Figure 11.16: Espesor dos sensores. As liñas punteadas corresponden as tolerancias especificadas na orde de compra.

O principal obxetivo de facer a metroloxía dos sensores era a de medir o seu espesor e o seu abombamento. Un resumen dos datos tomados móstrase na Figura 11.16 e na Figura 11.17. De acordo cos valores de tolerancia admitidos, tódolos sensores excepto un cumpren coas especificacións (liña de puntos). Además os sensores de 150 μm de espesor están máis abombados ca os de 200 μm, fenómeno éste que tamén era agardado.

Os láseres son empregados a miúdo en instrumentación para comprobar as propiedades dos sensores. Neste caso, empregamos dous láseres distintos, un de 660 nm e outro de 1060 nm para caracterizar un módulo construído cun sensor tipo R de 200 μm de espesor. A Figura 11.18a amosa a profundidade de penetración do láser en función da enerxía do fotón. Pódese comprobar que o láser de 660 nm resulta completamente absorvido nas primeiras decenas de micras, mentras que o láser de 1060 nm atravesa todo o sensor. En consecuencia, o voltaxe de deplexión únicamente pode ser medido co láser de 1060 nm.

Representando o cociente sinal-ruido fronte a voltaxe de polarización do sensor podemos ver cal é a voltaxe de deplexión (Figura 11.18b). De aquí podemos concluir que as primeiras deceas de micras son deplexionadas cun voltaxe de -10 V, e para deplexionar o sensor completo fan falla arredor de -100 V. Este valor é consistente co obtido nas curvas CV.

O sensor tamén foi probado con partículas β^-. Decidiuse empregar unha fonte de ^{90}Sr xa que é unha fonte case pura de β^-, sen case emitir gammas.

Fixéronse medidas do cociente sinal-ruido coa fonte de ^{90}Sr para varios voltaxes de polarización, e os resultados están representados na Figura 11.19. A voltaxe de deplexión obtida está arredor dos -100 V, o cal é consistente co xa visto nas

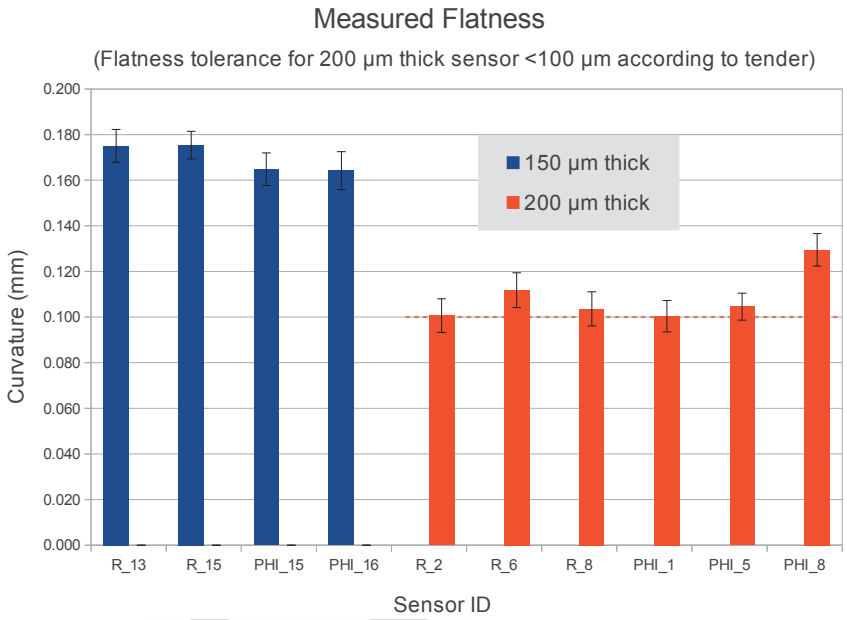

Figure 11.17: Abombamento dos sensores. As liñas punteadas corresponden as tolerancias para os sensores de 200 μm de espesor.

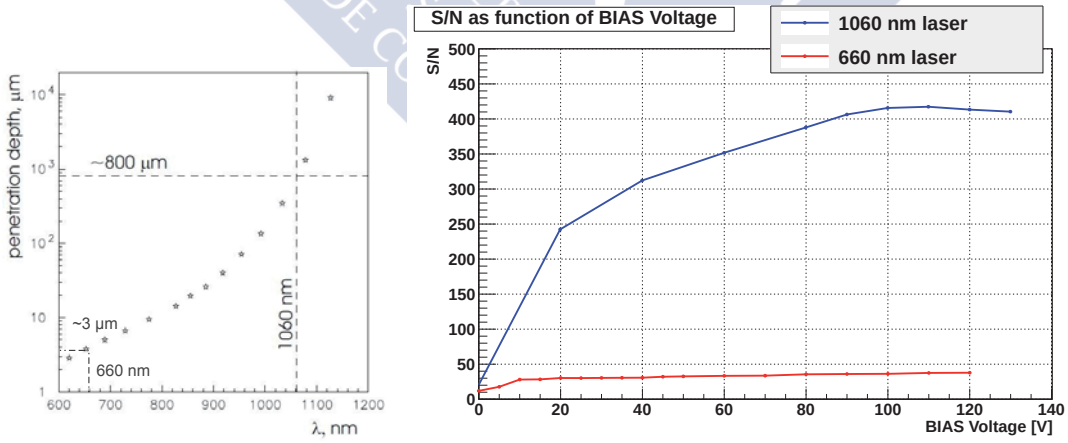

(a) (b)

Figure 11.18: A Figura (a) amosa a profundidade de penetración para os dous láseres empregados. A Figura (b) amosa o cociente sinal-ruido en función da voltaxe de polarización do sensor.

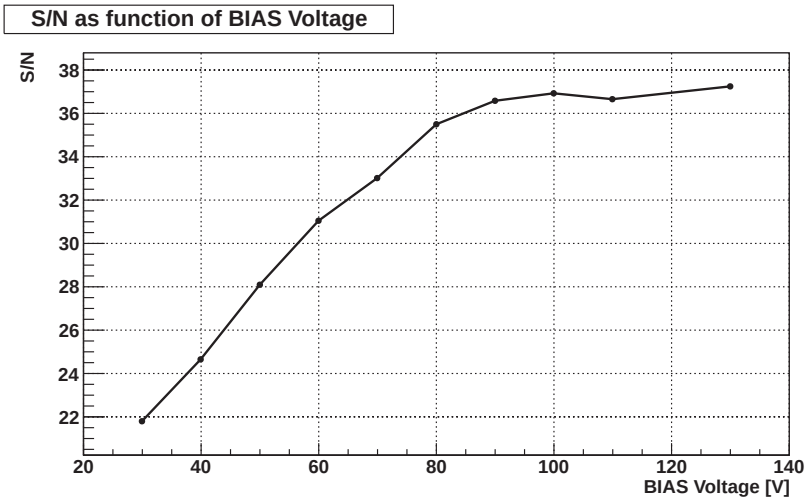

Figure 11.19: Cociente sinal-ruido correspondente a partículas β^- en función da voltaxe de polarización. Apréciase como o cociente permanece prácticamente constante por riba de -100 V.

ID	**ASIC**	**Espesor do sensor**	**Distancia ao borde**	**Irradiación**
E11_W0171	Timepix	200 μm	400 μm	None
W20_D6	Medipix3	200 μm	400 μm	2.5×10^{15} n_{eq}/cm^2
W20_F6	Medipix3	200 μm	250 μm	2.5×10^{15} n_{eq}/cm^2

Table 11.1: Principais características dos dispositivos analizados. Tódolos dispositivos foron producidos no CNM, empregando sensores tipo n^+-sobre-p e dous aneis de garda.

curvas CV e as probas con láser.

As funcións de axuste as curvas de sinal e de ruído amósanse na Figura 11.20 resultando nun cociente sinal-ruido de 33. Leváronse a cabo estudios para determinar se había algunha relación entre este cociente e a lonxitude das micropistas que lían a sinal, atopándose que o cociente mantense sempre constante.

11.3.4 Prototipos de píxeles para o futuro VELO

Como parte do progama para desenvolver o futuro VELO, varios dispositivos Medipix e Timepix foron probados nas instalacións do SPS. Este traballo recolle o traballo feito sobre tres destes dispositivos, fabricados nas instalacións do CNM de Barcelona. As súas características principais están recollidas na Táboa 11.1.

As curvas IV correspondentes os dispositivos de píxeis analizados amósanse na Figura 11.21. Estas curvas xa adiantan que o comportamento do sensor Medipix W20_F6 é moito peor ca o de W20_D6. As curvas IV considéranse un indicador fiable, e neste caso indican que o sensor W20_F6 ten danos graves dalgún tipo.

Ambos sensores foran soldados a ASICs Medipix3 antes de seren irradiados,

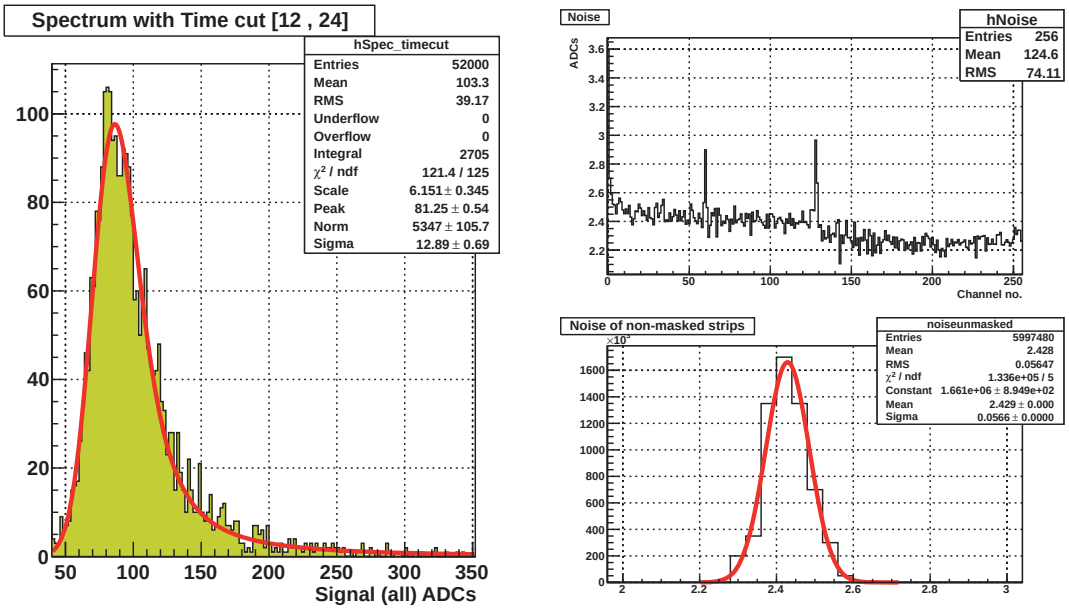

Figure 11.20: Espectro da enerxía depositada polas β^- procedentes da fonte ^{90}Sr. O cociente sinal-ruido calcúlase dividindo o valor máis probable da sinal entre o do ruído, obtendo un valor de 33.

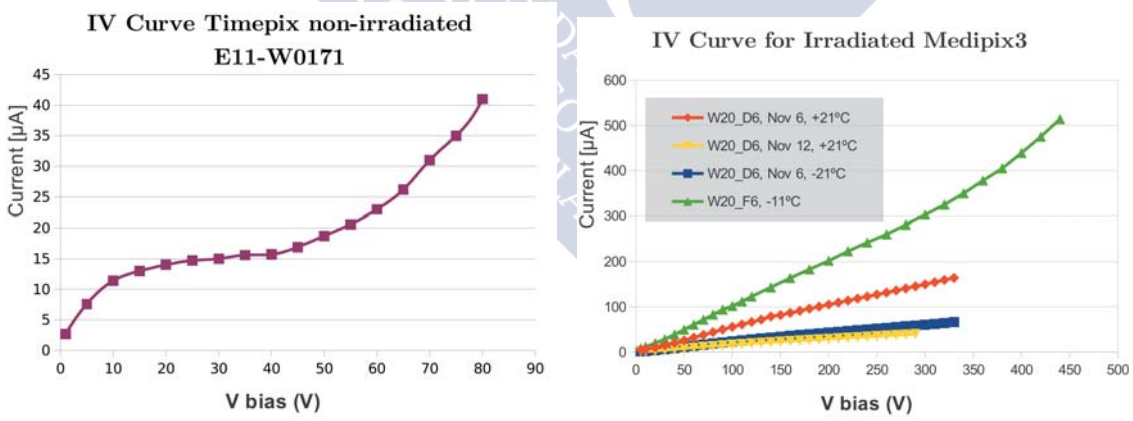

(a) E11_W0171 IV Curve

(b) W20_D6 and W20_F6 IV curves

Figure 11.21: A Figura 11.21a corresponde á curva IV para o Timepix E11_-W0171 a temperatura ambiental ($\simeq$ +23ºC). A Figura 11.21b é a curva IV para os sensores Medipix irradiados medidas a diferentes temperaturas.

os cales son fabricados para soportar doses de radiación máis elevadas das empregadas neste caso. Por desgraza os sensores non foron testados antes da irradiación, polo que non podemos concluír que os danos vistos nas curvas IV sexan consecuencia exclusiva das irradiacións.

O obxetivo principal das probas levadas a cabo en Novembro de 2012 na área experimental do SPS foi a de medir a eficiencia dos sensores Medipix3 irradiados. Ambos dispositivos foron micro-soldados polo método do *bump-bonding* a Medipix3 ASICS, e irradiados con neutróns nas instalacións que a colaboración RD50 ten en Ljubjana ata unha dose de 2.5×10^{15} $1\text{MeVn}_{\text{eq}}/\text{cm}^2$. A Figura 11.22 amosa parte dos datos obtidos. A sinal tan pobre obtida polo dispositivo W20_F6 indica, coma xa fixera a curva IV, que este dispositivo ten un comportamento moito peor ca W20_D6.

Tal e como se pode apreciar na Figura 11.23 a eficiencia dos dispositivos irradiados está por debaixo das dos non-irradiados. O procedemento de análese dos datos foi validado empregando datos doutro Medipix3 non irradiado (o W20_-B6) o cal acadou unha eficiencia próxima ó 100%.

Os datos das probas con feixes de partículas amosaron que a eficiencia dos dispositivos aumenta coa voltaxe de polarización, e disminúe co parámetro de corte THL tal e como se ve na Figura 11.24. Para aillar as ineficiencias dos efectos de distribución da carga xerada entre varios píxeles, calculouse a dependencia da eficiencia co punto no que as partículas impactan dentro do píxel. A Figura 11.25 amosa cómo a eficiencia cae bruscamente cando as partículas impactan na periferia dos píxeis, onde os efectos de distribución de carga son maiores. A Figura 11.26 amosa cómo a eficiencia pode acadar o 95% cando non temos en conta os efectos da dispersión de carga.

A Figura 11.27 amosa a resolución do dispositivo E11_W0171 (o cal proporciona información sobre a carga depositada nos píxeis) e o dispositivo W20_-D6 (que únicamente proporciona información binaria). O ángulo óptimo para dispositivos Medipix/Timepix é 15.3º. Este valor é consistente coa Figura 11.27, onde se ve que a mellor resolución ($\sim$ 5 μm) alcánzase a 14 grados. A gráfica amosa que a resolución do dispositivo E11_W0171 polarizado a 40 V é lixeiramente mellor a baixo ángulo que cando está polarizado a 60 V. O motivo é que a carga ten máis tempo de espallarse cando o campo eléctrico e menor, e polo tanto o cálculo do centro de gravidade do clúster é máis preciso. A resolución binaria para estes dispositivos é de 15.8 μm, o cal é consistente ca resolución alcanzada polo dispositivo irradiado W20_D6.

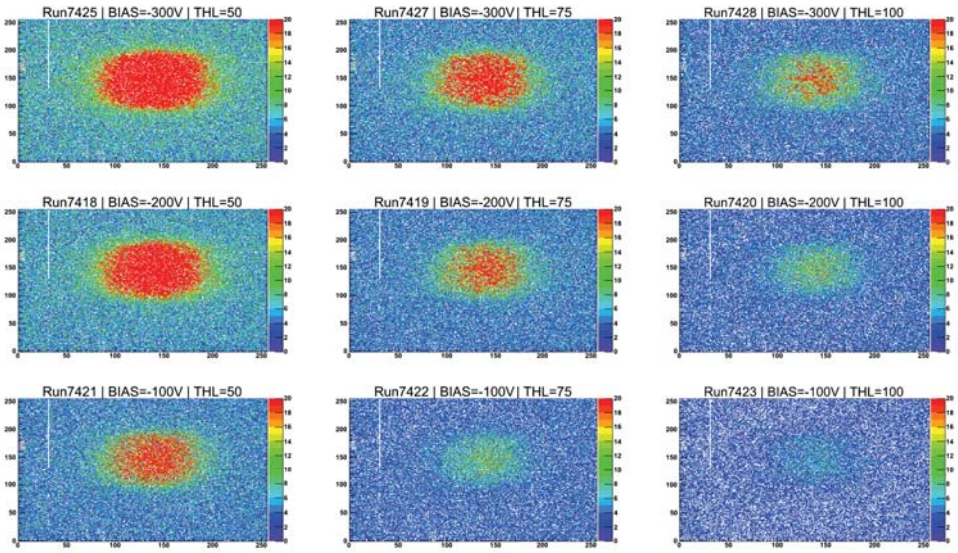

(a) W20_D6 Raw data

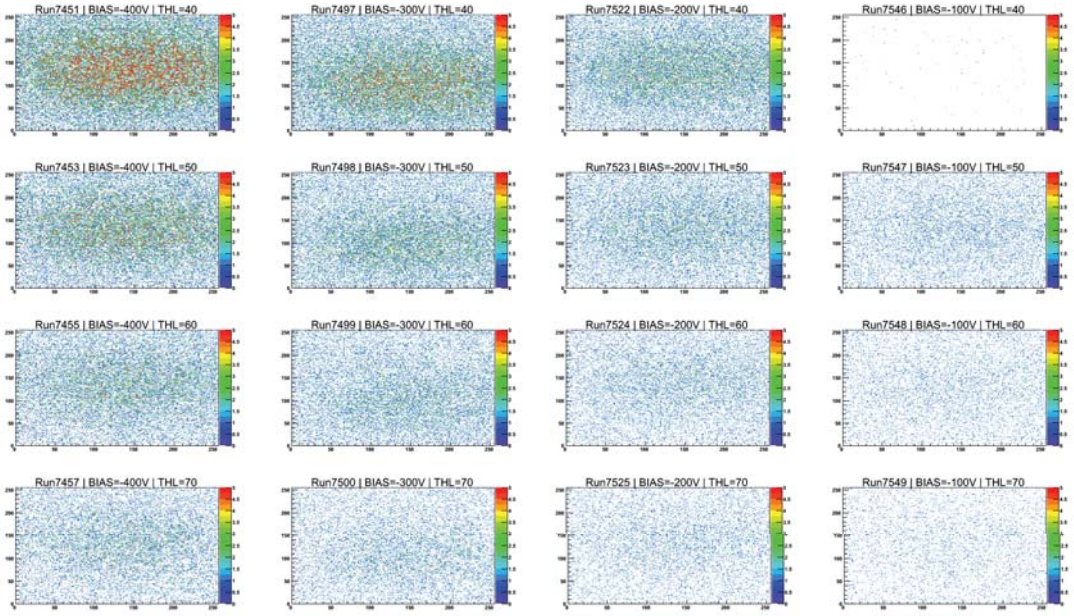

(b) W20_F6 Raw data

Figure 11.22: Mapa de impactos para varias configuracións de valores de corte (THL) e voltaxe de polarización. Estas gráficas foron obtidas empregando o menos número de partículas incidentes, e nelas vese cláramente coma o sensor W20_F6 ten unha eficiencia moi inferior a W20_D6.

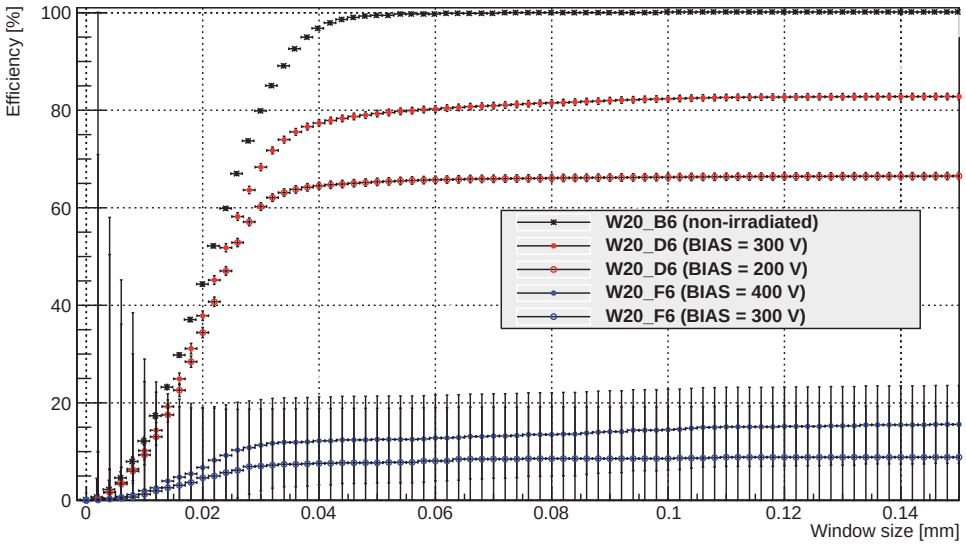

Figure 11.23: Eficiencias dos dispositivos Medipix3 W20_B6 non irradiado e os Medipix3 irradiados W20_D6 e W20_F6 con diferentes voltaxes de polarización.

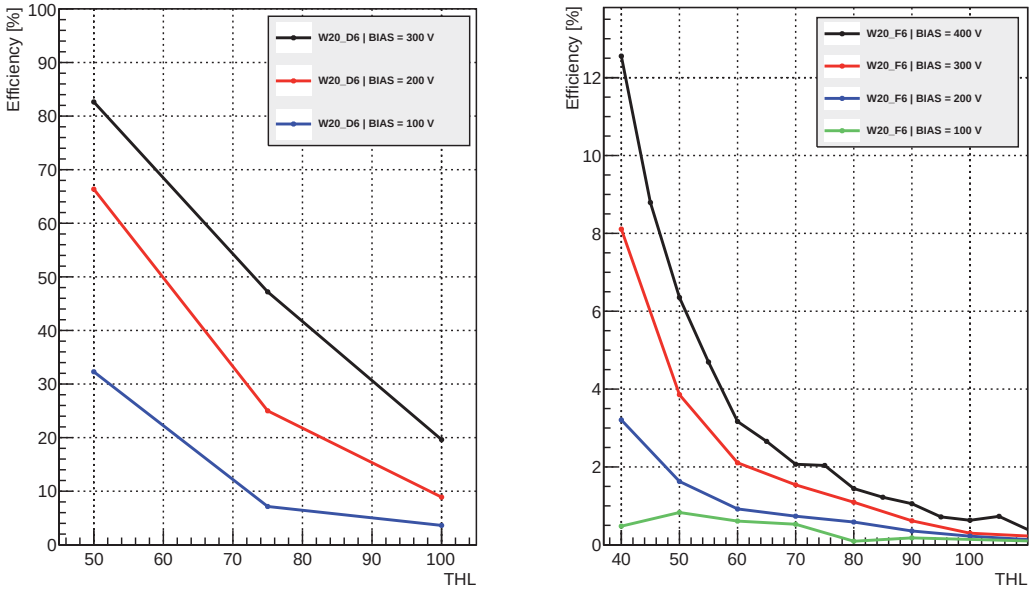

Figure 11.24: Eficiciencia dos dispositivos irradiados W20_D6 e W20_F6 en función da voltaxe de polarización e do parámetro umbral THL.

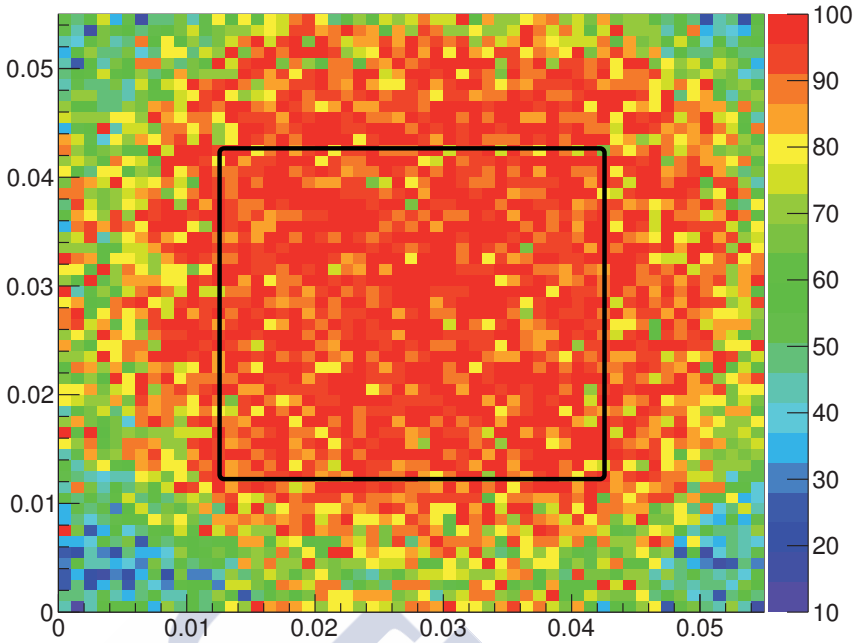

Figure 11.25: Eficiencia do dispositivo irradiado W20_D6 en función do punto no que a partícula impacta dentro do píxel.

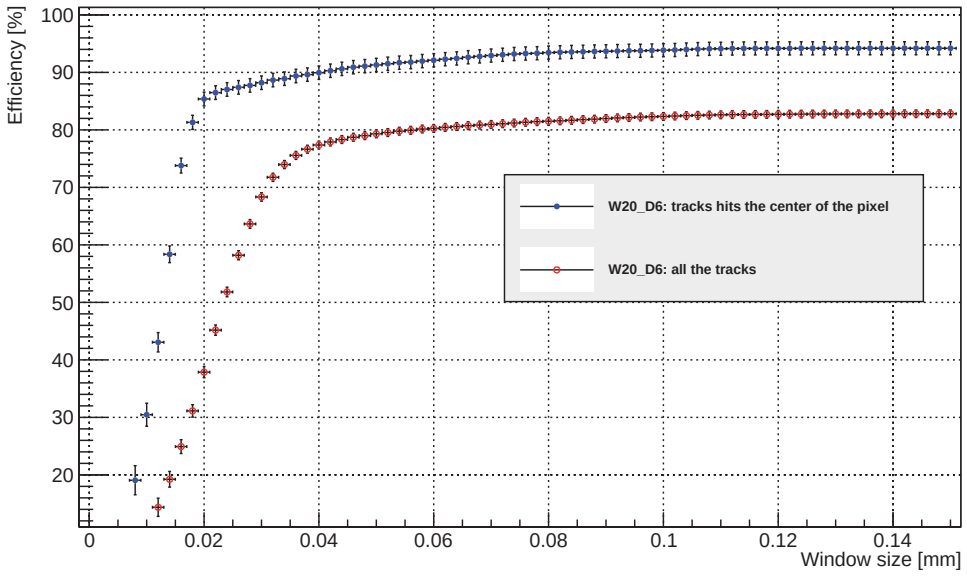

Figure 11.26: Eficiencia do Medipix3 W20_D6 para tódalas trazas e para unha selección das trazas que impactan no medio dos píxeles.

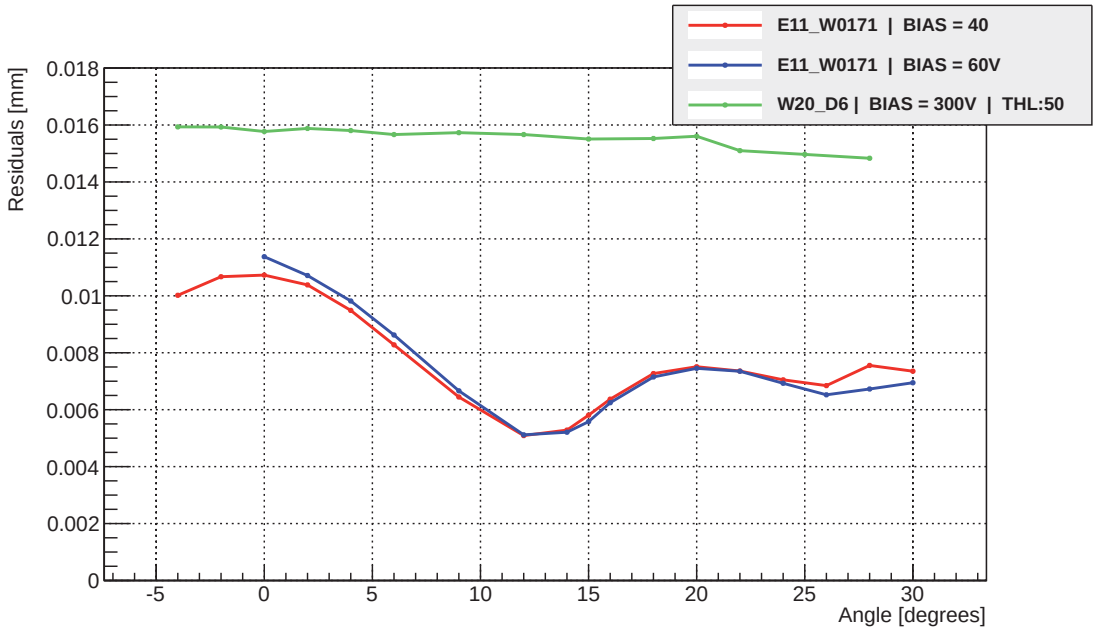

Figure 11.27: Resolución dos dispositivos E11_W0171 e W20_D6 en función do ángulo das partículas incidentes.

Appendices

USC
UNIVERSIDADE
DE SANTIAGO
DE COMPOSTELA

A

Test-beam runs

In this appendix a summary information about the data taking runs are detailed for the different sensors.

A.A PR01

Run Number	PR01 Position (mm)	PR01 angle (degrees)
Run035_PR01Run004	44	10.1
Run036_PR01Run005	44	5.1
Run037_PR01Run006	44	2.6
Run038_PR01Run007	44	7.6
Run039_PR01Run008	44	0.1
Run040_PR01Run009	44	-2.4
Run041_PR01Run010	83.5	0
Run042_PR01Run011	83.5	-3
Run043_PR01Run012	85.5	3
Run044_PR01Run013	85.5	7
Run045_PR01Run014	85.5	11.3
Run046_PR01Run015	85.5	14

Table A.1: Runs taken in June 2010 with the PR01 sensor. Position values are referred to the motion system coordinates, so only relative values are meaningful. Rows with yellow background correspond to those runs where the beam was pointing at the 60 μm region, while in the rest the beam was hitting the 40 μm regions.

Run Number	DØ Position (mm)	DØ bias (V)	DØ angle (degrees)	Comments
4039	43	170	0	Angle Scan
4040	43	170	5	
4041	43	170	6	
4042	43	170	8	
4043	43	170	10	
4046	43	170	-2	
4047	43	170	-4	
4048	43	200	0	BIAS Scan
4049	43	170	0	
4050	43	150	0	
4051	43	130	0	
4052	43	110	0	
4053	43	90	0	
4056	23	170	0	X Scan
4057	33	170	0	
4058	43	170	0	
4059	53	170	0	

Table A.2: Runs taken in August 2011 with the DØ sensor. Position values are referred to the motion system coordinates.

A.B Timepix: E11_W0171

Run	Bias	Angle
Run7001	-40	0
Run7002	-40	-2
Run7003	-40	-4
Run7004	-40	2
Run7005	-40	4
Run7006	-40	6
Run7007	-40	9
Run7008	-40	12
Run7009	-40	14
Run7010	-40	15
Run7011	-40	16
Run7012	-40	18
Run7013	-40	20
Run7014	-40	22
Run7015	-40	24
Run7016	-40	26
Run7017	-40	28
Run7018	-40	30
Run7019	-60	30
Run7020	-60	28
Run7021	-60	26
Run7022	-60	24
Run7023	-60	22
Run7024	-60	20
Run7025	-60	18
Run7026	-60	16
Run7027	-60	15
Run7028	-60	14
Run7029	-60	12
Run7030	-60	9
Run7031	-60	6
Run7032	-60	4
Run7033	-60	2
Run7034	-60	0

Table A.3: E11_W0171 (THL=405) Timepix device. Background color is related to the bias voltage

USC
UNIVERSIDADE
DE SANTIAGO
DE COMPOSTELA

A.C Medipix: W20_D6

Run	Bias	THL	Angle
Run7418	-200	50	0
Run7419	-200	75	0
Run7420	-200	100	0
Run7421	-100	50	0
Run7422	-100	75	0
Run7423	-100	100	0
Run7425	-300	50	0
Run7427	-300	75	0
Run7428	-300	100	0
Run7429	-300	50	4
Run7430	-300	50	2
Run7431	-300	50	-2
Run7432	-300	50	-4
Run7433	-300	50	-6
Run7434	-300	50	-9
Run7435	-300	50	-12
Run7436	-300	50	-15
Run7437	-300	50	-18
Run7438	-300	50	-20
Run7439	-300	50	-22
Run7440	-300	50	-25
Run7441	-300	50	-28

Table A.4: W20_D6 Medipix3 device. Background color is related to the bias voltage.

A.D Medipix: W20_F6

Run	Bias	THL	Angle
7451	-400	40	0
7452	-400	45	0
7453	-400	50	0
7454	-400	55	0
7455	-400	60	0
7456	-400	65	0
7457	-400	70	0
7458	-400	75	0
7459	-400	80	0
7460	-400	85	0
7461	-400	90	0
7462	-400	95	0
7463	-400	100	0
7464	-400	105	0
7465	-400	110	0
7466	-400	115	0
7467	-400	120	0
7468	-400	125	0
7469	-400	130	0
7470	-400	135	0
7471	-400	140	0
7472	-400	145	0
7473	-400	150	0
7474	-400	155	0
7475	-400	160	0
7476	-400	165	0
7477	-400	170	0
7480	-400	175	0
7482	-400	180	0
7483	-400	185	0
7484	-400	190	0
7485	-400	195	0
7486	-400	200	0
7487	-400	205	0
7488	-400	210	0
7489	-400	215	0
7490	-400	220	0
7491	-400	225	0
7492	-400	230	0
7493	-400	235	0
7494	-400	240	0
7495	-400	245	0
7496	-400	250	0
7497	-300	40	0
7498	-300	50	0
7499	-300	60	0
7500	-300	70	0
7501	-300	80	0
7502	-300	90	0
7503	-300	100	0
7504	-300	110	0
7505	-300	120	0
7506	-300	130	0
7507	-300	140	0
7508	-300	150	0
7509	-300	160	0
7511	-300	170	0
7513	-300	180	0
7514	-300	190	0
7515	-300	200	0
7516	-300	210	0
7517	-300	220	0
7518	-300	230	0
7520	-300	240	0
7521	-300	250	0
7522	-200	40	0
7523	-200	50	0
7524	-200	60	0
7525	-200	70	0
7526	-200	80	0
7527	-200	90	0
7528	-200	100	0
7529	-200	110	0
7530	-200	120	0
7531	-200	130	0
7532	-200	140	0
7533	-200	150	0
7534	-200	160	0
7535	-200	170	0
7536	-200	180	0
7537	-200	190	0
7538	-200	200	0
7541	-200	210	0
7542	-200	220	0
7543	-200	230	0
7544	-200	240	0
7545	-200	250	0
7546	-100	40	0
7547	-100	50	0
7548	-100	60	0
7549	-100	70	0
7550	-100	80	0
7551	-100	90	0
7553	-100	110	0
7554	-100	120	0
7555	-100	130	0
7556	-100	140	0
7557	-100	150	0
7558	-100	160	0
7559	-100	170	0
7560	-100	180	0
7561	-100	190	0
7562	-100	200	0
7563	-100	210	0
7564	-100	220	0
7565	-100	230	0
7566	-100	240	0
7567	-100	250	0
7568	-100	100	0
7569	-400	50	4
7570	-400	50	2
7571	-400	50	-2
7572	-400	50	-4

Table A.5: Medipix3 W20_F6 device runs. Background color is related to the bias voltage.

B
Metrology

In this appendix the metrology data for all the Hamamatsu sensors are presented. The methodology to obtain the (X,Y,Z) coordinates of each point is explained in Chapter 7.3.3

B.A R-sensors

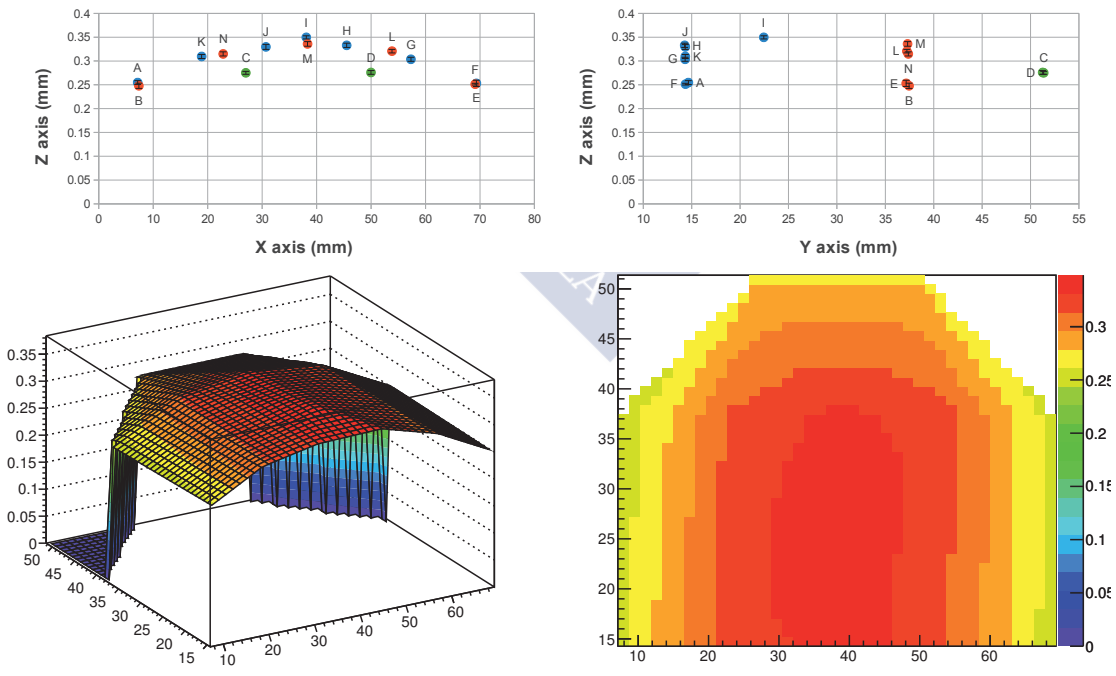

Figure B.1: R_2 sensor. 200 μm thick.

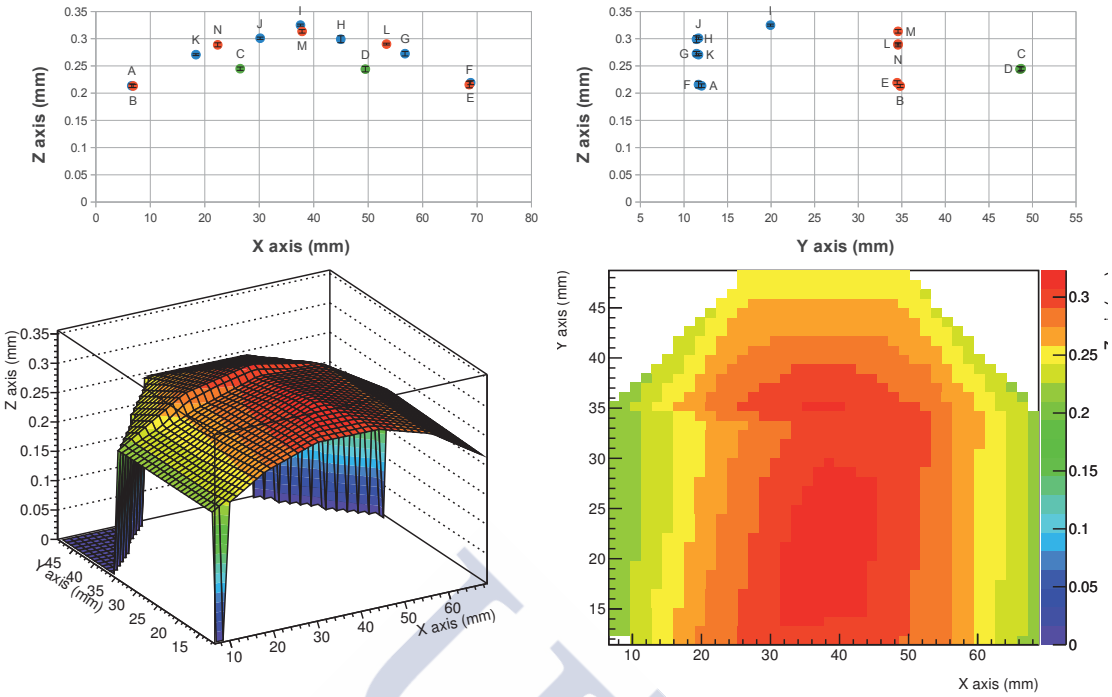

Figure B.2: R_6 sensor. 200 μm thick.

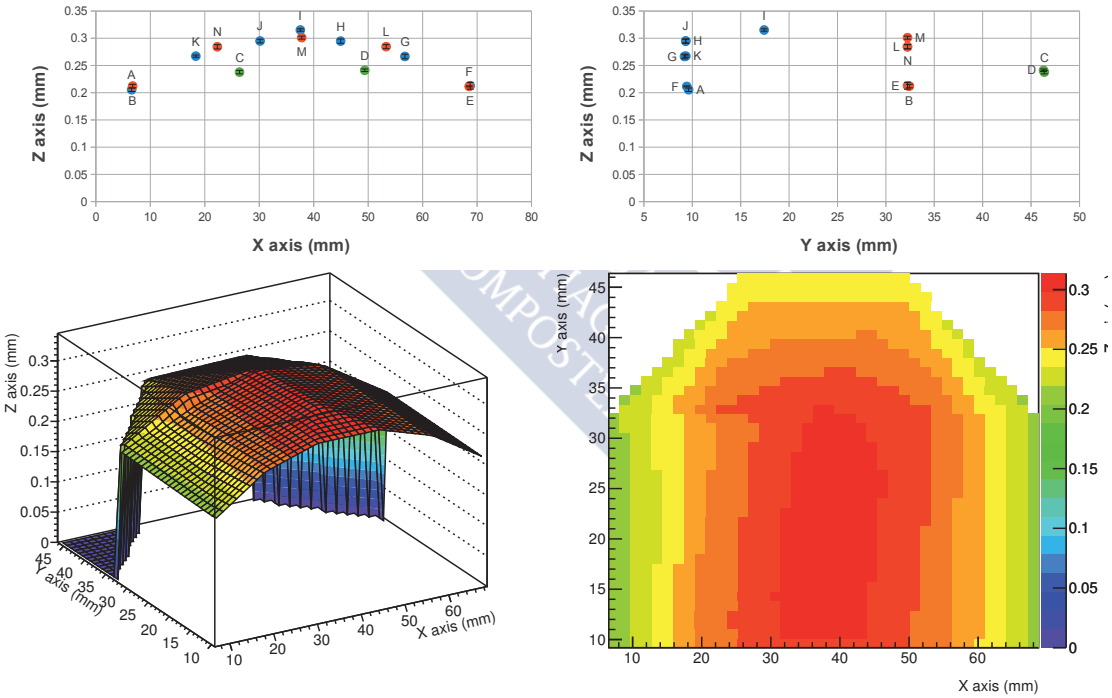

Figure B.3: R_8 sensor. 200 μm thick.

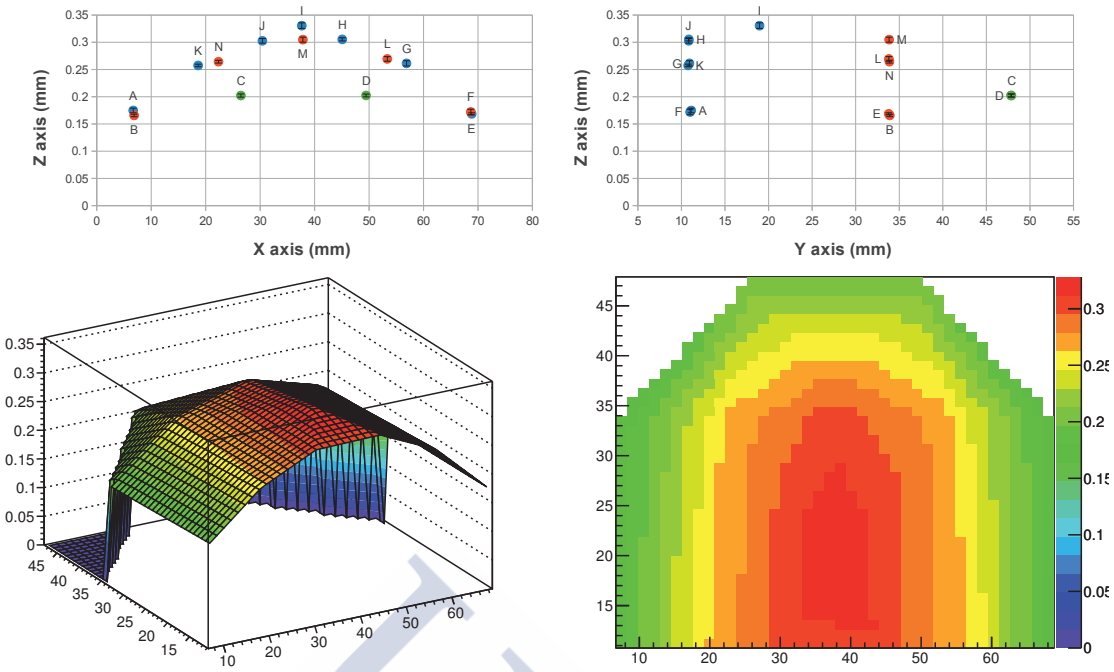

Figure B.4: R_13 sensor. 150 μm thick.

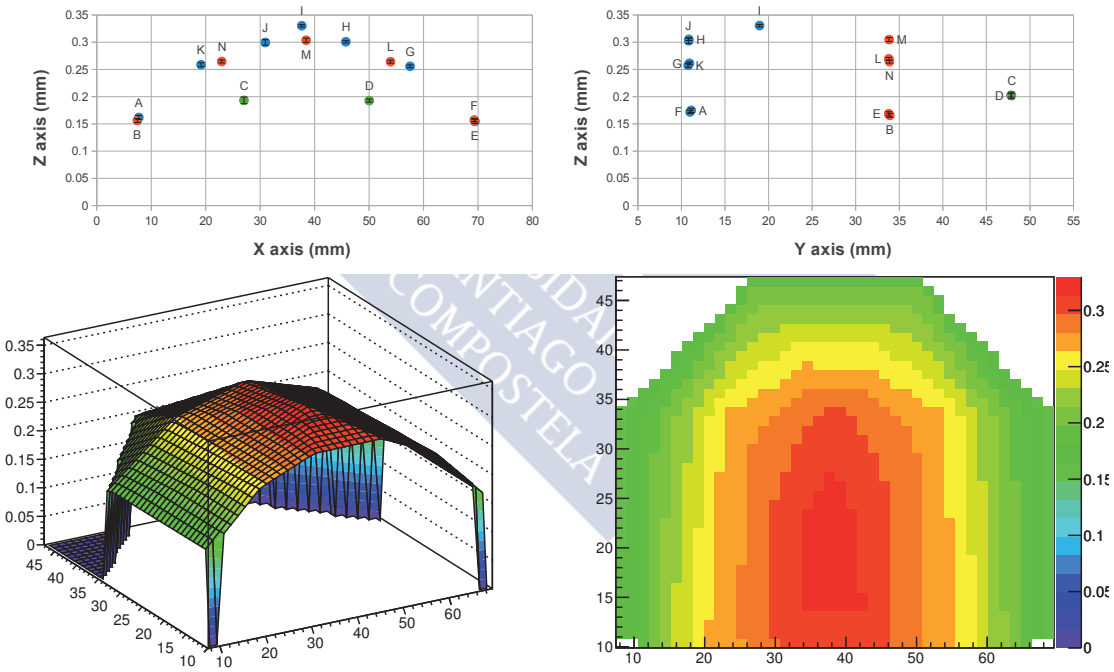

Figure B.5: R_15 sensor. 150 μm thick.

B.B PHI-sensors

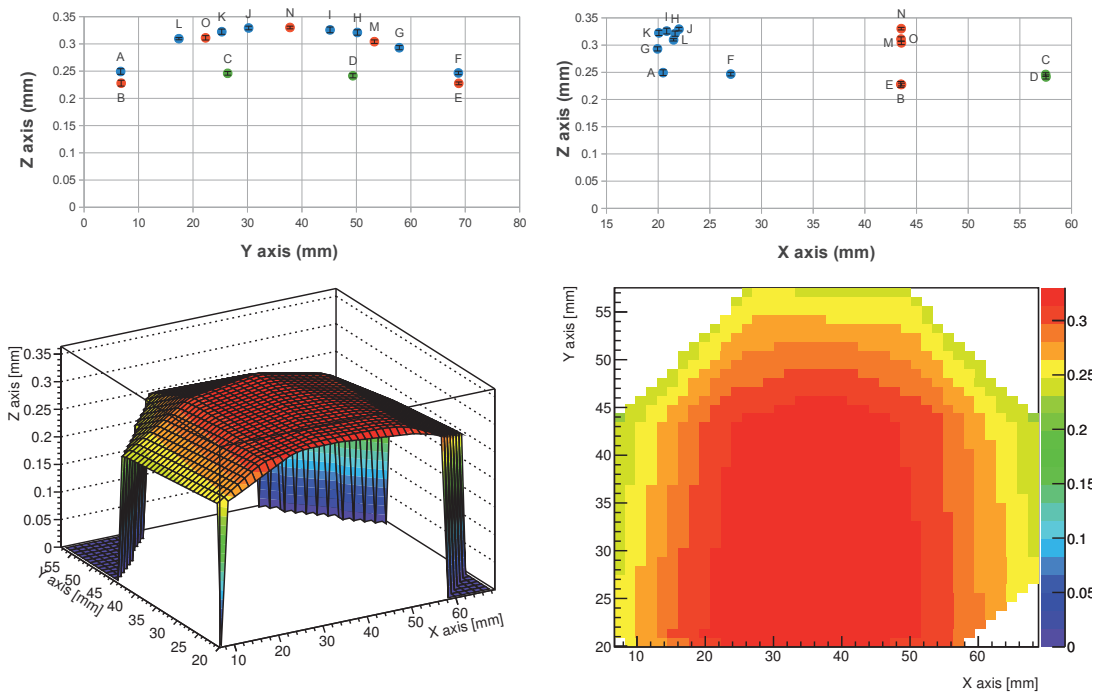

Figure B.6: PHI_1 sensor. 200 μm thick.

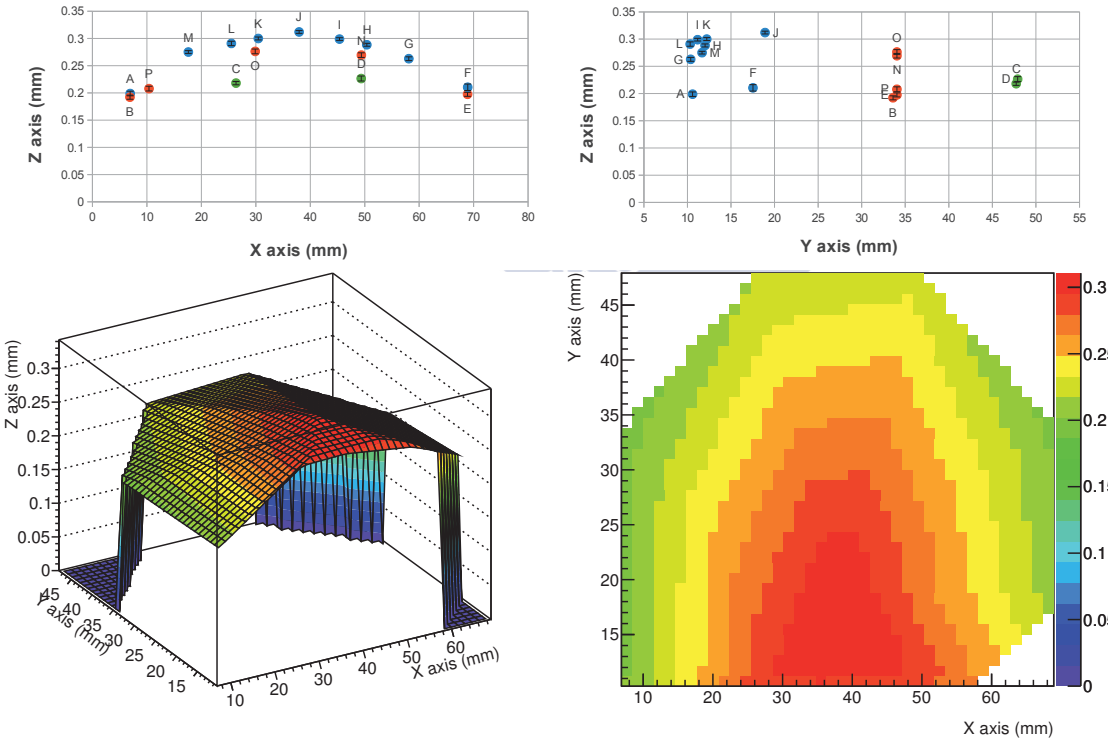

Figure B.7: PHI_5 sensor. 200 μm thick.

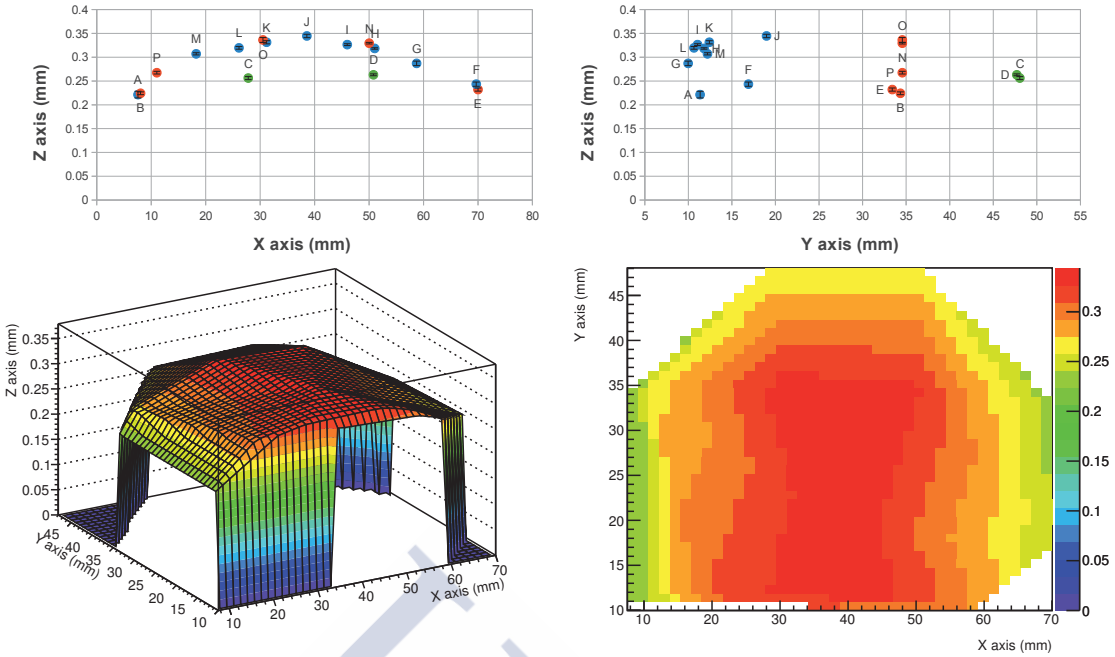

Figure B.8: PHI_8 sensor. 200 μm thick.

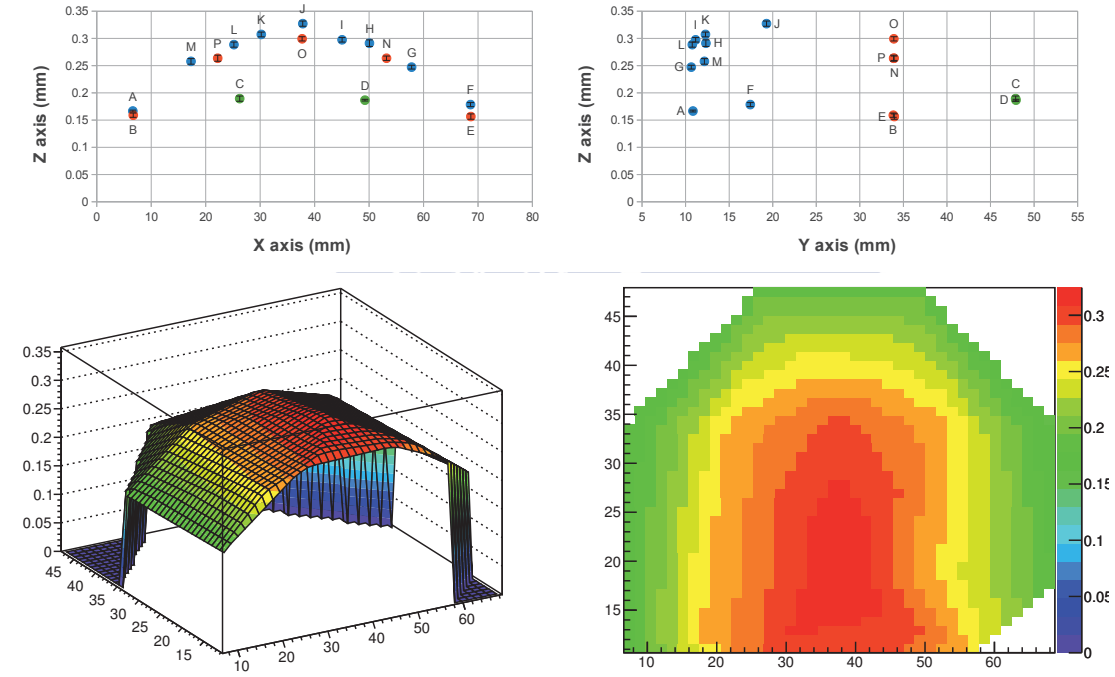

Figure B.9: PHI_15 sensor. 150 μm thick.

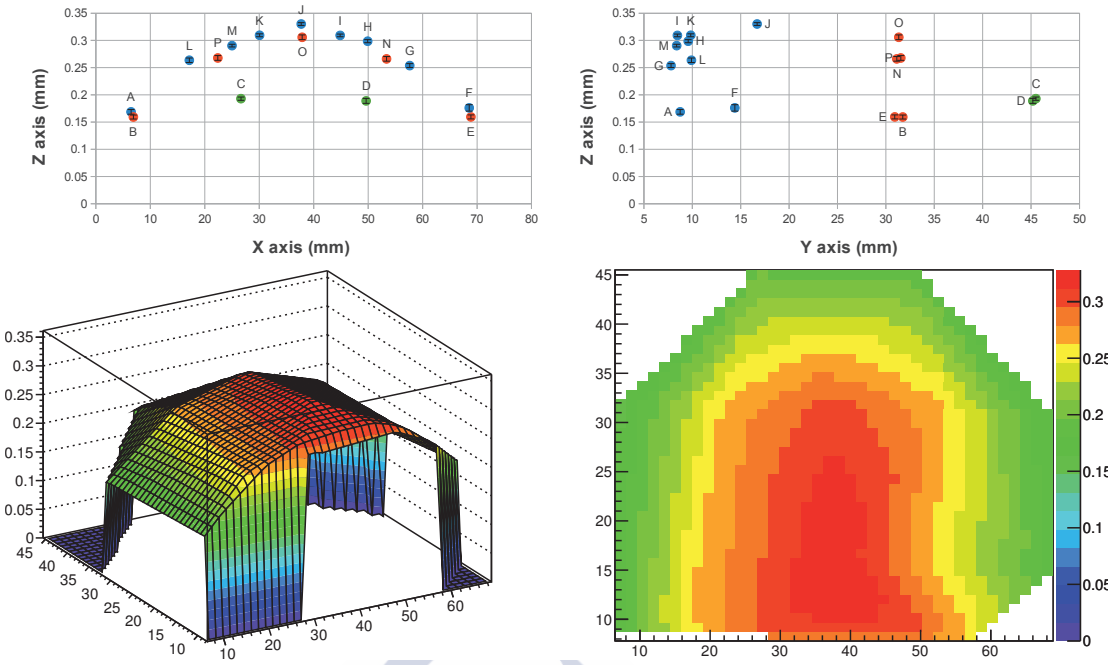

Figure B.10: PHI_16 sensor. 150 μm thick.

Bibliography

[1] The LHCb Collaboration. The LHCb Detector at the LHC. *Journal of Instrumentation*, 3(08):S08005, 2008.

[2] The ALPHA Collaboration. Confinement of antihydrogen for 1,000 seconds. *Nature physics*, 7:558–564, May 2011.

[3] D. Esperante. *Design and Development of Electronics and the Control Software for the Silicon Tracker of LHCb. oai:cds.cern.ch:1385876.* PhD thesis, Santiago de Compostela U., Santiago de Compostela, 2010. Presented 25 Oct 2010.

[4] A. Sambade. *Implementación y desarrollo de un sistema de control distribuido para el experimento LHCb del CERN.* PhD thesis, U. Coruña, La Coruña, 2007. Presented on 28 Feb 2007.

[5] W. Pauli. Letter to Lise Meitner, Gruppe der Radioaktiven bei der Gauvereins-Tatung, Tuebingen, 1930.

[6] C. L. Cowan et al. Detection of the tree neutrino: A confirmation. *Science*, 124:103–104, 1956.

[7] G. Arnison et al. Further evidence for charged intermediate vector bosons at the SPS collider. *Physics Letters B*, 129(3–4):273 – 282, 1983.

[8] G. Arnison et al. Experimental observation of lepton pairs of invariant mass around 95 GeV/c2 at the CERN SPS collider. *Physics Letters B*, 126(5):398 – 410, 1983.

[9] ATLAS collaboration. Observation of a New Particle in the Search for the Standard Model Higgs Boson with the ATLAS Detector at the LHC. *Physics Letters B*, 716(1):1–29, 2012.

[10] CMS collaboration. Observation of a new boson at a mass of 125 GeV with the CMS experiment at the LHC. *Physics Letters B*, 716(1):30–61, 2012.

[11] G. Baur et al. Production of Antihydrogen. *Physics Letters B*, 368:251–258, 1996.

[12] L. Evans and P. Bryant. LHC Machine. *Journal of Instrumentation*, 3(08):S08001, 2008.

[13] The ATLAS Collaboration. The ATLAS Experiment at the CERN Large Hadron Collider. *Journal of Instrumentation*, 3(08):S08003, 2008.

[14] The CMS Collaboration. The CMS experiment at the CERN LHC. *Journal of Instrumentation*, 3(08):S08004, 2008.

[15] The ALICE Collaboration. The ALICE experiment at the CERN LHC. *Journal of Instrumentation*, 3(08):S08002, 2008.

[16] Barbosa-Marinho et al. *LHCb VELO (VErtex LOcator): Technical Design Report. oai:cds.cern.ch:504321.* Technical Design Report LHCb. CERN, Geneva, 2001.

[17] The LHCb Collaboration. LHCb Reoptimized Detector Design and Performance Technical Design Report, Sept 2003. CERN-LHCC/2003-030, CERN.

[18] Barbosa-Marinho et al. *LHCb inner tracker: Technical Design Report.* Technical Design Report LHCb. CERN, Geneva, 2002. revised version number 1 submitted on 2002-11-13 14:14:34.

[19] The LHCb Collaboration. LHCb Outer Tracker Technical Design Report, Sept 2001. CERNLHCC/2001-024, CERN.

[20] Amato et al. *LHCb RICH: Technical Design Report. oai:cds.cern.ch:494263.* Technical Design Report LHCb. CERN, Geneva, 2000.

[21] Amato et al. *LHCb calorimeters: Technical Design Report. oai:cds.cern.ch:494264.* Technical Design Report LHCb. CERN, Geneva, 2000.

[22] Barbosa-Marinho et al. *LHCb muon system: Technical Design Report. oai:cds.cern.ch:504326.* Technical Design Report LHCb. CERN, Geneva, 2001.

[23] Barbosa-Marinho et al. *LHCb muon system: addendum to the Technical Design Report. oai:cds.cern.ch:600536.* Technical Design Report LHCb. CERN, Geneva, 2003.

[24] Barbosa-Marinho et al. *LHCb muon system: second addendum to the Technical Design Report.* Technical Design Report LHCb. CERN, Geneva, 2005. Submitted on 9 Apr 2005.

[25] R. Aaij et al. The LHCb trigger and its performance in 2011. *Journal of Instrumentation*, 8(04):P04022, 2013.

[26] B. Adeva et al. Silicon sensor probing and radiation studies for the lhcb silicon tracker. Technical Report LHCb-2005-033. CERN-LHCb-2005-033, CERN, Geneva, Aug 2005.

[27] A. Vollhardt. Neutron irradiation results for the lhcb silicon tracker data readout system components. Technical Report LHCb-2003-049, CERN, Geneva, Jul 2003.

[28] A. Vollhardt et al. Results of proton irradiation of components for the lhcb silicon tracker. Technical Report LHCb-2004-037. CERN-LHCb-2004-037, CERN, Geneva, Nov 2004.

[29] M. Agari et al. A radiation tolerant fiber-optic readout system for the lhcb silicon tracker. Technical Report LHCb-2005-032. CERN-LHCb-2005-032, CERN, Geneva, Aug 2005.

[30] D. Esperante and A. Vollhardt. Design and development of the Control Board for the LHCb Silicon Tracker. Technical Report LHCb-2007-153. CERN-LHCb-2007-153, CERN, Geneva, Jan 2008.

[31] A. Vollhardt and U. Straumann. *An Optical Readout System for the LHCb Silicon Tracker. oai:cds.cern.ch:836184*. PhD thesis, Univ. Zurich, Zürich, 2005.

[32] C. Gaspar et al. An integrated experiment control system, architecture, and benefits: the LHCb approach. *IEEE Transactions on Nuclear Science*, 51(3):513 – 520, june 2004.

[33] D. Breton et al. SPECS : A serial protocol for experiment control system in LHCb. 2005.

[34] Z. Guzik et al. Driving the LHCb front-end readout. *IEEE Transactions on Nuclear Science*, 51(3):508–12, 2004.

[35] The GOL project. CERN Gigabit Optical Link (GOL) transmitter ASIC.

[36] The QPLL project. CERN Quartz Phase-Locked Loop (QPLL) ASIC.

[37] The DCUF25 project. Cern dcuf25 chip. DCUF User Manual.

[38] R. Jacobsson et al. Readout supervisor design specifications. Technical Report LHCb-2001-012, CERN, Geneva, Mar 2001.

[39] F. Fontanelli et al. Embedded controllers for local board-control. In *Proceedings of the 14th IEEE-NPSS conference on Real time*, RTC'05, pages 64–68, Washington, DC, USA, 2005. IEEE Computer Society.

[40] M. Tobin. Performance of the LHCb Tracking Detectors. Sept 2012.

[41] C. Gaspar. LHCb Experiment Control System, 2012.

[42] C. Gaspar et al. An integrated experiment control system, architecture, and benefits: The LHCb approach. *IEEE Transactions on Nuclear Science*, 51:513–520, 2004.

[43] C. Gaspar and B. Franek. Tools for the automation of large control systems. *IEEE Transactions on Nuclear Science*, 53(3):974–979, 2006.

[44] O. Holme et al. The jcop framework. oai:cds.cern.ch:907906. Technical Report CERN-OPEN-2005-027, CERN, Geneva, Sep 2005.

[45] ETM. SIMATIC WinCC Open Architecture, 2012.

[46] C. Gaspar. LHCb ECS Guidelines. Technical Report 732486 v.3, CERN, Geneva, Apr 2000.

[47] C. Gaspar and B. Franek. Tools for the automation of large distributed control systems. In *Real Time Conference, 2005. 14th IEEE-NPSS*, pages 5 pp.–, 2005.

[48] S. M. Schmeling et al. The Detector Safety System for LHC Experiments. *IEEE Transactions on Nuclear Science*, 51:521–525, June 2004.

[49] R. Aaij et al. Absolute luminosity measurements with the LHCb detector at the LHC. oai:cds.cern.ch:1389907. *Journal of Instrumentation*, 7(arXiv:1110.2866. LHCB-PAPER-2011-015. CERN-PH-EP-2011-157):P01010. 47 p, Oct 2011.

[50] S. Löchner and M. Schmelling. The Beetle Reference Manual - chip version 1.3, 1.4 and 1.5, Nov 2006.

[51] G. Krocker. CP violation in B_s^0 mixing with LHCb. Technical Report arXiv:1112.0868, CERN, Dec 2011. Comments: Proceedings for PIC 2011, Vancouver.

[52] P. Collins. The LHCb VELO (VErtex LOcator) and the LHCb VELO upgrade. *Nuclear Instruments and Methods in Physics Research Section A: Accelerators, Spectrometers, Detectors and Associated Equipment*, 2012.

[53] A. Affolder et al. Radiation damage in the LHCb vertex locator. *Journal of Instrumentation*, 8(08):P08002, 2013.

[54] J. Harrison and A. Webber. Radiation damage in the LHCb VELO. *Nuclear Instruments and Methods in Physics Research Section A: Accelerators, Spectrometers, Detectors and Associated Equipment*, 2012.

[55] A. Hickling et al. Use of IT (current vs temperature) scans to study radiation damage in the LHCb VELO. Technical Report LHCb-PUB-2011-021. CERN-LHCb-PUB-2011-021, CERN, Geneva, Oct 2011.

[56] P. Rodriguez. Radiation Damage in the LHCb VELO. *CERN-Poster-2012-240*, Jul 2012.

[57] P. Collins et al. The LHCb VELO upgrade. *Nuclear Instruments and Methods in Physics Research Section A: Accelerators, Spectrometers, Detectors and Associated Equipment*, 636(1, Supplement):S185 – S193, 2011. 7th International Hiroshima Symposium on the Development and Application of Semiconductor Tracking Detectors.

[58] X. Llopart et al. Timepix, a 65k programmable pixel readout chip for arrival time, energy and/or photon counting measurements. *Nuclear Instruments and Methods in Physics Research Section A: Accelerators, Spectrometers, Detectors and Associated Equipment*, 581(1-2):485–494, 2007.

[59] G. Casse et al. Enhanced efficiency of segmented silicon detectors of different thicknesses after proton irradiations up to $1 \times 10^{16} n_{eq} cm^{-2}$. *Nuclear Instruments and Methods in Physics Research Section A: Accelerators, Spectrometers, Detectors and Associated Equipment*, 624(2):401 – 404, 2010. Proceedings of the 11th European Symposium on Semiconductor Detectors.

[60] G. Pellegrini et al. 3D double sided detector fabrication at IMB-CNM. *Nuclear Instruments and Methods in Physics Research Section A: Accelerators, Spectrometers, Detectors and Associated Equipment*, 2012.

[61] A. Nomerotski et al. Evaporative CO_2 cooling for upgraded LHCb VELO detector using microchannels etched in silicon. *Nuclear Instruments and Methods in Physics Research Section A: Accelerators, Spectrometers, Detectors and Associated Equipment*, 2012.

[62] A. Mapelli et al. Microfluidic cooling for detectors and electronics. *Journal of Instrumentation*, 7(01):C01111, 2012.

[63] P Rodríguez Pérez. http://stacks.iop.org/1748-0221/7/i=12/a=C12008The LHCb VERTEX LOCATOR performance and VERTEX LOCATOR upgrade. *Journal of Instrumentation*, 7(12):C12008, 2012.

[64] K. Akiba et al. Precision scans of the Pixel cell response of double sided 3D Pixel detectors to pion and X-ray beams. *Journal of Instrumentation*, 6(05):P05002, 2011.

[65] K. Akiba et al. Charged particle tracking with the Timepix ASIC. *Nuclear Instruments and Methods in Physics Research Section A: Accelerators, Spectrometers, Detectors and Associated Equipment*, 661(1):31 – 49, 2012.

[66] K. Akiba et al. The Timepix Telescope for high performance particle tracking. *Nuclear Instruments and Methods in Physics Research Section A: Accelerators, Spectrometers, Detectors and Associated Equipment*, 723(0):47 – 54, 2013.

[67] Bediaga et al. Letter of Intent for the LHCb Upgrade. Technical Report CERN-LHCC-2011-001. LHCC-I-018, CERN, Geneva, Mar 2011. Source document will follow.

[68] Bediaga et al. Framework TDR for the LHCb Upgrade. Technical Report CERN-LHCC-2012-007. LHCB-TDR-012, CERN, Geneva, Apr 2012.

[69] G. Lutz. *Semiconductor Radiation Detectors: Device Physic*. Accelerator Physics Series. Springer-Verlag, 1999. ISBN: 3-540-64859-3.

[70] Rossi et al. *Pixel Detectors: From Fundamentals to Applications (Particle Acceleration and Detection)*. Springer, March 2006. ISBN: 1611-1052.

[71] H. Spieler. *Semiconductor Detector Systems (Semiconductor Science and Technology)*. Oxford University Press, USA, October 2005. ISBN: 978-0-19-852784-8.

[72] C. Leroy and P.G. Rancoita. *Silicon solid state devices and radiation detection*. World Scientific, Singapore, 2012. ISBN: 978-981-4390-04-0.

[73] S. Ramo. Currents induced by electron motion. *Proceedings of the IRE*, 27(9):584 – 585, sept. 1939.

[74] Daniel Hynds. The Timepix telescope for charged particle tracking. Oct 2012.

[75] V.M. Abazov et al. The upgraded DØ detector. *Nuclear Instruments and Methods in Physics Research Section A: Accelerators, Spectrometers, Detectors and Associated Equipment*, 565(2):463 – 537, 2006.

[76] S. Abachi et al. Observation of the Top Quark. *Phys. Rev. Lett.*, 74:2632–2637, Apr 1995.

[77] Experimental High Energy Physics Group. University of Santiago de Compostela.

[78] Microoptica y Óptica GRIN. University of Santiago de Compostela.

[79] F. Rey-Garcia et al. Fabrication of Metal-on-Glass High-Pitch Adapters Between VLSI Electronics and Semiconductor Sensors by Laser Ablation. *Lightwave Technology, Journal of*, 31(14):2327–2331, 2013.

[80] M. Demarteau et al. Characteristics of the Outer Layer Silicon Sensors for the Run IIb Silicon Detector. *DØ Note*, 4308, March 2003.

[81] J. Visser et al. A Gigabit per second read-out system for Medipix Quads. *Nuclear Instruments and Methods in Physics Research Section A: Accelerators, Spectrometers, Detectors and Associated Equipment*, 633, Supplement 1(0):S22 – S25, 2011. 11th International Workshop on Radiation Imaging Detectors (IWORID).

[82] E. Perez. HPK microstrip prototypes electrical characterization @ Santiago.

[83] Alibava Systems. Compact System for Radiation Sensor Characterisation.

[84] E.N. Gimenez et al. Evaluation of the radiation hardness and Charge Summing Mode of a Medipix3-based detector with synchrotron radiation. In *Nuclear Science Symposium Conference Record (NSS/MIC), 2010 IEEE*, pages 1976 –1980, 30 2010-nov. 6 2010.

[85] R. Ballabriga et al. Medipix3: A 64 k pixel detector readout chip working in single photon counting mode with improved spectrometric performance. *Nuclear Instruments and Methods in Physics Research Section A: Accelerators, Spectrometers, Detectors and Associated Equipment*, 633, Supplement 1(0):S15 – S18, 2011. 11th International Workshop on Radiation Imaging Detectors (IWORID).

USC
UNIVERSIDADE
DE SANTIAGO
DE COMPOSTELA

Epilogue

¡PRA A HABANA!
V

Este vaise i aquel vaise,
e todos, todos se van,
Galicia, sin homes quedas
que te poidan traballar.
Tes, en cambio, orfos e orfas
e campos de soledad,
e nais que non teñen fillos
e fillos que non tén pais.
E tes corazóns que sufren
longas ausencias mortás,
viuvas de vivos e mortos
que ninguén consolará.

Follas Novas
Rosalía de Castro

USC
UNIVERSIDADE
DE SANTIAGO
DE COMPOSTELA